

# High resolution rotation sensor based on cold atom interferometry

Von der Fakultät für Mathematik und Physik  
der Gottfried Wilhelm Leibniz Universität Hannover

zur Erlangung des Grades

Doktor der Naturwissenschaften

Dr. rer. nat.

genemigte Dissertation

von

Thijs Jan Wendrich M.Sc.

geboren am 12. Februar 1980 in Dordrecht

2010

Referent: Prof. Dr. Rasel  
Korreferent: Prof. Dr. Pfnür  
Tag der Promotion: 14. Januar 2010

# Abstract

The very high sensitivity of matter-wave interferometry for detecting accelerations and rotations has made it to an ideal tool for applications in fundamental physics and metrology.

The apparatus presented in this thesis uses the synchronous operation of two counterpropagating atom interferometers to discriminate between accelerations and rotations. The ensembles of  $8 \mu\text{K}$  cold  $^{87}\text{Rb}$  atoms are launched with a velocity of about  $2.8 \text{ m/s}$  from two double-MOT sources on precisely controlled parabola trajectories into the interferometer chamber. After the preparation of the atoms in the ground state, a sequence of three atom-light interactions follows in the interferometry chamber to split, reflect and recombine the atoms, forming a Mach-Zehnder style interferometer. The beam splitter and mirror pulses use a two-photon Raman transition to be able to coherently transfer a large momentum to the atoms to enclose a large area. The detection of the atomic state is realized by measuring the fluorescence light in both output states in each interferometer. The setup is compact and transportable while still enabling sensitivities comparable to the best conventional sensors. When extrapolating the achieved values of  $10^7$  atoms/s with an interferometry time of  $2T = 46 \text{ ms}$  and signal to noise ratio of 32 to the inertially sensitive case, an area of  $17 \text{ mm}^2$  would be enclosed and the resolution would be  $7 \cdot 10^{-7} \text{ rad/s}\sqrt{\text{Hz}}$  for rotations and  $4 \cdot 10^{-6} \text{ m/s}^2\sqrt{\text{Hz}}$  for accelerations.

A high reliability laser system has been implemented with excellent stability and accuracy enabling more than day of measuring without any laser failures. The frequency of important laser systems can be set and modified with a phase locked loop technique with sub-Hz accuracy relative to the reference laser. An advanced electronic and software control system has been implemented that enables a high flexibility in the design of complex experimental patterns with many pulses and tight timing requirements on all channels.

This highly flexible and sensitive instrument is capable of measuring rotations and accelerations as well as measure the transition frequency. It is also applied for other studies related to number factorization with the Gauss-sum algorithm. Simultaneous loading and free flight operation with high repetition rates up to  $7 \text{ Hz}$  as well as inertially insensitive fringes across all three windows ( $2T = 46 \text{ ms}$ ) are shown in this work.

**Keywords:** Atom interferometry, laser cooling, inertial sensors

# Zusammenfassung

Die sehr hohe Empfindlichkeit von Materiewelleninterferometrie für die Messung von Rotation und Beschleunigung hat sie zu einem idealen Werkzeug für Anwendungen in der fundamentalen Physik und in der Metrologie gemacht.

Das in dieser Arbeit vorgestellte Gerät wird, benutzt den synchronen Betrieb zweier gegenläufiger atomarer Interferometer zur Unterscheidung von Rotation und Beschleunigung. Die Ensembles von  $8 \mu\text{K}$  kalten  $^{87}\text{Rb}$ -Atomen werden mit einer Geschwindigkeit von etwa  $2.8 \text{ m/s}$  von zwei Doppel-MOT Quellen auf genau kontrollierte Parabelbahnen durch die Hauptkammer gestartet. Nach der Präparation der Atome im Grundzustand folgt eine Sequenz von drei Atom-Licht-Wechselwirkungen welche die Atomen teilt, reflektiert und wieder rekombiniert, um so ein Mach-Zehnder ähnliche Interferometer zu realisieren. Für die Strahlteiler- und Spiegel-Pulse werden zwei-Photon Raman-Übergänge genutzt um kohärent einen großen Impuls auf die Atomen zu übertragen um damit eine große Fläche aufzuspannen. Die anschließende Bestimmung der Besetzung der atomaren Zustände wird mit Hilfe einer zustandsselektiven Fluoreszenzmessung realisiert. Der gesamte Aufbau ist kompakt und transportabel und hat zugleich eine Sensitivität, die mit den besten konventionellen Sensoren vergleichbar ist. Wenn man die erreichten Ergebnisse von  $10^7$  Atomen/s bei einer Interferometriezeit von  $2T = 46 \text{ ms}$  und einem Signal-zu-Rausch Verhältnis von 32 auf den inertial sensitiven Fall extrapolieren würde, dann wäre eine Fläche von  $17 \text{ mm}^2$  eingeschlossen und die Auflösung für Rotation  $7 \cdot 10^{-7} \text{ rad/s}\sqrt{\text{Hz}}$  und für Beschleunigung  $4 \cdot 10^{-6} \text{ m/s}^2\sqrt{\text{Hz}}$ .

Ein sehr zuverlässiges Lasersystem mit einer hervorragende Stabilität und Genauigkeit, welche es ermöglicht, einen ganzen Tag ohne ein Ausfall der Laser zu messen, wurde aufgebaut. Die Frequenz und Phase von wichtigen Lasersystemen wird mit einer Phase-Locked-Loop Methode mit sub-Hz Genauigkeit relativ zum Referenzlaser festgelegt und gesteuert. Ein fortschrittliches elektronisches und Software-Steuerungssystem, welches eine hohe Flexibilität in den Entwurf von komplexen experimentellen Abläufen mit viele Pulsen und engen zeitlichen Anforderungen auf alle Kanälen erlaubt, wurde implementiert.

Dieser sehr flexible und sensitive atominterferometrische Aufbau ist in der Lage Rotationen und Beschleunigungen ebenso wie atomare Übergangsfrequenzen zu messen. Des weiteren ist es für andere Studien angelehnt an die Faktorisierung von Zahlen mit Hilfe des Gauss Algorithmus angewandt worden. Das Laden der MOT mit zeitgleich der freie Flug mit hoher Taktrate bis zu  $7 \text{ Hz}$  ebenso wie Interferenzsignalen einer inertial insensitiven Interferometer über alle drei Fenster ( $2T = 46 \text{ ms}$ ) werden in dieser Arbeit gezeigt.

**Schlagwörter:** Atominterferometrie, Laserkühlung, Inertialsensoren



# Samenvatting

De zeer hoge gevoeligheid van materie-golf-interferometrie voor het meten van rotatie en versnelling had het tot een ideaal gereedschap in de fundamentele natuurkunde en metrologie gemaakt.

Het apparaat dat in dit werk voorgesteld wordt, maakt gebruik van twee gelijktijdige interferometers in tegenovergestelde richting ter onderscheiding van rotatie en versnelling. De ensembles van  $8 \mu\text{K}$  koude  $^{87}\text{Rb}$  atomen worden met een snelheid van ongeveer  $2.8 \text{ m/s}$  vanuit twee tweetraps MOT bronnen op precies gecontroleerde parabolische banen richting de hoofdkamer geschoten. Na het prepareren van de atomen in de grondtoestand volgt een rij van drie atoom-lichtwisselwerkingen die de atomen delen, reflecteren en weer samenvoegen om zo een soort Mach-Zehnder interferometer te vormen. De straaldeler- en spiegelpulsen gebruiken twee-foton-Raman-overgangen om coherent een grote impuls op de atomen over te brengen en zo een groot oppervlak te omsluiten. De aansluitende detectie van de atomare toestand is met behulp van toestandsselektieve fluorescentie metingen gerealiseerd. De gehele opbouw is compact en transportabel en heeft tegelijkertijd een sensitiviteit die vergelijkbaar is met de beste conventionele sensoren. Als men de bereikte resultaten van  $10^7$  atomen/s bij een interferometrie-tijd van  $2T = 46 \text{ ms}$  en een signaal-ruis-verhouding van 32 naar het inertiaal sensitieve geval zou extrapoleren, dan zou een oppervlakte van  $17 \text{ mm}^2$  worden ingesloten met een resolutie van  $7 \cdot 10^{-7} \text{ rad/s}\sqrt{\text{Hz}}$  voor rotatie en van  $4 \cdot 10^{-6} \text{ m/s}^2\sqrt{\text{Hz}}$  voor versnelling.

Een zeer betrouwbaar lasersysteem met een uitstekende stabiliteit en nauwkeurigheid is opgebouwd waarmee het mogelijk is een hele dag te meten zonder uitval in het lasersysteem. De frequentie en de fase van de belangrijkste lasersystemen worden met een Phase-Locked-Loop methode met sub-Hz nauwkeurigheid relatief tot de referentie-laser vastgelegd en gestuurd. Een geavanceerd elektronisch en software stuursysteem is geïmplementeerd dat een hoge flexibiliteit bij het ontwerpen van experimentele aflopen met veel pulsen met strikte timing eisen op alle kanalen mogelijk maakt.

Dit zeer flexibele en gevoelige apparaat is in staat om rotatie en versnelling als ook atomare overgangsfrequenties te meten. Verder is dit apparaat ook toegepast in andere studies gerelateerd aan het factoriseren van getallen met behulp van het Gauss-algoritme. Signalen van een inertiaal insensitieve interferometer over alle drie vensters ( $2T = 46 \text{ ms}$ ) als ook eerste metingen van het laden van de MOT met gelijktijdig metingen aan de vrije vlucht bij hogere herhaalfrequenties tot  $7 \text{ Hz}$  worden in dit werk getoond.

**Sleutelwoorden:** Atoom-interferometrie, laser-koelen, inertiaal-sensoren

# Contents

<b>1. Introduction</b>	<b>9</b>
1.1. Rotation measurements . . . . .	9
1.2. Matter wave interferometry . . . . .	11
1.3. Applications of high resolution rotation measurements . . . . .	13
1.4. This experiment . . . . .	13
1.5. This work . . . . .	14
<b>2. Theory</b>	<b>16</b>
2.1. Quantum mechanical description . . . . .	16
2.1.1. Detunings . . . . .	16
2.1.2. Rabi frequencies . . . . .	18
2.1.3. Time evolution . . . . .	19
2.1.4. Bloch sphere . . . . .	20
2.2. Phase contributions . . . . .	23
2.3. Signal to phase . . . . .	25
2.4. Thermal atoms . . . . .	27
2.5. Noise and tolerances . . . . .	28
2.5.1. MOT . . . . .	28
2.5.2. Start . . . . .	29
2.5.3. Interferometry . . . . .	29
2.5.3.1. Timing errors . . . . .	29
2.5.3.2. Frequency errors . . . . .	30
2.5.3.3. Temporal phase noise . . . . .	31
2.5.3.4. Intensity noise . . . . .	33
2.5.3.5. Alignment . . . . .	33
2.5.3.6. Wavefront . . . . .	35
2.5.4. State detection . . . . .	36
2.5.4.1. Temporal sensitivity . . . . .	37
2.5.4.2. Spatial sensitivity . . . . .	37
<b>3. Implementation</b>	<b>39</b>
3.1. Vacuum . . . . .	39
3.2. Vibration isolation . . . . .	39
3.3. 2D MOT . . . . .	40
3.4. 3D MOT with moving molasses . . . . .	42
3.5. State preparation . . . . .	46
3.6. Interferometry . . . . .	49
3.7. State detection . . . . .	52

## Contents

3.8. Combined state preparation and detection . . . . .	55
<b>4. Realization of the light fields</b>	<b>59</b>
4.1. Distribution and switching . . . . .	59
4.1.1. 2D-MOT light . . . . .	59
4.1.2. 3D-MOT/Molasses light . . . . .	59
4.1.3. Interferometry light . . . . .	61
4.1.4. pusher/blow away/detection . . . . .	62
4.2. Light source . . . . .	63
4.2.1. Reference Laser . . . . .	64
4.2.2. 2D-MOT cooling Laser . . . . .	65
4.2.3. 3D-MOT cooling Laser . . . . .	67
4.2.4. Repumping Laser . . . . .	67
4.2.5. Raman Master . . . . .	68
4.2.6. Raman Slave . . . . .	68
4.3. RF Frequency . . . . .	70
4.3.1. Reference oscillator . . . . .	70
4.3.2. 7 GHz chain . . . . .	70
4.3.3. Frequency distribution . . . . .	72
4.3.4. DDS . . . . .	72
4.3.4.1. AD9956 with phase locked VCO . . . . .	75
4.3.4.2. AD9852 . . . . .	75
4.4. Experiment Control . . . . .	76
4.4.1. Computers . . . . .	76
4.4.2. Main program . . . . .	78
4.4.3. FPGA . . . . .	79
4.4.3.1. Internal operation of “FPGA.vi” . . . . .	81
4.4.3.2. Timing of “FPGA.vi” . . . . .	82
4.4.3.3. Application . . . . .	83
<b>5. Atomic Measurements</b>	<b>84</b>
5.1. Rabi oscillations . . . . .	84
5.2. Frequency measurements . . . . .	87
5.3. Phase jump settling time . . . . .	90
5.4. Mach-Zehnder interferometry . . . . .	91
5.4.1. Inertially insensitive . . . . .	91
5.4.2. Inertially sensitive . . . . .	92
5.5. Gauss sum factorization . . . . .	95
5.6. High sample rate . . . . .	101
<b>6. Outlook</b>	<b>104</b>
<b>A. Rubidium-87 data</b>	<b>108</b>
<b>B. Derivation of the Sagnac equation</b>	<b>110</b>

## Contents

<b>C. CAD Drawings</b>	<b>113</b>
C.1. Vacuum chamber . . . . .	113
C.2. Bias coils . . . . .	115
<b>D. Electronic circuits</b>	<b>116</b>
D.1. AD9852 . . . . .	116
D.2. AD9956 . . . . .	117
D.3. PPG20 . . . . .	126
D.4. 100 to 10 MHz . . . . .	128
D.5. 100 to 400 MHz . . . . .	132
D.6. FreqGenFix and FreqGenFix2 . . . . .	133
D.7. VCO . . . . .	136
D.8. PLL_Beat . . . . .	137
D.9. Frequency to Voltage converter . . . . .	139
D.10.PID . . . . .	140
D.11.FPGA DAC . . . . .	144
D.12.Laser Current Driver . . . . .	145
D.13.Photodiodes . . . . .	146
<b>E. Source code</b>	<b>151</b>
E.1. Bias coil optimization . . . . .	151
E.2. Instantaneous frequency analysis . . . . .	160
E.3. Labview FPGA . . . . .	162
<b>List of symbols and abreviations</b>	<b>171</b>
<b>Bibliography</b>	<b>175</b>

# 1. Introduction

Front line research has always relied on high resolution sensors that operate at the limits of what is possible. For the current questions in geophysics and fundamental physics but also navigation, gyroscopes with very high resolution are needed.

## 1.1. Rotation measurements

Methods for measuring rotations can be divided in two groups, one that looks at the motion relative to some other object, and one that looks at the deviations from an ideal local inertial frame. One of the oldest examples of measuring rotations by looking at the relative motion to another object is astronomy: based on the movement of the stars in the night sky, it is obvious that the earth (or the sky) is rotating at about  $360^\circ$  per day. Modern very long base line interferometry methods [1] can measure the earth rotation rate relative to very distant quasars with a resolution of  $1 \cdot 10^{-14}$  rad/s<sup>1</sup>.

Traditional methods for measuring rotations as deviations from the ideal inertial frame either used the conservation of momentum of a rigid body, or used the wave nature of light.

The Foucault pendulum [4] in 1851 in the Panthéon in Paris was the first laboratory experiment that directly showed that the Earth was rotating. It is based on the fact that a swinging pendulum will continue to swing in the same direction it has started when there are no other forces acting upon it, it therefore showed that it was the earth that was rotating and not the pendulum.

The first gyroscope based on a heavy spinning sphere, which is carefully supported to avoid any torques from the suspension, was designed by Bohnenberger [5] in 1817. It makes use of the conservation of momentum which, in the absence of additional torques, keeps the rotation axis constant and it is therefore the suspension that is moving around it. Unfortunately the technology of that time could not keep the sphere in motion long enough to also show the rotation of the earth. The first practical gyroscopes that could do that came from the beginning of the 20th century when electric motors were added to the system to replace the momentum lost due to friction.

The best mechanical gyroscopes today are the ones used by the satellite mission Gravity Probe B [6]. They are extremely well polished spheres operating in free fall in vacuum, with the angles read out by SQUIDs [7]. They were sensitive enough [8] to detect the frame dragging effect as predicted by Lense and Thirring [9].

---

<sup>1</sup>VLBI actually measures angles, not rotation rate, with a typical accuracy of 0.2 milliarcsecond [2, 3], and which are typically tracked over 24 hours.

## 1. Introduction

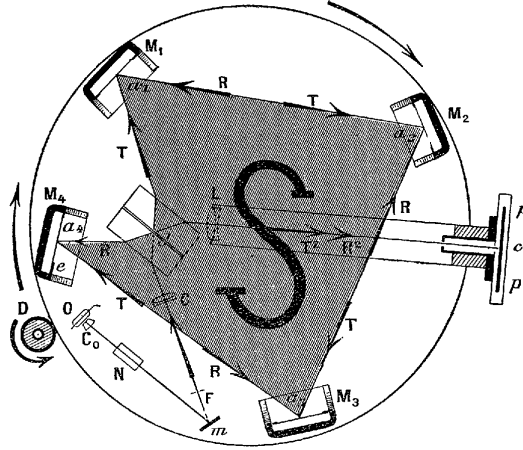


Figure 1.1.: The original setup of the interferometer used by Sagnac. The light source is a lamp at point O, the beam splitter is at J, and observed is with a photographic film between P and P'. Reproduction from [10].

The first optical rotation sensor was the interferometer Sagnac [11, 10] built in 1913, which splits a light wave and sends the two beams in opposite direction through the same loop and afterwards overlaps them again so that constructive or destructive interference can be observed at the output. The resulting phase difference is then given by:

$$\phi_{Sagnac} = \frac{2\pi}{\lambda c} 4\vec{\Omega} \cdot \vec{A}, \quad (1.1)$$

with  $c$  the velocity of light,  $\vec{\Omega}$  the rotation rate and  $\vec{A}$  as the enclosed area. The Mach-Zehnder-like interferometer that is used for the matter waves has a phase shift that is only half of the Sagnac shift. A somewhat elaborate derivation of this equation for a generic interferometer (Sagnac, Mach-Zehnder or other type) is given in appendix B.

The main parameters one can use to improve the sensitivity are the enclosed area and the wavelength. Because the phase shifts are rather small, the famous Michelson, Gale, Pierson experiment [12] of 1925 needed a very large area of  $612 \times 339 \text{ m}^2$  to measure a phase shift of 1.48 rad due to the earth rotation.

The invention of the ring laser gyroscope by Macek and Davis in 1963 [13] allowed for a much better accuracy because it replaces the phase measurement of the passive Sagnac interferometer with a frequency measurement. The frequency difference between the clockwise and counterclockwise mode of the ring laser is given by:

$$\Delta f_{ringlaser} = \frac{4\vec{A} \cdot \vec{\Omega}}{\lambda l}, \quad (1.2)$$

with  $l$  the length of the perimeter of the enclosed area.

The current best [14] ring laser gyroscope is ‘‘G’’ in Wettzell [15], with a square shape of  $4 \times 4 \text{ m}^2$  operating at 633 nm with a difference frequency of 349 Hz

## 1. Introduction

which can easily be measured to some ppm giving an effective rotation resolution of  $10^{-10}$  rad/s/ $\sqrt{\text{Hz}}$ . There are even larger ring laser gyroscopes up to  $21 \times 40 \text{ m}^2$  [14] in operation but they suffer from mechanical instability.

### 1.2. Matter wave interferometry

In order to realize a matter wave interferometer, one has to be able to control the particles of the matter wave, that is the atoms, very accurately. This involves a method to collimate the matter wave, as well as having a way to coherently manipulate the matter wave to make beam splitters and mirrors.

For the operation of an interferometer one also needs to have a well defined wavelength, which for a matter wave means a well defined velocity, but the coherence does not always need to be as good as that of a laser, in fact some early interferometers used a light bulb as light source.

The purpose of cooling of atoms for matter wave interferometry is twofold: first to increase the effective number of atoms by collimating the cloud or beam of atoms, and second to increase the coherence length. To achieve this, the atoms need to be slowed down to velocities of a few cm/s (in a moving frame).

Cooling via collisions with the walls of a vacuum chamber, even when they are cooled with liquid helium is not enough, as the velocities corresponding to such temperatures are about 30 m/s for rubidium. Cooling with light has turned out to be far more effective.

It is based on laser light that is red detuned relative to a transition frequency and depends on the Doppler shift to shift the transition to or away from the resonance resulting in a velocity dependent force on the atoms that slows down the atoms. This so called Doppler cooling was predicted by Hänsch [16] in 1975 and experimentally achieved in 1985 by Chu [17].

The Magneto Optical Trap (MOT) which not only cools but also captures a cloud of cold atoms was developed shortly afterwards in 1987 by [18], it is based on the application of Doppler cooling along all three axis in combination with a spatially dependent magnetic field.

Temperatures below the Doppler limit were first experimentally observed in 1988 [19] and shortly afterwards theoretically explained [20, 21] by also taking into account the substructure of the atoms.

For ground based atom interferometers, like the one presented in this thesis, this was enough.

The race towards even lower temperatures continued however with sub-recoil cooling [22] and finally Bose-Einstein condensation (BEC) [23, 24] in 1995 enabling more exotic methods like QND and squeezing [25].

In order to do interferometry the atoms have to behave like a wave. This took the development of quantum mechanics which started in 1905 when Einstein proposed that light comes in particles, the so called photons, each carrying an energy given by [26]:

## 1. Introduction

$$E_{\text{photon}} = h \cdot f = \frac{hc}{\lambda}, \quad (1.3)$$

with  $h$  as Plank's constant,  $c$  the speed of light,  $f$  the frequency of the light and  $\lambda$  the wavelength of the light. In the same year Einstein also published his famous equation for the energy of a particle with mass  $m$  [27]:

$$E_{\text{atom}} = mc^2. \quad (1.4)$$

It took until 1924 before it was realized that atoms and photons have more in common than being particles with a common property of energy, when de Broglie proposed the idea that not only light is a wave with particle properties but that also matter can be treated as wave with the wavelength given by [28]:

$$\lambda = \frac{h}{p} = \frac{h}{mv}, \quad (1.5)$$

with  $p$  the impulse of a particle with velocity  $v$  and mass  $m$ . This opened up the way for doing matter wave interference.

Using equation 1.4 and 1.5 the Sagnac phase of equation 1.1 can be replaced with a more general version:

$$\phi_{\text{Sagnac}} = \frac{4\pi E}{hc^2} \vec{\Omega} \cdot \vec{A}. \quad (1.6)$$

Here  $E$  is the energy of the particles used to do the interferometry. A simple comparison of the energy of a photon ( $\lambda = 633$  nm, 2 eV) with the energy of an atom (rubidium-87,  $8 \cdot 10^{10}$  eV) shows that there is a huge gain of about 10 orders of magnitude in sensitivity possible if the other parameters stay constant. Or one can get the same sensitivity of the Michelson-Gale-Pierson experiment with only a few square millimeter instead of 29 soccer fields.

The first atom interferometer with carefully controlled beam splitters based on (microwave) light was introduced by Ramsey in 1950 in his paper on spectroscopy with separate oscillating fields [29], although not recognized as an interferometer at that time. This method is still used for atomic clocks.

In 1989 Bordé [30] proposed the use of the momentum of optical photons to obtain larger recoil velocities to realize highly sensitive atom interferometers for the measurement of inertial forces.

The first (intentional) atom interferometers were Riehle [31] in 1991 using a calcium beam apparatus showing that the Sagnac effect can cause offsets in optical clocks and at the same time by Kasevich and Chu [32] using a gravimeter setup using sodium atoms.

After that many atom interferometers were build measuring the local gravity  $g$  [33, 34], Newtons gravitational constant  $G$  [35, 36],  $h/m$  ( $\alpha$ ) [37] and rotations [38, 39].



### 1.3. Applications of high resolution rotation measurements

The most obvious application for measurements of inertial forces is navigation. To obtain a position from a given starting position and measurements of acceleration and rotation one has to integrate over them, which requires very accurate measurements as the resulting error grows rapidly.

One of the things of interest in the geo-sciences are the tiny variations of the daily rotation rate of the earth (about  $7.27 \cdot 10^{-5}$  rad/s<sup>2</sup>). These so called “length of day” fluctuations are on the scale of a few ms [40] per day or a few parts in  $10^8$  of the earth rotation ( $7 \cdot 10^{-13}$  rad/s), they are mostly due to tidal motions of the oceans and atmosphere and other effects that are not yet entirely understood [41]. More compact and sensitive instruments than the current generation of large ring lasers are required [14] to better investigate these weak signals.

The rotational components of seismic events (earthquakes) are also a subject of current investigations [42, 41].

The effects of interest in fundamental physics are mostly related to general relativity and will be not measurable on earth but only in orbit.

One of the most interesting effects in fundamental physics related to rotations are the geodetic precession and the frame dragging effect [9] as predicted by general relativity. The Gravity Probe B [8] experiment has succeeded in measuring the frame dragging effect. The proposed HYPER satellite [43] would improve on that and reach  $10^{-16}$  rad/s in one year (enough to also measure the galactic rotation rate of one round per 200 million years).

Gravitational waves [44] as also predicted by general relativity, have rotational components that several authors have considered [45, 46] for detection.

### 1.4. This experiment

The goal of this work is to realize a compact high resolution rotation sensor based on atom interferometry with cold atoms that would be transportable, stable, reliable and flexible. The work presented here builds on the previous work of Jentsch [47] and Müller [48].

The transportability is necessary for precision experiments to make calibrations to known standards, and to make comparisons with other devices of similar precision to find out what the limitations of the experiments are. As such high precision experiments are rarely build more than once in one place, there is a need to be able to move the experiment to other locations.

Furthermore the experiment should be reliable and stable enough to be able to operate over long periods of time and be able to average over long periods to detect

---

<sup>2</sup>This is slightly more than  $2\pi$  rad per 24 hour because the earth is also rotating around the sun.

## 1. Introduction

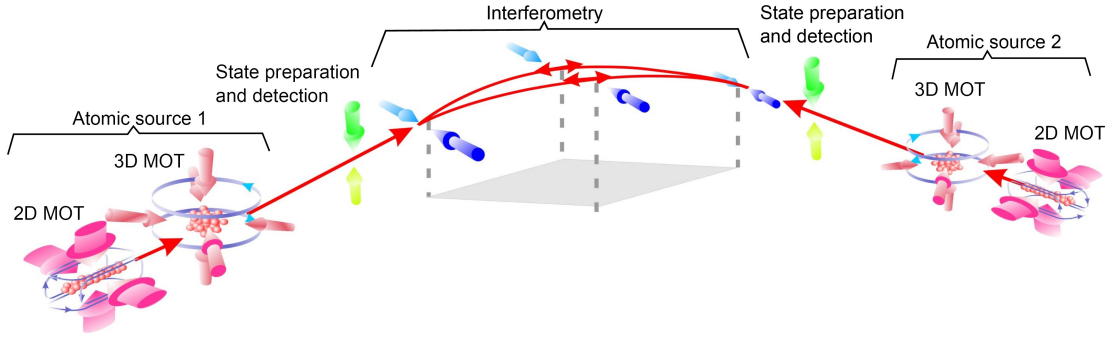


Figure 1.2.: Schematic overview of the experimental setup showing the symmetric set up with the two-stage atomic sources, the state preparation and detection zones and the central interferometry zone.

very small signals and also measure signals with a long period as are common in geophysics.

The flexibility is necessary because cold atom rotation sensors are a new field of research, where it is still important to be able to test different methods like continuous or pulsed mode of operation, or different interferometer sequences. Also for the investigation of systematic effects it will be important to test many different parameters.

To achieve these goals, the setup of figure 1.2 has been chosen. The use of cold atoms allows much lower velocities compared to [49] resulting in a more compact setup with better stability. The cold atom sources have each a two stage Magneto Optical Trap (MOT) to ensure a low atomic temperature with a high flux. The actual interferometer uses three pulses to split, reflect and recombine the atoms, forming a Mach-Zehnder style interferometer. The beam splitter and mirror pulses use a two-photon Raman transition to be able to transfer a (relatively) large momentum to the atoms to enclose a large area. Because of the Mach-Zehnder style half loop trajectory, it is also sensitive to acceleration. The use of counterpropagating atomic trajectories allows to separate rotation from acceleration [39]. The chosen trajectories are flat parabolas, in contrast to the steep parabolas of [50], this also allows to investigate concepts for a possible space mission (HYPER [43], MWXG [51]) where the trajectory would be a straight line as there is no gravity to compensate.

With the targeted values of  $10^8$  atoms and a drift time of  $2T = 50$  ms, an area of  $22 \text{ mm}^2$  would be enclosed and the shot noise limited resolution would be  $2 \cdot 10^{-9} \text{ rad/s}\sqrt{\text{Hz}}$  for rotations and  $1 \cdot 10^{-8} \text{ m/s}\sqrt{\text{Hz}}$  for accelerations.

### 1.5. This work

Chapter 2 describes the theory and ideas behind this gyroscope as well as some of its limitations. The chapters 3 and 4 describe the the actual hardware implementation. Chapter 3 revolves around the core components like the atomic sources, the vacuum and the magnetic fields (“hardware package”) and chapter 4 (as well

## *1. Introduction*

as appendix D and E) has the details about the used lasers, light manipulations, electronics and control systems (“support systems”). Chapter 5 shows the results of the device. Chapter 6 gives an outlook of things to come, things to improve and things to think about.

## 2. Theory

In this chapter the key parameters and design equations are derived to be able to estimate the performance of the Mach-Zehnder configuration of an atom interferometer for rotation measurement.

Section 2.1 describes the interaction between the light fields and the atoms, section 2.2 describes the main phase contributions. Section 2.3 goes into detail about how to extract the phase from the atomic measurement also in the case for less ideal situations. Section 2.4 describes the key properties of the cloud of thermal atoms. Section 2.5 goes into detail about the temporal behavior of the various components due to the pulsed nature of the interferometer sequence as well as estimates of noise and other limitations.

### 2.1. Quantum mechanical description

To do any useful atom interferometry one needs atoms with long living states, to avoid spontaneous decay that destroys the coherence. The two hyperfine splitted ground states of rubidium 87 are a frequent choice for this, especially the magnetically insensitive  $m_f = 0$  Zeeman-substates. In order to realize a high sensitivity for inertial forces one needs also to be able to transfer large momenta to the atoms. Unfortunately the recoil velocity of the microwave photons that can directly drive this transition is only about  $1.0 \cdot 10^{-7}$  m/s. This can be improved by using a stimulated Raman transition with two optical photons, giving a total recoil velocity of 11.8 mm/s. Such transitions occur in a  $\Lambda$ -system like that of figure 2.1. The atom effectively absorbs a photon from one light field and emits another photon into the second light field.

In the following discussion the ground state  $|g\rangle$  and the excited state  $|e\rangle$  are a combination of the internal state and the external impulse of the rubidium 87 atoms and are defined as:

$$\begin{aligned} |g\rangle &= \left| 5^2S_{1/2}, F = 1, m_f = 0, 0 \right\rangle \\ |e\rangle &= \left| 5^2S_{1/2}, F = 2, m_f = 0, +\hbar \vec{k}_{eff} \right\rangle . \end{aligned} \quad (2.1)$$

Here  $|e\rangle$  has an additional momentum due to the absorbed photon momentum  $\vec{k}_{eff}$  of the two photon transition.

#### 2.1.1. Detunings

The effective wave vector for the two photon Raman transition is given by:

## 2. Theory

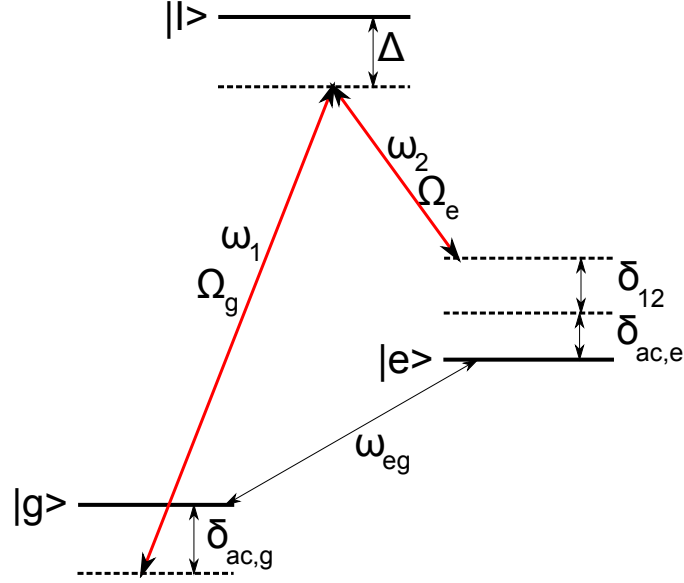


Figure 2.1.: Schematic of the two-photon Raman transition with the relevant detunings.

$$\vec{k}_{eff} = \vec{k}_1 - \vec{k}_2 \quad (2.2)$$

This has a minus sign because the atom absorbs a photon from the first light field and emits it into the second light field. The interferometer as shown in this thesis can operate with two types of Raman transition, one which has the wave vectors  $\vec{k}_1$  and  $\vec{k}_2$  in the same direction with very little momentum transfer, and one which has  $\vec{k}_1$  and  $\vec{k}_2$  in the opposite direction with very high momentum transfer.

Due to the extra momentum of the excited state, it has an extra velocity which causes a Doppler shift given by [52]:

$$\delta_{Doppler} = \frac{\vec{p} \cdot \vec{k}_{eff}}{m} \quad (2.3)$$

with  $m$  as the mass of the atoms and  $\vec{p}$  the momentum of the atoms ( $m \cdot \vec{v}$ ). The recoil shift is given by:

$$\delta_{recoil} = \frac{\hbar |\vec{k}_{eff}|^2}{2m}. \quad (2.4)$$

The presence of light fields also shift the energy levels. These so called AC-Stark shifts of the ground and excited level are given by [53]:

$$\begin{aligned} \delta_{ac,g} &= \frac{|\Omega_g|^2}{4\Delta} + \frac{|\Omega_e|^2}{4(\Delta - \omega_{eg})}, \\ \delta_{ac,e} &= \frac{|\Omega_e|^2}{4\Delta} + \frac{|\Omega_g|^2}{4(\Delta + \omega_{eg})} \end{aligned} \quad (2.5)$$

## 2. Theory

with  $\Delta$  as the detuning of the two light fields with respect to the  $|5^2P_{3/2}, F' = 1\rangle$  level.

With that the differential AC-Stark shift becomes:

$$\delta_{ac} = \delta_{ac,e} - \delta_{ac,g}. \quad (2.6)$$

The total detuning between the light fields and the shifted atomic transition becomes:

$$\delta = (\omega_1 - \omega_2) - \omega_{eg} - \delta_{Doppler} - \delta_{recoil} - \delta_{ac}, \quad (2.7)$$

with  $\omega_1$  and  $\omega_2$  as the angular frequencies of the two light fields and  $\omega_{eg}$  is the difference frequency between the  $|g\rangle$  and  $|e\rangle$  states (without any shifts).

The detuning without AC Stark shift is:

$$\delta_{12} = \delta + \delta_{ac}. \quad (2.8)$$

### 2.1.2. Rabi frequencies

In the presence of a light field, a two-level atom will show oscillations with the characteristic Rabi frequency in the probability function of its Eigenstates, see also figure 2.2.

The Rabi frequencies of the two individual transitions of the Raman transition, describing the transition rate between the ground and intermediate level in the presence of a light field, are [54]:

$$\Omega_g = \sqrt{\frac{I_1}{2I_{sat}}} \Gamma, \quad (2.9)$$

$$\Omega_e = \sqrt{\frac{I_2}{2I_{sat}}} \Gamma \quad (2.10)$$

with  $\Gamma$  as the natural linewidth,  $I_{sat}$  as the saturation intensity and  $I_1$  and  $I_2$  as the intensity of master and slave laser.  $\Gamma$  and  $I_{sat}$  are properties of the used atomic species, the typical values of rubidium 87, which was used for this thesis, are given in appendix A.

The combined Rabi frequency, describing the transition rate between the ground and excited state for the Raman transition, is:

$$\Omega_0 = \frac{\Omega_e^* \Omega_g}{2\Delta}. \quad (2.11)$$

The effective Rabi frequency of this transition in the presence of detunings is:

$$\Omega_{eff} = \sqrt{\Omega_0^2 + \delta^2}. \quad (2.12)$$

## 2. Theory

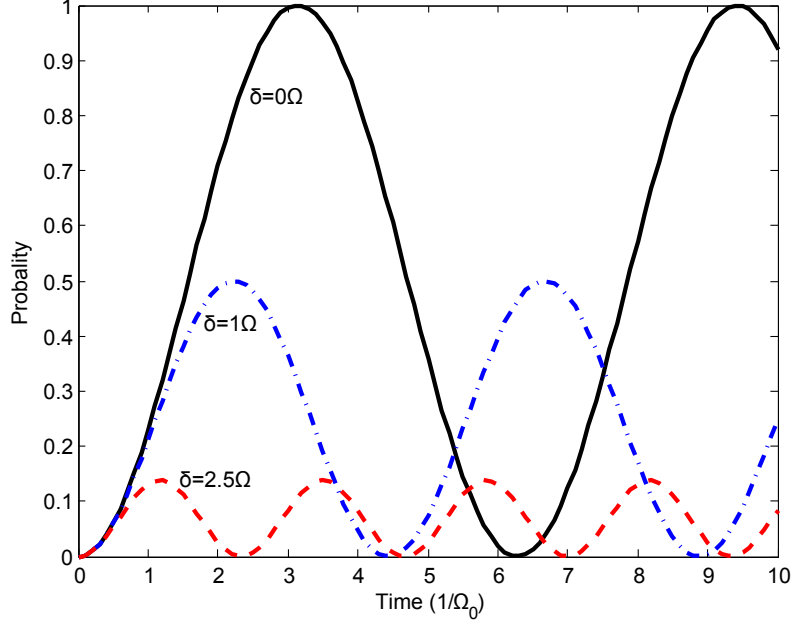


Figure 2.2.: The probability to find an atom in the excited state ( $P(|e\rangle)$ ) when starting in the ground state in the presence of a light field as a function of time for different detunings  $\delta = 0, 1, 2.5\Omega_0$ .

### 2.1.3. Time evolution

The atomic state can be defined as  $|\Psi\rangle = c_g(t)|g\rangle + c_e(t)|e\rangle$ . The time evolution of the state vector  $\vec{C} = (c_g, c_e)$  can be described with :

$$\vec{C}_{end} = \mathbf{m} \cdot \vec{C}_{start} \quad (2.13)$$

The matrix  $\mathbf{m}$  describes the time evolution of the effective two level system:

$$m = \begin{pmatrix} \cos(\Omega_{eff}t/2) - i\frac{\delta}{\Omega_{eff}} \sin(\Omega_{eff}t/2) & -e^{i\phi}i\frac{\Omega_0}{\Omega_{eff}} \sin(\Omega_{eff}t/2) \\ -e^{-i\phi}i\frac{\Omega_0}{\Omega_{eff}} \sin(\Omega_{eff}t/2) & \cos(\Omega_{eff}t/2) + i\frac{\delta}{\Omega_{eff}} \sin(\Omega_{eff}t/2) \end{pmatrix} \quad (2.14)$$

with  $\phi$  as the phase of the light field.

For the an atom interferometer some values of  $\Omega_{eff}t$  have a special meaning. For  $\Omega_{eff}t = \pi/2$ , on resonance ( $\delta = 0$ ), the matrix  $\mathbf{m}$  becomes:

$$\mathbf{m}_{\pi/2} = \begin{pmatrix} \frac{1}{2}\sqrt{2} & -e^{i\phi}i\frac{1}{2}\sqrt{2} \\ -e^{-i\phi}i\frac{1}{2}\sqrt{2} & \frac{1}{2}\sqrt{2} \end{pmatrix}. \quad (2.15)$$

Because this matrix transfers half of the ground state to the excited state and vice versa it is also called a beam splitter.

For  $\Omega_{eff}t = \pi$ , also on resonance, the matrix becomes:

$$\mathbf{m}_{\pi} = \begin{pmatrix} 0 & -ie^{i\phi} \\ -ie^{-i\phi} & 0 \end{pmatrix}. \quad (2.16)$$

## 2. Theory

As this matrix indicates, it exchanges the population of the ground and excited level, hence the name mirror-pulse.

For the free evolution the matrix  $\mathbf{m}$  simplifies to:

$$\mathbf{m}_{free} = \begin{pmatrix} e^{-i\delta t/2} & 0 \\ 0 & e^{i\delta t/2} \end{pmatrix}. \quad (2.17)$$

which shows a phase shift depending on the detuning and the time of free evolution.

The probability of finding an atom in the ground state is finally given by:

$$P(|g\rangle) = |c_g|^2, \quad (2.18)$$

and the excited state by:

$$P(|e\rangle) = |c_e|^2. \quad (2.19)$$

The entire interferometer sequence is then described by a concatenation of such matrices. The standard case shown in figure 2.2 is the evolution of an atom starting in the ground state in the presence of a continuous light field:

$$P_{Rabi}(|e\rangle) = \left| \mathbf{m}(t) \begin{pmatrix} 1 \\ 0 \end{pmatrix} \right|^2 = \frac{\Omega_0^2}{\Omega_{eff}^2} \left( \frac{1}{2} - \frac{1}{2} \cos(\Omega_{eff} t) \right). \quad (2.20)$$

The output state of the Mach-Zehnder sequence for an atom starting in the ground state is given by:

$$\vec{C}_{end} = \mathbf{m}_{\pi/2,3} \mathbf{m}_{free} \mathbf{m}_{\pi,2} \mathbf{m}_{free} \mathbf{m}_{\pi/2,1} \begin{pmatrix} 1 \\ 0 \end{pmatrix} \quad (2.21)$$

The probability of finding an atom in the excited state for this sequence is (without detuning:  $\delta = 0$ ):

$$P_{MZ}(|e\rangle) = \frac{1}{2} - \frac{1}{2} \cos(\phi_{int}) \quad (2.22)$$

With  $\phi_{int}$  as the total collected phase of the interferometer due to the light fields.

### 2.1.4. Bloch sphere

The transformation from the complex vector  $\vec{C}$  to the Bloch sphere gives an intuitive picture of what is going on, especially in the case of unusual or imperfect pulse sequences. This is realized by mapping the complex 2 component vector  $\vec{C}$  onto the real 3 component vector  $\vec{b}$  [55]:

$$\vec{b} = \begin{pmatrix} c_g c_e^* + c_g^* c_e \\ i(c_g c_e^* - c_g^* c_e) \\ |c_e|^2 - |c_g|^2 \end{pmatrix}. \quad (2.23)$$



## 2. Theory

This vector has unit length. The position  $(0, 0, 1)$  or north pole indicates the excited state and the position  $(0, 0, -1)$ , south pole, indicates the ground state. Any measurement of the atomic state is a measurement of the Z-component of this Bloch-vector. Measurements in the other directions are not possible.

In this model equation 2.14 becomes [47]:

$$\mathbf{M} = \begin{pmatrix} u_x^2 + (1 - u_x^2) k_c & u_x u_y (1 - k_c) - u_z k_s & u_x u_z (1 - k_c) + u_y k_s \\ u_x u_y (1 - k_c) + u_z k_s & u_y^2 + (1 - u_y^2) k_c & u_y u_z (1 - k_c) - u_x k_s \\ u_x u_z (1 - k_c) - u_y k_s & u_y u_z (1 - k_c) + u_x k_s & u_z^2 + (1 - u_z^2) k_c \end{pmatrix}, \quad (2.24)$$

with

$$\begin{aligned} k_c &= \cos(\Omega_{eff}\tau), \\ k_s &= \sin(\Omega_{eff}\tau), \\ u_x &= \frac{\Omega_0}{\Omega_{eff}} \cos(\phi), \\ u_y &= -\frac{\Omega_0}{\Omega_{eff}} \sin(\phi), \\ u_z &= \frac{\delta}{\Omega_{eff}}. \end{aligned} \quad (2.25)$$

This is a generic rotation matrix for a rotation around an arbitrary axis  $\vec{u} = (u_x, u_y, u_z)$  with angle  $\Omega_{eff}\tau$ .

The free evolution then becomes a rotation around  $(0, 0, 1)$  with angle  $\delta\tau$ :

$$\mathbf{M}_{free} = \begin{pmatrix} \cos(\delta\tau) & -\sin(\delta\tau) & 0 \\ \sin(\delta\tau) & \cos(\delta\tau) & 0 \\ 0 & 0 & 1 \end{pmatrix}. \quad (2.26)$$

The beam splitter  $(\pi/2)$  and mirror  $(\pi)$  operations (assuming  $\delta \ll \Omega_0$ ) are rotations around  $(\cos(\phi), -\sin(\phi), 0)$  with angles  $\Omega_{eff}\tau = \pi/2$  and  $\pi$ :

$$\mathbf{M}_{\pi/2} = \begin{pmatrix} \frac{1}{2}(1 + \cos(2\phi)) & -\frac{1}{2}\sin(2\phi) & \sin(\phi) \\ -\frac{1}{2}\sin(2\phi) & \frac{1}{2}(1 - \cos(2\phi)) & -\cos(\phi) \\ \sin(\phi) & \cos(\phi) & 0 \end{pmatrix}, \quad (2.27)$$

$$\mathbf{M}_{\pi} = \begin{pmatrix} \cos(2\phi) & -\sin(2\phi) & 0 \\ -\sin(2\phi) & -\cos(2\phi) & 0 \\ 0 & 0 & -1 \end{pmatrix}. \quad (2.28)$$

The phase  $\phi$  is phase of the light fields. For an atom in the ground or excited state (north or south pole) the phase does not make much sense, one typically sets it to something convenient like 0 or  $90^\circ$  to simplify the calculations.

The  $\pi/2$ - $\pi$ - $\pi/2$ -sequence is again described by a concatenation of matrices, similar to equation 2.21:

$$\vec{\mathcal{C}}_{end} = \mathbf{M}_{\pi/2,3} \mathbf{M}_{free} \mathbf{M}_{\pi,2} \mathbf{M}_{free} \mathbf{M}_{\pi/2,1} \begin{pmatrix} 0 \\ 0 \\ -1 \end{pmatrix}, \quad (2.29)$$

but with a more intuitive visual picture to it as figure 2.3 shows.

## 2. Theory

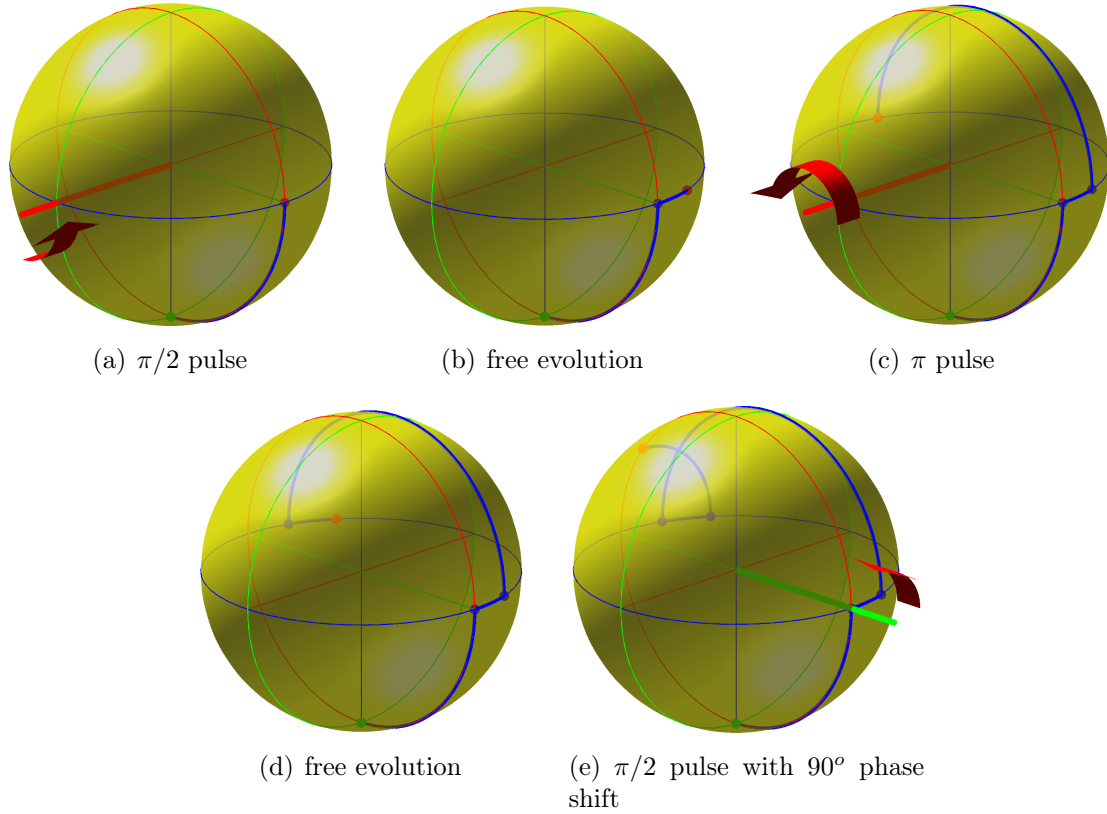


Figure 2.3.: The Mach-Zehnder pulse sequence ( $\pi/2$ - $\pi$ - $\pi/2$ ) on the Bloch sphere (with a  $90^\circ$  phase shifted final pulse). The thick blue line is the path of the atomic state, the red arrows represent operations with a light field. Figure (a) shows the first  $\pi/2$ -pulse, (b) is some drift during the first period of free evolution, (c) shows the  $\pi$ -pulse, (d) shows a drift during the second period of free evolution, and (e) is the last  $\pi/2$ -pulse which has a  $90^\circ$  phase shift. The final measurement is along the vertical (blue) axis (here about 20% in  $|g\rangle$  and about 80% in  $|e\rangle$ ).

## 2. Theory

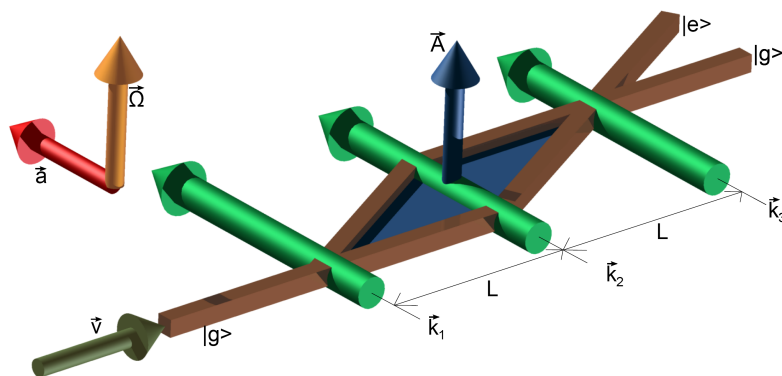


Figure 2.4.: Schematic of the Mach-Zehnder interferometer showing the direction of the various parameters involved for a Mach-Zehnder for rotation measurement. It also shows the most sensitive directions for rotation and acceleration.

Table 2.1.: Targeted values of the interferometer for estimating the expected performance for the shot noise limited case and for deriving the requirements of the subcomponents.

Parameter	Symbol	Value
Drift time	$T$	25 ms
Interaction time	$\tau_{\pi/2}$	10 $\mu$ s
Cycle time	$T_c$	1 s
Wavelength	$\lambda$	780 nm
Effective wave vector	$k_{eff}$	$1.61 \cdot 10^7$ rad/m
Number of atoms	$N$	$10^8$ atoms/shot
Velocity	$v_l$	3.0 m/s
Enclosed area	$A$	22 mm <sup>2</sup>

## 2.2. Phase contributions

This section discusses some of the phase contributions of the Mach-Zehnder configuration shown in figure 2.4.

The total phase of the interferometer can be described as a sum of various influences [56]:

$$\phi_{int} = \phi_{laser} + \phi_{rot} + \phi_{acc} + \dots \quad (2.30)$$

Where the laser phase is the contribution of the light field without external disturbances. The main contributions of interest are the rotation and acceleration term. The laser contribution contains noise but also has some technical applications. Refer to [57, 58, 59, 60, 61, 62, 63] for a more complete description of possible phase shift terms like gravity gradient, gravity waves, higher orders terms, cross terms etc.

The interferometer phase due to the phase shift of the light fields can be directly

## 2. Theory

derived from equation 2.21:

$$\phi_{laser} = \phi_1 - 2\phi_2 + \phi_3 \quad (2.31)$$

with  $\phi_n$  the phase of the light field at the  $n$ -th pulse.

The enclosed area  $\vec{A}$ , which is important for the rotation phase, is given by:

$$\vec{A} = \vec{v}_l T \times \vec{v}_{recoil,eff} T = \frac{\hbar}{m} \vec{v}_l \times \vec{k}_{eff} T^2. \quad (2.32)$$

With the targeted interferometer parameters of table 2.1 an enclosed area of 22 mm<sup>2</sup> would be achieved, with a maximum separation of 0.29 mm between the two paths.

The phase due to a rotation  $\vec{\Omega}$  is according to equation 1.1 with the wavelength given by equation 1.5 given by:

$$\phi_{rot} = 2\vec{\Omega} \cdot \left( \vec{k}_{eff} \times \vec{v}_l \right) T^2, \quad (2.33)$$

with  $\vec{v}$  as the velocity of the atoms and  $T$  the time between the light pulses.

As a function of lengths this becomes:

$$\phi_{rot} = 2\vec{\Omega} \cdot \left( \vec{k}_{eff} \times \vec{v}_l \right) \left( \frac{L}{|\vec{v}_l|} \right)^2 = 2\frac{m}{\hbar} \vec{A} \cdot \vec{\Omega}. \quad (2.34)$$

These two equations show that the sensitivity scales quadratically with the time up to the maximum length available, after which one can only increase the available time by reducing the velocity which gives only a linear increase in sensitivity. The velocity is actually a time dependent function due to gravity but in the equations above one should take the average velocity. For maximum sensitivity the wave vector and the atomic velocity should be perpendicular to each other as well as to the rotation vector. This equation also shows that the interferometer can only measure the projection of the rotation vector onto the normal vector of the enclosed area, that means it can only measure one component of the rotation vector. Other orientations of the light fields and/or other interferometer architectures like the butterfly figure with a  $\pi/2 - \pi - \pi - \pi/2$ -sequence of ref. [38] are needed to measure the other components.

The phase contribution due to acceleration is given by:

$$\phi_{acc} = \vec{a} \cdot \vec{k}_{eff} T^2 = \vec{a} \cdot \vec{k}_{eff} \left( \frac{L}{|\vec{v}_l|} \right)^2, \quad (2.35)$$

where  $\vec{a}$  is the acceleration due to vibrations as well as gravitation. It is maximal for accelerations parallel to the wave vector.

Even in the ideal case these phase contributions can not be measured infinitely accurate because they are measured via measurements of the probability of a limited number of atoms  $N$ , resulting in a phase resolution of  $1/\sqrt{N}$  [rad]. For the target values of table 2.1 this would result in a shot noise limited resolution of  $2 \cdot 10^{-9}$  (rad/s)/ $\sqrt{\text{Hz}}$  for rotations, and  $1 \cdot 10^{-8}$  (m/s<sup>2</sup>)/ $\sqrt{\text{Hz}}$  for accelerations.

## 2. Theory

In the vertical direction the acceleration term due to gravity for the targeted values of table 2.1 would be huge:  $9.88 \cdot 10^4$  rad. For more optimized gravimeters, where one uses this term, it is even larger. In the horizontal direction this acceleration term should be zero in the ideal case. But even a small tilt of the beams by  $1 \mu\text{rad}$  (that is  $1 \mu\text{m}$  at  $1 \text{ m}$ ) would result in a phase shift of  $98.8 \text{ mrad}$ . Because of the high sensitivity, the phase noise of the interferometer due to vibrations is also expected to be relatively large.

The rotational phase for the projection of the daily earth rotation on the vertical at Hannover for the targeted values of table 2.1 will be only  $3.5 \text{ rad}$ . Therefore it is very desirable to be able to distinguish rotations from accelerations. This is possible by making use of the velocity dependence of the rotational contribution, which is lacking in the acceleration. The best method for that is to use two counterpropagating atomic trajectories without flipping the wave vectors as well. The very popular configuration of the interferometer light fields is making use of the Doppler shift (previous implementation of this experiment [48] as well as others [39, 38]) not only flips the atomic velocity but also flips the wave vector, which is not desirable for a rotation measurement. This way acceleration becomes a common mode signal, while rotation becomes a differential mode signal. This separation is improved by having many common mode components like sharing the beam splitters and having identical (but opposite) launch velocities. The phase of the individual interferometers can then be described with:

$$\phi_{\text{left}} = \phi_{\text{laser}} + \phi_{\text{acc}} + \phi_{\text{rot}} \quad (2.36)$$

$$\phi_{\text{right}} = \phi_{\text{laser}} + \phi_{\text{acc}} - \phi_{\text{rot}} \quad (2.37)$$

The atom interferometer also has a temporal dependence for the sensitivity to inertial forces. During the loading and launching it is not sensitive to inertial forces, only during the interferometry sequence the device can measure inertial forces. The corresponding sensitivity function is:

$$g_{\text{rot}}(t) = \sum_n \text{rect} \left( \frac{t - nT_c}{2T} \right) \quad (2.38)$$

Here  $\text{rect}(t)$  is the rectangle function (1 for  $|t| < 1/2$ , 0 otherwise) and  $T_c$  is the cycle time of the experiment. In the frequency domain the sensitivity function becomes:

$$H_{\text{rot}}(f) = \text{sinc}(\pi f 2T) \sum_n \delta(f - n/T_c) \quad (2.39)$$

### 2.3. Signal to phase

The output signal of the interferometer is generally described with:

$$S = P(|e\rangle) = \xi \sin(\phi_{\text{int}}) + \theta \quad (2.40)$$

## 2. Theory

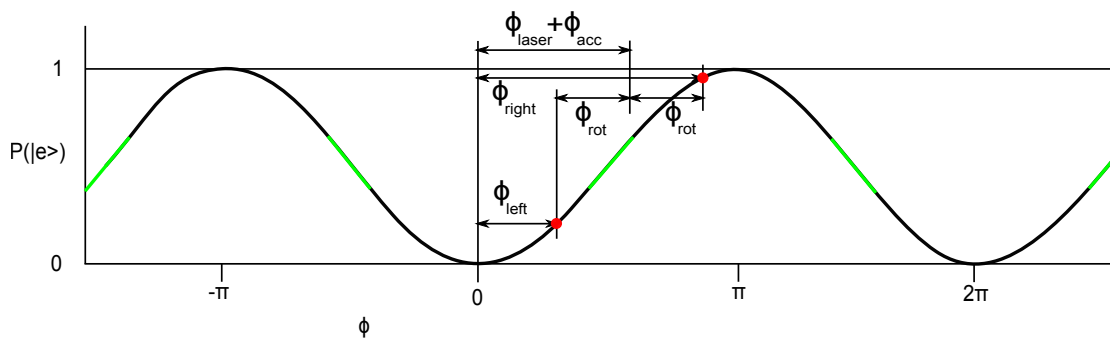


Figure 2.5.: The output signal as a function of the interferometer phase. It also shows the various phases for an example signal with two counterpropagating interferometers. The green segments on the curve indicate the linear areas with maximum sensitivity.

For an ideal signal that goes from 0 to 1, the parameters  $\xi$  and  $\theta$  are 0.5 as in the ideal case of equation 2.22. In practice they are less and need to be experimentally determined.

To get the phase from a measured signal one uses:

$$\phi_{int} = \arcsin\left(\frac{S - \theta}{\xi}\right) \approx \frac{S - \theta}{\xi} \quad (2.41)$$

Where the small angle approximation ( $|\phi_{int}| \ll 1$ ) has been used to replace the arcsin with its argument. The location of small angle is also the location of maximum sensitivity.

Unfortunately when aiming for a high sensitivity one tends to go away from the small phase approximation. In fact for the values of table 2.1 the resulting rotational phase shift for one interferometer is about 3.5 rad, far beyond any possible approximation. For a single interferometer one can compensate this phase with a phase of the laser fields. With two simultaneous counterpropagating interferometers only one can be properly compensated but not both at the same time because the rotation phase is differential (opposite sign) while the laser phase is common mode (same sign in both interferometer), see also figure 2.5.

Another complicating factor related to the very high sensitivity is that the unwanted common mode phase (mainly acceleration) is also very large and (probably) very noisy.

Some proposed solutions to these problems are:

- Using only sensitivities that put the phase difference between the two interferometers at multiples of  $\pi$ . This may be an option for very high sensitivity interferometers, where changing the sensitivity a small bit may shift the signal to a multiple of  $\pi$ . For example when the phase difference is  $1000.25 \cdot \pi$ , which prevents having both interferometer in the linear regime, changing the sensitivity by a factor of only 0.99975 brings the difference phase to  $1000\pi$ , where both interferometer can measure a zero phase.

## 2. Theory

- For every phase difference there is a laser offset that best minimizes the deviation from  $0^\circ$ :

$$\phi_{laser} = \begin{cases} \pi/2 & \text{for } |(\phi_{left} - \phi_{right}) \bmod 2\pi| < \pi/2 \\ 0 & \text{otherwise} \end{cases} \quad (2.42)$$

The worst case in this situation is when the phase difference is  $\pi/2$ ,  $\phi_{left} = -\phi_{right} = \pi/4$ , which is an operating point with 70% of the  $0^\circ$ -sensitivity.

- Compensating and measuring both interferometer alternately puts one interferometer in the best spot at the expense of the other which results in a maximum sensitivity for the first but the lower sensitivity of the second will limit the common mode suppression. Combining two such measurements, in which different interferometers are compensated, would also have a limited common mode suppression as the two measurements did not have there beam splitting pulses at the same time.
- Using the quadrature method takes two shots, where the laser offset phase alternates between 0 and  $90^\circ$  irrespective of the signal phase, to determine the phase of the individual interferometers. This would also have a limited common mode suppression as the two measurements did not have there beam splitting pulses at the same time.
- Combining several measurements of both interferometers to get a set of coordinates  $\vec{S}_i = (S_{left,i}, S_{right,i})$  one can use ellipse fitting methods [64] to obtain the phase difference, similar to the phase measurement in a Lissajous graph. For this to work, the common mode phase has to be spread over the entire ellipse, either due to external common mode noise or due to sweeping the laser phase. This takes many shots where only the phase difference needs to be stable. Signals with difficult to measure phases (near  $90^\circ$ ) are no problem.

All solutions presented here, except the last one, will only work if the common mode noise is predictable, otherwise it is not guaranteed that the measurement will be in the high sensitive regime.

When the signals are several fringes large, one also needs to either add apriory knowledge about the fringe number or use a multi shot algorithm that gives the magnitude of the signal (course/fine measurement or a “synthetic wavelength”[65]) because phase measurements are typically limited to something like  $360^\circ$  or less.

Since the difference between the very well known signal (daily earth rotation) and the unknown/less known signals is several orders of magnitude the apriory method would be feasible.

### 2.4. Thermal atoms

Because we are using ensembles of atoms with non-zero temperature, it will be useful to have a description of the atomic cloud.

## 2. Theory

The probability density function of thermal atoms as a function of position and velocity (in the moving frame of the ensemble) is a Maxwell-Boltzmann distribution given by [53]:

$$P(\vec{r}, \vec{v}, t) = \tilde{N} e^{-\frac{\vec{r}^2}{2(\sigma_0^2 + t^2 \sigma_v^2)} - \frac{\vec{v}^2}{2\sigma_v^2}} \quad (2.43)$$

with  $\tilde{N}$  a normalization factor such that the integral of  $P$  is the total number of atoms and is for all  $t$  constant,  $\sigma_0$  is the radius of the cloud at  $t = 0$ ,  $\sigma_v$  is the radius of the velocity distribution, which is time independent during the free expansion.

The temperature as a function of velocity is given by [53]:

$$\mathbb{T} = \frac{1}{3} \frac{m}{k_B} \sigma_{v,3D}^2 \quad (2.44)$$

This is for a 3 dimensional gas, with the RMS velocity  $\sigma_{v,3D}$  defined as:

$$\sigma_{v,3D} = \sqrt{\sigma_{v_x}^2 + \sigma_{v_y}^2 + \sigma_{v_z}^2} = \sqrt{3\sigma_{v,1D}^2} \quad (2.45)$$

with  $\sigma_{v_{x,y,z}}$  as the velocity width in the 3 orthogonal directions. In a symmetrical velocity distribution this can be simplified by measuring the velocity width in only one direction ( $\sigma_{v,1D}$ ), changing equation 2.44 to:

$$\mathbb{T} = \frac{m}{k_B} \sigma_{v,1D}^2. \quad (2.46)$$

This can be used to measure the temperature of the cloud based on measurements of the cloud size ( $\sigma_1$  and  $\sigma_2$ ) in one direction at different times ( $t_1$  and  $t_2$ ):

$$\mathbb{T} = \frac{m}{k_B} \frac{\sigma_1^2 - \sigma_2^2}{t_1^2 - t_2^2}. \quad (2.47)$$

This can also be reshaped to give cloud radius as a function of time:

$$\sigma(t) = \sqrt{\sigma_0^2 + \frac{k_B}{m} \mathbb{T} t^2}. \quad (2.48)$$

## 2.5. Noise and tolerances

This section looks into the main parameters for noise, and stability limits for the different parts of the measurement cycle.

### 2.5.1. MOT

The MOT itself has very little influence on the interferometer output. The exact atom number is not relevant as the chosen detection method normalizes the result on the available number of atoms. The main requirement here is to load as many atoms as possible as fast as possible. The targeted values here are  $10^8$  atoms per shot, since that will be about the limit of what the detection can resolve at the



## 2. Theory

shot noise level. The excess atoms should be used to increase the number of shots per second.

### 2.5.2. Start

The velocity is a scaling factor in the sensitivity. To ensure that the velocity is not the limiting factor the accuracy of the velocity has to be better than that of the phase measurement:

$$\frac{u(v)}{v} < \frac{u(\phi)}{\phi_{rot}} = \frac{1/\sqrt{N}}{2\frac{m}{\hbar}\vec{A} \cdot \vec{\Omega}} \quad (2.49)$$

Because the accuracy of the phase measurement is independent on the magnitude of the signal, the relative resolution of a rotation measurement depends on the magnitude of the measured rotation signal. Therefore the accuracy requirement on the velocity also depends on the magnitude of the rotation signal. For the targeted parameters of table 2.1 with the earth rotation as the largest signal, this means a relative velocity accuracy of better than  $3 \cdot 10^{-5}$ .

Also the launching determines how well the trajectories overlap and therefore influences how well rotation and acceleration can be separated.

Varying accelerations during the launch causes variations in the position of the cloud of atoms. This causes the atoms to be in different places in the interferometry beams during the interferometry pulses as intended, resulting in slightly different Rabi frequencies with corresponding signal errors, as well as sampling the wavefront during the interferometry pulses around varying positions which introduces a sensitivity to wavefront errors [66, 67]. These position variations also have influences on the state detection (see section 2.5.4).

The launching procedure also determines the temperature and cloud size. Due to finite size of the light fields not all atoms will see the same intensity and have the same Rabi frequency. The velocity distribution due to temperature also introduces a Doppler shift in the Raman process. Additionally the thermal velocity distribution introduces a spread in  $v$  in equation 2.33, but as long as the resulting spread in phase stays in the linear regime one averages over it, and the velocity distribution has no effect, see also section 2.5.3.6.

### 2.5.3. Interferometry

The phase noise in the interferometry zone can be split in two components: a time dependent component and a position dependent component. This last one can again be split in a direction and a phase.

#### 2.5.3.1. Timing errors

The effect of errors in the interferometer pulse lengths  $\tau$  or the Rabi frequency  $\Omega_{eff}$  are most easily recognized when using the Bloch sphere where they result in a change of the rotation angles. It effectively puts the atomic state on a circle

## 2. Theory

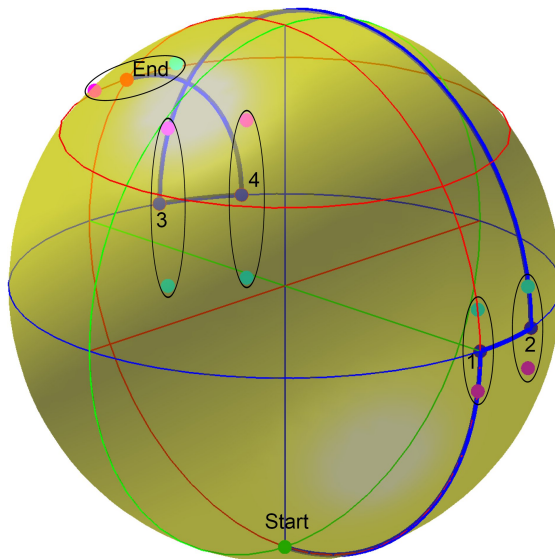


Figure 2.6.: Following the trajectory in the case of errors in the pulse length ( $\Omega \cdot \tau$  not exactly  $\pi$  or  $\pi/2$ ) of the Mach-Zehnder sequence, it is easy to see that the sensitivity to such errors is, in first order, zero. The blue line is the same as in figure 2.3, and is the case without errors. The cyan colored dots have a longer pulse, the magenta colored dots have a shorter pulse. All final states are on a circle parallel to the equator, and all give the same interferometer result.

parallel to the equator, as shown in figure 2.6. The output signal of the Mach-Zehnder is therefore first order insensitive to errors in the pulse length or the Rabi frequency.

Errors in the free propagation time can show up as a phase shift:

$$u(\phi_{free}) = \delta_{free}(T_2 - T_1) \quad (2.50)$$

with  $T_1$  and  $T_2$  the duration of the first and second period of free propagation and  $\delta_{free}$  the detuning of the laser frequency with respect to the atomic transition. Because the free propagation times are identical up to about 1 ns, a detuning up to 100 kHz can be tolerated before it causes a phase offset of  $10^{-4}$  rad, which is identical for both interferometer.

### 2.5.3.2. Frequency errors

The detuning is split in two parts, one for the light pulses ( $\delta_{ac}$ , this is mainly the AC-Stark shift) and one for the free propagation ( $\delta_{free}$ ). There are also two effects of such errors, the first one is a phase shift ( $\phi(t) = \int^t f dt$ ) which because of the symmetric nature of the Mach-Zehnder structure, as also indicated by equation 2.31, is zero, and the second one is a change of the maximum excitation probability.

In the case of an AC Stark shift there are two operating points of interest: first where the shift is zero ( $\delta_{AC} = 0$ ), and second where it is insensitive to intensity

## 2. Theory

fluctuations ( $\frac{d\delta_{AC}}{dI_1} = 0$  and  $\frac{d\delta_{AC}}{dI_2} = 0$ ). The second condition is not achievable as the AC Stark shift is a linear function of the intensity, this would require zero intensity.

When there is an AC Stark shift present it is automatically varying due to the pulsed nature of the interferometer sequence. In that case there are two special frequencies for the Raman laser system: one for the free running atom without the AC Stark shift, and one for the atom light interaction including the AC Stark shift. Mach-Zehnder style interferometers are not sensitive to frequency shifts. For the phase of a Mach-Zehnder style interferometer this makes no difference since offset frequencies do not induce additional phases in the output phase of the interferometer. The presence of a detuning during the atom light interaction however does reduce the amplitude of the fringes. As long as  $\delta_{ac} \ll \Omega_0$  then the effect of an AC Stark shift can be neglected.

### 2.5.3.3. Temporal phase noise

The sensitivity  $g$  of the interferometer output phase is determined by the infinitesimal small change in output probability of the interferometer  $\delta P$  (as defined in equation 2.22) for an infinitesimal small phase jump  $\delta\phi$  at time  $t$  according to [68]:

$$g(t) = 2 \lim_{\delta\phi \rightarrow 0} \frac{\delta P(\delta\phi, t)}{\delta\phi} \quad (2.51)$$

The output phase of the interferometer for a given laser phase is then:

$$\phi_{int} = \int \frac{d\phi_{laser}(t)}{dt} g(t) dt \quad (2.52)$$

The temporal sensitivity of the interferometer phase due to phase noise in the light fields (due to lasers, fibers, or reference oscillators) is a piecewise function [47]:

$$g_p(t) = \begin{cases} 0 & 0 < t < t_s \\ \sin(\Omega_{eg}(t - t_s)) & t_s < t < t_s + \tau \\ 1 & t_s + \tau < t < t_s + \tau + T \\ \sin(\Omega_{eg}(t - t_s - T)) & t_s + \tau + T < t < t_s + 3\tau + T \\ -1 & t_s + 3\tau + T < t < t_s + 3\tau + 2T \\ \sin(\Omega_{eg}(t - t_s - 2T)) & t_s + 3\tau + 2T < t < t_s + 4\tau + 2T \\ 0 & t_s + 4\tau + 2T < t < T_c \end{cases} \quad (2.53)$$

In the case of a constant frequency offset ( $\frac{d\phi_{laser}(t)}{dt} = f_{offset}$ ), the interferometer phase of equation 2.52 becomes zero, indicating that frequency offsets do not cause phase offsets. This is also obvious from equation 2.31 because a detuning means that the phase is a linear function of time ( $\phi_n = f \cdot n \cdot T$ ). Phase and frequency noise on the other hand do not cancel.

## 2. Theory

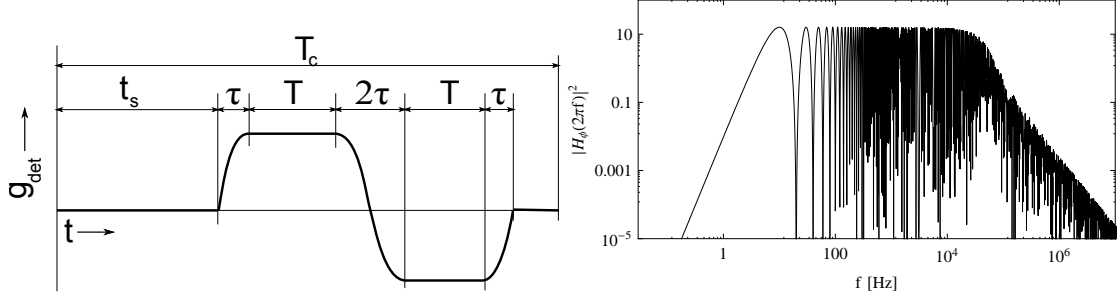


Figure 2.7.: Left: The light field phase noise sensitivity function as a function of time ( $g(t)$ ). Right: Its Fourier transform ( $H_\phi(f) = f \cdot G_s(f)$ ), the dots indicate the sampling points of repeating mode ( $G_d(f)$ ). The Fourier transform is for the targeted parameters of table 2.1.

Since the actual phase noise is not known as a function of time but as a spectral density, equation 2.53 has to be Fourier transformed which gives the weighting function:

$$G_p(f) = \frac{1}{T} \left( e^{-2\pi i(t_s + \frac{1}{2}T + \tau)f} \text{sinc}(\pi f T) - e^{-2\pi i(t_s + \frac{3}{2}T + 3\tau)f} \text{sinc}(\pi f T) \right) + \chi \quad (2.54)$$

with  $\chi$  the high frequency components due to the edge shape (the sin parts in  $g(t)$ ), they become relevant at frequencies around  $1/(2\tau)$ , in practice that is about 50 kHz. The use of different pulse shapes, like Gaussian, only changes the high frequency components  $\chi$ , but the leading terms remain unchanged.  $K$  is a normalization factor [47]. The weighting function has minima at multiples of  $1/T$  because there the signals average away over the drift time  $T$ , see also figure 2.7.

Operating in pulsed mode with repetition frequency  $1/T_c$ , over infinite time, results in the discrete Fourier series:

$$G_{p,pulsed}(f) = \frac{1}{T_c} \sum_n G_p(f) \delta(f - n/T_c) \quad (2.55)$$

with  $\delta$  as the Dirac delta function. Because the interferometer is operating in pulsed mode, the exact function becomes a pulse train, indicating that it is not sensitive to signals at frequencies other than multiples of the repetition rate, like every sampling system. This effect happens because the Fourier transform goes from minus infinity to plus infinity. The non-zero components have minima at  $1/T$  which corresponds to signals that average away over the drift time  $T$ .

The resulting phase noise of the interferometer due to phase noise in the light field is then given by:

$$u^2(\phi) = \int_0^\infty S(f) f^2 |G_{p,pulsed}(f)|^2 df \quad (2.56)$$

with  $S(f)$  as the single side band power spectral density of the light field phase

## 2. Theory

noise, the  $f^2$  term is to convert the phase noise sensitivity to a frequency noise sensitivity.

### 2.5.3.4. Intensity noise

The effect of an AC Stark shift due to intensity fluctuations can be split in two parts: a phase shift, and a change of the effective Rabi frequency.

The actual AC Stark shift is a time dependent function:

$$\delta_{AC}(t) = \delta_{AC}(I_1(t), I_2(t)) \left( \text{rect} \left( \frac{t - t_s}{\tau} \right) + \text{rect} \left( \frac{t - t_s - T}{\tau} \right) + \text{rect} \left( \frac{t - t_s - 2T}{\tau} \right) \right) \quad (2.57)$$

$I_1$  and  $I_2$  are the intensities of the two lasers of the Raman system as a function of time. The three rectangle functions are the pulse shape of the interferometer. They also show that there can only be an AC Stark shift when there is light, which limits the sensitivity to only these pulses. It is easy to see that in the case of a constant intensity, the output phase of the interferometer according to equations 2.52 and 2.53 remains zero.

The corresponding sensitivity function for phase noise due to laser intensity noise is:

$$g_{I,AC,l}(t) = \frac{d\delta_{AC}}{dI_l} \cdot \begin{cases} 0 & 0 < t < t_s \\ \sin(\Omega_{eg}(t - t_s)) & t_s < t < t_s + \tau \\ 0 & t_s + \tau < t < t_s + \tau + T \\ \sin(\Omega_{eg}(t - t_s - T)) & t_s + \tau + T < t < t_s + 3\tau + T \\ 0 & t_s + 3\tau + T < t < t_s + 3\tau + 2T \\ \sin(\Omega_{eg}(t - t_s - 2T)) & t_s + 3\tau + 2T < t < t_s + 4\tau + 2T \\ 0 & t_s + 4\tau + 2T < t < T_c \end{cases} \quad (2.58)$$

where the two lasers of the Raman system are identified with  $l \in \{1, 2\}$ . Its Fourier transform contains only the (neglected) high frequency components of equation 2.54:

$$\begin{aligned} G_{I,l}(f) = & \frac{d\delta_{AC}}{dI_l} \frac{1}{\tau} (+\text{sinc}(\pi(f + 1/\tau)\tau) + \text{sinc}(\pi(f - 1/\tau)\tau) \\ & + e^{-i2\pi f(T+\tau/2)} (\text{sinc}(\pi(f + 1/\tau)2\tau) + \text{sinc}(\pi(f - 1/\tau)2\tau)) \\ & + e^{-i2\pi f(2T+3\tau)} (\text{sinc}(\pi(f + 1/\tau)\tau) + \text{sinc}(\pi(f - 1/\tau)\tau)) \end{aligned} \quad (2.59)$$

The resulting phase noise is again given by equation 2.56.

### 2.5.3.5. Alignment

When considering the effect of alignment, one has to distinguish between the optics before the main chamber and those behind it, because before the main chamber

## 2. Theory

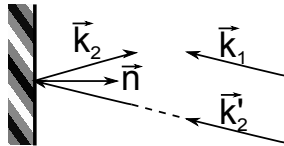


Figure 2.8.: Reflection from the mirror.  $\vec{k}_1$  and  $\vec{k}_2'$  come from a common fiber outcoupler,  $\vec{k}_2$  is the reflection of  $\vec{k}_2'$  on the mirror with surface normal  $\vec{n}$ . The angles are strongly exaggerated.

the two light fields have a strong common mode suppression, with only errors on the scale of the microwave wavelength left over, whereas after the main chamber there is only one light field without any common mode suppression which therefore has sensitivities on the scale of the optical wavelength.

Based on simple considerations of the wave vectors and the mirror, the orientation of the fiber outcouplers is not very critical as it cancels with the reflected beam, see also figure 2.8. The reflection of  $\vec{k}_2'$  on a mirror with normal  $\vec{n}$  is given by:

$$\vec{k}_2 = \vec{k}_2' - 2\vec{n} \left( \vec{k}_2' \cdot \vec{n} \right). \quad (2.60)$$

Assuming only small angles, the resulting effective wave vector becomes:

$$\vec{k}_{eff} = 2\vec{n} \left| \vec{k}_2' \right| + \left( \vec{k}_1 - \vec{k}_2' \right) \approx 2\vec{n} \left| \vec{k}_2' \right|. \quad (2.61)$$

This shows clearly that the direction of the effective wave vector is dominated by the orientation of the mirror, the second term is typically 5 orders of magnitude smaller and close to parallel to the normal of the mirror.

For a high excitation probability the normal of mirror should be perpendicular to the direction of the atoms such that the Doppler shift caused by the projected velocity of the atoms on the effective wave vector is much less than the Fourier width of the light pulses of the interferometry:

$$\vec{v}_{at} \cdot \vec{k}_{eff} = |v| |k_{eff}| \cos(\alpha) \ll \frac{1}{\tau_\pi}. \quad (2.62)$$

This should be achieved for both counterpropagating atomic ensembles. For the values of table 2.1 this means that the angle  $\alpha$  between the atomic velocity and the normal of the mirror needs to be better than 1 mrad.

To avoid large common mode interferometer offset phases, the projection of gravity on the effective wave vector needs to be small:

$$\phi_{acc} = \vec{g} \cdot \vec{k}_{eff} T^2 = |\vec{g}| \left| \vec{k}_{eff} \right| \cos(\beta) T^2 \ll 1. \quad (2.63)$$

This gives a requirement for the angle  $\beta$  between the direction of gravity and the normal of the mirror to be better than 10  $\mu\text{rad}$ .

## 2. Theory

### 2.5.3.6. Wavefront

When making a measurement, one does not interrogate a single atom but always the entire ensemble. Due to the thermal distribution, each atom samples a slightly different part of the wavefront. The final measurement is therefore the average of the wavefront  $\phi$  weighted with the probability density distribution of the atomic ensemble  $P$ :

$$S_{avg} = \int P(\vec{x}) \sin(\phi(\vec{x})) d\vec{x} \quad (2.64)$$

When we assume a well collimated light field, and only small phase and wavefront errors ( $\phi(\vec{x}) \ll 1$ ) then the measured phase can be approximated with:

$$\phi_{avg} = \int \frac{1}{\sigma_w \sqrt{2\pi}} e^{-\frac{x^2+y^2}{2\sigma_w^2}} \phi(x, y) dx dy \quad (2.65)$$

Here  $\sigma_w$  is the radius of the atomic cloud at the position and time of interest,  $\phi(x, y)$  is a two dimensional map of the wavefront errors, expressed in radian, and is basically a sum of the errors of the optics behind the main chamber:

$$\phi(x, y) = 2\pi \frac{2}{\lambda} \int n(x, y, z) dz = 2\pi \frac{2}{\lambda} \sum_m h_m(x, y) \quad (2.66)$$

with the integral of the refractive index  $n(x, y, z)$  over optical path from the atoms to the mirror,  $h_m(x, y)$  is the wavefront error map of the  $m$ th optical component and can be directly measured with a Shack-Hartmann sensor [69], and  $\lambda$  the wavelength of light field (about 780 nm). The factor of 2 is because the components are in double pass.

In the linear regime ( $|\phi| \ll 1$ ) the averaging over the entire atomic cloud causes no errors, in the edge regime ( $\phi = \pm\pi/2$ ) however there is a bias towards the linear area. This reduces the apparent contrast (not the true contrast) because the contrast is usually measured by bringing the interferometer into the non-linear regime ( $\phi = \pm\pi/2$ ) to measure the signal amplitude, causing errors in the scaling factor.

The difference, due to temperature, in cloud size at the beginning and end of the interferometry cycle mean they sample the wavefront at different locations resulting in a differential phase offset for the two interferometer. The center window has no contribution because it is sampled by both atomic clouds after the same expansion time, with the same cloud size. The effective sensitivity function for wavefront errors in the differential atom interferometer is:

$$g_w(\vec{x}) = \frac{1}{2\pi\sigma_1^2} e^{-\frac{\vec{x}^2}{2\sigma_1^2}} - \frac{1}{2\pi\sigma_3^2} e^{-\frac{\vec{x}^2}{2\sigma_3^2}} \quad (2.67)$$

With  $\sigma_1$  and  $\sigma_3$  the radius of the atomic cloud in the first and third interferometry window, figure 2.9 shows a typical shape of this function. The motion of the atoms during the interferometry pulses is neglected as it is much smaller than the cloud size, it would be a convolution with  $\vec{v} \cdot \tau_{\pi/2}$  (about 30  $\mu\text{m}$ ).

## 2. Theory

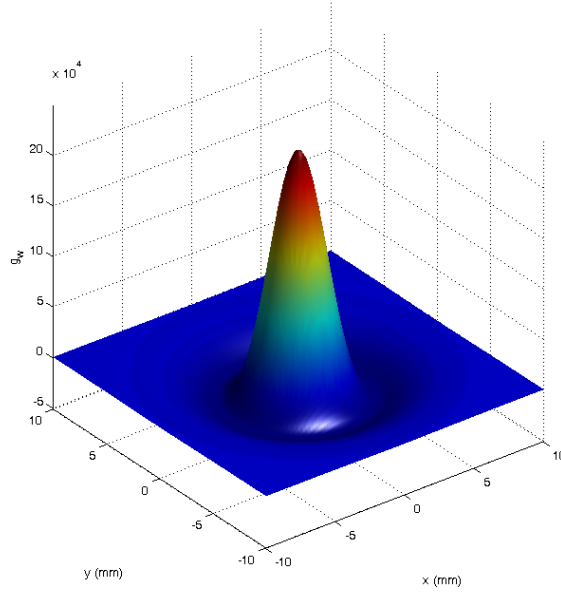


Figure 2.9.: The wavefront sensitivity function  $g(\vec{x})$ , for  $\sigma_0=1$  mm,  $T = 10 \mu\text{K}$ ,  $t_1 = 47$  ms,  $t_2 = t_1 + 2 \cdot 25$  ms. The Fourier transform is a rescaled version of this because it is a linear combination of Gauss functions.

The 2D Fourier transform of this function is:

$$H_w(\vec{\kappa}) = e^{-2\pi\sigma_1^2\pi\vec{\kappa}^2} - e^{-2\pi\sigma_2^2\pi\vec{\kappa}^2} \quad (2.68)$$

$\vec{\kappa}$  is the spatial frequency ( $\frac{2\pi}{\lambda}$ ). The resulting phase error is then:

$$u_w^2(\phi) = \int S_w(\vec{\kappa}) |H_w(\vec{\kappa})|^2 d\vec{\kappa} \quad (2.69)$$

With  $S_w$  as the power spectral density of the wavefront surface.

This wavefront error is a systematic differential offset.

### 2.5.4. State detection

The state detection makes use of the two internal states used in the interferometer by measuring the fluorescence light. The amount of fluorescence light is governed by the scattering rate [54]:

$$R_{sc} = \left(\frac{\Gamma}{2}\right) \frac{(I_{det}/I_{sat})}{1 + 4(\Delta_{det}/\Gamma)^2 + (I_{det}/I_{sat})}. \quad (2.70)$$

For a reliable state detection the scattering rate should be independent of laser parameters like detuning and intensity. This is possible with a high intensity ( $I_{det}/I_{sat}$ ) (“power broadening”) to eliminate the sensitivity to laser intensity fluctuations, and small detuning ( $\Delta_{det}$ ) to avoid sensitivity to laser frequency noise.



## 2. Theory

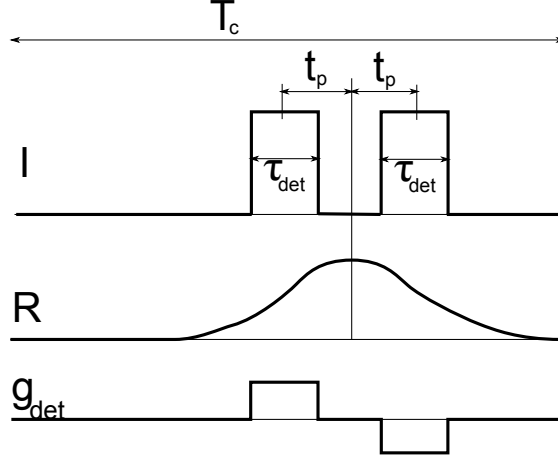


Figure 2.10.: Timing parameters for the detection, as well as the scattering rate.

The detuning can not be chosen to be zero, where it would be first order insensitive, because that causes excessive heating of the atomic cloud which changes its velocity profile dramatically.

### 2.5.4.1. Temporal sensitivity

Because the state detection consists of two pulses, it also has a time dependent sensitivity function:

$$g_{det}(t) = \sum_n \text{rect}\left(\frac{t - t_p + nT_c}{\tau_{det}}\right) - \text{rect}\left(\frac{t + t_p + nT_c}{\tau_{det}}\right) \quad (2.71)$$

Here  $T_c$  is the cycle time,  $2t_p$  is the time between the center of two pulses,  $\tau_{det}$  is the length of the pulses, see also figure 2.10. The sensitivity function for intensity noise in the state detection is then:  $g_{det,I}(t) = g_{det}(t) \frac{\partial R_{sc}}{\partial I}$ , the same for frequency noise is then:  $g_{det,\Delta}(t) = g_{det}(t) \frac{\partial R_{sc}}{\partial \Delta_{det}}$ .

The Fourier transformed form of equation 2.71 is:

$$H_{det}(f) = (e^{-2\pi i f t_p} \text{sinc}(\pi f \tau_{det}) - e^{2\pi i f t_p} \text{sinc}(\pi f \tau_{det})) \sum_n \delta(f - n/T_c). \quad (2.72)$$

This causes only phase noise, not phase offsets.

### 2.5.4.2. Spatial sensitivity

The scattering rate in the actual state detection also has a strong spatial dependency which is normally seen as a Gaussian pulse shape on the photodiode as a function of time and can be modeled as:

$$R(t) = e^{-\frac{t^2}{2\sigma_d^2}} R_{sc} \quad (2.73)$$

## 2. Theory

$\sigma_d$  is the effective radius of the detection zone (in seconds). The thermal width of the atoms is hidden in  $\sigma_d$ , it does not explicitly show up in the detection error. The typical detection consists of two light pulses on opposite sides of the detection scattering rate curve. If the starting position or the velocity have an error then both detection pulses will shift with opposite sign on this curve.

The output signal of the complete state detection in the linear regime ( $\phi = 90^\circ$ ) as a function of a timing error  $t_e$  is then:

$$S(t_e) = \frac{\frac{1}{2}R(-t_p + t_e)}{R(t_p + t_e)} = \frac{1}{2}e^{\frac{2t_e t_p}{\sigma_d^2}} \quad (2.74)$$

The corresponding error in the output due to an error in the timing is:

$$u(S) = \frac{dS(t_e)}{dt_e}u(t_e), \quad (2.75)$$

with:

$$u(t_e) = \sqrt{\left(T_f \cdot \frac{u(v_l)}{v_l}\right)^2 + \left(\frac{u(x)}{v_l}\right)^2}. \quad (2.76)$$

With  $T_f$  as the flight time between launch and detection. The error has been split into a component from the atomic velocity and a component from errors in the starting position. These errors cause only phase noise and signal offsets but not phase offsets because of the chosen detection scheme.

When shifting the entire error budget of the detection for achieving shot noise level on either one these effects one can derive the following conditions for the velocity and position error:

$$\frac{u(v_l)}{v_l} < \frac{\sigma_d^2}{t_p T_f \sqrt{N}} \quad (2.77)$$

$$u(x) < \frac{v_l \sigma_d^2}{t_p \sqrt{N}} \quad (2.78)$$

With the usual target values of table 2.1 and  $t_p = 0.6$  ms,  $\sigma_d = 3$  ms,  $T_f = 107$  ms one becomes a relative velocity requirement of better than  $1.4 \cdot 10^{-5}$ , and a start position more accurate than  $4.5 \mu\text{m}$ .

## 3. Implementation

This chapter describes the central components that make up the rotation sensor. This includes the vacuum system, the atomic sources, atomic state preparation, interferometry and the final state detection. The laser systems, light manipulation systems and electronics that all connect via optical fibers and electrical cables to the experiment are described in chapter 4.

### 3.1. Vacuum

Because the cold atoms are sensitive to collisions with atoms of the background gas, we need a vacuum system to obtain long lifetimes of the cold atoms.

The vacuum system shown in figure 3.1 can be divided into two sides, one for the atomic manipulation and one for the pumps. The pump section of the vacuum uses standard CF-40 parts made from non-magnetic steel. The vacuum system is initially pumped down with a turbo-molecular pump to about  $1 \cdot 10^{-8}$  mbar after which the valve is closed and the turbo pump is removed from the system, to avoid any vibrations coming from the pump. In the UHV range the pressure is maintained by an ion-getter pump (30 l/s, Vacom 40SDI2HSCNN) and a titanium sublimation pump (Hositrاد SB-1020 TSP) giving a final pressure of about  $5 \cdot 10^{-10}$  mbar after a moderate bake-out. A UHV pressure sensor (Varian 580) is used to measure the pressure.

The 2D-, 3D- and Interferometer chambers are made of aluminum with lead seals between the aluminum parts and with indium for the aluminum-glass seals. There is a differential pumping stage between the 2D and the 3D chambers with a hole of 4 mm and a length of 20 mm to maintain a high Rubidium pressure in the 2D-MOT while maintaining a clean high vacuum for the 3D-MOT and the interferometry. This results in a high loading rate with long lifetimes. Refer to appendix C.1 for more details.

The atoms come from an ampule in an oven based on commercial Swagelok parts that typically operates at room temperature, but can be heated when necessary to further increase the atomic flux.

The overall length of the vacuum system is about 90 cm and is built on a non-magnetic breadboard of  $120 \times 90$  cm.

### 3.2. Vibration isolation

The suppression of vibrations is necessary for two reasons. First: the atom interferometer is sensitive to accelerations as shown in section 2.2 and second: part of

### 3. Implementation

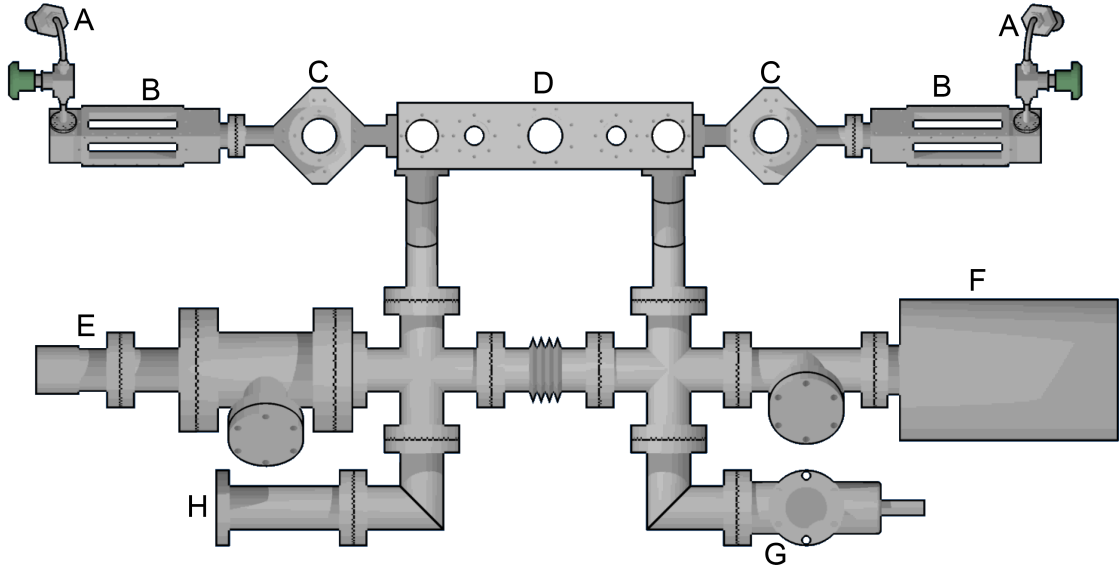


Figure 3.1.: Top view of the vacuum system. A: atom oven, B: 2D MOT, C: 3D MOT, D: main chamber, E: titanium sublimation pump, F: ion getter pump, G: valve for turbo molecular pump, H: UHV sensor.

the optics around the main chamber form an optical interferometer that is sensitive to movements on the nanometer scale.

An active vibration isolation system (TableStable AVI 350-M) is used to reduce the vibration level in the range of 1 to 200 Hz. For higher frequencies it provides passive isolation, for lower frequencies there is no isolation (see figure 3.2). The effects on the interferometer signal are currently being investigated.

A commercial seismometer (Guralp CMG 40-T) has been used to measure the vibrations for various setups, on the ground, with vibration isolation on and off, on the optical table, as well as on various locations in the institute, see figure 3.3. It was finally decided to put the experiment directly on the floor on the vibration isolation system, in our lab.

### 3.3. 2D MOT

The 2D MOT has been optimized to produce a high intensity beam of cold atoms to quickly load the 3D MOT.

The 2D MOT has 5 beams, 4 of them are large cooling beams with 30 mW each, red detuned by about  $1.8 \Gamma$  (11 MHz) from the cooling transition ( $|F = 2\rangle \rightarrow |F' = 3\rangle$ ) that shine in from the side, see also figure 3.4. The fifth is the “pusher” beam with 3 mW  $1.8 \Gamma$  (11 MHz) blue detuned enhancing the output by a factor of 2 shining in from behind. The main cooling beams also contain each 0.5 mW of repumping light, which is on resonance with the repumping transition ( $|F = 1\rangle \rightarrow |F' = 2\rangle$ ). This produces a beam with  $5 \cdot 10^9$  cold atoms/s, of which 50% can be captured by the 3D MOT, the beam itself has a typical velocity of 20 m/s.

### 3. Implementation

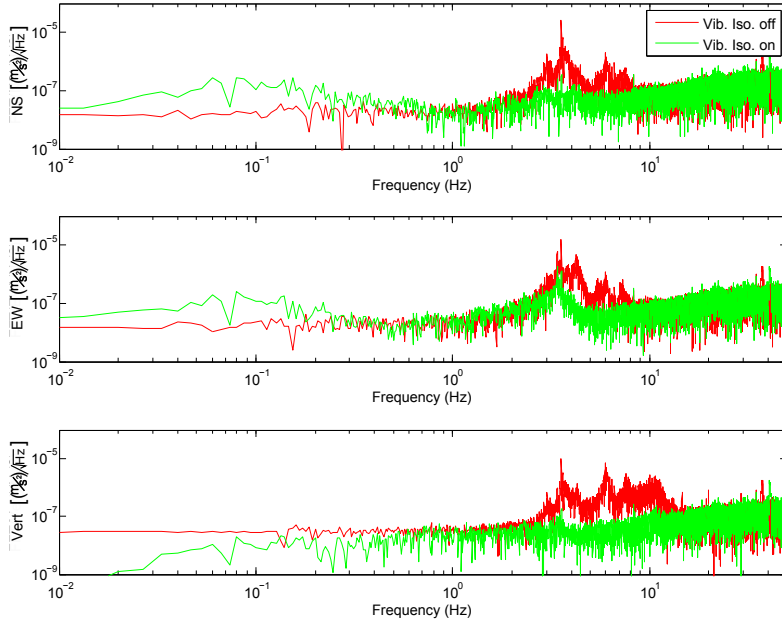


Figure 3.2.: Spectrum of vibration with vibration isolation on and off in three directions, at the location of the experiment (4<sup>th</sup> floor lab, position D in figure 3.3). The atomic beam is in east-west direction, the lasers are in north-south direction, gravity is vertical.

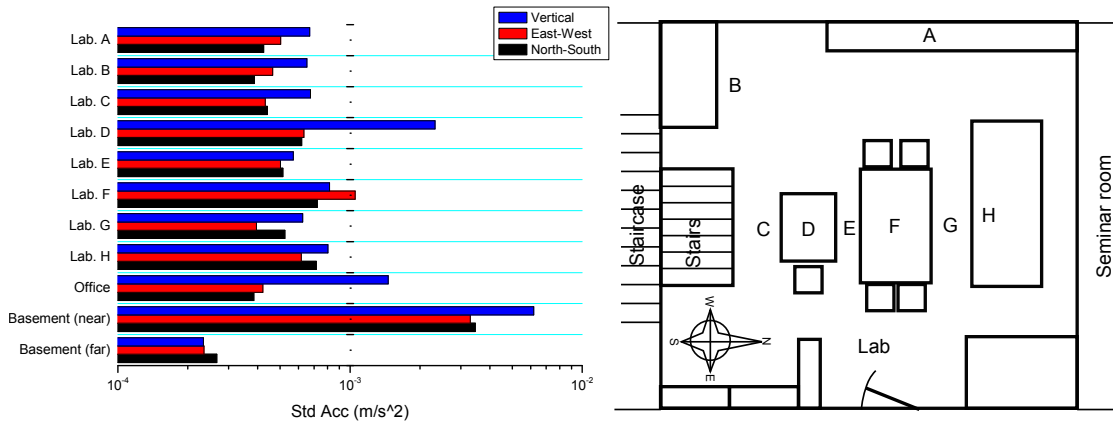


Figure 3.3.: Left: Summary of seismometer investigation of various locations, standard deviation in three directions. Right: map of locations. The atomic beam is in east-west direction, the lasers are in north-south direction, gravity is vertical. A: on the ground near the window, B: on the ground, C on the ground next to the experiment, D: on the experiment breadboard, E on the ground, F on the optical table with the laser systems, G: on the ground, H on another optical table. The far end of the basement is very quiet but has an unstable floor, the near end of the basement houses some heavy pumps.

### 3. Implementation

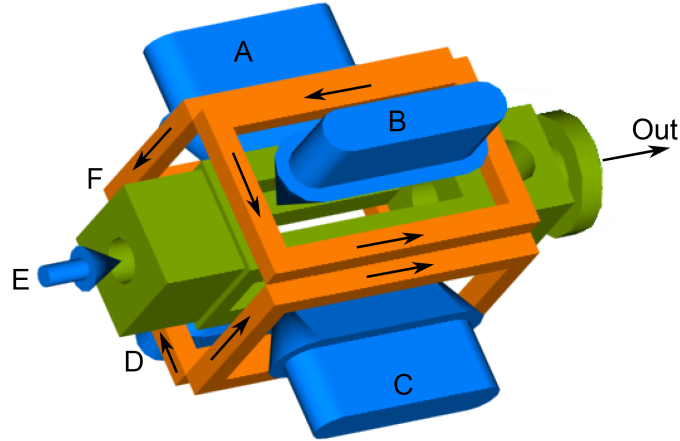


Figure 3.4.: Overview of the 2D-MOT. A-D: main cooling beams, E: pusher beam, F: magnetic coils. The arrows on the coils indicate the direction of the current in the magnetic coils. The beam of cold atoms leaves the 2D MOT through the flange on the right side.

For the cooling of the atoms in the 2D MOT a magnetic quadrupole field is needed which is generated with four coils as shown in figure 3.4, the key parameters are in table 3.1. The coils for the 2D MOT are switched on and off by analog programming of the power supplies.

The atoms come from an ampule in an oven that can be heated when necessary but it is typically operated at room temperature.

The cooling beams make use of a shortened beam expander shown in figure 3.5. The first lens is a negative cylinder lens that increases the divergence of the beam in one direction, while maintaining the natural divergence of the fiber in the other direction. Because of the short distances involved, the introduced astigmatism is still very small. The second lens is a simple plan-convex lens that has been cut to a rectangular shape. The resulting beam has an elliptical shape. In front of the cylinder lens there is a quarter wave plate to obtain the necessary circular polarization.

The pusher beam uses a commercial fiber coupler<sup>1</sup> to create a collimated beam with linear polarization. The output flux of the 2D MOT did not significantly depend on the polarization that was used.

## 3.4. 3D MOT with moving molasses

The 3D-MOT has six light beams, oriented in a “110” orientation. The 4 beams in the horizontal plane are shining in on  $45^\circ$  diagonals to the direction of the atoms, with the vertical beams at  $90^\circ$ , as shown in figure 3.6. Each of the six beams has 9 mW of cooling light with a variable detuning between  $2.5 \Gamma$  and  $23 \Gamma$  as well as 0.3 mW of repumping light (not detuned).

<sup>1</sup>Schäfter und Kirchhoff 60FC-4-A4,5-02, focal length: 4.5 mm

### 3. Implementation

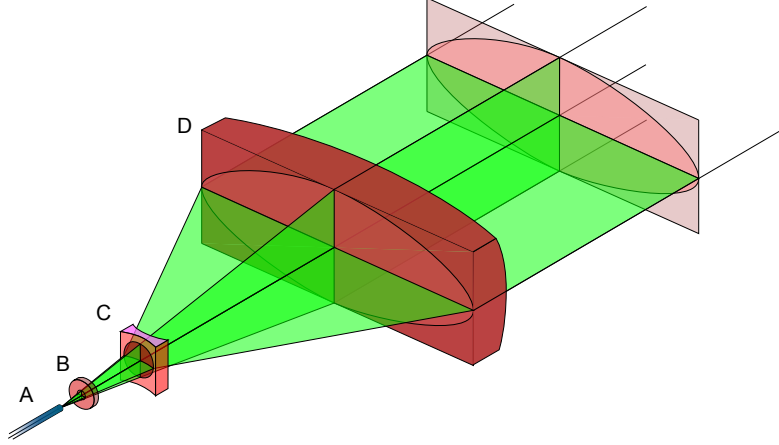


Figure 3.5.: The beam expansion telescope for the 2D MOT. A: fiber, B: quarter wave plate, C: cylinder lens, D: spherical lens in square shape.

Table 3.1.: Parameters of the magnetic field coils.

	2D	3D	Bias
size (mm)	55×95	$\phi$ 46	98×278
distance (mm)	70	60	73
number of windings per coil	64	45	4
number of coils	4	2	2
wire thickness (mm)		0.85	1.2×0.035
typical current (A)	4	4	1
field strength (G)			400mG@1A
field gradient (G/cm)	18.5G/cm@3A	12G/cm@3A	
Switching time (rising/falling) (ms)	25 / 10	<0.1 / 1	1 / 5

### 3. Implementation

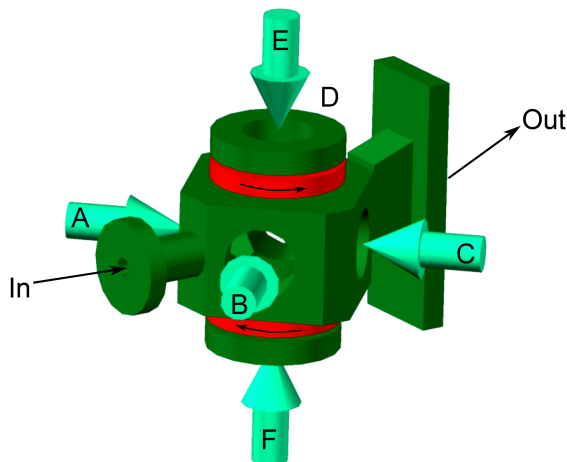


Figure 3.6.: Overview of the 3D MOT. The arrows on the coils indicate the direction of the current in the magnetic coils. The beam of cold atoms from the 2D MOT enters through the round flange on the left side. The clouds of cold atoms leave through the rectangular flange on the right side.

The out-coupling telescopes make use of a two lens beam expander. First a negative lens to increase the divergence and shorten the overall length, and finally a positive lens to create a collimated beam with a diameter of 30 mm ( $1/e^2$ ) in a system which is only 70 mm long. There is a quarter wave plate between the fiber and the first lens to convert the linear light from the fiber into circular light for the atoms.

The 3D-MOT operates in 3 distinct modes:

1. A static magneto optical trap optimized for capturing as fast as possible as many atoms from the 2D-MOT as possible, to get a high signal to noise ratio in the interferometer and a high cycle time.
2. Near resonant moving molasses to accelerate the atoms to the necessary velocity and direction for the parabola trajectory through the main chamber. This is necessary because to accelerate the atoms from 0 to 2.79 m/s in less than 1 ms one needs a high scattering rate.
3. Far off resonant moving molasses to cool the atoms to the sub-Doppler temperatures needed to keep the size of the atomic cloud small and to further reduce the velocity distribution to improve the efficiency of the velocity selective Raman transitions in the interferometry.

Because the atoms follow a parabolic trajectory due to gravity in the main interferometry chamber, the launch direction from the 3D MOT needs to be about  $15^\circ$  up. In a zero gravity environment, like the proposed space satellite missions HYPER[43], one can use the simpler 111-orientation with a fixed direction and only one velocity component.



### 3. Implementation

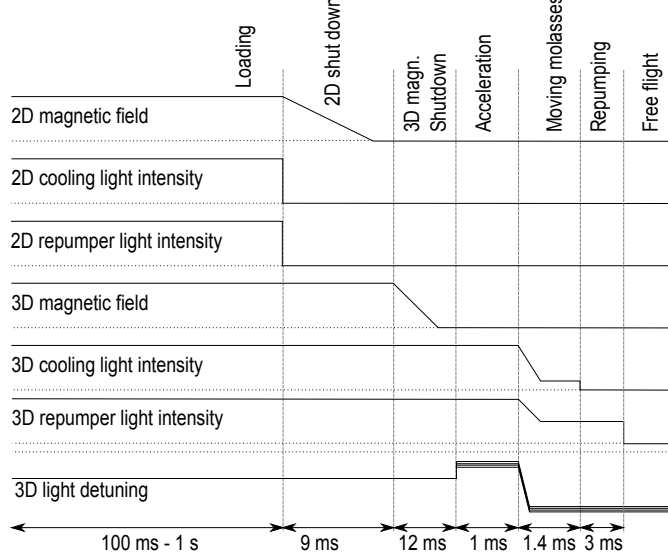


Figure 3.7.: Experimental sequence of launch.

To achieve the desired trajectory the beams are divided into 4 groups, each with their own frequency. The two beams coming from the side of the 2D-MOT (in figure 3.6 beam A and B) have the same frequency as well as the two beams coming from the side of the main chamber (C and D) and determine the horizontal velocity ( $v_{horiz}$ ). The beams coming from above (E) and below (F) determine the vertical velocity ( $v_{vert}$ ). The frequencies of the individual beams are given by:

$$\begin{aligned}
 F_A = F_B &= F_0 - \sqrt{2}Dv_{horiz} \\
 F_C = F_D &= F_0 + \sqrt{2}Dv_{horiz} \\
 F_E &= F_0 - Dv_{vert} \\
 F_F &= F_0 + Dv_{vert}
 \end{aligned}
 \tag{3.1}$$

with  $F_0$  the frequency of the cooling transition including any global detuning and  $D$  the Doppler shift rate (about 1.28 MHz/m/s for a wavelength of 780 nm). This way it is possible to independently control the horizontal and vertical velocity of the atoms, allowing different parabola trajectories as well as optimizing the overlap between the two counter-propagating atomic trajectories, without any mechanical alignment changes by just changing the frequencies. This way horizontal velocities up to 10 m/s can be obtained (but only a narrow band of velocities result in a parabola trajectory that reaches the 3D-MOT on the other side). The typical trajectory starts with 2.79 m/s in the horizontal direction and 0.73 m/s in the vertical direction, the resulting parabola has a height of 27 mm.

The temporal sequence of launching is shown in figure 3.7. After a loading time of 100 ms to 1 s the optical and magnetic fields of the 2D-MOT are shut down. When the magnetic field of the 2D-MOT has sufficiently decayed, the 3D-MOT switches to acceleration mode by first switching off its magnetic field and then frequency shifting its light closer to resonance and applying the Doppler shift to accelerate the atoms. After 1 ms the frequency is shifted far away from the

### 3. Implementation

resonance, together with the Doppler shift, for the sub-Doppler moving molasses cooling for about 1.4 ms after which the light is shut off, releasing  $10^8$  atoms with a temperature of 8  $\mu\text{K}$  and a velocity of 2.79 m/s onto a parabolic trajectory through the main chamber.

The stability of the starting position has been tested by looking at the position of the cloud of atoms just before launching, the results are shown in figure 3.8. The standard deviation in launch direction is 23  $\mu\text{m}$  and perpendicular 8.5  $\mu\text{m}$ . The velocity stability has been tested with the light-sheet method, the results are shown in figure 3.9. The relative standard deviation of the velocity is  $3 \cdot 10^{-4}$ , and fits with the expected velocity based on the chosen Doppler shift.

For the cooling of the atoms in a 3D-MOT a magnetic quadrupole field is needed, which generated by two coils in (roughly) anti-Helmholtz configuration at each MOT, as also shown in figure 3.6. The key parameters of the coils are in table 3.1.

For the final moving molasses cooling stage and for the interferometry it is important to remove any external magnetic fields like that of the earth (0.48 G), therefore a mu-metal shielding is used around the entire breadboard holding the vacuum system, reducing the external fields by a factor 50. Also a separate shield has been added around the ion-getter pump since it has two large magnets and is in close proximity to sensitive areas.

The coils for the 3D-MOT field are switched with solid state relays (SSR) in about 1 ms (1/e-decay time). Without the SSR the switching times would have been three times longer. The switching times of the 3D-MOTs are limited by induced currents in the aluminium vacuum chambers [70].

## 3.5. State preparation

The goal of the state preparation is to bring the atoms to the ground state ( $|F = 1, m_f = 0\rangle$ ) of the interferometer. When the atoms come out of the MOT/-Molasses they are spread out over all  $m_f$ -substates of both  $|F = 1\rangle$  and  $|F = 2\rangle$ -state. The state preparation is done in several steps:

1. Repumper light together with the Zeeman-selection light, which is  $\pi$ -polarized resonant light on the  $|F = 2\rangle \rightarrow |F' = 2\rangle$ -transition, is shined in. Because the selection rules forbid the  $|F = 2, m_f = 0\rangle \rightarrow |F' = 2, m_f = 0\rangle$ -transition, this brings the atoms in the dark state  $|F = 2, m_f = 0\rangle$ .
2. The repumper is shone in a little longer to make sure the  $|F = 1\rangle$ -state is empty.
3. A  $\pi$ -Raman pulse brings the atoms from  $|F = 2, m_f = 0\rangle$  to  $|F = 1, m_f = 0\rangle$ . This Raman pulse is also velocity selective, transferring only the atoms with (near) zero velocity in the direction of the Raman beam, reducing the velocity width of the cloud of atoms in the direction of the beams. It comes from the same optical setup as the interferometry beams (see next section).

### 3. Implementation

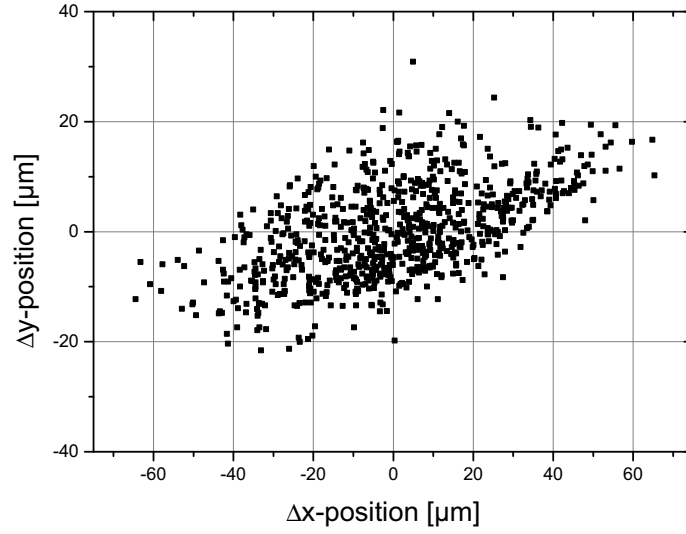


Figure 3.8.: The starting position of the center of the cloud of atoms just before launch for 789 shots in 28 minutes.  $x$  is the direction of launch,  $y$  is the direction of the interferometry beams. The standard deviation in launch direction is  $23 \mu\text{m}$  and perpendicular  $8.5 \mu\text{m}$ . The images were recorded with a camera with an effective pixel size of  $85 \mu\text{m}$ , and each cloud had a full width at half maximum of about  $1.3 \text{ mm}$ .

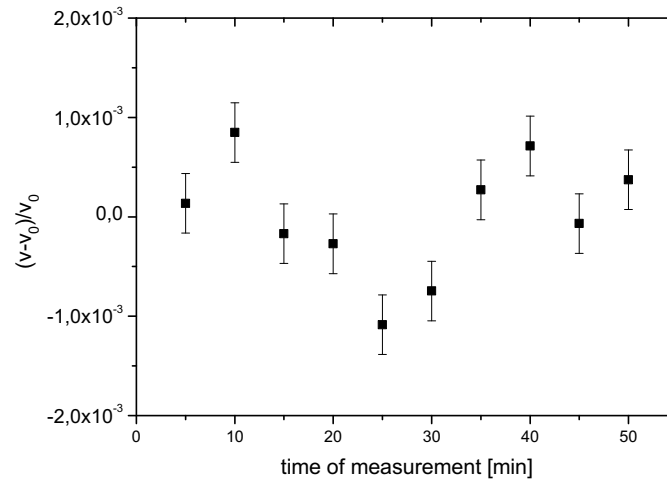


Figure 3.9.: Relative stability of the measured atomic velocity for a 50 minute sequence, measured with the light sheet method. The actual velocity  $v$  is compared to the value  $v_0$ , which is calculated from the applied frequency difference for the moving molasses. Each displayed point is the mean value of 5 minutes of consecutive measurements.

### 3. Implementation

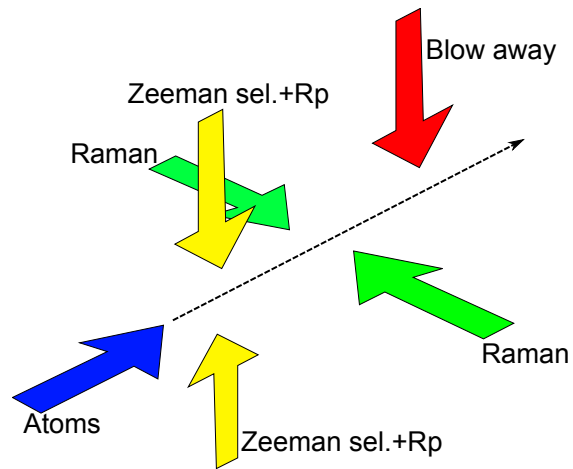


Figure 3.10.: Schematic showing the directions of the various beams involved in the atomic state preparation.

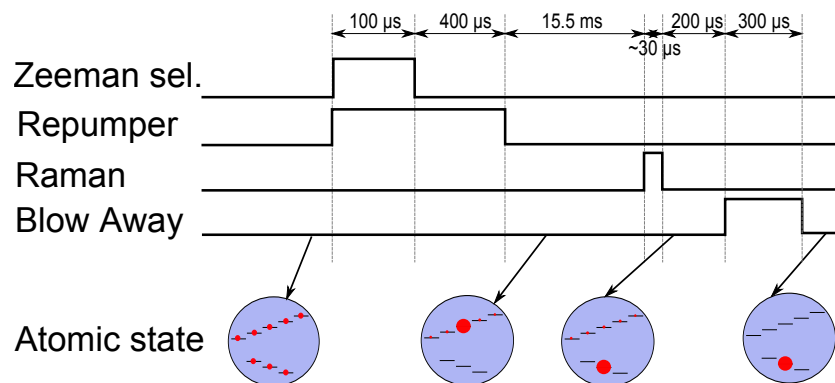


Figure 3.11.: Timing of the state preparation, with an energy level diagram with the Zeeman substates of the  $|F = 1\rangle$  and  $|F = 2\rangle$  states, schematically showing the distribution of the atoms.

### 3. Implementation

Table 3.2.: Measured number of atoms during the state preparation in percent of the number of atoms launched from the 3D-MOT/molasses.

	$ F = 1\rangle$	$ F = 2\rangle$
Initial	15%	85%
After Zeeman-sel. and repumper	3.5%	92%
After blow away (final)	9.5%	0.1%

4. Finally some resonant light on the cooling transition is shined in to blow away the remaining atoms in the  $|F = 2\rangle$ -state. As this involves spontaneous decay, it also removes any remaining coherence in the initial state of the atoms for the actual interferometer.

Figure 3.10 shows the position of the beams involved. The technical details like lenses and windows and wave plates is in section 3.8 because of the spatial overlap with the state detection. Due to limitations of the optical access in the central chamber, part of the state preparation has to be done in the interferometry zones. The shared Raman light also ensures proper alignment of the velocity selective Raman pulse relative to the interferometry pulses, at the expense of shortening the available interferometry length. The length of the velocity selective Raman pulse in the preparation is longer than the Raman pulses in the interferometry to ensure that the atoms can be manipulated with a high efficiency in the interferometry. Table 3.2 summarizes the measured transfer efficiencies during this preparation.

## 3.6. Interferometry

In the interferometry zone the atoms are split, reflected and recombined using Raman transitions to form a Mach-Zehnder interferometer. Each of the three pulses is based on the absorption of a  $\sigma^+$ -polarized photon from one light field, that is emitted again as a  $\sigma^+$ -photon in a second light field that has the opposite direction such that  $2\hbar k$  photon momentum is transferred to the atom which also changes its internal state between  $|F = 1, m_f = 0\rangle$  and  $|F = 2, m_f = 0\rangle$  ( $\Delta m_f = 0$ ).

The two light fields with opposite directions are realized by sending  $\sigma^+$  and  $\sigma^-$ -light in one direction through the main chamber but reflecting back only one of the two ( $\sigma^-$ ) which after reflection and two passes through a quarter wave plate becomes  $\sigma^+$ , this way only transitions with  $\Delta m_f = 0$  can be driven. The presence of a magnetic bias field lifts the degeneracy of the Zeeman-substates and prevents the occurrence of transitions between other internal states. This also prevents the co-propagating velocity in-selective transition due to the co-propagating light fields ( $\sigma^+$  and  $\sigma^-$  from one side) which would drive the transition  $|F = 1, m_f = 0\rangle \rightarrow |F = 2, m_f = +2\rangle$ .

Each of the three interferometry pulses is applied in a separate window, enabling a long drift time of up to  $2T = 46$  ms, with each window having an independent

### 3. Implementation

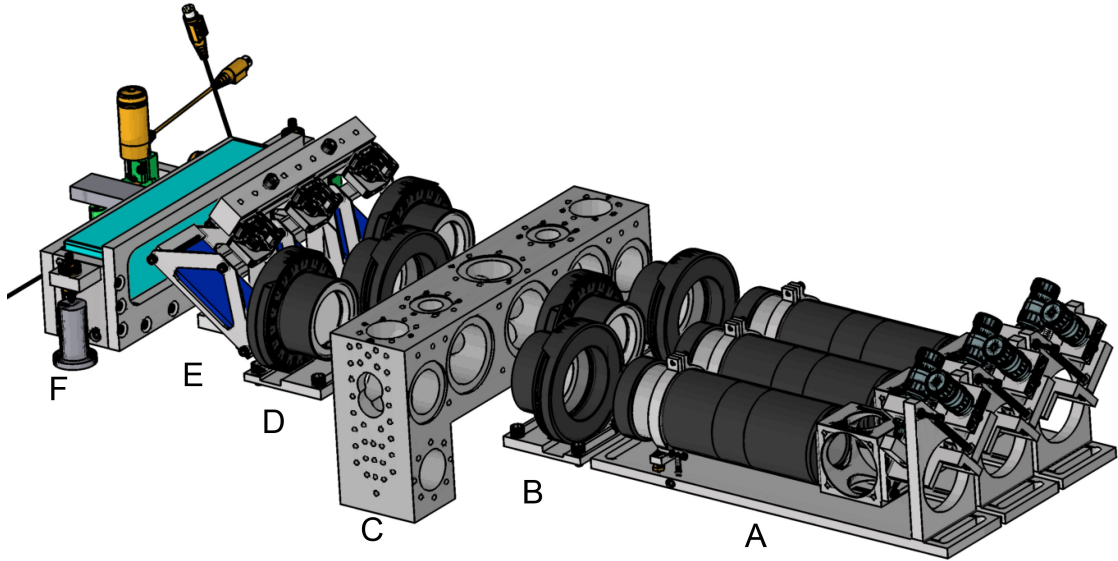


Figure 3.12.: Overview of the optical setup for the interferometry zone. A: fiber out coupler (fiber connector with one lens), B, D: quarter wave plate, C: main chamber, E: polarization filter, F: mirror.

optical fiber, avoiding non-polarizing beam splitters. It does however need to filter the polarizations before reflecting the light back through the main chamber. Having three fibers each carrying both light fields (in opposite polarizations) makes them only sensitive to phase fluctuations on the wavelength of the RF beat note (44 mm) but not the of the optical wavelength (780 nm). This method is also sensitive to phase changes, at the length of the microwave transition, between the three fibers in the time between the Raman pulses. The absolute phase difference between the three paths, though, disappears from the differential interferometry signal, only drifts remain.

This solution has been chosen as it promises the best performance without excessive complexity in comparison to some of the alternatives that were also considered:

1. Everything through one fiber: This needs extremely good non-polarizing optics to maintain the power balance between the two polarizations due to AC Stark shift.
2. Independent fibers for each side (one or three per side): This needs an optical phase locked loop on the fibers because they are sensitive to changes on the scale of the optical wavelength.
3. Frequency shifting the back-reflection like in reference [71]: This is a complicated but high performance solution, with the advantage of common mode rejection on the fibers and also suppression of the effect of parasitic reflexions in the interferometer because of the frequency shift.

The interferometry zone consists of the middle three windows of the central vac-

### 3. Implementation

uum chamber. The light for each window is delivered by an independent fiber<sup>2</sup> (with opposite linear polarization for each of the two optical frequencies) and collimated to 48 mm beams ( $1/e^2$  diameter) (which is further limited by the 40 mm diameter of the windows of the vacuum chamber) with a single achromatic lens (Newport PAC087,  $f=200$  mm). A large quarter wave plate (Fichou<sup>3</sup>) before the vacuum chamber transfers the light from linear to circular, to pass with  $\sigma^+$  and  $\sigma^-$ -polarization through the atoms. Another quarter wave plate behind the vacuum chamber turns the polarization back to linear for the following polarization filter (B.Halle<sup>4</sup>) which removes one of the two polarizations. The final optical component is the large mirror (Fichou<sup>5</sup>) that forms a common reference plane for all three beams. This way there are two polarizations in forward direction and only one in reverse. The entire setup for the interferometry is shown in figure 3.12.

The large mirror can be rotated around two axis with piezo stepper motors (Newport PZC200KT), and has an additional piezo actuator<sup>6</sup> for very precise alignment round its long axis (to compensate for gravitational acceleration). The beam expanders can be optionally equipped with a fast photodiode to measure the phase of the beatnote after the fiber to enable a compensation of any drift should it be necessary.

The alignment of the interferometry beams with respect to gravity is realized by aligning the beams with a penta prism on the back reflexion from a water surface [48]. The horizontal alignment is given by the back reflection from the large mirror. This also ensures that all three beams are parallel.

For the precise manipulation of the atomic states in an atom interferometer it is necessary to separate the various internal states to avoid any degeneracy. This is achieved by adding a bias field which separates the Zeeman states, so one can address each transition separately. The atomic states used by the interferometer are the  $m_f = 0$  substates which have no linear Zeeman effect and are only to second order sensitive to the magnetic field. The bias field needs to be homogeneous to avoid additional phase shifts (even though magnetically insensitive states are used, and symmetric trajectories should cancel any remaining common mode phase offsets).

These bias coils have been numerically optimized using a finite element method based on plain Biot-Savart equations with the available space as boundary conditions to achieve the most homogeneous field possible, see also appendix E.1. The resulting field is shown in figure 3.13. The optimized coils have been implemented as printed circuits boards (PCB) with two windings on each PCB side and are as big as possible while maintaining symmetry (the Helmholtz condition would have required far bigger coils), the CAD drawing is shown in appendix C.2. The offset

<sup>2</sup>Schäfter und Kirchhoff PMC-780-5.0-NA012-3-APC-700-P

<sup>3</sup>Custom component with specification:  $\phi$  40 mm, 780 nm, delay  $<\lambda/300$ , wavefront  $<\lambda/10$

<sup>4</sup>Custom component with specification: size  $80 \times 40$  mm, thickness 8 mm, angle of incidence  $55^\circ$ , wavelength 780 nm, flatness  $\lambda/20$ , transmission  $T_s < 1\%$ ,  $T_p > 95\%$

<sup>5</sup>Custom component with specification: zerodur, size  $50 \times 190$  mm, thickness 40 mm, flatness  $\lambda/20$  over  $170 \times 40$  mm, protected gold coating for 780 nm.

<sup>6</sup>Piezomechanik PSt150/7/20VS12VbS

### 3. Implementation

field strength is about 400 mG/A with a typical current of 1 A. These and other key parameters of the coils can be found in table 3.1. The coils for the bias field are switched by analog programming of the power supplies, and are only active during the state preparation, interferometry and state detection.

## 3.7. State detection

The simplified optical setup for the state detection is shown in figure 3.14. The technical details like lenses, windows and wave plates are in section 3.8 because of the spatial overlap with the state preparation.

The detection of the atomic state consists of several steps:

1. First the number of atoms in the upper state  $|F = 2\rangle$  is measured ( $N_2$ ) by detecting the fluorescence light while shining in  $\sigma^+$ -polarized resonant light on the closed transition  $|F = 2\rangle \rightarrow |F' = 3\rangle$  for 0.8 ms,
2. Then the atoms from the lower state  $|F = 1\rangle$  are transferred to the upper state  $|F = 2\rangle$  by applying  $|F = 1\rangle \rightarrow |F' = 2\rangle$  light (“repumper”) for 0.4 ms,
3. Again the number of atoms in the upper state is measured in the same way as in the first step, resulting in a measurement of the total number of atoms ( $N_{all}$ ) for 0.8 m,
4. After about 22 ms, when all atoms have left the detection zone, the background signal is measured ( $N_{bg}$ ) while shining in the same light of steps 1 and 3 for 0.8 ms.

The resulting photodiode signal is shown in figure 3.15. These measurements are combined to get the signal (S):

$$S = \frac{N_2 - N_{bg}}{N_{all} - N_{bg}}, \quad (3.2)$$

S=0 means all atoms are in the lower  $|F = 1\rangle$  state, S=1 means all atoms are in the  $|F = 2\rangle$  state.

The sensor noise will ultimately be given by the shot noise of the atoms:

$$u(S) = \frac{\sqrt{N}}{N}. \quad (3.3)$$

This means that in a shot noise limited sensor with  $1 \cdot 10^8$  atoms, the signal (ratio of the atomic states  $|F = 1\rangle$  and  $|F = 2\rangle$ ) can only be measured to about  $1 \cdot 10^{-4}$ .

Most of the time these fringes do not go from 0 to 1 but have a reduced amplitude  $\xi$  and some offset, see also equation 2.40, this modifies the noise limit:

$$u(S_{eff}) = \frac{\sqrt{N}}{2\xi N}. \quad (3.4)$$



### 3. Implementation

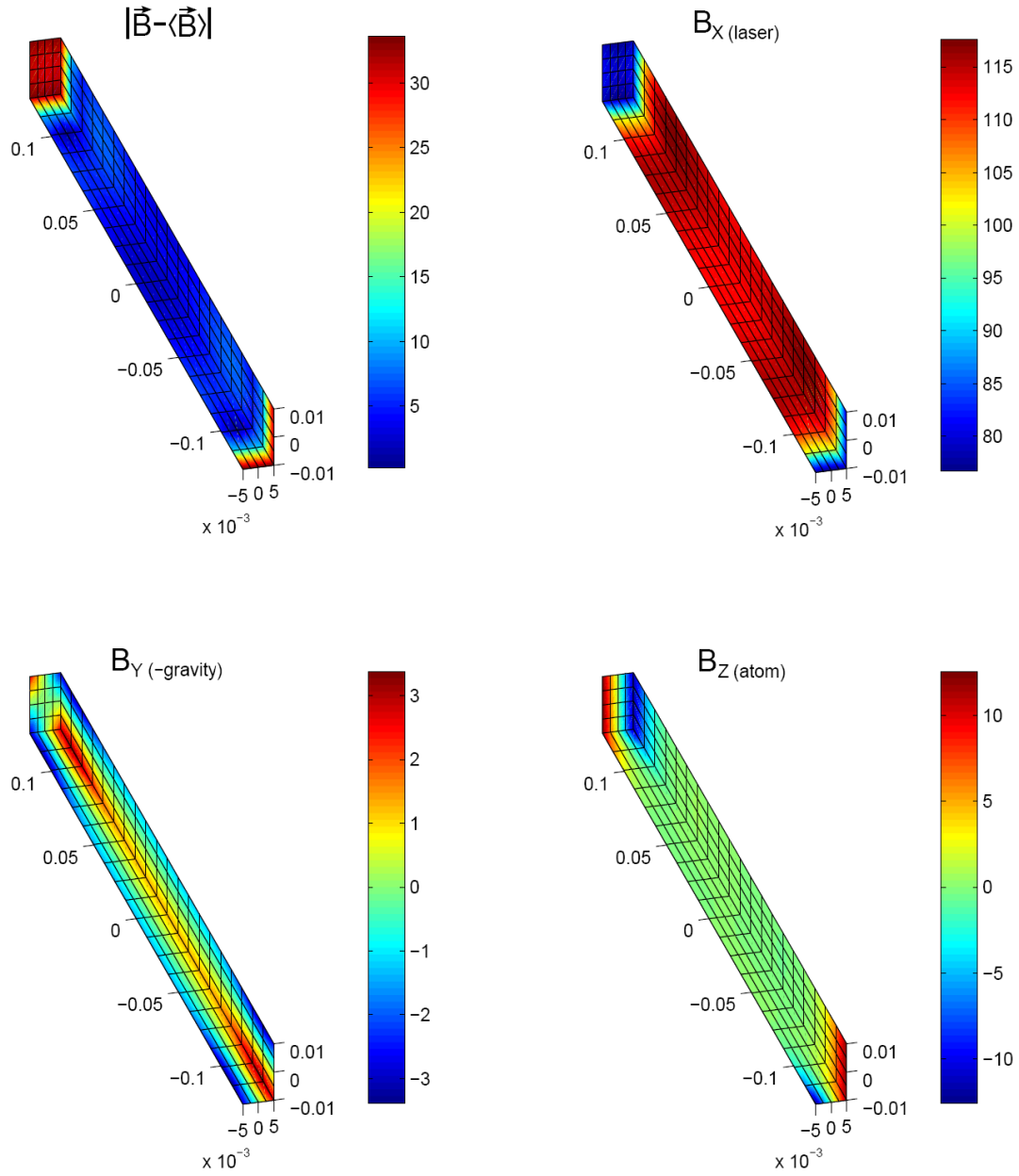


Figure 3.13.: Bias field. Absolute deviation from mean field, as well as the deviation split up in the three orthogonal directions. The simulated volume is  $10 \times 20 \times 250$  mm, covering all five windows of the main chamber. The spatial coordinates are in meter, the magnetic field (colorbar) is in mG/(A·coil).

### 3. Implementation

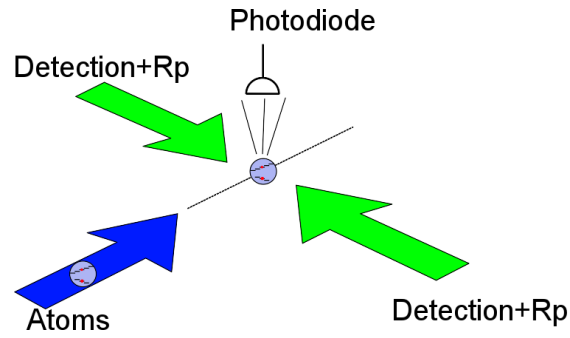


Figure 3.14.: Schematic showing the directions of the various beams involved in the atomic state detection.

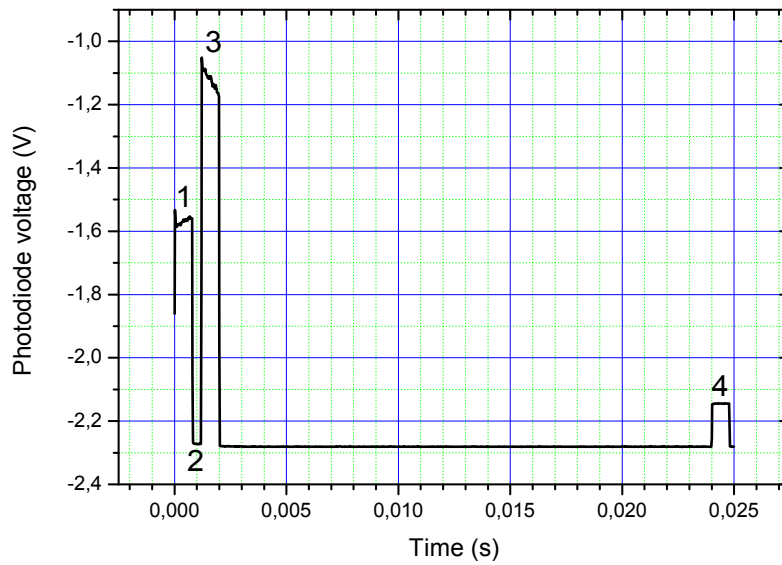


Figure 3.15.: Image of the recorded photodiode signal. Pulse 1 measure the number of excited atoms  $N_2$ , pulse 3 measures the total number of atoms  $N_{all}$ , pulse 4 measure the background signal  $N_{bg}$ . At position 2 one can also see some additional scattered light from the repumper.

### 3. Implementation

Meaning that for the same  $10^8$  atoms and a fringe amplitude ( $2\xi$ ) of 0.2 one can only measure  $5 \cdot 10^{-4}$ . This reduced contrast can come from finite atomic temperature (velocity distribution) and Gaussian intensity distributions, errors in state preparation and detection, etc..

The technical noise sources which go into the state detection are laser noises, photodiode electronic noise and digitization, see also table 3.3.

The laser noise of the detection light is given in section 4.2.1. As a change in the light field results in a change of the scattering rate according to equation 2.70, this also influences the detection signal. This can be suppressed by using a strong light field of several  $I_{sat}$  to get power broadening.

The photo diode noise consists of electric noises of the photodiode and its amplifiers circuit (see also appendix D.13). Analysis of the circuit shows that the current noise of the first amplifier is the main source of electronic noise. The large offset that this amplifier has, is fortunately not a problem for the chosen detection scheme.

Due to the large offset current of the first amplifier in the photodiode circuit there is a 2 V offset on the photodiode signal so that we must use the  $\pm 5$  V range of the 16 bit analog to digital converter (ADC) even though the signal is only a few 100 mV, resulting in a relative resolution of  $1.5 \cdot 10^{-3}$ . Because the light pulses are 0.8 ms long, one can average over 40 data points (50 kHz sample rate) resulting in a digitization noise limit of  $2 \cdot 10^{-4}$ . A better scaling and offset in the photodiode circuit could make better use of the available resolution, resulting in one order of magnitude better digitization noise.

The photon shot noise is determined by the number of scattered photons from the atoms received by the photodiode, determined by intensity and frequency of the light fields and by the solid angle the photodiode sees. When more then one scattered photon per atom is received by the photodiode then the photon shot noise can be neglected.

Offset and scaling errors in the photodiode signal are not relevant because the atomic signal is normalized.

Because of the velocity of the atoms they are not fixed to one position in the detection beams, resulting in a Gaussian pulse shape when they travel through the detection zone. In the 2 ms they travel about 6 mm and the Gaussian distribution does become noticeable, for this reason the  $N_2$  and the  $N_{all}$  measurements are symmetrically around the center, see also section 2.5.4. Velocity and timing errors will cause offsets in the measured state population, but these can be removed with the appropriate algorithm to estimate  $\xi$  and  $\theta$  in equation 2.40.

## 3.8. Combined state preparation and detection

Because the state preparation and detection are, due to symmetry, in the same location the actual optical setup is a little more complicated than one would expect from the individual descriptions in section 3.5 and 3.7. The two functions can be combined because they are needed at different moments in time.

### 3. Implementation

Table 3.3.: Noise budget of the state detection for one shot of the atoms on one photodiode, assuming  $1 \cdot 10^8$  atoms, with a 100 mV signal. The photon shot noise is based on the number of photons on the photodiode to cause a 100 mV signal.

	Abs.	Normalized
Laser: relative intensity noise	$2 \cdot 10^{-3}$	$1 \cdot 10^{-3}$ *1
Laser: FM	50 kHz	$10^{-4}$
Electronic (Bandwidth=1 kHz)	11 $\mu$ V	$1 \cdot 10^{-4}$
-Photodiode	$1.9 \cdot 10^{-9}$ V/ $\sqrt{\text{Hz}}$	
-Amp1 (LMH6624)	$3.5 \cdot 10^{-7}$ V/ $\sqrt{\text{Hz}}$	
-Amp2 (OP37)	$8 \cdot 10^{-9}$ V/ $\sqrt{\text{Hz}}$	
Digitization ( $\pm 5$ V / 16 bit, 40 samples)		$2 \cdot 10^{-4}$
Measured detection noise *2		$1 \cdot 10^{-2}$
Atomic shot noise ( $1 \cdot 10^8$ atoms)		$1 \cdot 10^{-4}$
Photon shot noise		$1.6 \cdot 10^{-5}$
Launch velocity		$2.3 \cdot 10^{-3}$
Launch position		$6 \cdot 10^{-4}$

\*1: Without spectral weighting.

\*2: Based on atomic measurements without interferometry and state preparation.

The Zeeman selection light of the state preparation and the photodiode for the state detection both need to go in the same window. Since this window is only 20 mm wide they have to share their optical paths. This has been realized by having the photodiode (appendix D.13) look down from above with the Zeeman selection light being coupled in from the side with an uncoated surface beam splitter (Linos G390138000). This throws away 90 to 99 % of the Zeeman-selection and repumping light, but since only 70 respectively 300  $\mu$ W are needed this is not a problem. This way the scattered light from the atoms for the state detection loses only about 5 %, which is acceptable. They also share the first lens ( $f=100$  mm). The preparation has its fiber output at the focal length from this lens resulting in a collimated beam, whereas the detection has two additional lenses ( $f=30$  mm each) to focus the scattered light from the atoms onto the photodiode, see also figure 3.16. The mirror for retroreflecting the Zeeman selection light (as well as some of the scattered light for the detection) is mounted inside the vacuum chamber with a UHV-compatible glue (for practical reasons).

The detection and repumper light, which shines in horizontally with 22 mW respectively 3.5 mW, is collimated with a single lens ( $f=175$  mm).

Due to space limitations in the first window, it was necessary to move the velocity selective Raman pulse of the preparation to the second window, therefore also moving the blow away to the second window. The blow-away beam is sent in from above without any lenses, using the natural divergence to illuminate the entire atomic cloud, it has a  $10^\circ$  angle from the vertical to leave more space for the actual interferometry, see also figure 3.17. This also reduces the space available for the interferometry, of the originally planned [47] drift time ( $2T$ ) of 50 ms only

### 3. Implementation

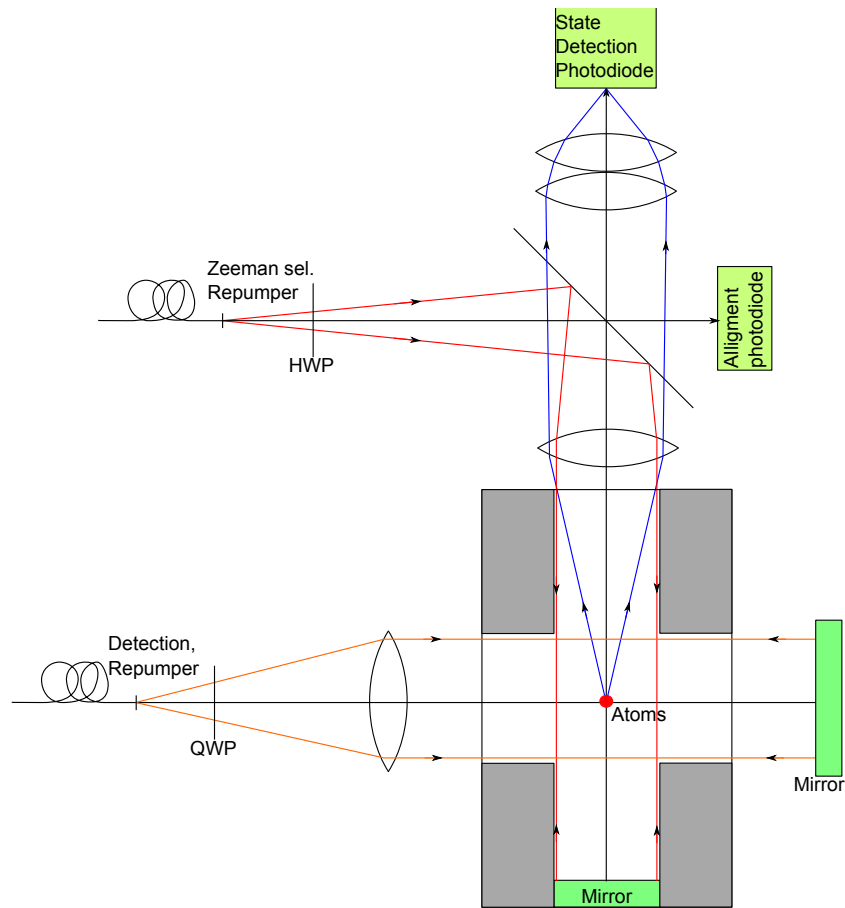


Figure 3.16.: Cross section of the first window of the main chamber with the optics for the first half of the state preparation (Zeeman selection and repumper light from above) and the complete state detection (detection and repumper light from the side).

46 ms are available, which with a velocity of 2.79 m/s, results in an enclosed area of 17 mm<sup>2</sup>.

### 3. Implementation

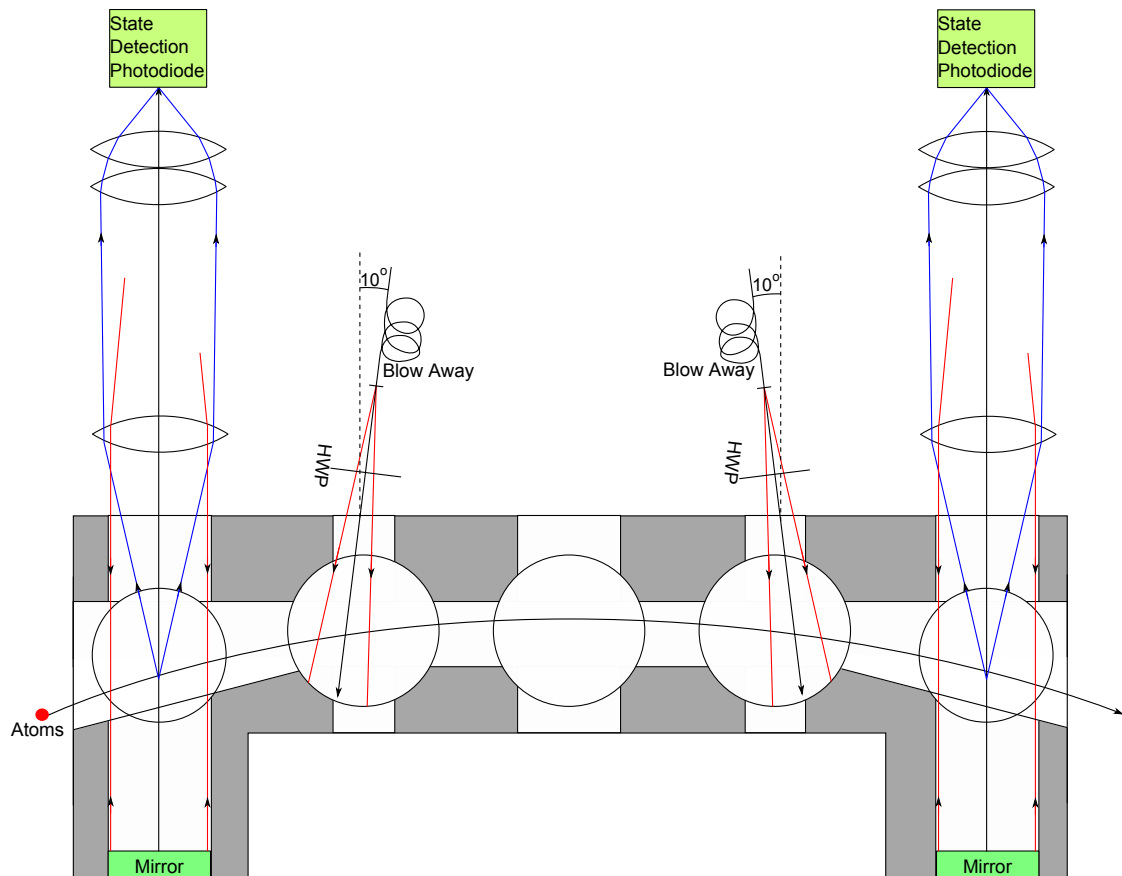


Figure 3.17.: Cross section of the optical setup parallel to the atomic trajectory, showing the orientation of the blow away beams. The state preparation and detection is shown only partially, a more complete view is figure 3.16 which is orthogonal to this view. The interferometry setup, which uses the three central windows, is shown in figure 3.12.

## 4. Realization of the light fields

In order to generate the light for the many beams of the previous chapter, a complex laser system has been realized which has been split in two components: The light sources 4.2, which generate the light and also does some large frequency manipulations, and a switching and distribution system 4.1, which brings the light from the lasers to the atoms as well as doing a lot of power switching and most (smaller) frequency shifting. For all these manipulations accurate, low noise RF signal generators are needed which are described in section 4.3, as well as an extensive timing and control system, which is shown in section 4.4, which uses conventional computers as well as FPGAs to obtain the necessary accuracy and speed.

### 4.1. Distribution and switching

The light distribution and switching systems has been subdivided, closely related to the experimental stages of chapter 3, in 2D, 3D, interferometry and pusher/blow away/detection which operate largely independent.

#### 4.1.1. 2D-MOT light

The light from the laser for the 2D-MOT is overlapped with light from the repumping laser and send with 8 fibers to both 2D MOTs as shown in figure 4.1. The repumping light is orthogonally polarized with respect to the cooling light. Shutters in front of the fiber couplers are used to switch off the light. Each shutter controls two fibers. The double-pass AOM for the repumping light has only to shift the frequency back to resonance, its switching ability is not explicitly needed here. This AOM is shared with the pusher-blow-away-detection (section 4.1.4) and the 3D-MOT/molasses (section 4.1.2) light distribution and switching block. Therefore when the 2D MOT is active, state preparation and detection, are not properly possible.

The shutters have a delay of about 9 ms which is compensated in the experimental sequence. The total switching time of the light is about 2.7 ms.

#### 4.1.2. 3D-MOT/Molasses light

The frequency manipulations for the cooling and launching from the 3D-MOT are divided into two components: a large common frequency jump and a smaller differential frequency jump. The common frequency jump, which is the key parameter

#### 4. Realization of the light fields

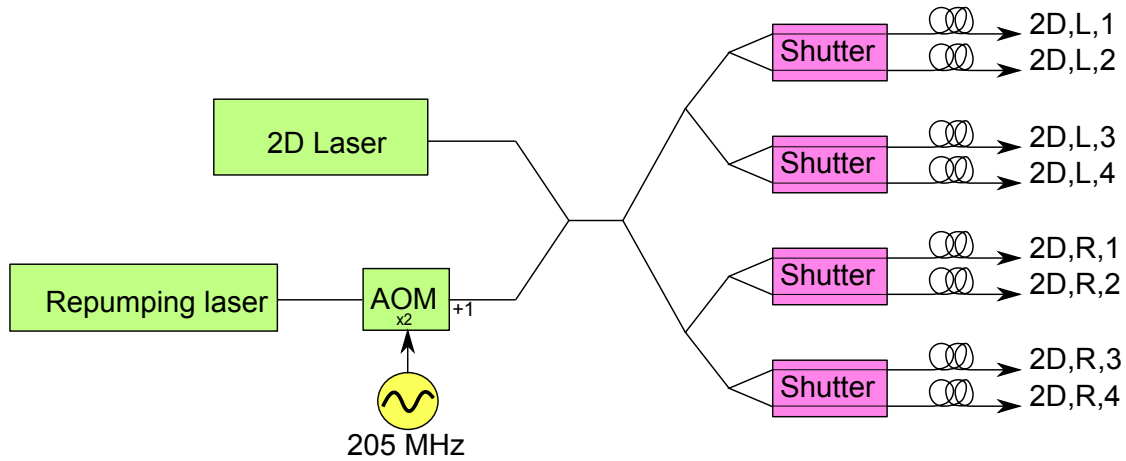


Figure 4.1.: Schematic of the light source for the 2D MOT. Each of the shutters switches two beams at the same time.

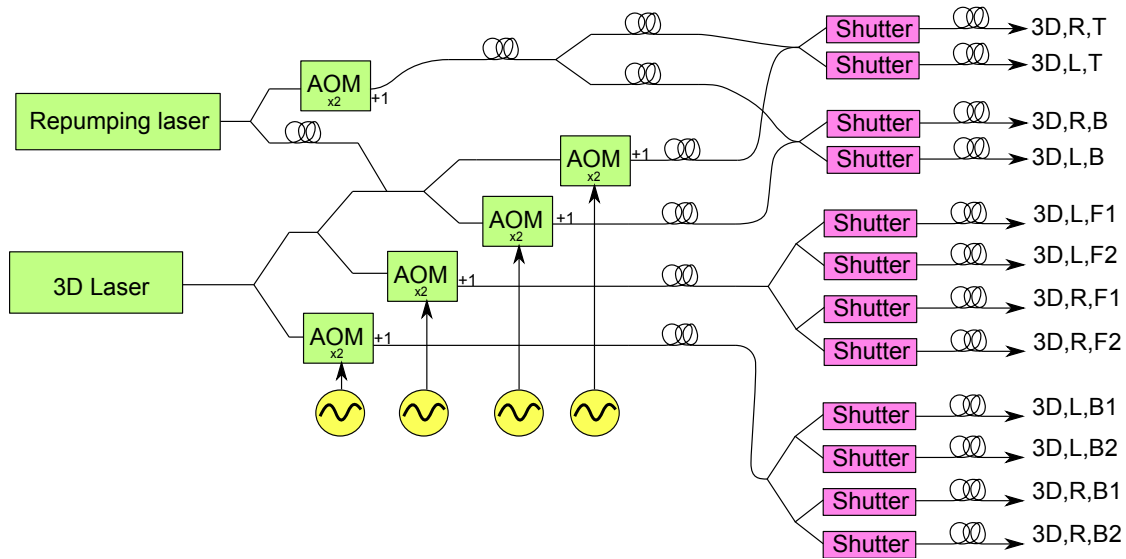


Figure 4.2.: Schematic of the light switching and distribution for the 3D MOT. This way four different cooling frequencies can be obtained, that are split into 2 or 4 fibers, depending on destination. There are two fibers for light from top (T) and two from the bottom (B) and four for the front (F1, F2) and back (B1, B2) beams, each output exists twice for each MOT (L: Left, R: Right).



#### 4. Realization of the light fields

for molasses cooling, is made with the laser itself (see section 4.2.3) enabling very large frequency jumps. Only the small differential component, for the Doppler shift to launch the atoms, in the 3D-MOT/molasses light is realized with AOMs as shown in figure 4.2. This way the AOMs always operate near optimum, avoiding any differences between the AOMs at higher detunings as was the case in the previous set-up [48]. To ensure a stable alignment into the fiber the AOMs are used in double-pass. The oscillators for these AOMs are all VCOs phase locked to DDS generators (see section 4.3.4.1) with a common reference oscillator (section 4.3.3). This ensures a very accurate frequency difference (mHz) despite the very high frequency (around 205 MHz). An analog attenuator in the DDS card is used to ramp down the RF power to realize the optical power reduction for the optical molasses. To switch the light off, the RF power to the AOMs is shut off, and additionally shutters are used to remove the remaining stray light.

The frequency of the cooling light is given by:

$$\begin{aligned}
 f_A &= f_B = f_{3D} + 2f_{AOM,back} \\
 f_C &= f_D = f_{3D} + 2f_{AOM,front} \\
 f_E &= f_{3D} + 2f_{AOM,top} \\
 f_F &= f_{3D} + 2f_{AOM,bottom}
 \end{aligned}
 \tag{4.1}$$

With  $f_{3D}$  as the frequency of the 3D-MOT/molasses cooling laser as defined in equation 4.4 and  $f_A, f_B \dots f_F$  defined in equation 3.1.

The repumping laser is fed into this system in two ways, first in front of the AOMs to have it Doppler shifted and intensity ramped together with the cooling beams and second via a commercial fiber splitter<sup>1</sup> without Doppler shift generating a constant background of repumping light. This construction was designed to optimize the launch sequence. One port of this fiber splitter is used here and one port is used for the pusher-blow-away-detection (section 4.1.4).

#### 4.1.3. Interferometry light

The optical circuit for light distribution and switching for the interferometry is shown in figure 4.3. Both Raman lasers are overlapped on a polarizing beam splitter, resulting in a crossed polarization which is needed for the interferometry. One output of the beam splitter goes to a fast photodiode to phase lock the frequency difference of the two Raman laser systems to a stable microwave reference, the other output is switched with several AOMs to realize the Mach-Zehnder pulse sequence and delivered to the interferometer via three optical fibers. From the beam splitter on the two light fields share the beam path ensuring good common mode rejection.

The first AOM is used to generate the pulse sequence. Since the middle and outer beams of the interferometer are not needed at the same time, power is shifted between these two areas with the second AOM. When a beam is off, there are at least two AOMs in its path off, ensuring a good suppression of leakage light, see

---

<sup>1</sup>OZ Optics FOBS-14P-11111-5/125-PPPPP-780-25/25/25-40-3A3A3A3A3A-3-2,2,2,2,2

#### 4. Realization of the light fields

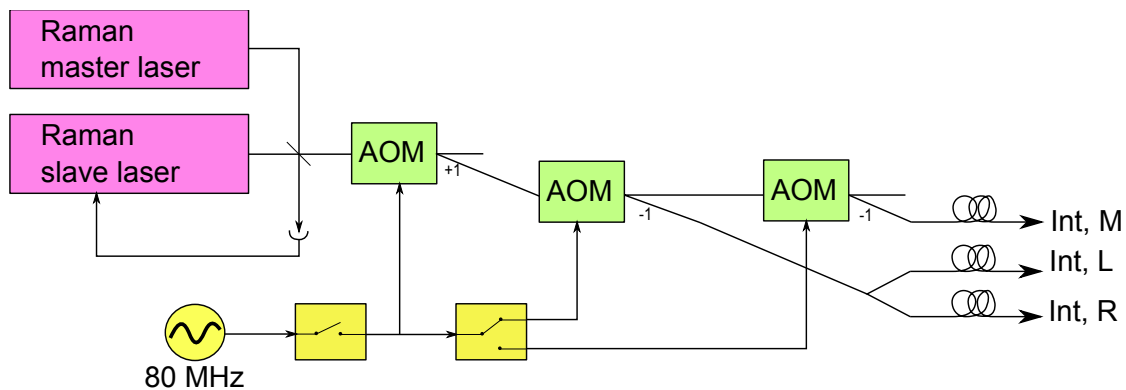


Figure 4.3.: Schematic of the Interferometry light switching and distribution. The two light fields have opposite polarization, and are always overlapped to improve common mode rejection. There are three outputs for the interferometer (L: left, M: middle, R: right).

Table 4.1.: Function table for the AOMs in the light switching and distribution system for the interferometry, see also figure 4.3.

Interferometry zone	AOM1	AOM2	AOM3
off	off	off	off
Left+Right	on	on	off
Middle	on	off	on

also table 4.1. The AOMs are switched on and off with RF switches (MiniCircuits ZYSW-2-50DR and ZYSWA-2-50DR) controlled by digital signals from the FPGA (section 4.4.3), resulting in square wave pulses. The AOM frequency, given by a free running VCO, does not show up in the interferometer light because the two active AOMs in each beam path have opposite frequency shift and cancel each other. The switches and AOMs need about 100 ns to switch on or off, which is far less than the typical interferometer pulse length of 10  $\mu$ s.

#### 4.1.4. pusher/blow away/detection

The pusher of the 2D-MOT, the Zeeman-selection and blow away of the state preparation as well as the detection light are all supplied by the same laser and light distribution setup shown in figure 4.4.

The main light source for these applications is the amplified output of the reference laser (see section 4.2.1) which is frequency shifted with AOMs to get the right frequency.

Because the frequencies for pusher, blow away and detection are very close they share there AOMs. The frequency of each of these two AOMs is switched between two different frequencies, giving a total of four different frequency sets, see table 4.2. This is possible since only one of the functions is used at any time. As a different frequency also means a different angle at the AOM output, this disables

#### 4. Realization of the light fields

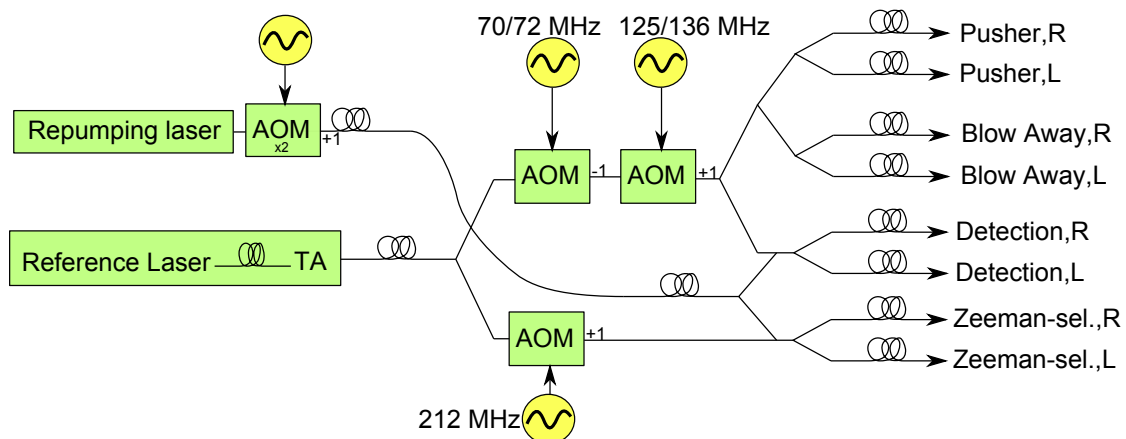


Figure 4.4.: Schematic of the light distribution and switching for the pusher, blow away and detection beams. All outputs occur twice because of the counterpropagating interferometry (L: Left, R: Right).

Table 4.2.: AOM settings for pusher, blow away and detection.

Function	AOM1 (MHz)	AOM2 (MHz)	Detuning rel. to atoms ( $\Gamma$ )
Pusher	-70	+136	+1.8
Blow Away	-70	+125	0
Detection	-72	+125	-0.3
(not used)	-72	+136	+2.2

light into the unwanted outputs. The frequency of these AOMs is given by two phase locked oscillators (appendix D.6).

The Zeeman-selection light has its own AOM, with the frequency given by a VCO, to shift the frequency of the reference laser to the  $|F = 2\rangle \rightarrow |F' = 2\rangle$ -transition.

The repumping light, which has to be delivered through the same fibers as the Zeeman-selection and the detection light, is supplied by the commercial fiber splitter of the 3D-MOT/molasses light distribution section. The repumping light is switched with the same AOM as the repumping light for the 2D-MOT.

## 4.2. Light source

This section introduces the various laser systems and their stabilizations that generate the light for the various distribution and switching systems of the previous section. Because of the extensive use of frequency offset locking methods the absolute frequency of a laser depends on the frequency of other lasers, figure 4.5 shows the frequency stabilization dependencies between the various laser systems. Despite the use of offset locking techniques, each laser system still has a very simple saturation spectroscopy to aid in finding the correct transition during start-up. Table 4.3 summarizes the key parameters of all lasers that are described in the

#### 4. Realization of the light fields

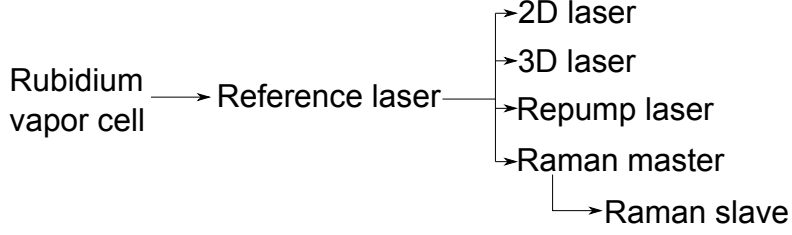


Figure 4.5.: Overview of the chain of frequency stabilizations between the various laser systems. The reference laser is the only one stabilized directly on a rubidium transition, all other laser use a frequency offset lock.

Table 4.3.: Overview of key parameters of the various laser systems.

Laser	Power (mw)	Linewidth (kHz)	Optical frequency	Beat note
Reference	25	100	$ F = 2\rangle \rightarrow  F' = 3\rangle$ -55 MHz	-
Ref-TA	550	“	Ref	-
2D-MOT	620	1000	$ F = 2\rangle \rightarrow  F' = 3\rangle$ -1.8 $\Gamma$	244 MHz
3D-MOT	900	150	$ F = 2\rangle \rightarrow  F' = 3\rangle$ -425..-548 MHz	370-493 MHz
Repumper	250	200	$ F = 1\rangle \rightarrow  F' = 2\rangle$ -410 MHz	6.2 GHz
Raman Master	1420	150	$ F = 2\rangle \rightarrow  F' = 1\rangle$ -676 MHz	1.1 GHz
Raman Slave	1260	“	$ F = 1\rangle \rightarrow  F' = 1\rangle$ -676 MHz	6.835 GHz

following subsections.

##### 4.2.1. Reference Laser

The reference laser is an interference filter stabilized external cavity diode laser [72, 73, 74] that is stabilized on a Rubidium transition using the Modulation Transfer Spectroscopy method [75]. The main purpose of this laser is to supply a stable reference frequency to all other laser systems. Because its light is also used for the blow away, pusher and detection beams, it is amplified in a tapered amplifier (TA) with the seed-light coming from a fiber to reduce the day-to-day maintenance effort. The reference laser and the TA are described in detail in reference [73].

The Modulation Transfer Spectroscopy is a type of saturation spectroscopy where the modulated pump beam is combined with a frequency shifted probe beam as shown in figure 4.6. This results in an error signal that has very little offset and drift. The pump beam is modulated with an EOM at 7 MHz. The oscillator for the EOM as well as the demodulation circuits are shown in appendix D.3. The laser output frequency  $f_{ref}$  is given by:

$$f_{ref} = f_{atom} - \frac{1}{2}f_{AOM} \quad (4.2)$$

The EOM frequency is not part of the shift, it only modulates the signal to enable a lock onto the top of the Doppler free atomic transition. The atomic frequency

#### 4. Realization of the light fields

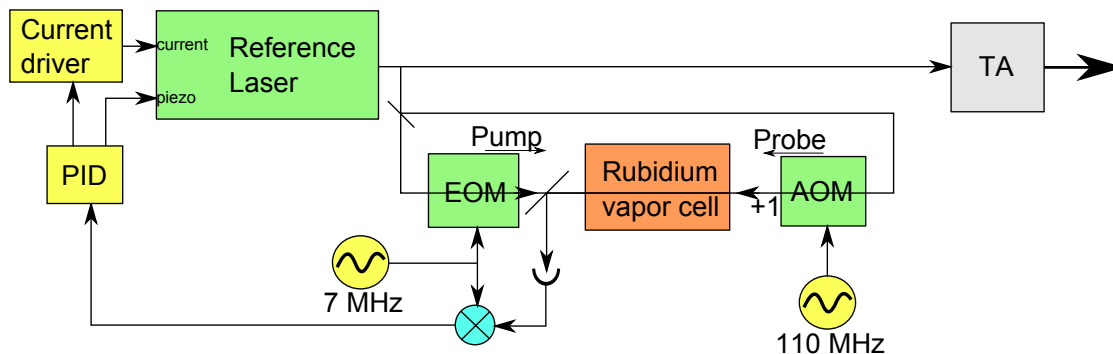


Figure 4.6.: Overview of the reference laser and the MTS lock. This is the primary frequency reference for the experiment as it is the only system that directly stabilizes onto a rubidium transition ( $|F = 2\rangle \rightarrow |F' = 3\rangle$ , the amplified output itself is 55 MHz below that). All other laser systems are stabilized relative to this one.

$f_{atom}$  is the frequency of the transition  $|F = 2\rangle \rightarrow |F' = 3\rangle$  where the reference laser is locked onto. The 110 MHz signal ( $f_{AOM}$ ) for the AOM comes from a VCO (MiniCircuits POS-150) that is phase locked to the reference oscillator, see also section 4.3.3 and appendix D.6.

Because this laser system is so important to the entire experiment, stability measurements with a frequency comb have been made, shown in figure 4.7. A direct inspection of the data shows a maximum deviation of up to 300 kHz. The stability is limited by the quality of the lock, which should be a fraction of the linewidth. The stability of the AOM is more than enough due to the very high stability of the reference oscillator. It also turned out that the linewidth of the laser strongly depends on the current source, the one shown in appendix D.12 turned out to be the best one available [73] and is used for almost all of our lasers except the 2D-MOT laser.

#### 4.2.2. 2D-MOT cooling Laser

The cooling light for the main beams of the 2D-MOT is provided by a commercial Littrow external cavity diode laser with tapered amplifier (Toptica TA100).

This laser uses a simple frequency lock based on a frequency to voltage converter (see appendix D.9) that locks the beat frequency between this laser and the reference laser as shown in figure 4.8. Because the difference frequency between the 2D-MOT laser and the reference laser is only a few 10 MHz, the light of the 2D-MOT laser is shifted with an AOM 200 MHz away so that the beat frequency for the locking scheme is higher, resulting in a larger capture range and a more robust operation. The laser output frequency is given by:

$$f_{2D} = f_{ref} + f_{AOM,2D} - f_{fv,2D} \quad (4.3)$$

The AOM frequency is provided by a free running VCO (appendix D.7). The effective locking frequency  $f_{fv}$  of the frequency to voltage converter is set by a

#### 4. Realization of the light fields

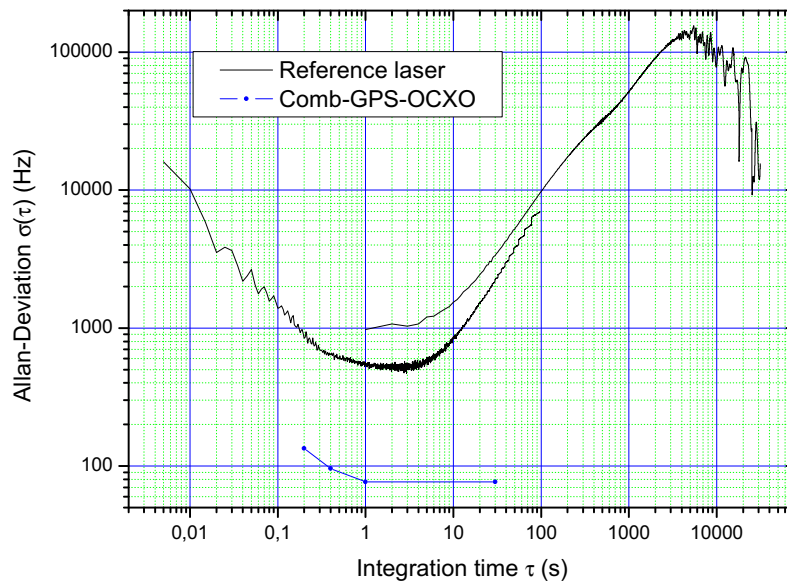


Figure 4.7.: Allan deviation between the reference laser and a frequency comb locked to GPS. The graph shows two data sets, the longest one was 35 hours. The blue line at the bottom shows the limit of the comb reference.

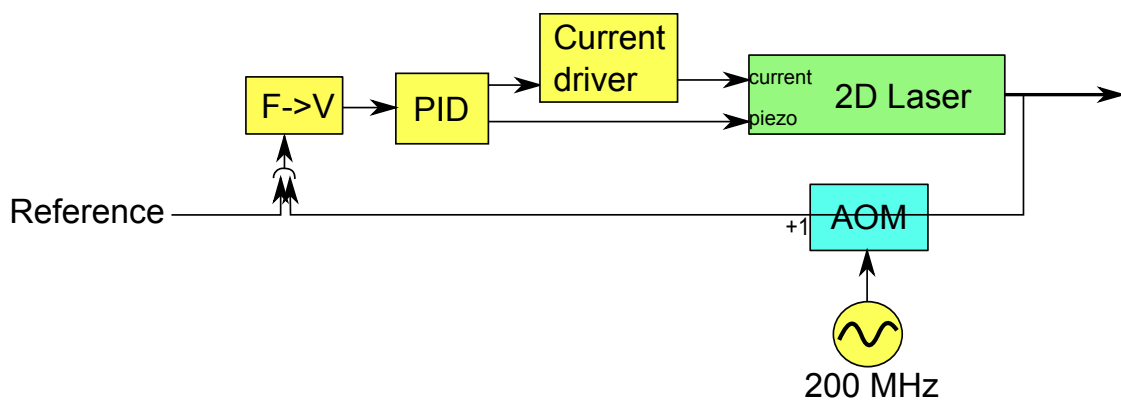


Figure 4.8.: Overview of the 2D laser locking scheme.

#### 4. Realization of the light fields

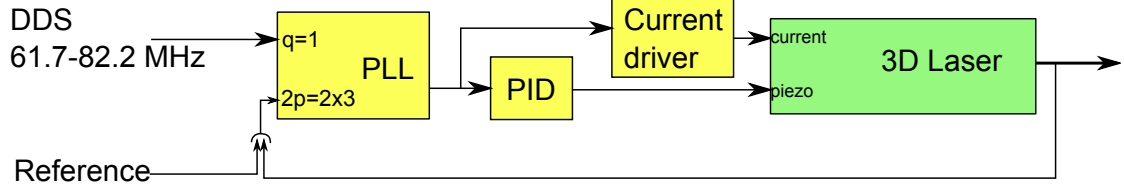


Figure 4.9.: Overview of the 3D laser locking scheme

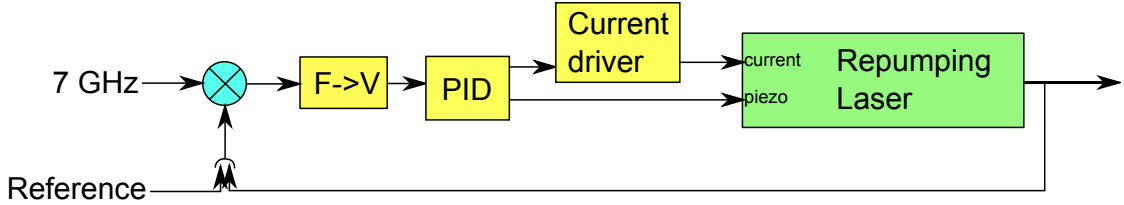


Figure 4.10.: Overview of the repumping laser locking scheme.

control voltage from the computer to about 244 MHz.

#### 4.2.3. 3D-MOT cooling Laser

The light for the 3D MOT/molasses is provided by an interference filter stabilized external cavity diode laser [72] with tapered amplifier. An optical phase locked loop as shown in figure 4.9 stabilizes the beat frequency with the reference laser on a RF reference frequency given by a DDS (section 4.3.4.1) with the resulting laser frequency given by:

$$f_{3D} = f_{ref} - 2 \frac{p}{q} f_{dds,3D} \quad (4.4)$$

The factor 2 is due to a fixed frequency divider in the circuit for the frequency division and phase locking which can be found in appendix D.8. With a DDS frequency  $f_{dds,3D}$  of 61.7 to 82.2 MHz and a multiplier ratio ( $2p/q$ ) of  $2 \times 3/1$ , this results in a beat frequency of 370.2 (acceleration) to 493.2 MHz (end of molasses).

The laser runs between 425 MHz and 548 MHz below the actual transition because the AOMs for the Doppler shift (see section 4.1.2) will shift it back by 410 MHz to be between  $-2.5 \Gamma$  and  $-23 \Gamma$ .

#### 4.2.4. Repumping Laser

The repumping light is provided by an interference filter stabilized self seeded external cavity tapered amplifier diode laser [72].

This laser is locked relative to the reference laser with the scheme shown in figure 4.10. The beat frequency is mixed with 7.0 GHz from the reference (section 4.3.2) and then converted with the frequency to voltage converter (appendix D.9) to a voltage that is fed into a PID that controls the laser. The resulting frequency is described with:

#### 4. Realization of the light fields

$$f_{rp} = f_{ref} - f_{7G} + f_{fv,rp} \quad (4.5)$$

With  $f_{fv,rp}$  as the effective frequency of the frequency to voltage converter. The repumping laser is operating about 410 MHz below the actual transition ( $|F = 1\rangle \rightarrow |F' = 2\rangle$ ).

##### 4.2.5. Raman Master

The first light field for the Raman transitions of the interferometry zone is generated with an interference filter stabilized external cavity diode laser [72] with tapered amplifier.

It uses a frequency locking technique based on a frequency to voltage converter combined with a frequency comb, see also figure 4.11. The beat frequency from the photodiode is mixed with a RF frequency comb (Herotek GC1026RC) fed by a frequency synthesizer (Rode&Schwartz SML01). The resulting signal is low pass filtered, to select the frequency component corresponding to the distance between the beat frequency and the nearest comb line, before going into a frequency to voltage converter (appendix D.9). The low pass filter is necessary to remove any higher frequency components which would disturb the frequency to voltage converter. The resulting error signal is shown in figure 4.12. This method has two death zones, first when the beat frequency gets too close to a comb line, and second when the beat frequency is further than the low-pass filter away from a comb line, that is in the middle between two comb lines. In these cases one should just change the comb frequency.

This method allows us to lock the laser to any frequency up to about 10 GHz. Because this method does not distinguish between the different comb lines, one needs to manually tune the laser to the correct starting point before activating the lock. The laser frequency is finally given by:

$$f_{R1} = f_{ref} - r \cdot f_{comb} \pm f_{fv,R1} \quad (4.6)$$

With  $r$  as the comb line number and  $f_{fv,R1}$  as the effective frequency of the frequency to voltage converter, the sign corresponds to the upper and lower side of the comb line. This frequency lock determines the detuning  $\Delta$  from the intermediate state in the Raman transition (see also figure 2.1), where  $\Delta = 676$  MHz was used for most of the measurements (the beat frequency is 1.1 GHz relative to the reference laser,  $f_{comb} = 1$  GHz,  $r = 1$ ,  $f_{fv,R1} = 100$  MHz, upper sideband).

##### 4.2.6. Raman Slave

The second light field for the interferometry is provided by an identical interference filter stabilized external cavity diode laser [72] with tapered amplifier as the Raman master. Several generations of both Raman lasers have been built and tested for the utilization as beam splitting lasers for atom interferometry [76, 66], the current version is described in detail in [77], it will therefore only be described briefly here.



#### 4. Realization of the light fields

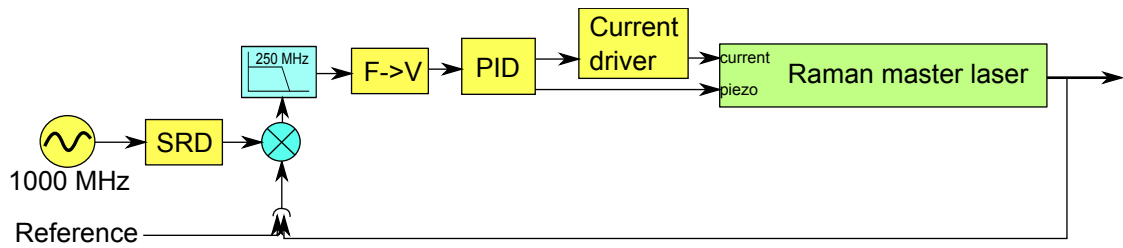


Figure 4.11.: Locking scheme of the Raman master laser. Although it typically is operated at 1.1 GHz this scheme can lock to any frequency up to about 10 GHz from the reference laser. The error signal behind the frequency to voltage converter is shown in figure 4.12.

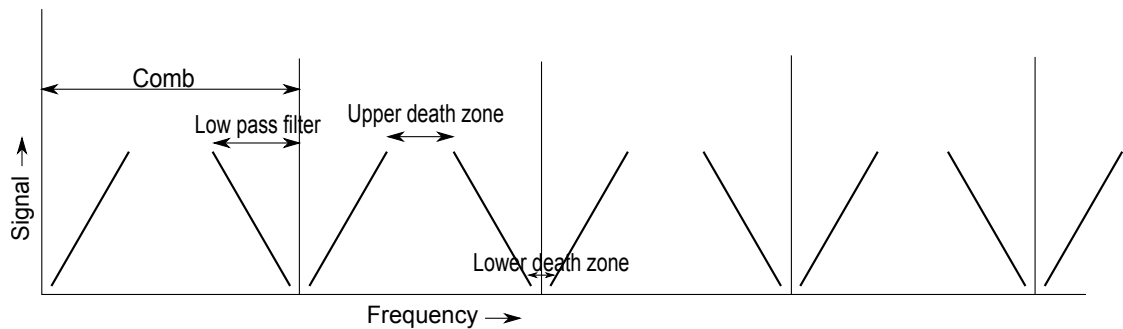


Figure 4.12.: Error signal for the frequency locking of the Raman master as a function of the offset frequency. The error signal repeats itself around every comb mode. Frequencies too close or too far away from the comb mode produce unstable error signals.

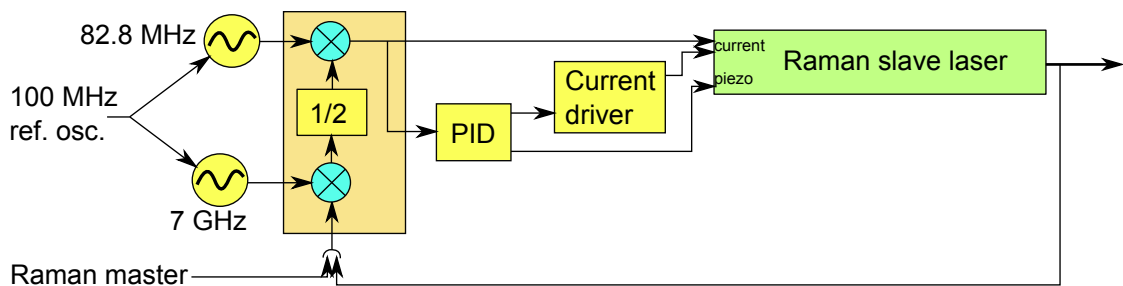


Figure 4.13.: Overview of the Raman slave locking scheme

## 4. Realization of the light fields

This optical phase locked loop uses a two stage process to down-convert the 6.835 GHz beat signal to a DC error signal that is used to correct the laser frequency, see also figure 4.13. The first stage is an analog mixer that mixes the beat signal with a low noise 7 GHz reference signal (section 4.3.2). The resulting 165.6 MHz are then frequency divided in a digital divide-by-two <sup>2</sup> before being compared with the 82.8 MHz signal from a DDS (section 4.3.4.2) in a digital phase frequency detector that generates the error signal. The exact values are experimentally determined. The final frequency of the slave laser is given by:

$$f_{R2} = f_{R1} + f_{7G} - 2f_{DDS,R2} \quad (4.7)$$

The DDS (section 4.3.4.2) has a frequency of about 82.8 MHz, and allows fast and accurate phase and frequency jumps for the various interferometer algorithms (Ramsey, Mach-Zehnder or even Factorization (section 5.5)).

This is a very important phase locked system, since all its phase noise turns up in the final interferometer phase measurement. A lot of effort has therefore been spend on reducing the phase noise (see also references [76, 66, 77], with the current version described in the last one). These highly optimized systems have achieved feedback bandwidths of up to 6.2 MHz and an estimated interferometer phase noise of only 3.2 mrad for  $2T = 46$  ms and  $\tau_\pi = 11$   $\mu$ s.

### 4.3. RF Frequency

#### 4.3.1. Reference oscillator

The very low phase noise reference is a commercial 100 MHz oscillator (Spectra Dynamics DLR-100). It is based on a 100 MHz quartz oscillator (Wenzel SC Premium) which is phase locked to a 5 MHz quartz oscillator (Wenzel Bluetop) with a bandwidth such as to maintain the lower phase noise of the two. The resulting phase noise at 100 MHz is shown in figure 4.14. Optionally it can also be locked to a hydrogen maser for improved accuracy.

#### 4.3.2. 7 GHz chain

The multiplication chain is shown in figure 4.15, it consists of two paths, one generates the 300 MHz reference frequency for the AD9852 DDS (section 4.3.4.2) for the second stage of the Raman phase lock (section 4.2.6), the other path generates the 7 GHz for the first mixing stage of the Raman phase lock (section 4.2.6) as well as for the frequency stabilization of the repumping laser (section 4.2.4).

---

<sup>2</sup>The use of the divide-by-two is to be historically explained, as the used circuit originates from BNM-SYRTE in Paris [78]. At the time of development, the best DDS had a clock frequency of only 300 MHz, and was only capable of output frequencies up to about 100 MHz. At the time of writing this thesis, DDS chips with clock frequencies at 500 MHz and higher are available, which can easily generate the 165 MHz directly.

#### 4. Realization of the light fields

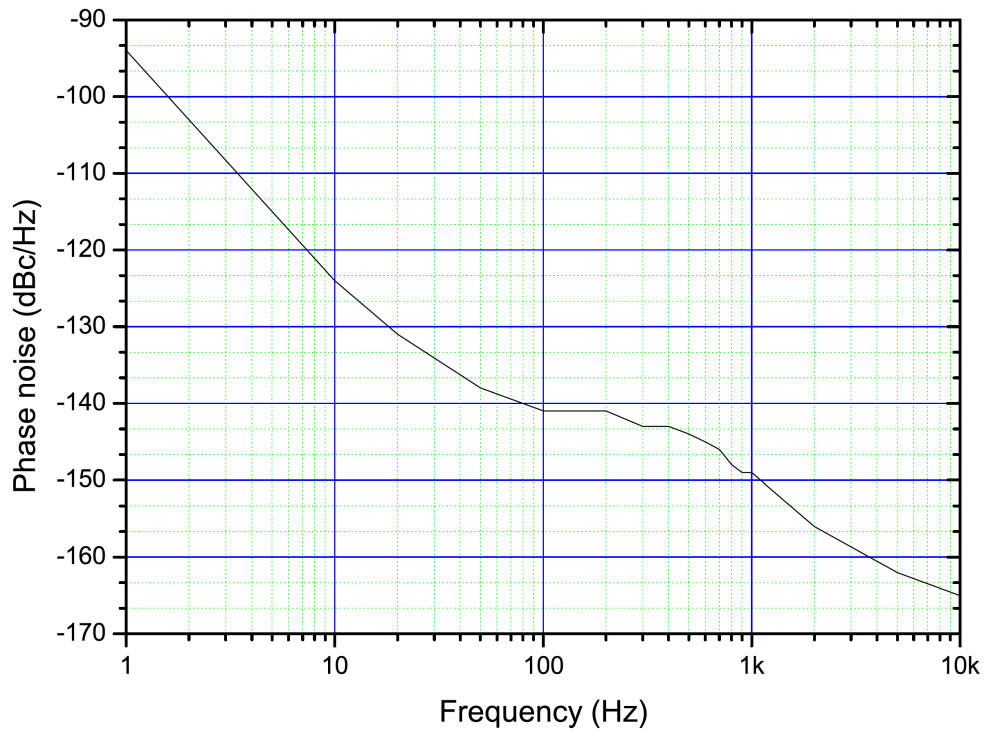


Figure 4.14.: Measured phase noise of the 100 MHz reference (single side band, at 100 MHz). The bump around 300 Hz is due to the transition from the 10 MHz quartz oscillator on the left to the 100 MHz oscillator on the right.

#### 4. Realization of the light fields

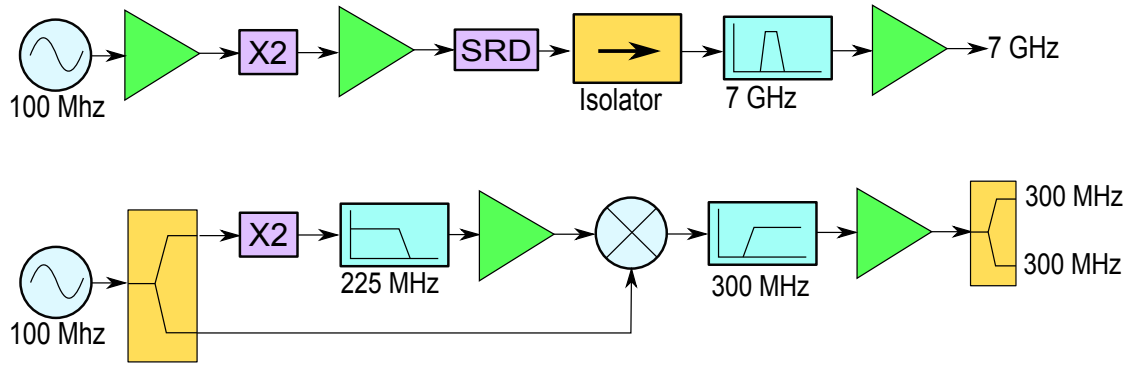


Figure 4.15.: Schematic of the multiplication chains used to realize the low noise 300 MHz and 7 GHz for the high stability phase locked loop of the Raman slave laser.

The 300 MHz is generated by frequency doubling (MiniCircuits RK-2) the 100 MHz and mixing (MiniCircuits TUF-3) the filtered (SCLF-225) and amplified (MAV-11) 200 MHz again with 100 MHz. This is filtered (SCHF-300) and amplified (ERA-5SM) and split (LRPS-2-1J) to provide two low noise 300 MHz outputs.

The 7 GHz starts by doubling the 100 MHz to 200 MHz (MiniCircuits RK-2). This signal is amplified (MiniCircuits MAV-11SM and AA Opto-electronic AMP.50-200.A6) and fed into a step recovery diode (Herotek GC200RC) creating a comb of frequencies from which a band pass filter (Tiger TGF221-7000MHz-04), after a RF-isolator (Tiger TGG-402), picks the 7.000 GHz harmonic which after another low-noise amplifier (LA6013N1505-3mh) is output as the 7 GHz reference signal. The resulting phase noise is shown in figure 4.16. Comparison with figure 4.14 indicates that the combined phase noise at 7 GHz will be limited by the reference.

#### 4.3.3. Frequency distribution

Even though the free running oscillator has been optimized for extra low phase noise for the Raman system, its frequency accuracy is also very good. It is therefore also used as the master oscillator for all other devices. The reference has three output ports, two of which are dedicated to the Raman system. To avoid any possible disturbances from less critical systems, nothing else is connected to these two ports. The last port has a 1-to-8 power splitter (MiniCircuits ZCSC-8-1) to supply the other users which includes the DDS-generators of the 3D-MOT, Synthesizers and others. The complete frequency distribution chain is shown in figure 4.17.

#### 4.3.4. DDS

Direct digital synthesis (DDS) [79] or numerically controlled oscillator, is a modern digital technique to generate RF signals with very high precision and at the same

#### 4. Realization of the light fields

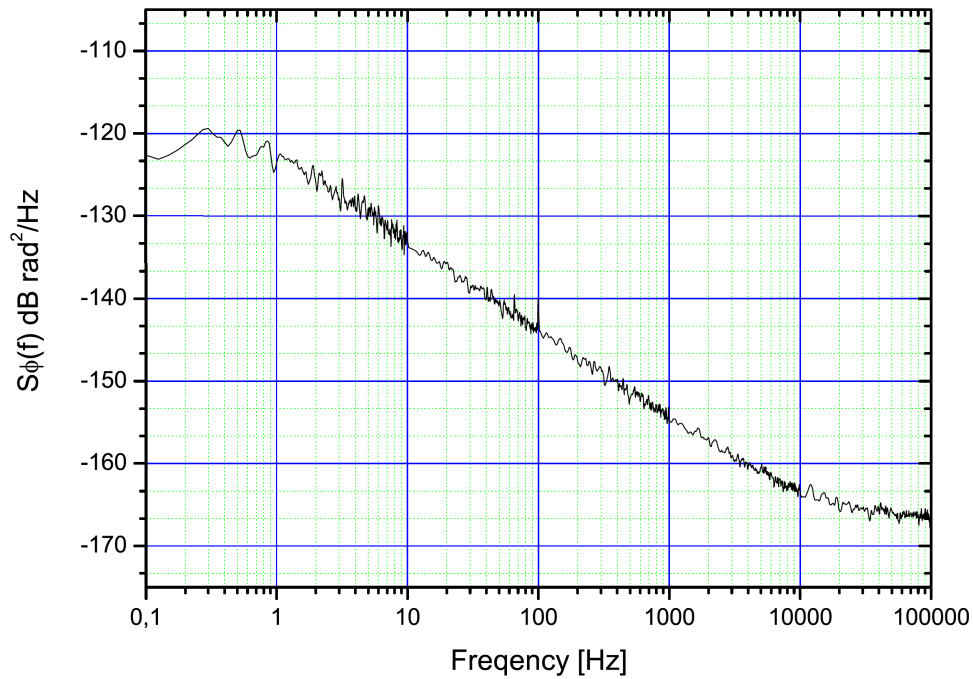


Figure 4.16.: Measured phase noise of the 7 GHz frequency multiplication chain, converted to its equivalent noise at 100 MHz for comparison to figure 4.14. The actual phase noise at 7 GHz is 37 dB higher.

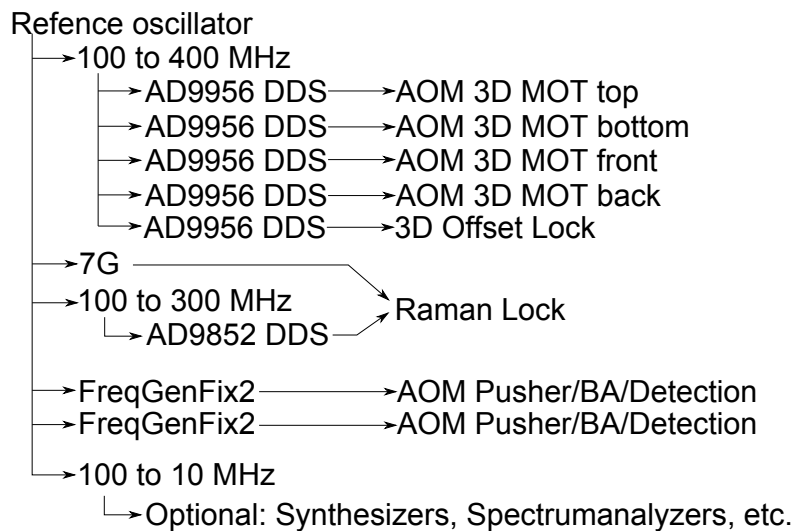


Figure 4.17.: Overview of the RF frequency distribution chain showing the signal path for the various devices that are locked to the low noise 100 MHz reference oscillator.

#### 4. Realization of the light fields

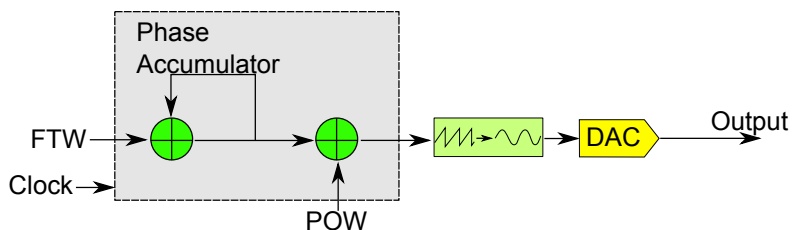


Figure 4.18.: Schematic of Direct Digital Synthesis. The feedback loop of the phase accumulator is executed once every clock cycle. All signals on the left of the DAC are digital words.

time very fast control and it is, by definition, always phase locked to the reference clock.

A DDS is a counter (the phase accumulator) which adds a certain value, the frequency tuning word (FTW), each clock tick. This value is sent to a phase-to-amplitude table which then goes to the digital to analog converter (DAC), see also figure 4.18. There is often also an additional sum function implemented that adds a phase offset word (POW) to the phase accumulator before it goes to the DAC, this allows phase shifting of the output signal.

It needs an external reference clock signal. For best performance they need to be supplied with the highest frequency the chip can handle (without using the internal frequency multiplier to avoid its extra phase noise). This method is digital by nature and therefore limited to frequencies up to half the sample frequency (Nyquist theorem [80]) and introduces some harmonics which need to be filtered out.

The output frequency is given by:

$$f_{DDS} = \frac{n_f}{2^{b_f}} f_{clock} \quad (4.8)$$

The frequency is basically expressed as a fraction of the clock frequency. The phase offset is expressed as a fraction of  $2\pi$ :

$$\phi = \frac{n_\phi}{2^{b_\phi}} 2\pi \quad (4.9)$$

The FTW ( $n_f$ ) and POW ( $n_\phi$ ) are both integers of a certain number of bits ( $b_f$  respectively  $b_\phi$ ). Because the FTW typically has 32 or more bits, one needs to be careful with the calculations since most programming languages are still limited to integers of 32 bits, only the “double” floating point with 53 significant bits would be adequate, resulting in some trickery to get all 48 bits for the used AD9956 and the AD9852. All calculations have been realized in software. A summary of all DDS circuits used is given in table 4.4, with the two main variants described in the following two subsections.

#### 4.3.4.1. AD9956 with phase locked VCO

The DDS for the 3D MOT/molasses distribution and switching system has been realized in the form of an ISA add-on card for computers. The ISA bus was used because it offers a simple method to quickly control peripherals (faster than most modern busses), can support many add-on cards and has good documentation available (besides various websites, also reference [81]). The ISA bus is relatively old and no longer available in desktop computers, but it is still available in industrial computers.

The card uses the AD9956 (Analog Devices) in combination with a VCO (Mini-Circuits POS-300) which is phase locked to the DDS with some dividers which are also included in the AD9956. This way it is possible to achieve frequencies around 200 MHz, beyond what the AD9956 can directly achieve. The key parameters are shown in table 4.4. The DDS is controlled by a CPLD (Altera EPM7128S) which translates between the parallel ISA-bus of the computer and the serial format of the DDS. The circuit is shown in appendix D.2.

This chip can do phase and frequency jumps, and has 8 sets of phase/frequency settings that can be externally selected. The amplitude control has been realized with an analog attenuator controlled by an external voltage. Originally the attenuator was controlled by an 8 bit DAC with only 4 amplitude settings realized in the CPLD (8 did not fit) controlled by the same connector as the phase/frequency.

For the starting of the atoms, less than 8 different frequencies are used, so that they can be programmed in advance and the FPGA only supplies the 3 register select signals. The assignment of which frequency goes into which register has been automated in the main program (section 4.4.2), so that one chooses the frequency and the computer takes care of the technical details.

The RF signal during the critical start sequence has been directly measured using a broadband oscilloscope with a large memory. This data has been sliced in short sections in which the “instantaneous frequency” was estimated with a two stage algorithm. In the first stage a fast Fourier transform gives a rough estimate, which is used in the second stage to start a least squares fitting routine for a sine wave, see also appendix E.2, the result is shown in figure 4.19. This allows for a much more accurate frequency estimate than one expects to be possible due to Fourier.

The measured data of the several such cards with the AD9956 with 300 MHz VCO (used for the Doppler shift in the 3D-MOT/molasses) shows a slew rate of 300 kHz/ $\mu$ s and settling time of about 40  $\mu$ s, which is fast enough for the 3D-MOT/molasses. The AD9956 with a 100 MHz VCO (for the large common frequency jump of the 3D-MOT/molasses laser) has not been measured, but has a similar performance, which is faster than the 3D-MOT/molasses laser lock can follow.

#### 4.3.4.2. AD9852

The DDS for the Raman system is based on the AD9852 with minimal parts around it (see appendix D.1), all digital components to support the AD9852 are

## 4. Realization of the light fields

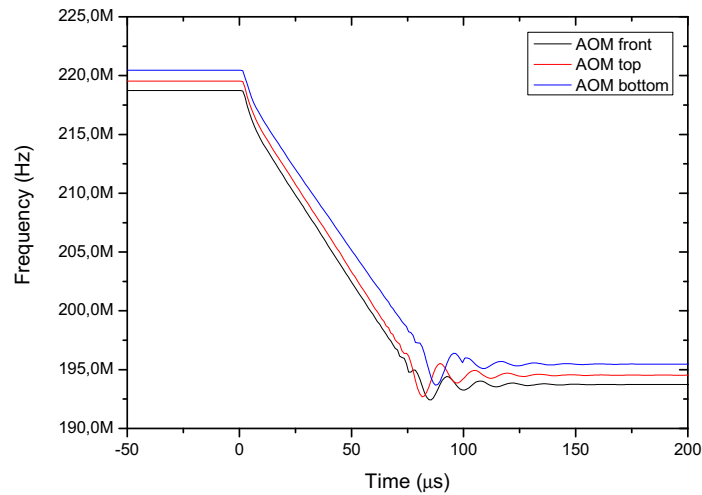


Figure 4.19.: Measured instantaneous frequencies of the DDS during the start phase. Measured using the technique described in the text with a segment length of  $1 \mu\text{s}$ . Shown is the jump from acceleration to molasses in a previous setup that did all frequency changes with AOMs. The current setup uses much smaller frequency jumps.

programmed in the FPGA. There is a 100 MHz low pass filter (MiniCircuits SLP-100) at the output. This chip has only 2 sets of phase/frequency/amplitude settings, (the amplitude is not used for the Raman system). More complicated phase and frequency patterns are created by alternate updating one register while using the other during the experimental sequence. The key parameters are shown in table 4.4. The delay time is 300 ns from the change of the register select signal to a change in the output frequency (given by the internal pipeline delay of the chip). Before that about  $2.5 \mu\text{s}$  are needed to load the new data into the registers. The phase resolution of 0.38 mrad may seem a bit coarse when trying to measure smaller phases, but this resolution is a digital step size limit and not a noise limit. This phase resolution will also not limit the resolution of the interferometer because the DDS only has to enable operation near the middle of a fringe to maximize its sensitivity and need not be exactly on the middle of a fringe. Also jumps of  $90^\circ$  and  $180^\circ$  can be realized without error as these phase jumps correspond to exact binary words.

## 4.4. Experiment Control

### 4.4.1. Computers

The computer system for the experiment consists of two computers connected over the network, the first machine (“messrechner”) runs Windows with Labview 8.0 and



#### 4. Realization of the light fields

Table 4.4.: Summary of the key parameters of the various DDS frequency generators used.

	AD9852	AD9956	AD9956 + POS-300 ( $\times 8$ )	AD9956 + POS-100 ( $\times 3$ )
	Interferometry: phase & frequency	for com- parison only	3D-MOT: Doppler shift	3D-MOT: common freq. shift
$f_{clk}$ (MHz)	300	400	400	400
$f_{out}$ (MHz)	0.08-100	0-150	140-235	42-84
$P_{out}$ (dBm)	-5	-5	+3	+1
$f_{step}$ (Hz)	$1 \cdot 10^{-6}$	$1.4 \cdot 10^{-6}$	$1.1 \cdot 10^{-5}$	$4.3 \cdot 10^{-6}$
$\phi_{step}$ (mrad)	0.38	0.38	3.1	1.2
number of profiles	2	8	8	8
$\tau_{settling}$	300 ns	73 ns	40 $\mu s$	40 $\mu s$

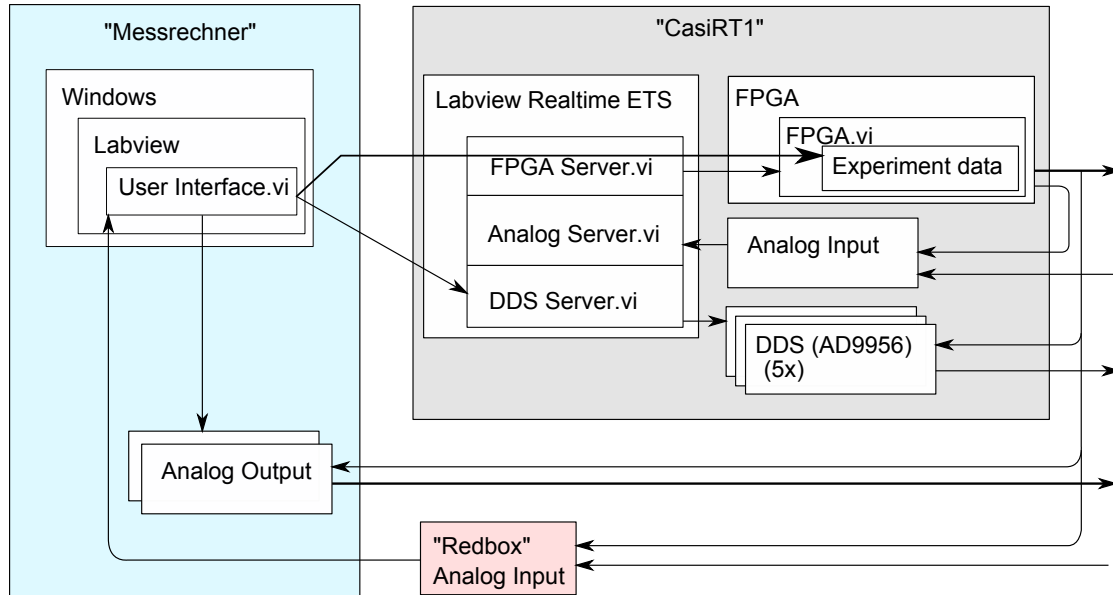


Figure 4.20.: Overview of the computer systems and there components.

#### 4. Realization of the light fields

the second machine uses “NI Labview realtime ETS” as operating system. The “real-time”-feature (meaning: reliable and repeatable timing) is not used, only the remote control capability, as all time critical jobs are executed in dedicated hardware. The first machine contains two analog output cards (NI-PCI6733) with each 8 analog output channels and an USB input device (Meilhaus ME-REDLAB PMD-1608FS) with 8 channels at 50 kHz sample rate. See also figure 4.20.

The second machine has 5 self-build DDS cards (see section 4.3.4.1 and appendix D.2), one FPGA card (NI PCI-7811R) (see section 4.4.3) and one low speed analog input card (NI PCI-6040E) with 16 channels with 12-bit resolution.

The first machine is used to create the desired experimental sequence and send it to the various output devices. It also reads the results from the photodiodes in the state detection via the USB input device. Separate data recorder programs on this machine record the laboratory temperature (via the PCI-6040E) and the vacuum pressure, as measured by the ion getter pump, and are running continuously, collecting long term data about the laboratory environment.

The second machine runs a labview server program which supplies three services: the slow analog inputs, the DDS cards and the FPGA. The analog inputs run at there full speed of 50 kHz and are numerically filtered to reduce the sample rate and increase the resolution. They are used to monitor environmental parameters like the temperature and to read out the seismometer, it also has a channel to synchronize with the rest of the experiment.

The DDS service receives phase and frequency information over the network connection and programs the DDS cards for the 3D-MOT/molasses accordingly.

The FPGA service starts the FPGA card and supplies it with the experimental sequence it receives over the network to generate the necessary digital control signals for switching shutters, AOMs and others as well as program the DDS for the Raman slave laser. The Labview realtime operating system has a similar service to communicate with the FPGA but it turned out to be not reliable enough.

#### 4.4.2. Main program

The labview-program “UserInterface.vi”, running on the main computer, is the place where all experimental sequences are defined. These sequences are described in a matrix like structure, with a column describing the state of every available output at a certain moment in time and the top value indicating the duration of the column, a row describes the temporal sequence of an output channel, see also figure 4.21.

Several items in the matrix can also accept symbolic values, that can be swepted to scan a certain volume of the parameter space, most notably: the duration and the frequency and phase of the Raman system. When scanning over multiple parameters, it will scan over the volume, with one shot for every combination of the swepted parameters. Scanning over unused parameters simple repeats a certain set of parameters.

This program also records and interpretes the photodiode signal and shows the result for a quick view of the experimental data.

#### 4. Realization of the light fields

The code of this front panel takes the data and adds the parameters to the matrix and feeds it to the various output devices. After interpreting the parameters it simplifies the data, combining identical columns, the DDS (MOT) registers get assigned as well as there triggers, and finally the data is split into the various output devices and send to them. This includes generating the code for the FPGA. After that the program (for single shots) waits until the FPGA has finished its program by looking at the program counter of the FPGA before reading the photodiode signal. It then saves the photodiode signal and the current parameters as well as there implementation in the matrix data on the hard disk before preparing the parameters and data for the next shot.

##### 4.4.3. FPGA

The Field Programmable Gate Array (FPGA) [82] is a NI PCI-7811R (National Instruments) computer add-on card in the second computer. The card is based on the Xilinx Virtex 2, containing about 1 million gates (10,000 flipflops and about 60 kilobyte of memory) and has 160 digital input/output pins of which only 50% are used in the current set-up. It is being programmed in Labview with the FPGA extension. The program shown here for the experiment was designed with Labview 8.0 and its software limitation of one 16 kB memory block of 16 bit times 8192 elements, which makes it rather cumbersome to get larger elements at a time. Because of this memory bottleneck and its limited size combined with the relatively large and complex data to process it was decided to use a processor like algorithm. When using a later version of Labview, like 8.20, it may be useful to redesign the program to make use of its better memory features.

The purpose of the FPGA program is to output the requested digital signals at the correct time. It controls 32 digital channels for switching AOMs, shutters and triggers as well as send phase and frequency data to the DDS frequency generators of the Raman-system over a special 40 bit wide port and control an 8 bit digital to analog converter. The 8 bit DAC (see appendix D.11) is used for synchronizing the slow analog input from the NI PCI-6040E with the experimental cycle. The DAC should increment once every experimental cycle.

A very simple pattern generator with uncompressed data would require about 10 byte per 10 ns, or 1 GB/s. Such high data rates are possible in FPGAs, but the memory would then only last a few  $\mu$ s. Previous generations of the experiment used this algorithm though, at a lower speed of 100 kHz so the computer could keep up. But since a normal experimental sequence has only about 50 states, there is a huge gain for data compression possible. The chosen FPGA program enables to store the temporal information in a run-length compressed style and have only output data when things change.

The resulting FPGA program can generate pulses as short as 210 ns with a resolution of 10 ns on all 32 digital outputs. The conversion from a human readable format of the experimental sequence on the main computer to executable binary code for the FPGA.vi has been implemented in the main program.

The following three subsections describe the internal operation of the “FPGA.vi”,

#### 4. Realization of the light fields

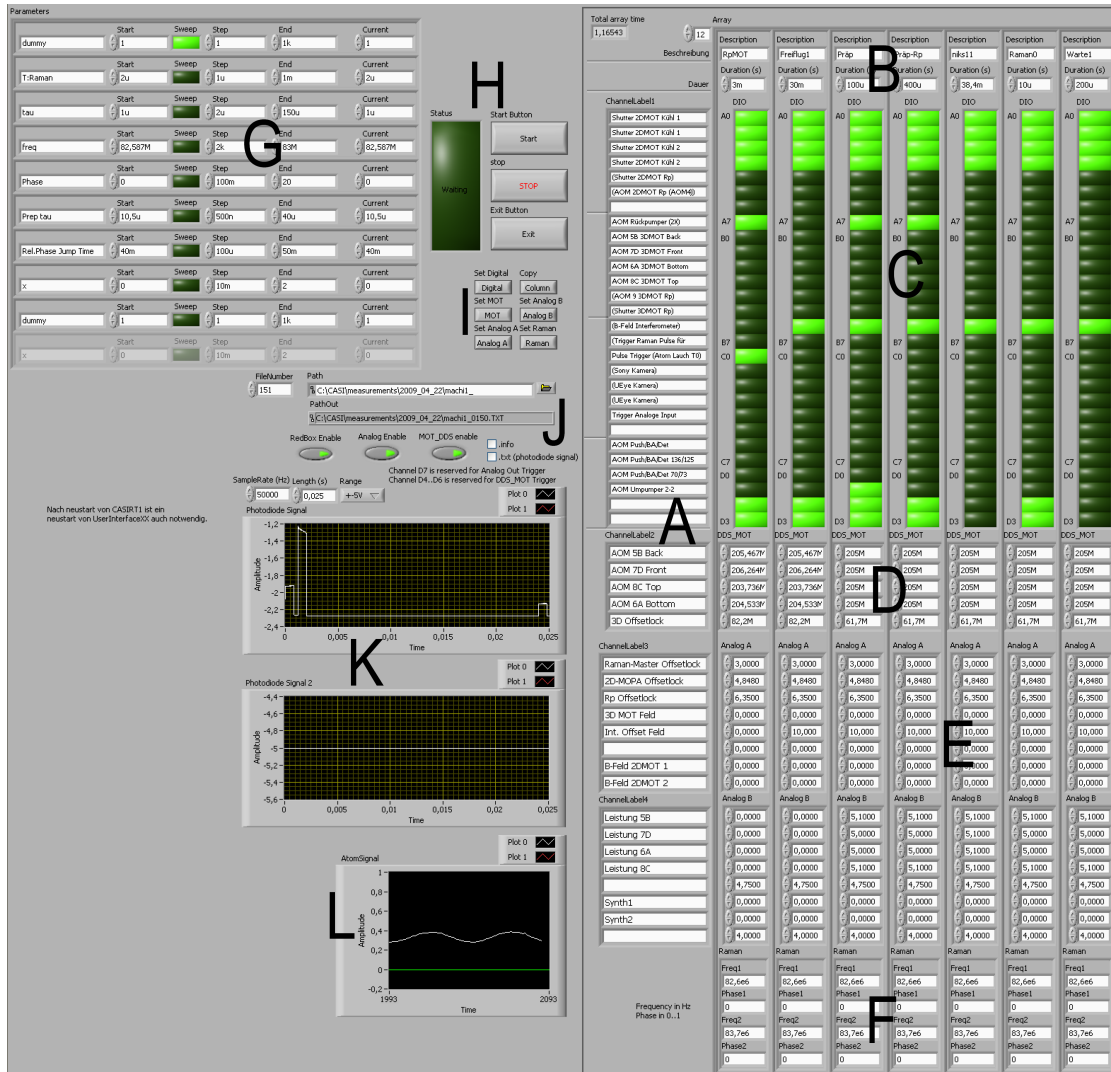


Figure 4.21.: Front panel of the main vi. Right, “matrix”: A: channel labels, B: duration, C: digital out, D: DDS (MOT) frequency, A: analog out, F: DDS (Raman) out. Left: G: parameter sweep settings, H: big start button, I: quick buttons to change whole rows, J: output file settings, K: photodiode signals, L: preliminary interpretation of photodiode signal. The right side has been shortened, the actual width is about three times the page width.

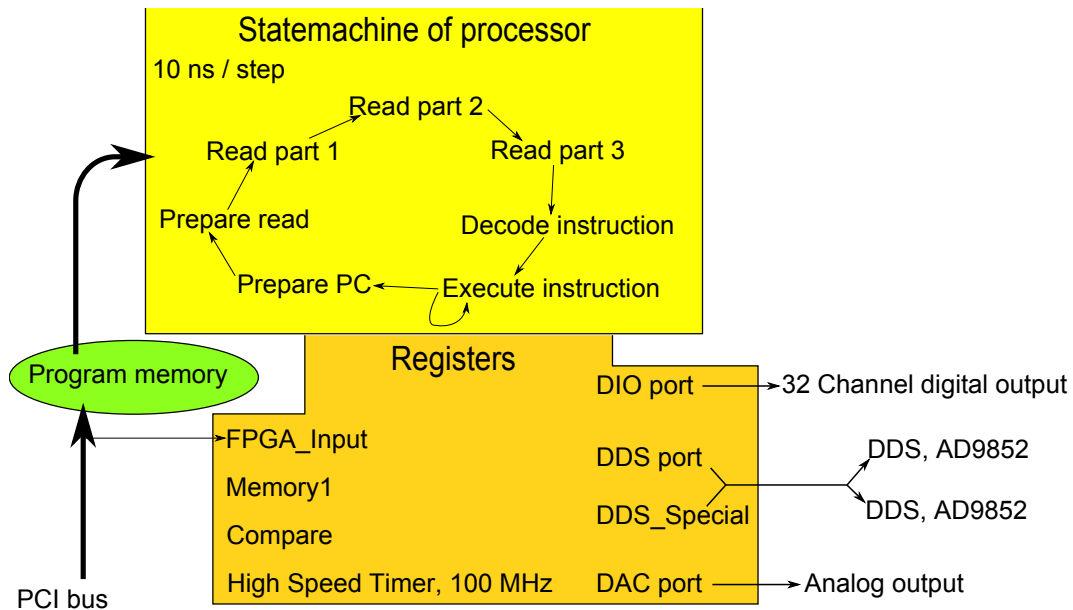


Figure 4.22.: Schematic of FPGA program. The upper part shows the state machine with the seven steps needed to execute an instruction, with each step taking only 10 ns. The lower part shows the 8 registers that are manipulated by the state machine.

its timing behavior and the typical sequence of commands used.

#### 4.4.3.1. Internal operation of “FPGA.vi”

The desire to work with run-length compressed data, as well as having the ability repeat sequences has resulted in a processor-like system, with input-output devices, instruction memory and some registers to store a few results. Each instruction has a fixed length of 6 bytes containing the instruction code, the source and destination registers as well as any constants. There are 5 possible instructions:

- NOP “no operation”, a place holder for debugging,
- Wait causes the program to wait until a specific register (typically the timer “HST”) has reached a certain value,
- SET puts a constant in a specific output register like DDS or DIO,
- ADD adds a constant value to a register, to count a number of cycles or to increase DAC,
- JMP makes a conditional or unconditional jump to some other address to repeat a cycle.

All of these instructions can operate on any of the 8 registers. The most important registers are:

#### 4. Realization of the light fields

DIO	32 digital output channels,
DAC	an 8 bit analog output,
DDS	two 16 bit ports to send data to two AD9852 DDS frequency generators,
HST	a high speed timer running at 100 MHz.

This instruction set has some features that have been added with future requirements in mind. Like the “add” instruction on the “memory1” register (realizing a counter) in combination with a conditional jump which would allow the program to repeat a certain experimental sequence a number of times and then switch to another sequence a number of times and come back to the first one after that. The exact Labview source code with complete tables of instructions and registers can be found in appendix E.3.

##### 4.4.3.2. Timing of “FPGA.vi”

The timing requirements for the “FPGA.vi” are governed by the pulses of the Raman-system which has pulse lengths of about 10  $\mu$ s which need to be accurately controlled on the level of 10 ns. This means execution speeds of 100 MHz (2.5 times faster than NI claims the card can do). To reach this speed some optimizations were necessary which complicated the program a little bit. The program makes extensive use of pipelining and “single cycle timed loops” to obtain these very high speeds.

A single instruction takes 7 cycles to execute (or more in the case of “wait”). The first two cycles are used to prepare the address for the read cycles. The following 3 cycles are needed to read the data. Cycle number 6 is used to decode the instruction. Cycle number 7 is used to read, modify and write data as requested by the instruction, see also figure 4.22.

To avoid problems with the DDS because of the long cables, they communicate at a reduced speed of 10 MHz. A first-in-first-out buffer (FIFO) compensates the difference in data rate between the main loop and the DDS. This way it takes 7 cycles at 100 MHz and 3 cycles at 10 MHz to transfer 1 byte.

Because of this rather complicated instruction execution method, the timer is an independent counter running at the full speed of 100 MHz counting the number of clock-ticks since the last reset or counter overflow (about 42 seconds). This way the “WAIT HST” instruction waits for an “absolute” time without having to worry about how many cycles an instruction or group of instructions exactly uses.

The most complicated experimental state (worst case) is when everything changes, this takes about 11 instructions (2 DIO, 2 IOUpdate, 6 DDS, 1 Wait) which limits the shortest pulse to about 2500 ns. The simplest case takes only 3 instructions or 210 ns. The pulse length resolution in all cases is 10 ns, given by the resolution of the high speed timer. An example of an experimental sequence is shown in figure 4.23. In practice the pulse length is limited by the NI PCI6733 analog output cards which are triggered by the FPGA, they appear to need at least about 10  $\mu$ s

#### 4. Realization of the light fields

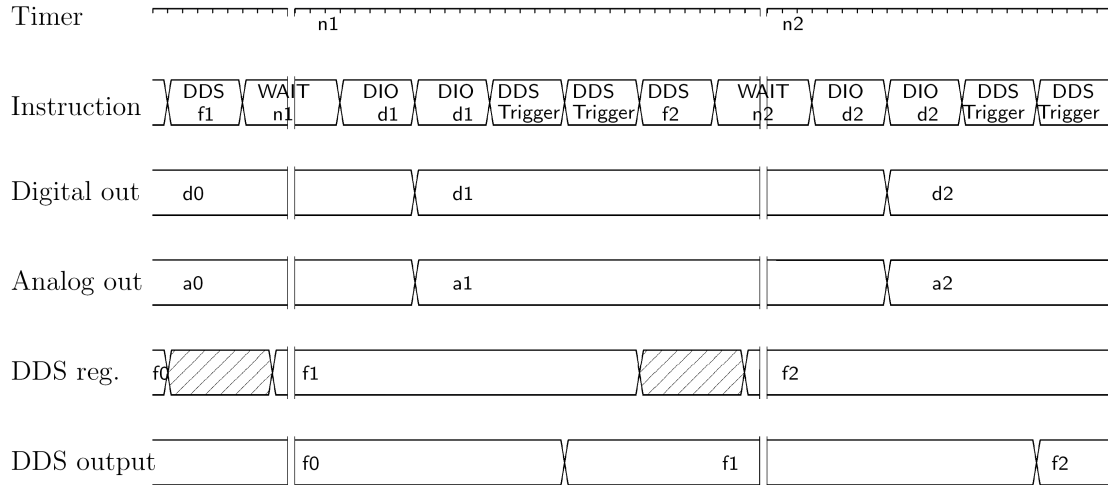


Figure 4.23.: Timing diagram of the FPGA. It shows the output signal for a (simplified) row of instructions (the program). The digital outputs are instantaneous, the analog output is triggered with the digital output. The DDS is programmed in the previous round, which takes some time in which its state is not defined, and switches to the new frequency at the appropriate instruction. The WAIT instructions are shortened in this diagram as they take most of the time in a real sequence. The time axis is not to scale.

between triggers, this can be improved with more efficient use of the hardware in the main program.

#### 4.4.3.3. Application

A typical experimental sequence/program for the FPGA has an initialization section which resets the DDS to a known state, resets the DAC and sets the timer to zero. Then comes the experimental sequence with several blocks of up to 8 “set DDS” commands and a “set DIO” as well as a “wait timer” command and the end of sequence is build by a jump-command to either the start of the sequence to repeat everything or to the jump command itself to wait until a system reset. The DDS registers are set up in the previous experimental state, with the IO update at the start of the actual experimental state to achieve accurate timing of the frequency and phase changes.

## 5. Atomic Measurements

The device described in the previous chapters has led to the measurements on the atom interferometer shown in this chapter. The initial characterization consists of measurements on Rabi oscillations, followed by frequency measurements with the Ramsey sequence. These results are used to realize Mach-Zehnder sequences, but also for a realization of the Gauss-sum factorization algorithm. The last section looks at increasing the repetition rate.

### 5.1. Rabi oscillations

To optimize the beam splitting and mirror pulses of the interferometer, Rabi oscillations are recorded at various positions in each window. Figure 5.1 shows several of such measurements in the central window as an example. These measurements show several deviations from the ideal behavior: there is a decay and the oscillation period depends on the location in the window.

Because the light field has a Gaussian distribution, the effective Rabi frequency becomes a function of the position. This function is not sampled in a single point, but over a certain range because the atomic cloud has a non-zero width. This results in a gradient of the internal state across the cloud, which in itself is not a loss of coherence, but because only the average state of the entire cloud is measured, this does show up as a reduction of the contrast. This internal state gradient increases with increasing pulse length, causing an exponential decay. This plays an even bigger roll for the off-center positions of figure 5.1, as the gradients in the light field are larger. In the center of the window this effect is the smallest, but the cloud is large enough to be influenced by higher order gradients.

In addition, the spontaneous decay due to the Raman light fields also results in an exponential decay of the Rabi oscillation. The spontaneous decay at the typical detunings and intensities is a few 100 Hz, which is a loss of few percent per 100  $\mu$ s.

In the Doppler sensitive case, which is needed to create an inertially sensitive interferometer, the contrast is even more reduced because the light pulse only interacts with a fraction of the cloud of atoms due to the thermal velocity of the atoms which causes a Doppler shift. Because the pulse length determines its Fourier width, longer pulses are more velocity selective resulting in an even stronger decay of the Rabi oscillation.

Figure 5.2 summarizes the resulting length of a  $\pi$ -pulse as well as the attainable efficiency for each of the three windows. The actual value of the Rabi frequency is measured before each interferometry measurement series as it depends on the available laser power, detuning and operating mode used for the interferometry.



## 5. Atomic Measurements

The obvious variation of the pulse length and efficiency also has consequences for any interferometer sequence that uses them and one has to compensate for that in order to obtain a good interferometer signal (see also section 5.5 and figure 5.15).

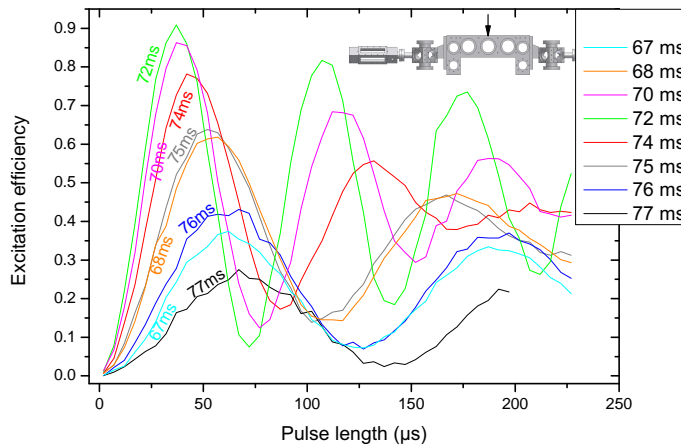


Figure 5.1.: Doppler insensitive Rabi oscillations for several positions in the central window. The position is indicated as time since the end of the acceleration phase in the 3D-MOT/molasses, see also figure 5.2.

## 5. Atomic Measurements

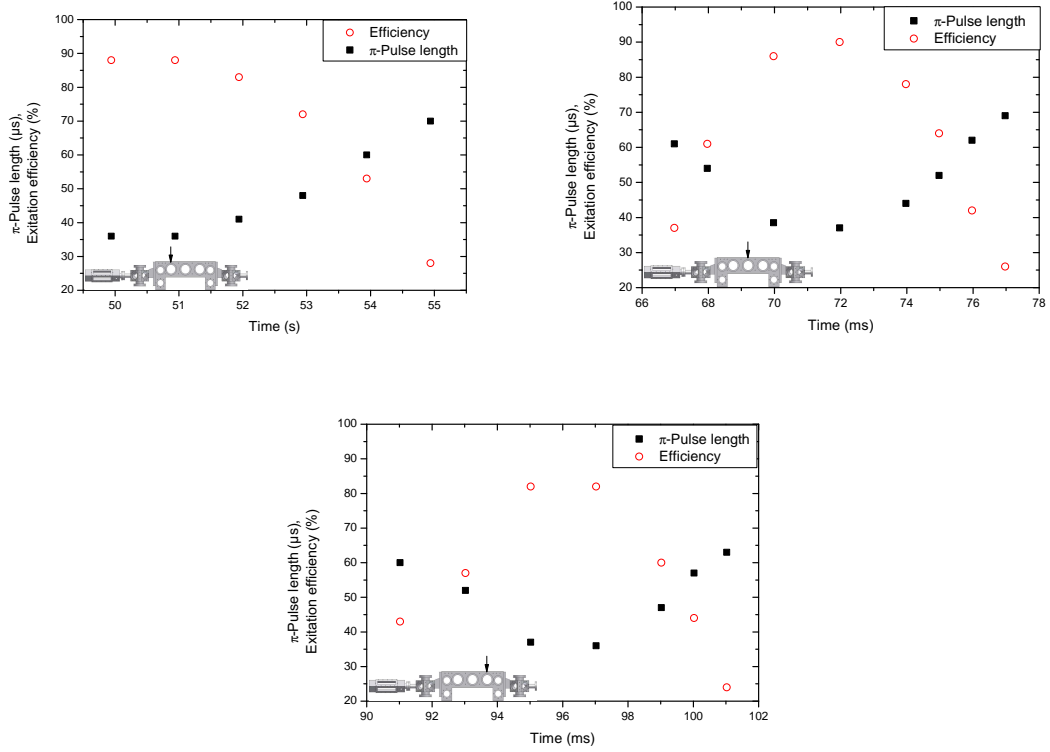


Figure 5.2.: Efficiency of the Rabi oscillation and length of the resulting  $\pi$ -pulse in the Doppler insensitive configuration. The starting point of the time axis corresponds to the end of the acceleration phase in the 3D MOT, before the moving molasses. The available time for interferometry in the first window is less than in the other two windows because part of the state preparation has to be realized in this window as well. The last window should also have a state preparation, but for this measurement there was none.

## 5.2. Frequency measurements

A single interferometer pulse of about  $\pi$ -length can be used to measure a spectrum with a rather coarse resolution that is Fourier limited by the length of the pulse. Figure 5.3 shows such a spectrum in the presence of a magnetic bias field to separate the Zeeman substates, showing all three  $\Delta m_f = 0$  transitions as groups of three peaks (one for the parasitic Doppler insensitive and one for each of the two Doppler sensitive transitions ( $+k_{eff}$ ,  $-k_{eff}$ )) for a slightly tilted mirror. The final interferometer will use only one of the Doppler sensitive sidebands. The Doppler sensitive and insensitive in the graph occur together, even though the polarization was aligned for Doppler sensitive-only, because of some parasitic polarization effect due to too good retroflected alignment.

A more precise spectrum can be obtained by using a Ramsey sequence with two  $\pi/2$ -pulses with pulse length  $\tau$  and a drift time  $T$  in between as is common in microwave atomic clocks [29]. The resulting interference signal is given by:

$$P_{Ramsey}(|e\rangle) = \frac{1}{2} \text{sinc}^2\left((\omega_{atom} - \omega_{laser})\frac{\tau}{2}\right) (1 + \cos((\omega_{atom} - \omega_{laser})T)). \quad (5.1)$$

The Ramsey sequence only works with the Doppler insensitive transitions, as it is not a spatially closed interferometer. For the Doppler sensitive transitions only single-pulse frequency measurements are used. Figure 5.4 shows a complete fringe pattern of the  $m_f = 0$  transition. The fringe width is given by  $1/T$ , the fringe envelope width is determined by the Fourier width of the individual  $\pi/2$ -pulses. The longest Ramsey fringes possible with the apparatus are shown in figure 5.5 with a drift time of 46 ms, resulting in fringes of only 21.7 Hz wide.

For long drift times the fringes become very narrow and it becomes difficult to identify the central fringe. This can be solved by varying the drift time a little bit. The central fringe (maximum) stays, where as the other fringes move, as shown in figure 5.6.

With these techniques it has been possible to measure several frequency dependent effects, which have been described in more detail in [48]. Most of these measurements were done with a drift time of 1 ms. The AC-Stark shift, which is controlled by the power balance of the two interferometry lasers, has been estimated to 150 Hz. The second-order Zeeman shift of the  $m_f = 0$  transition for the interferometry is estimated to be 1.4 Hz due to the magnetic bias field. Also the residual magnetic field has been estimated to be 10 mG, which indicates a magnetic field reduction of a factor 50 due to the mu-metal shield.

## 5. Atomic Measurements

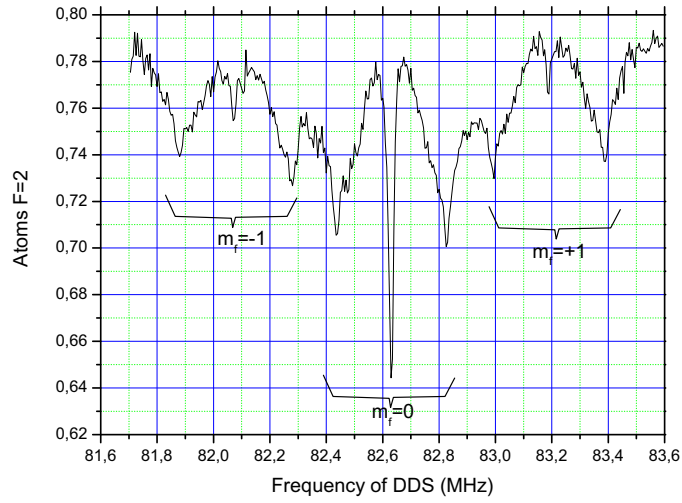


Figure 5.3.: Coarse spectrum using only one Raman pulse without polarization filtering and only a (slightly tilted) mirror for retroreflex, showing the three  $\Delta m_f = 0$  transitions each with one sharp Doppler insensitive peak and two broad Doppler sensitive sidebands, for the  $+k_{eff}$  and the  $-k_{eff}$  transition. The pulse length is  $100 \mu\text{s}$ . The signal is inverted because of a different state preparation which only consisted of repumper and Zeeman selection light which results in the majority of atoms to start in the  $|F = 2, m_f = 0\rangle$  state.

## 5. Atomic Measurements

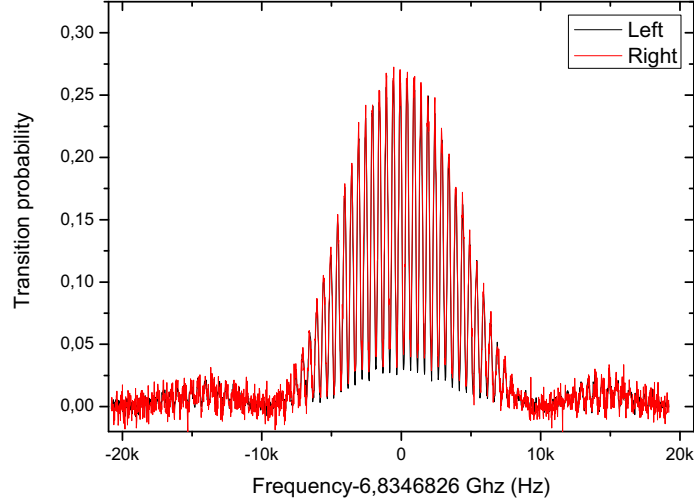


Figure 5.4.: Ramsey spectrum of the  $m_f = 0$  transition using the Doppler insensitive configuration. The fringe width is determined by the drift time  $T = 2$  ms, and the envelope is determined by the pulse length  $\tau = 100$   $\mu$ s. The graph has two curves because of the two counter-propagating atomic sources.

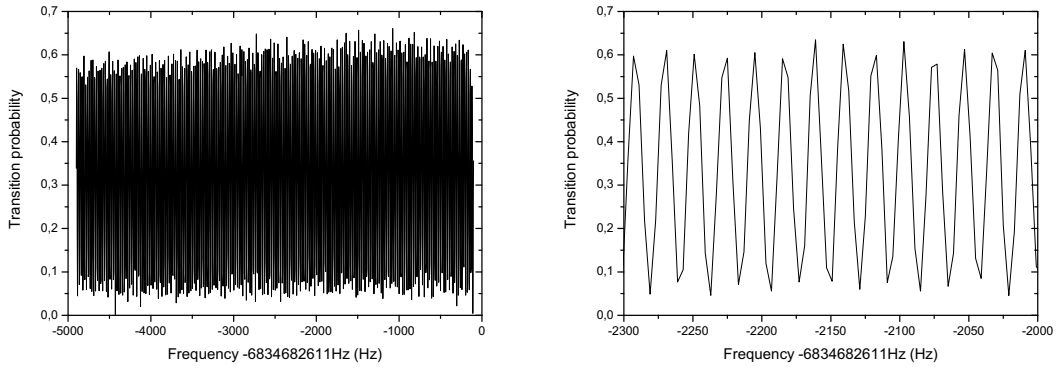


Figure 5.5.: Velocity insensitive Ramsey fringes with  $T = 46$  ms (21.7 Hz fringe width) of the  $m_f = 0$  transition. The  $\pi/2$ -pulses are 19  $\mu$ s long, resulting in an envelope width of about 53 kHz of which only a small section is shown (5 kHz on the left and 300 Hz on the right). Both have been sampled with 4 Hz. The frequency axis shows the frequency difference between the two interferometry lasers relative to the datasheet value of the rubidium hyperfine ground state splitting, without any corrections.

## 5. Atomic Measurements

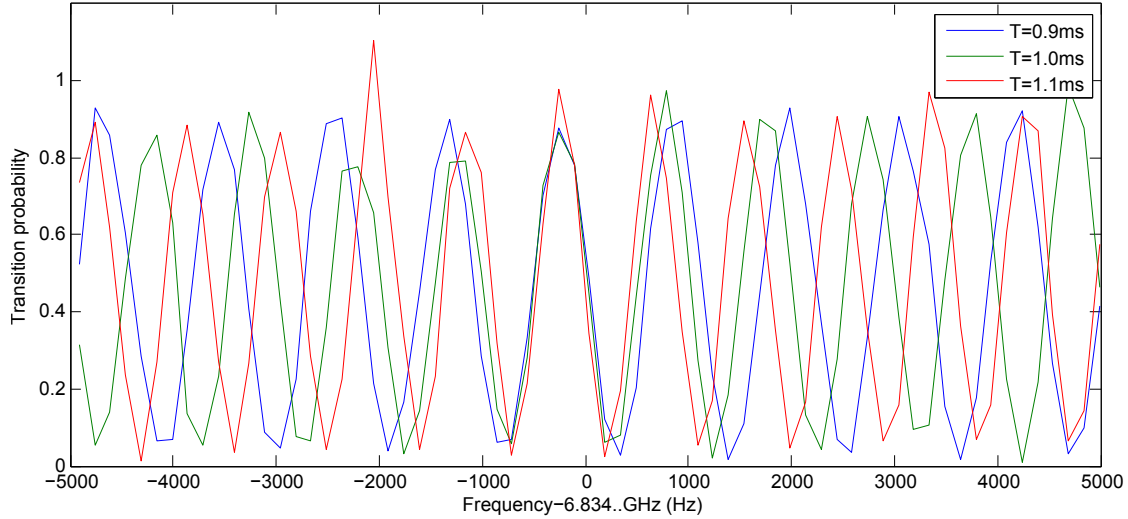


Figure 5.6.: Several high resolution Ramsey fringes of the  $m_f = 0$  transition with slightly different drift times to distinguish the central fringe which is 250 Hz below the datasheet value (without correcting for any shifts) using the Doppler insensitive configuration. The length of the  $\pi/2$ -pulses was 20  $\mu\text{s}$ .

### 5.3. Phase jump settling time

In the Ramsey interferometer the phase change is generated by a difference between the internal “clock” of the atoms and the frequency difference of the Raman laser system without any special manipulations. In the Mach-Zehnder and Gauss sum sequences (section 5.5) however the phase of the Raman light needs to make specific jumps.

To measure the settling time of the optical phase lock of the Raman laser system a sequence of two  $\pi/2$ -pulses was used, with a phase shift of  $180^\circ$  for the second pulse and a varying delay between the two pulses. If the phase of the second pulse is still  $0^\circ$  (the phase lock is still in the starting position) then all atoms end up in the upper state; when the phase is  $180^\circ$  (the phase lock has completed the jump) then the atoms end up in the lower state. The results shown in figure 5.7, show a settling time of 3.9  $\mu\text{s}$  ( $1/e$ -value). This settling time is much shorter than even a single  $\pi/2$ -pulse (25  $\mu\text{s}$ ), which explains why even zero setup time does not result in all atoms in the excited state; the phase change is washed out by the “long” pulses. The high feedback bandwidth of the Raman slave laser should however provide settling times on the order of 100 ns.

This sequence is also a Ramsey interferometer which is sensitive to frequencies. Interpreting figure 5.7 as  $1/4$  of a sine wave, even when it does not look like a piece of a sine wave, would give a frequency error of 13 kHz. The typical frequency errors however are less than 1 kHz and are only visible on a much longer time scale.

One should note that this measurement was done with the old setup[48] which

## 5. Atomic Measurements

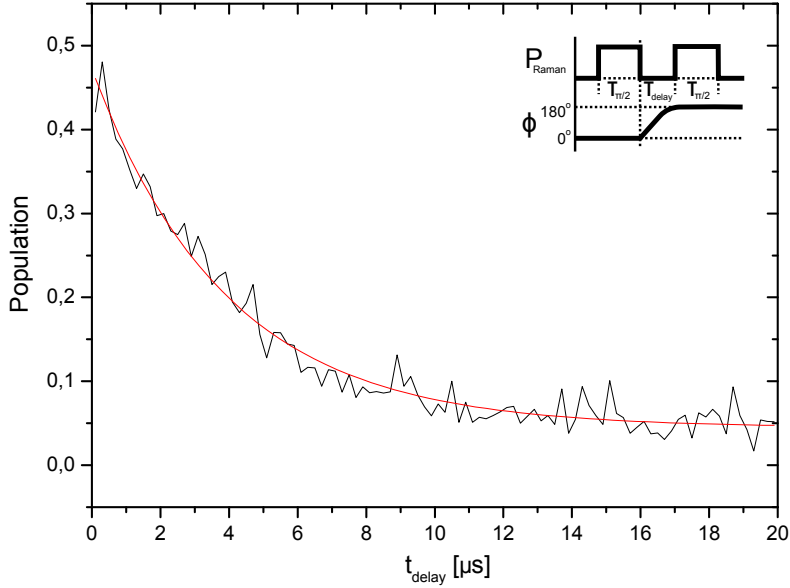


Figure 5.7.: Settling time of the phase locked loop. A simple simple exponential decay was fitted on this data (red line), giving a time constant of  $3.9 \mu\text{s}$ , which is much shorter than the  $\tau_{\pi/2}$ -pulse length of  $25 \mu\text{s}$ . The inset shows a sketch of the power and phase of the pulse sequence.

used a commercial synthesizer<sup>1</sup> with an analog phase modulation controlled by a digital to analog card<sup>2</sup>. They need about  $3 \mu\text{s}$  to make a phase jump, which make it the limiting element in this measurement and not the optical phase locked loop. The current DDS-based setup delivers faster phase jumps as reference signal for the OPLL and is also more accurate. In practical use the phase jump is completed in a time more than one order of magnitude less than the shortest time used by any interferometer sequence (Mach-Zehnder or Gauss sum).

## 5.4. Mach-Zehnder interferometry

### 5.4.1. Inertially insensitive

In order to characterize the signal from the Mach-Zehnder sequence and to be able to extract the phase from the signal, the offset and amplitude of the signal has to be measured, see also section 2.3. This can be done by sweeping the phase of the light field of the last pulse. The resulting oscillating signal of such a measurement is shown in figure 5.8. It shows a contrast of 88%, a signal to noise ratio of 32 and a phase noise of 32 mrad for an inertially insensitive sequence with a length of  $2T = 46 \text{ ms}$ , and a pulse length of  $\tau_{\pi/2} = 19 \mu\text{s}$  with  $10^7$  atoms. For these long interferometer times, all three light pulses are applied in three different windows.

<sup>1</sup>Fluke 6080A/AN, its modulation rate is specified as 100 kHz, which implies a settling time of about  $3 \mu\text{s}$ .

<sup>2</sup>NI PCI-6733, settling time  $2.8 \mu\text{s}$  to 1 LSB.

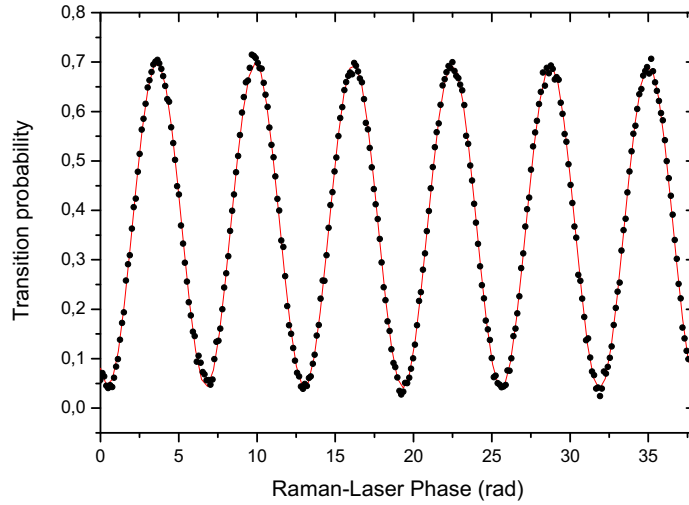


Figure 5.8.: Interference fringes for the Mach-Zehnder sequence (Doppler insensitive) when sweeping the laser phase of the last pulse, with  $2T = 46$  ms,  $\tau_{\pi/2} = 19$   $\mu$ s. Each of the three light pulses was applied in a different window. This measurement has a signal to noise ratio of 32.

These are the longest drift times the current setup can achieve without redesigning the vacuum chamber for steeper trajectories.

The phase noise is about two orders of magnitude above the expected shot noise level. The most dominant noise source is the electronic noise of the photodiode and its digitization, as already shown in section 3.7. The actual photodiode signals are even smaller than table 3.3 assumes. The phase noise of the Raman laser is estimated to be about 3.2 mrad, which is also above the shot noise level, but this is currently not limiting the interferometer, it will however be far more difficult to improve than the electronic noise.

#### 5.4.2. Inertially sensitive

The interference fringes for the inertially sensitive Mach-Zehnder type interferometer are measured in the same way as in the previous section by sweeping the phase of the light field of the last pulse. The measurements in this section were made with a simple retroreflex from the big mirror with a small angle, without polarization filtering, using the Doppler shift to separate the  $+\vec{k}_{eff}$  from the  $-\vec{k}_{eff}$ -transition. The resulting signal, shown in figure 5.9, shows a contrast of 30 % and a phase noise of 0.13 rad for a drift time of 4.5 ms.

The contrast is less because the velocity selective Raman transition can only excite a fraction of the atomic cloud, even when the state preparation has preselected this velocity group. This reduction in contrast also reduces the available signal to noise ratio and the resulting phase resolution.



## 5. Atomic Measurements

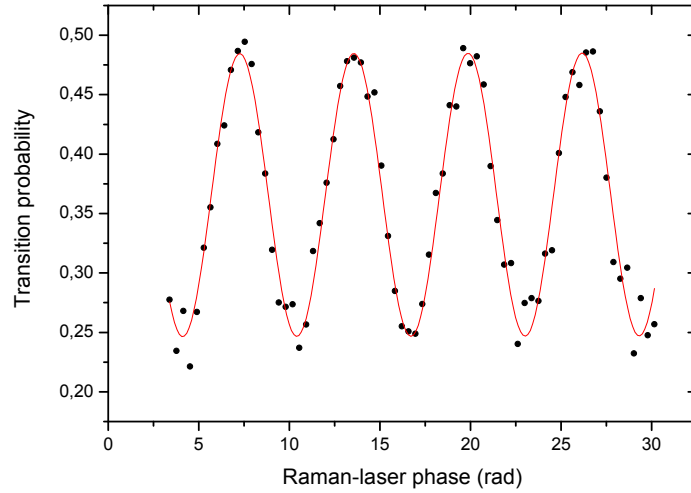


Figure 5.9.: Graph of the interference signals for the inertially sensitive Mach-Zehnder sequence in the central window with  $T = 4.5$  ms. This graph shows a phase noise of 0.13 rad (single shot) and a signal contrast of 30%. The red line is a sine fitted on the data.

When checking for phase offsets and similar systematic errors, it is useful to change the direction of the wave vector. This changes the sign of both the rotational and accelerational phase, but not that of some static phase offset like laser phase or mirror offset. This is a different kind of sign change as that of section 2.2 where the direction of the atoms is flipped to distinguish rotation from acceleration, here it separates inertial from non-inertial. The sum and difference signals of such an experiment are:

$$\begin{aligned}\phi_+ &= (\phi_i + \epsilon) + (-\phi_i + \epsilon) = 2\epsilon \\ \phi_- &= (\phi_i + \epsilon) - (-\phi_i + \epsilon) = 2\phi_i\end{aligned}\tag{5.2}$$

with the inertial phase  $\phi_i = \phi_{rot} + \phi_{acc}$  and  $\epsilon$  is a phase offset. The flipping of the effective wave vector for the measurement of figure 5.10 has been realized by switching the laser frequency to the other Doppler sideband of figure 5.3.

The quadratic dependence of the inertial phase shift in the measurements can be interpreted as the projection of gravity on the direction of the laser beams (see also equation 2.63) with an angle of 1.1 mrad or by a rotation rate of the earth of 45 cycles per day. At the time of the measurement these two causes could not be distinguished due to a defect in the second atomic source, but it should be obvious that a deviation of 1.1 mrad from the horizontal is the most plausible cause.

The fringes at  $T > 4.5$  ms are close to the limit of the optical window and laser beam, which results in significant increase in losses and phase noise. The largest achieved enclosed area is  $0.82 \text{ mm}^2$  at  $T = 5$  ms. The highest resolution however

## 5. Atomic Measurements

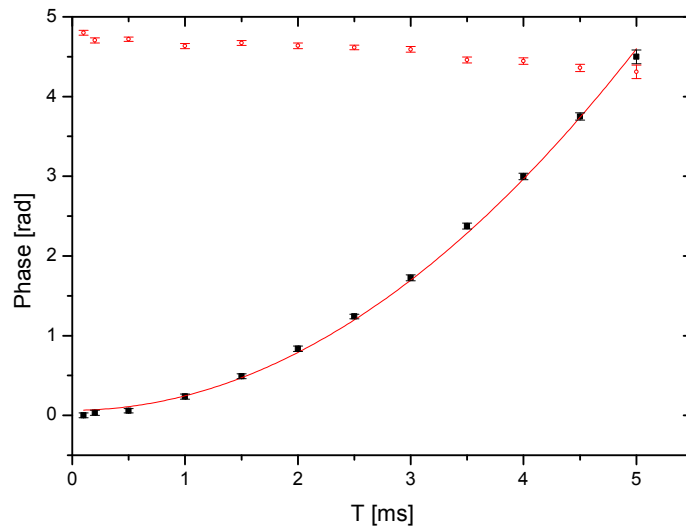


Figure 5.10.: Phase as a function of drift time. Upper line: half of the sum of signal and its flipped version, giving the offset signal. Lower line: half of the difference of signal and its flipped version, giving the inertial contribution. Each data point is a combination of two measurements like that of figure 5.9. This graph also shows that the differential phase contribution scales quadratically with the drift time  $T$  as expected for the inertial contribution. The fitted model for the inertial data points is  $\phi_- = a + bT^2$ , with  $a = 0.064$  and  $b = 1.81 \cdot 10^5 \text{ s}^{-2}$ . A multiple of  $2\pi$  has been added to some of the data points, where appropriate.

## 5. Atomic Measurements

has been obtained for  $T = 4.5$  ms (area is  $0.665$  mm<sup>2</sup>) because of its better phase noise, the single shot phase noise is  $0.13$  rad which results in a rotation resolution of  $7.0 \cdot 10^{-5}$  rad/s, and an acceleration resolution of  $3.9 \cdot 10^{-4}$  m/s<sup>2</sup>. This is about 2 orders of magnitude better than [48] and is nearly enough to see the earth rotation with only a single measurement. A typical fringe measurement like that of figure 5.9 is a sine wave, which is used to extract far more than just the phase noise, but since it is fitted on about 70 points, it should already be able to see a fraction of the earth rotation (if one could distinguish it from an acceleration contribution).

To estimate the resolution at  $T = 23$  ms, which has an area of  $17.4$  mm<sup>2</sup> and is the maximum time possible in the current setup, the phase noise for that drift time has to be estimated. A lower bound is given by the inertially insensitive signals with  $31$  mrad. The inertially sensitive data at  $T = 4$  ms already has  $0.11$  rad phase noise, and a linear extrapolation results in  $0.29$  rad of phase noise for a single measurement. The lowest noise estimate would result in a resolution of  $7 \cdot 10^{-7}$  rad/s, the highest would be  $6 \cdot 10^{-6}$  rad/s.

With the current setup, the inertially sensitive Mach-Zehnder interferometer has been shown for sequences where all three pulses were applied in the same window. The results shown were made in the central window, but also the other two windows show similar results (with some restrictions in available space). Also inertially insensitive interferometer signals across three windows have been shown. The full-size three window inertially sensitive Mach-Zehnder however is still subject of current investigations.

### 5.5. Gauss sum factorization

To show the flexibility the apparatus has, a Gauss sum factorization algorithm has also been implemented [83]. This algorithm uses far more complicated sequences of light pulses than normally used for the measurement of inertial forces. Factorization is a subject related to cryptography, which relies on the fact that the time required for finding the prime factors of a large integer scales exponentially with the number of digits and the algorithm shown here is no exception to that.

The Gauss sum factorization algorithm uses a series of  $\pi$ -pulses with specific phase shifts. To obtain the correct starting point and to measure the result, it also needs a  $\pi/2$ -pulse with  $90^\circ$  phase shift before and after the  $\pi$ -pulse sequence. Because the spatial path of the Gauss sum algorithm, just like that of the Ramsey interferometer, is not inherently closed, it can therefore only function with the Doppler-insensitive Raman transition. This also avoids any additional inertial phase shifts.

The first  $\pi/2$ -pulse with  $90^\circ$  phase shift puts the starting point of the atomic state on the equator of the Bloch model with  $0^\circ$  phase (which means that Raman pulses with  $0^\circ$  phase shift have no effect). The main part of the algorithm takes place in the equatorial plane of the Bloch sphere model. Here a  $\pi$ -pulse is effectively mirroring the atomic state around an axis with the phase shift of the  $\pi$ -pulse. The phase  $\phi_{int,k}$  of the interferometer after  $k$   $\pi$ -pulses is then given by:

## 5. Atomic Measurements

$$\phi_{int,k} = \phi_k - 2\phi_{int,k-1}, \quad (5.3)$$

with  $\phi_k$  as the phase of the  $k$ th  $\pi$ -pulse. This recursive equation results in the series:

$$\begin{aligned} \phi_{int,0} &= 0 \\ \phi_{int,1} &= 2\phi_1 \\ \phi_{int,2} &= 2\phi_2 - 2\phi_1 \\ \phi_{int,3} &= 2\phi_3 - 2\phi_2 + 2\phi_1, \\ &\vdots \end{aligned} \quad (5.4)$$

from which the generic expression for the interferometer phase can be derived:

$$\phi_{int,k} = 2 \sum_{x=1}^k (-1)^{k-x} \phi_x. \quad (5.5)$$

For the factorization with the Gauss algorithm a specific phase has to be applied to the  $\pi$ -pulses:

$$\phi_k(\mathfrak{l}) = \begin{cases} 0 & \text{for } k = 0 \\ (-1)^k \pi \frac{\mathfrak{N}}{\mathfrak{l}} (2k-1) & \text{for } k > 0. \end{cases} \quad (5.6)$$

Here  $\mathfrak{N}$  is the number to be factorized and  $\mathfrak{l}$  is a possible factor that is to be tested. The resulting phase of the interferometer then becomes:

$$\phi_{int,k} = \begin{cases} 0 & \text{for } k = 0 \\ 2\pi \frac{\mathfrak{N}}{\mathfrak{l}} (-1)^k \sum_{x=1}^k (2x-1) & \text{for } k > 0 \end{cases} \quad (5.7)$$

Which can be further simplified by making use of the Gauss rule ( $\sum_{k=1}^m k = \frac{1}{2}m(m+1)$ ) which gave this algorithm its name. The resulting phase of the interferometer after  $k$   $\pi$ -pulses with the phase of equation 5.6 is:

$$\phi_{int,k} = 2\pi \frac{\mathfrak{N}}{\mathfrak{l}} (-1)^k k^2 \quad (5.8)$$

Finally, the detected signal after  $\mathfrak{m}$  pulses (and the obligatory  $\pi/2$ -pulses) is then:

$$c_{\mathfrak{m}}(\mathfrak{l}) = \cos\left(2\pi \mathfrak{m}^2 \frac{\mathfrak{N}}{\mathfrak{l}}\right) \quad (5.9)$$

When  $\mathfrak{l}$  is not a factor of  $\mathfrak{N}$  ( $\frac{\mathfrak{N}}{\mathfrak{l}} \notin \mathbb{N}$ ),  $c_{\mathfrak{m}}(\mathfrak{l})$  becomes a chaotic function because the cosine oscillates increasingly fast with increasing  $\mathfrak{m}$ . Note that the path of the atomic state is only chaotic (predictable with enough calculational power and accuracy) and not random (not predictable irrespective of calculational power and accuracy). When  $\mathfrak{l}$  is a factor of  $\mathfrak{N}$  ( $\frac{\mathfrak{N}}{\mathfrak{l}} \in \mathbb{N}$ ) is a factor however, the cosine is

## 5. Atomic Measurements

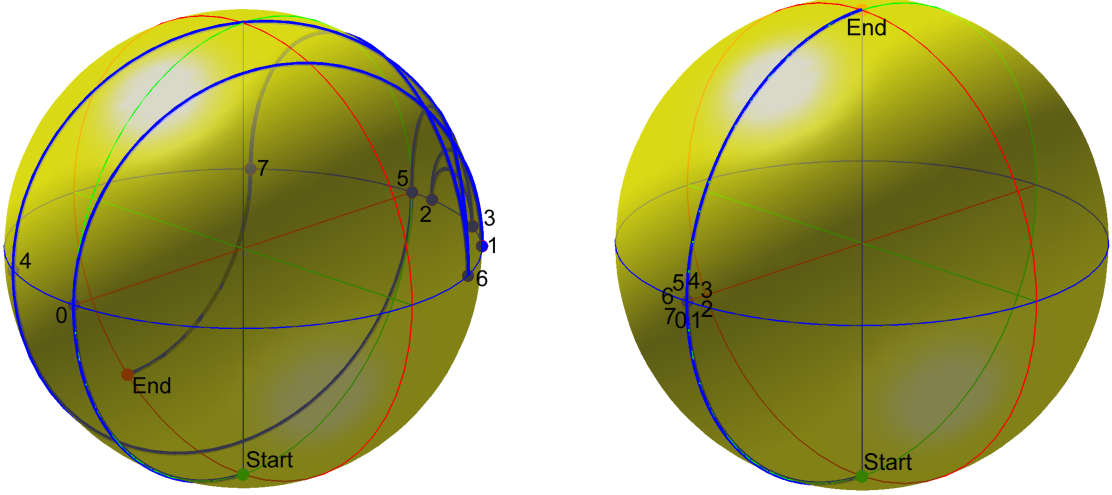


Figure 5.11.: Schematic of the idea of the Gauss sum algorithm for factorization on the Bloch sphere. After a sufficient number of pulses the path becomes chaotic for a non-factor (left), whereas for a factor it stays in one place (right). Calculated here for  $\mathfrak{N}=263193$ ,  $l=150$  (left) or 151 (right),  $M=7$  ( $8 \pi$ -pulses). The numbers in the graph indicate the end point after the  $m$ th pulse.

always sampled in a maximum. Figure 5.11 shows the path of the atomic state on the Bloch sphere for a factor and for a non-factor. Despite the different behavior, a single value of  $c_m(l)$  does not yet reliably distinguish factors from non-factors, because also a non-factor can produce, by chance, a value similar to a factor, as a typical sequence of  $c_m$  shows in figure 5.12.

Averaging over  $c_m(l)$  for the values  $m = 0$  to  $M$  (taking a total of  $M + 1$  interferometer sequences) gives:

$$\mathcal{C}_{\mathfrak{N}}^{(M)}(l) = \frac{1}{M+1} \sum_{m=0}^M \cos\left(2\pi m^2 \frac{\mathfrak{N}}{l}\right). \quad (5.10)$$

This function has the ability to distinguish between factors and non-factors: the value of  $\mathcal{C}_{\mathfrak{N}}^{(\infty)}$  is 1 when  $l$  is a factor of  $\mathfrak{N}$ , and 0 when  $l$  is not a factor of  $N$ . For finite  $M$  this becomes more of a statistical thing, the factors are still 1, but the non-factors are now “near” zero. The contrast between factors and non-factors is defined by [84]:

$$\mathcal{V} = \frac{\mathcal{C}_{\mathfrak{N}}^{(M)}(factor) - \mathcal{C}_{\mathfrak{N}}^{(M)}(non - factor)}{\mathcal{C}_{\mathfrak{N}}^{(M)}(factor) + \mathcal{C}_{\mathfrak{N}}^{(M)}(non - factor)} \quad (5.11)$$

Figure 5.13 shows a measurement of  $\mathcal{V}$  for different number of sequences. To get a significant distinction between factors and non-factors,  $M$  needs to be large enough, but not too large to avoid excessive amounts of work. Ref. [85] considers  $M > \sqrt[4]{\mathfrak{N}}$  optimal in respect of the problem of ghost factors (values of  $l$  that look like a factor but are not a factor). Many test values however can be identified as

## 5. Atomic Measurements

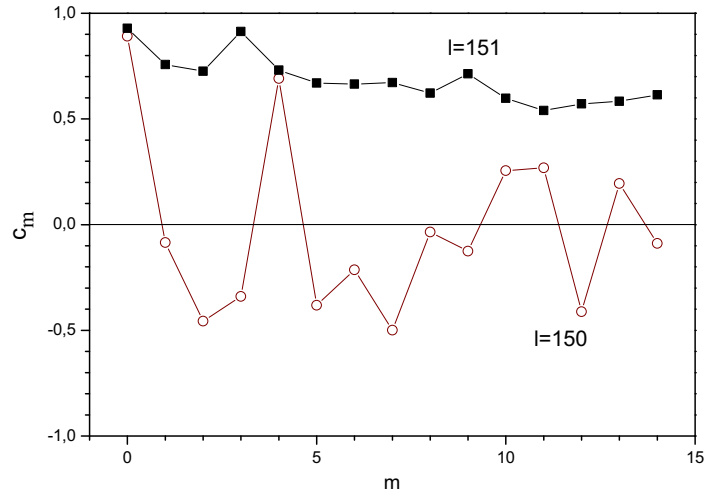


Figure 5.12.: The summation terms  $c_m(l)$  for  $m$  up to 14 (up to  $m+1=15$   $\pi$ -pulses), for a factor and for a non-factor for  $\mathfrak{N} = 263193 = 3 \times 7 \times 83 \times 151$ . The factor  $l = 151$  stays high, where as the non-factor  $l = 150$  averages out to zero.

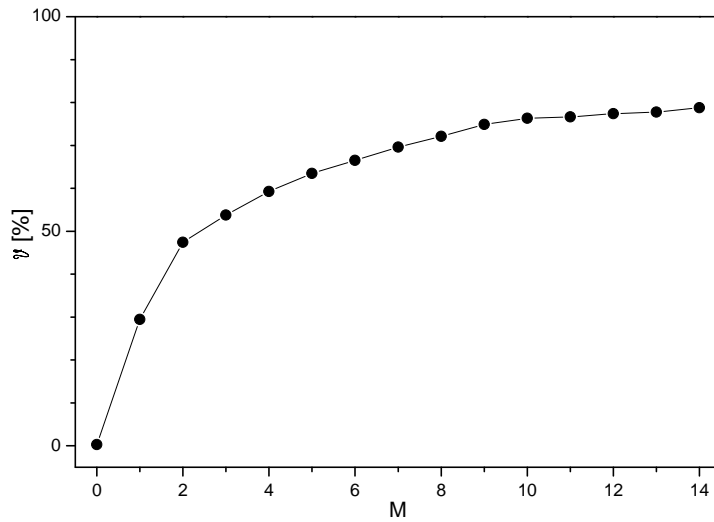


Figure 5.13.: Measured contrast for the factorization of  $N = 263193$  for up to 15  $\pi$ -pulses ( $M = 14$ ).

## 5. Atomic Measurements

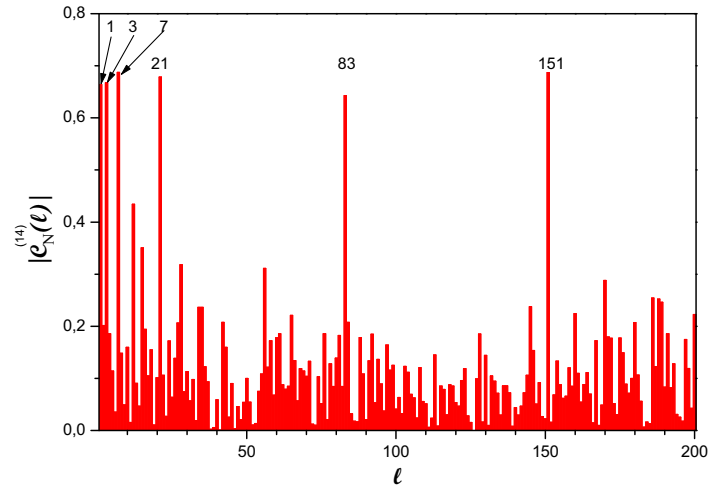


Figure 5.14.: Gauss sum factorization of the number  $\mathfrak{N} = 263193 = 3 \times 7 \times 83 \times 151$  for up to  $M + 1 = 15$  number of pulses. Note:  $21 = 3 \times 7$  is also a factor. Shown here is the absolute value of  $C_{\mathfrak{N}}^{(14)}$  for the test factors  $l$  up to 200. The dominant peaks correspond to the factors, where as the background are the non-factors.

non-factors for much smaller  $M$  as can be seen in figure 5.14 which was recorded with  $M = 15$  where according to the criterion it should have been measured with at least  $M = 23$ . Another application of this is to cut the summation of equation 5.10 short when a small value of  $c_m(l)$  appears, which is a clear sign of a non-factor. It can also help to sum over a different set of  $\mathbf{m}$  instead of just 0 to  $M$  [86].

In practice the maximum number of pulses is limited by the available signal contrast (accuracy of the pulses) and by the time and space available to apply the pulses, since the atoms are moving. The measurements in this section were made with a velocity of 4.4 m/s in a single Raman beam with an effective diameter of 30 mm and 100  $\mu\text{s}$  between the pulses, resulting in a maximum of about 20 pulses. The current setup uses a lower velocity of 2.79 m/s and has the ability to use three windows to apply pulses allowing therefore up to 100 pulses.

To find every factor one needs to evaluate  $C_{\mathfrak{N}}^{(M)}(l)$  for every  $l$  between 1 and  $\sqrt{\mathfrak{N}}$ , figure 5.14 shows the resulting spectrum for the example number  $\mathfrak{N} = 263193 = 3 \times 7 \times 83 \times 151$ . Note that also  $21 = 3 \times 7$  is a factor in this example, the algorithm only identifies factors, but it does not say if a factor is a prime-factor or not.

Due to its many pulses the Gauss sum sequence is more sensitive than the Mach-Zehnder sequence to imperfections in the pulses. One of those errors is the Gaussian intensity distribution of the light fields which results in a varying Rabi frequency across the atomic trajectory, which results in a varying length of the light pulses. To correct for this a simple quadratic dependence was assumed, and due to technical limitations of the setup at the time of the measurement, the ideal pulse lengths were mapped onto three different pulse length values. Despite this

## 5. Atomic Measurements

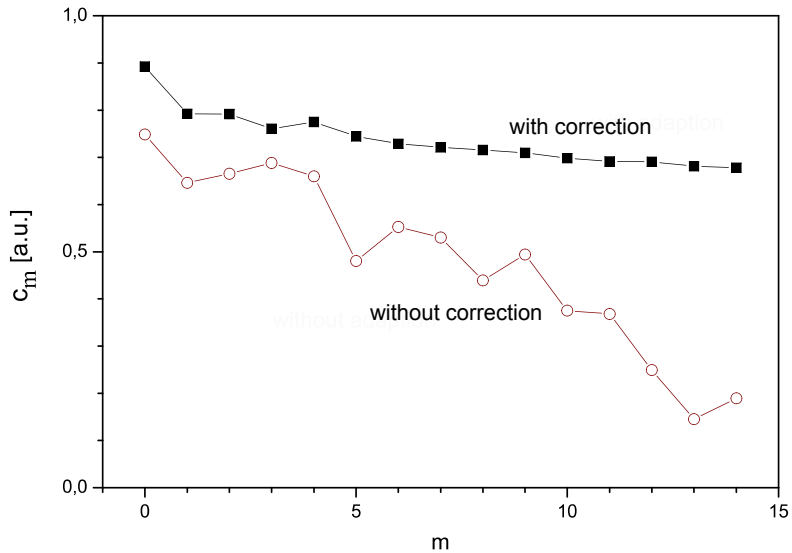


Figure 5.15.: The summation terms  $c_m(l)$  as a function of  $m$  for the factor  $l = 7$ , with and without the parabolic compensation of the pulse length.

rudimentary compensation, the results shown figure 5.15 show a significant contrast improvement. The current implementation can give every pulse the correct length, which should further increase the signal contrast.

Also the pulse sequence itself has an influence on the effect of errors. During a perfect sequence, the algorithm does not change the atomic state for a factor (apart from the two obligatory  $\pi/2$ -pulses), in practice however there are disturbances. The consequences are most obvious for a sequence of  $\pi$ -pulses with alternating phases 0 and  $180^\circ$  and comparing the result with a sequence of  $\pi$ -pulses with zero phase shift. Both occur with a factor and should produce the same atomic state. The all-zero phase shift sequence however has a growing error propagation, quickly losing in contrast. The alternating sequence on the other hand can compensate some errors, because two neighboring pulses have almost the same, but opposite, error that cancels out, maintaining good contrast. For the non-factor situation these errors make no real difference, they just turn an already chaotic path into an even less predictable path, both of which average out to zero.

The algorithm in its current form is of limited practical use for factorizing numbers for two reasons: (1) since the quotient  $\mathfrak{N}/l$  is calculated explicitly to get the phase in equation 5.6 by a computer to program the frequency generator, (2) since it tests every value of  $l$ , which makes it just another variant of the trial division algorithm<sup>3</sup>. There first argument can be softened a bit as there are some ideas about generating the phase in some other way, for example by making use of the Zeeman effect [87]. The second argument can be reduced to only checking the prime numbers, but even then it is less efficient than most other factorization

<sup>3</sup>The trial division algorithm simply divides  $\mathfrak{N}$  by  $l$  and looks at the remainder. This is (probably) the simplest and slowest of all factorization algorithms, at least for large  $\mathfrak{N}$ , which is the only case of interest.



algorithms.

## 5.6. High sample rate

In the standard experimental sequence, the atomic source is shut down during the flight through the main chamber, this means a death time of about 140 ms for the atomic source. Also during the loading time, no interferometry measurements are done. It would be useful to do the interferometer and the loading of the next cloud at the same time as shown in figure 5.16. This would increase the sample rate which results in a better sampling of fast transients, as well as increase the effective number of atoms per second, which improves the resolution of the interferometer. When doing so one has to consider the influence of the active MOT, with its magnetic fields and its stray light, on the free flying ensemble and the interferometry.

The first and most obvious problem is that one needs to give the atoms some time to leave the 3D-MOT chamber before activating it again to load the next cycle, otherwise they would be recaptured and added to the next cloud and effectively never launch. The scattered light and the cooling light would also cause strong heating if the atoms were still too close. Figure 5.17 shows some measurements of the number of atoms and the temperature as a function of the death time for launch velocities of 2.79 m/s. Death times less than 4 ms are catastrophic, the atoms are then only 12 mm away, a safe time is 10 ms, which gives about 30 mm. Figure 5.18 shows the number of atoms as a function of the repetition rate. The increase in the effective number of atoms per second with increasing repetition rate, despite the increase in death time per second, is explained with the fact that the number of atoms in the 3D-MOT is saturating at longer loading times and can not make full use of the available flux from the 2D-MOT. This offers another way of increasing the resolution per second, without the technical difficulties of increasing the resolution per shot.

The experimental cycle time was limited to 7 Hz. It could have been extended to the maximum of 25 Hz, limited by the MOT switching procedure (at 25 Hz it would have had no loading time), by rewriting the sequence for three simultaneous clouds but the signal per shot was already so small that this was not considered useful.

These measurements show that high repetition rates are possible without significant degradation of the cloud temperatures, and with an increase in the effective number of atoms per second. Unfortunately the interferometry system was not available at the time of this investigation, therefore the influence of the stray light and magnetic field of the MOTs on the interferometry could not be tested. But since it will be a fixed non-inertial offset, it can be removed with a calibration. Also the symmetry of the device should be able to put this contribution in the common mode (acceleration) term.

## 5. Atomic Measurements

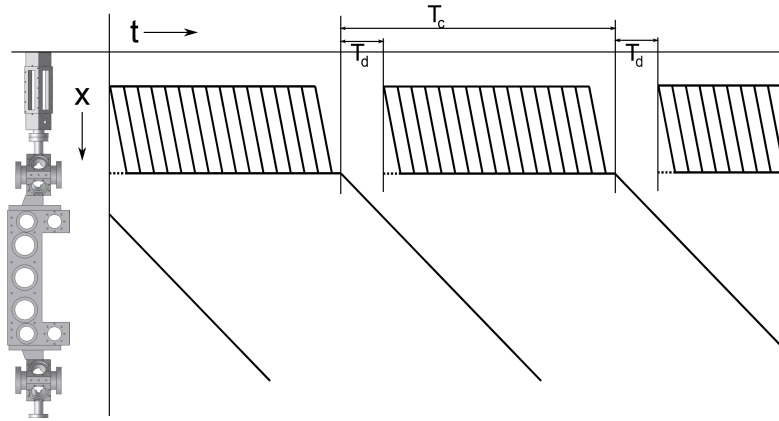


Figure 5.16.: Experimental sequence with overlapping loading and free flight. The position of the atoms is on the vertical axis, as indicated by the side view of the vacuum chamber, the thick lines indicate where the atoms are and when the 2D and 3D MOTs are active.

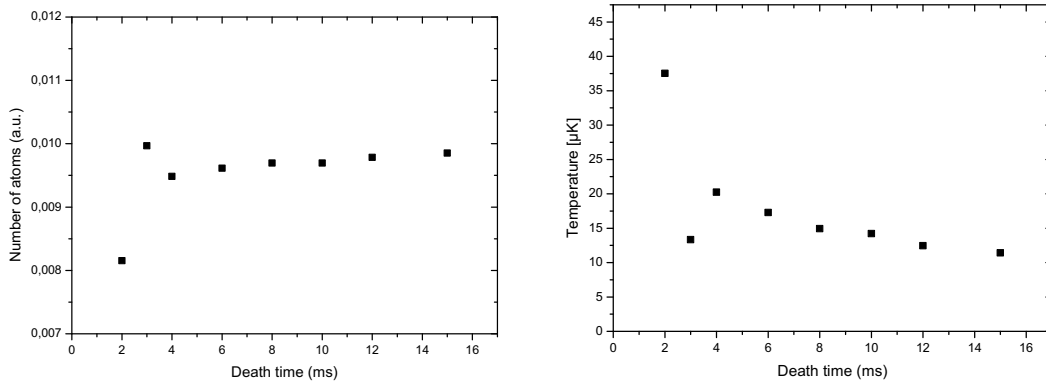


Figure 5.17.: Measurements of the number of atoms (left) and the temperature of the launched atoms (right) as a function of the death time. There are big losses when the death time is less than 4 ms because the atoms have not yet left the 3D MOT.

## 5. Atomic Measurements

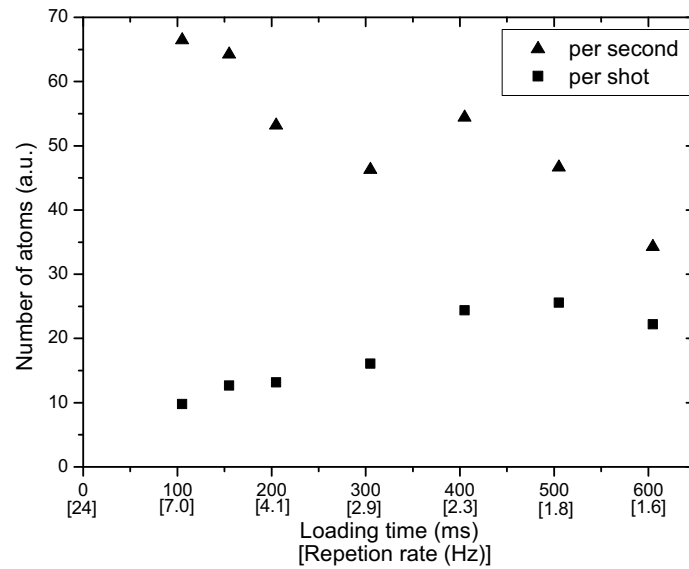


Figure 5.18.: Measurements of the number of atoms per shot and per second for different loading times. The horizontal axis is the loading time as well as the corresponding repetition rate. Switching and death time is 42.4 ms. Cycle times faster than 7 Hz were not tested as that would have required to set up the sequence for 3 simultaneous clouds, which was not considered useful.

## 6. Outlook

As show by the results of the previous chapter, a highly flexible and sensitive instrument has been realized that is capable of measuring rotations and accelerations as well as measure the transition frequency like an atomic clock and can even be used to do number factorization with the Gauss-sum algorithm.

The laser system has been improved to provide far better stability and accuracy as before. Where before measurements sessions were on average limited to 20 minutes before some laser lock would fail, it can now last more than a day (limited by the human operator) enabling long integration times. All laser stabilizations have been upgraded with very reliable frequency offset locking techniques. The frequency of most important laser systems can be set and modified with a phase locked loop technique with sub-Hz accuracy relative to the reference laser.

The vacuum system has been improved and now allows to operate the rubidium ovens without heating, significantly reducing the temperature increase and corresponding pressure increase of the vacuum chamber enabling much longer measurement sessions.

The control electronics and software have been improved to allow more flexibility by enabling more complex sequences with more pulses as well as improving the timing resolution on all channels. The automatic sweeping of parameters of the experimental sequence allows for a more systematic investigation of the experiment. Also operation with high repetition rates has been shown.

Inertially sensitive and insensitive Mach-Zehnder fringes using only one window were shown before [48], inertially insensitive fringes across all three windows were shown in this work with the final steps to realize also inertially sensitive Mach-Zehnder fringes across all three windows being part of ongoing work.

When the results of the previous chapter can be extrapolated to the inertially sensitive configuration then they would indicate a rotation resolution of  $7 \cdot 10^{-7}$  (rad/s)/ $\sqrt{\text{Hz}}$ , which is 2.5 orders of magnitude away from the design target of  $2 \cdot 10^{-9}$  (rad/s)/ $\sqrt{\text{Hz}}$ . The differences in drift time (23 ms versus 25 ms) and velocity (2.79 m/s versus 3.0 m/s) only account for 10% less sensitivity. The key points to improve to reach this goal are the state detection, the effective number of atoms, and the phase noise.

The improvements in the state detection concern mainly the photodiode and its optical access. The scaling and offset of the photodiode should be modified to better match the range of the analog to digital converter. The optical access should also be improved to receive a larger portion of the scattered light which would increase the signal and reduce the relative influence of the electronic and digitization noise.

## 6. Outlook

The (effective) number of atoms can be improved by enhancing the efficiencies of the individual components of the state preparation and the interferometry. These depend largely on the spatial width and velocity width of the atomic cloud. The velocity width, which corresponds to a temperature, can be improved by a further optimization of the 3D-MOT/molasses or by narrowing the Fourier width of the velocity selective Raman pulse of the state preparation (at the expense of throwing away more atoms). The efficiency of the interferometry pulse can be improved by reducing the length of the pulses.

The spatial width of the cloud is determined by the atomic sources which can be reduced with a more advanced control of the magnetic fields. A reverse current pulse [70] during the shut down of the magnetic field of the 3D-MOT could suppress the induced currents in the vacuum chamber, which otherwise limit the shut down of the magnetic field. The faster switching of magnetic fields allows for less death time during the transition from MOT to molasses which results in a smaller cloud diameter which would improve the interferometer signal. The use of a compression MOT [88] which has a strong increase in field strength shortly before shutting down the field can be used to further reduce the MOT starting volume.

To significantly improve the optical access and simplify the state preparation and detection, a redesign of the main vacuum chamber would be necessary. Especially the double use of viewports for the state preparation and detection could then be solved and allow for a better optimization of each of them. The range of drift times ( $T$ ) of the Mach-Zehnder interferometer sequence could also be improved, as it currently can not access the intermediate regime of about 5 to 17 ms between the one window sequence ( $T < 5$  ms) and the three window sequence ( $17 \text{ ms} < T < 27$  ms) because of the limited optical access. To achieve such wide optical access, the resulting chamber would be an all glass design.

Another component that could benefit from more optical access is the 3D-MOT chamber, where the diagnostics of the 3D-MOT/molasses can be simplified with the addition of extra windows to provide a better view for cameras and photodiodes to monitor the atomic cloud. The 2D-MOT vacuum chamber is currently being redesigned to improve the reliability of its vacuum seals with a more stiff design in titanium. Such modifications of the vacuum system are relatively easy to do because of the modular design.

A reduction of phase noise is possible by reducing the acoustic and vibrational noise on the experimental setup as well as on the interferometry laser and the optical fibers. Preliminary measurements have shown that there is a significant contribution from acoustic noise on the mirror vibrations which could be reduced with a passive acoustic isolation box. A further reduction requires active phase stabilization of the light after the fibers in addition to the present stabilization scheme close to the laser system. Such a stabilization scheme has been used by [71] for a single fiber that transported all the light. But even the optical phase when transporting the light in two separate fibers can be stabilized, even in pulsed mode, as shown by [89] with some effort. The use of an intensity stabilization for the interferometry laser system, that would act on the current of the tapered amplifiers, would help reduce any drifts due to AC Stark shifts and Rabi frequencies.

## 6. Outlook

Some calibration method or proof of rotation sensitivity would be useful. This could be realized by applying known external forces (rotation and/or acceleration) on the vibration isolation platform at a very slow rate so that the platform does not notice and compensate it. This would allow a simple calibration of the sensitivity factor of the interferometer, instead of assuming the earth rotates at a given rate. To verify the signal offset of the interferometer, a parallel measurement with another rotation sensor would be needed, this can be either another atomic rotation sensor, like the one in Paris [50], or a ring laser gyroscope, like the one in Wettzell [15] (or its smaller transportable cousin [90]).

To significantly enhance the sensitivity of the sensor one needs to enlarge the enclosed area or go to entirely different geometries [38]. The area enhancement can be achieved by increasing the flight time and path and/or increasing the momentum transfer. The first option means a longer device or a much steeper trajectory, both are at the expense of mechanical stability unless one goes to a microgravity environment (space). To achieve large increases in the enclosed area in this way one also needs to use a BEC because of the long expansion times.

To increase the momentum transfer in the beam splitters and mirrors, the number of photons that are absorbed and emitted per operation has to be increased. This can be achieved by either using multiple photons per pulse or by using multiple pulses. Ref. [91] has shown interferometry with 24-photon-momentum-transfer using Bragg diffraction, as well as a combination of Bragg and Bloch oscillations [92] which has more favorable technical scaling properties. The use of Bragg and/or Bloch diffraction however also requires a totally different state detection as the two interferometer outputs have the same internal atomic state. For high order Bragg/Bloch diffraction it will also be necessary to use a Gaussian pulse shape for the interferometry pulses [93]. Ref. [94] makes use of alternating directions of the Raman pulses to increase the area. The use of simultaneous Raman transitions with opposing directions as in [95] could also be of interest, as it is not sensitive to laser phase noise because both paths have the same internal state while still using a simple state detection based on the internal states, and it can also increase the area further with more pulses.

The use of very high order ( $>20$ ) photon momentum transfer, enables a spatially separate state detection where the two exits of the interferometer as well as the state preparation can then coexist side by side because the transverse velocity is high enough to be able to put a mechanical shield between state preparation and state detection. This can also be combined with the continuous mode of operation.

In order to reach the limits of what matter wave interferometry can do, one needs much longer flight times than one can reach in conventional laboratory setups. One way is to use very tall setups like the 10 m drop tower of the Kasevich-group [96], which is designed for gravity measurements. The other solution is to go to space to obtain the very long flight times with the added bonus of very low background vibration noise. Several proposals towards that goal have been produced like “HYPER-precision atom interferometry in space (HYPER)” [43] and “matter wave explorer of gravity (MWXG)” [51].

This project as well as several other projects of the institute for quantum optics

## 6. Outlook

are oriented towards the goal of realizing an inertial quantum sensor in space to do fundamental physics, to measure effect like the Lense-Thirring effect [97, 45] or gravitational waves [46], which can not be measured with conventional and earth bound sensors.

With the QUANTUS cooperation project [98, 99], in which the institute for quantum optics is a central player, compact and robust BEC apparatuses are being developed that operate under micro-gravity in the drop-tower in Bremen. They have already shown condensate lifetimes of more than 1 s [100] and are preparing to bring this technology into space as well.

The use of a Bose-Einstein condensate (BEC) in which all atoms are in the same ground state and share the same wave function, allows for many new and interesting techniques that make use of quantum mechanical phenomena like entanglement, quantum non-demolition measurement and squeezing, some of which have been investigated for application in an atomic inertial sensor [25]. The most obvious advantage of a BEC is the very low temperature and the corresponding very small thermal expansion which improves the interferometer contrast and allows for very long flight times (ref. [101]: 500 pK, remaining thermal velocity 1 mm/s). But the use of a BEC comes with some challenges: the number of atoms per shot is rather low (ref. [102]:  $20 \cdot 10^6$  atoms in 60 s) and the repetition rate is also low (ref. [103]:  $3 \cdot 10^3$  atoms in 3 s).

As indicated by the many possibilities to optimize and expand the presented experiment one can see that the area of inertial sensors based on atom interferometry an active subject of research is and will continue to give many interesting and fascinating options for the future.

# A. Rubidium-87 data

Table A.1.: Numerical values for some constants, mostly from [54]

Parameter	Symbol	Value
Speed of light (vacuum)	$c$	$2.997\,924\,58 \cdot 10^8$ m/s
Rotation rate of earth	$ \Omega_{earth} $	$7.2921150(1) \cdot 10^{-5}$ rad/s [40]
Location of experiment		$52.382\,45(10)^{\circ}$ North, $9.718\,68(10)^{\circ}$ East [104]
Boltzmann's constant	$k_B$	$1.380\,650\,3(24) \cdot 10^{-23}$ J/K
Planck's constant	$\hbar = \frac{h}{2\pi}$	$1.054\,571\,596(82) \cdot 10^{-34}$ Js

Table A.2.: Summary of the most relevant  $^{87}\text{Rb}$  parameters, mostly from [54].

Parameter	Symbol	Value
Wavelength ( $ 5^2S_{1/2}\rangle \rightarrow  5^2P_{3/2}\rangle$ )	$\lambda$	$780.241\,209\,686(13)$ nm
Frequency		$384.230\,484\,468\,5(62)$ THz
Mass	$m$	$1.443\,160\,60(11) \cdot 10^{-25}$ kg
Natural linewidth	$\Gamma$	$6.065(9)$ MHz
Recoil velocity	$v_{recoil}$	$5.8845$ mm/s
Frequency of clock transition	$\omega_{eg}$	$6\,834\,682\,610.904\,29(9)$ Hz
Wavelength of clock transition	$\lambda_{eg}$	$43.863\,405\,97$ mm
Doppler shift rate for 780.xxx nm	$1/\lambda$	$1.281\,654\,939$ MHz/(m/s)
Typical saturation intensity	$I_{sat}$	$1.669$ mW/cm <sup>2</sup>



A. Rubidium-87 data

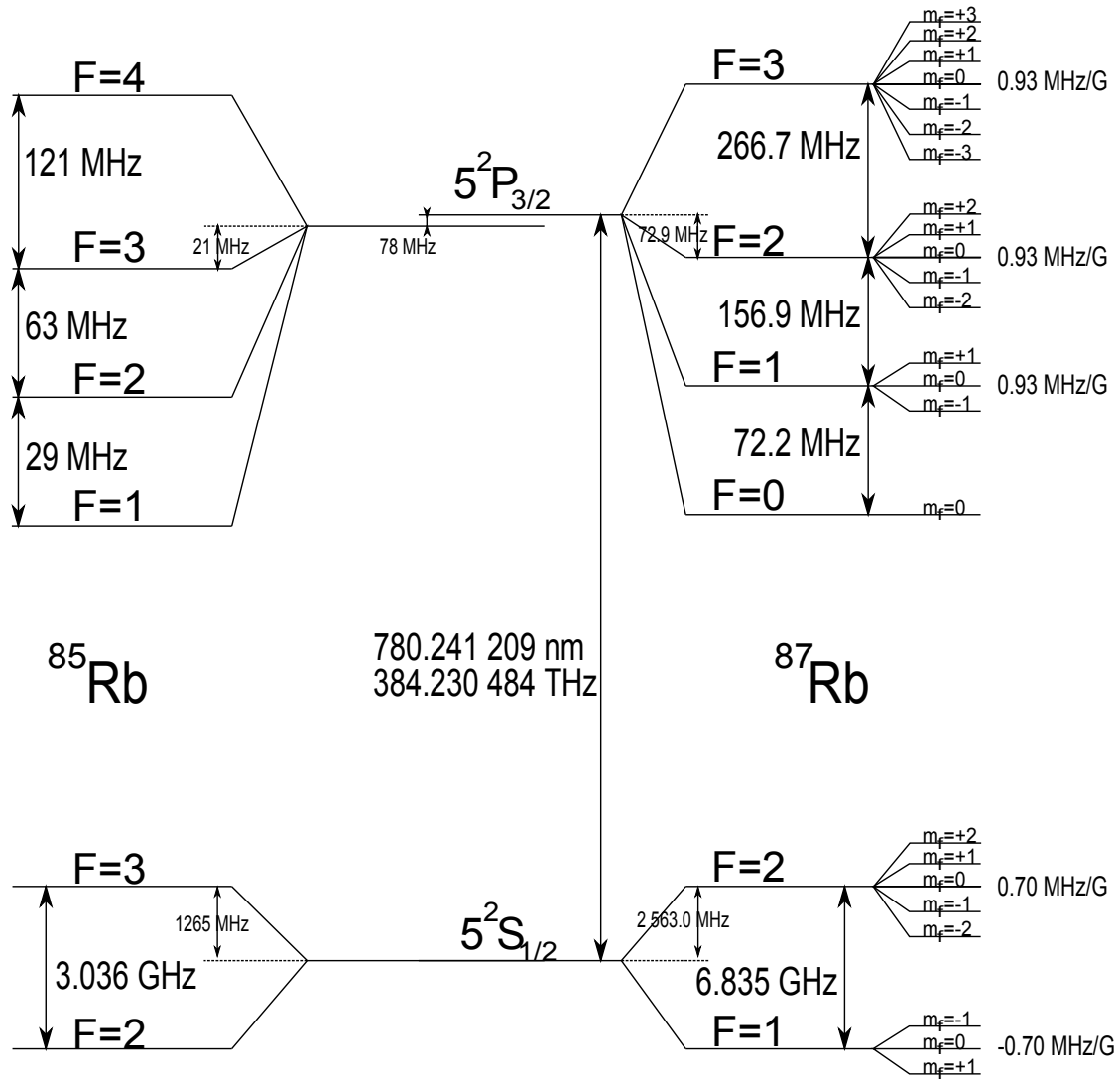


Figure A.1.: A level scheme with the relevant atomic states of the  $^{87}\text{Rb}$  D2 line [54]. The (simplified)  $^{85}\text{Rb}$  data [105] on the left is for reference as they also can be seen in spectroscopy with natural Rubidium.

## B. Derivation of the Sagnac equation

The most common “derivation” of the Sagnac equation assumes a flat circular geometry, which does not properly explain why the area shows up nor does it validate the use vectors (especially  $\vec{\Omega} \cdot \vec{A}$ ). The derivation given here assumes no specific geometry, it is even valid for complex three dimensional interferometer paths where the area is not intuitively clear. For completeness, the acceleration should also be included, but this has not been done. The derivation shown here has used some hints from ref. [106].

The apparent length  $dl$  of a path segment  $d\vec{r}$  in the presence of a rotation rate  $\vec{\Omega}$  and a velocity  $\vec{v}$  of the reference frame traversed in a time  $dt$ , see also figure B.1, is:

$$dl = |d\vec{r}| + \left( \vec{v} + \vec{\Omega} \times \vec{r} \right) \cdot \frac{d\vec{r}}{|d\vec{r}|} dt. \quad (\text{B.1})$$

Here  $\vec{r}$  is the position of the path segment relative to some origin, the origin itself disappears later on as it should. The term  $\vec{\Omega} \times \vec{r}$  gives the rotation induced velocity of which only the component in the direction of  $d\vec{r}$  stretches the apparent path.

Replacing  $dt$  with:

$$dt = \frac{|d\vec{r}|}{c}, \quad (\text{B.2})$$

where  $c$  is the velocity of the wave<sup>1</sup>, gives:

$$dl = |d\vec{r}| + \frac{1}{c} \left( \vec{v} + \vec{\Omega} \times \vec{r} \right) \cdot d\vec{r}. \quad (\text{B.3})$$

The phase  $\phi$  of an interferometer (Sagnac or Mach-Zehnder) using waves with a wavelength  $\lambda$  that travel across two different paths  $P_1$  and  $P_2$ , with the start and end points of both paths identical, is then given by:

$$\phi = \frac{2\pi}{\lambda} \left( \int_{P_1} dl - \int_{P_2} dl \right) \quad (\text{B.4})$$

Substituting equation B.3 into this equation and resorting the components gives:

---

<sup>1</sup>In the case of light,  $c$  is about  $3.0 \cdot 10^8$  m/s, in the case of matter waves it is only a few m/s.

## B. Derivation of the Sagnac equation

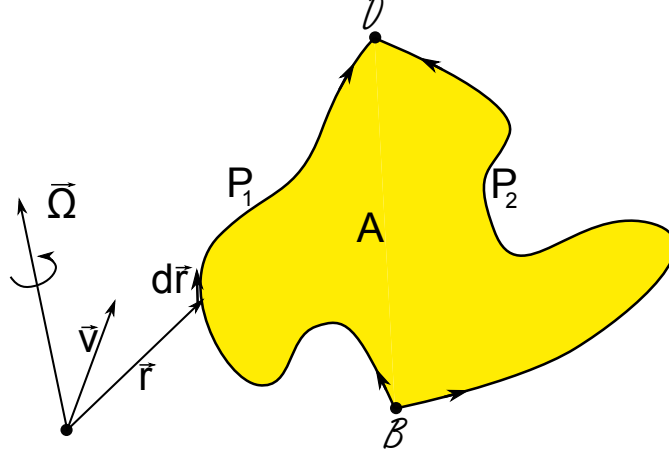


Figure B.1.: Schematic overview of an interferometer. The wave splits at point  $\mathcal{B}$  in two paths  $P_1$  and  $P_2$ , which together enclose an area  $A$ , and recombines in point  $\mathcal{D}$ . Here  $\vec{r}$  is the position of the path segment  $d\vec{r}$  relative to some origin, in the presence of a rotation rate  $\vec{\Omega}$ , and a velocity  $\vec{v}$ .

$$\phi = \frac{2\pi}{\lambda} \left( \int_{P_1} |d\vec{r}| - \int_{P_2} |d\vec{r}| + \frac{1}{c} \vec{v} \cdot \int_{P_1} d\vec{r} - \frac{1}{c} \vec{v} \cdot \int_{P_2} d\vec{r} + \frac{1}{c} \int_{P_1} \vec{\Omega} \times \vec{r} \cdot d\vec{r} - \frac{1}{c} \int_{P_2} \vec{\Omega} \times \vec{r} \cdot d\vec{r} \right). \quad (\text{B.5})$$

The propagation velocity of the wave has been assumed to be constant, and has therefore been taken out of the integration. The first two terms correspond to the lengths of the two paths, without external forces. In a Sagnac interferometer these two terms are identical as the waves travel through the same path (in opposite direction). In a Mach-Zehnder interferometer they are equal only in the ideal case (very good alignment).

The second pair of terms disappears in any interferometer because the integrals correspond to a vector from the starting point to the end point, which for both paths is identical. This also shows that the velocity of the reference frame can not be measured. Equation B.5 then reduces to:

$$\phi = \frac{2\pi}{\lambda c} \left( \int_{P_1} \vec{\Omega} \times \vec{r} \cdot d\vec{r} - \int_{P_2} \vec{\Omega} \times \vec{r} \cdot d\vec{r} \right). \quad (\text{B.6})$$

When using a loop where the two paths are identical but with opposite direction (which changes the sign in the integration) and the start and end point coincide, as in a Sagnac interferometer, equation B.6 becomes:

$$\phi = \frac{2\pi}{\lambda c} 2 \oint_{P_1} \vec{\Omega} \times \vec{r} \cdot d\vec{r}. \quad (\text{B.7})$$

When using a loop with different start and end points, like in the Mach-Zehnder interferometer, the phase becomes:

## B. Derivation of the Sagnac equation

$$\phi = \frac{2\pi}{\lambda c} \oint_{P_1+\bar{P}_2} \vec{\Omega} \times \vec{r} \cdot d\vec{r}. \quad (\text{B.8})$$

Where the two different paths, which only need to share the start and end points, are combined to form a single closed path. The bar over  $P_2$  indicates that it is traversed in reverse direction. Note the factor of two difference when compared to the Sagnac case.

Continuing the derivation only for the Mach-Zehnder case, as that is the most relevant case for this thesis, equation B.8 can be rewritten to:

$$\phi = \frac{2\pi}{\lambda c} \oint_{P_1+\bar{P}_2} \vec{\Omega} \cdot (\vec{r} \times d\vec{r}). \quad (\text{B.9})$$

When assuming that the rotation rate is constant, the dot product can be taken out of the integration:

$$\phi = \frac{2\pi}{\lambda c} \vec{\Omega} \cdot \oint_{P_1+\bar{P}_2} (\vec{r} \times d\vec{r}). \quad (\text{B.10})$$

Where the integral can be replaced by making use of the definition of the area vector:

$$\vec{A} = \frac{1}{2} \oint \vec{r} \times d\vec{r}. \quad (\text{B.11})$$

This definition is necessary since a closed path in three dimensions alone does not uniquely define a surface (think about a rubber sheet, when all edges are fixed, the central part can still be deformed). For simple intuitive flat paths, the integral corresponds to twice the area enclosed by the path. The rotation phase of a Mach-Zehnder-like interferometer is then finally given by:

$$\phi = \frac{2\pi}{\lambda c} 2\vec{\Omega} \cdot \vec{A}. \quad (\text{B.12})$$

Which is the familiar expression for the Sagnac phase for Mach-Zehnder-like interferometers.

There are some subtleties hidden in the simple description above, see reference [41] for a more thorough description.

## C. CAD Drawings

### C.1. Vacuum chamber

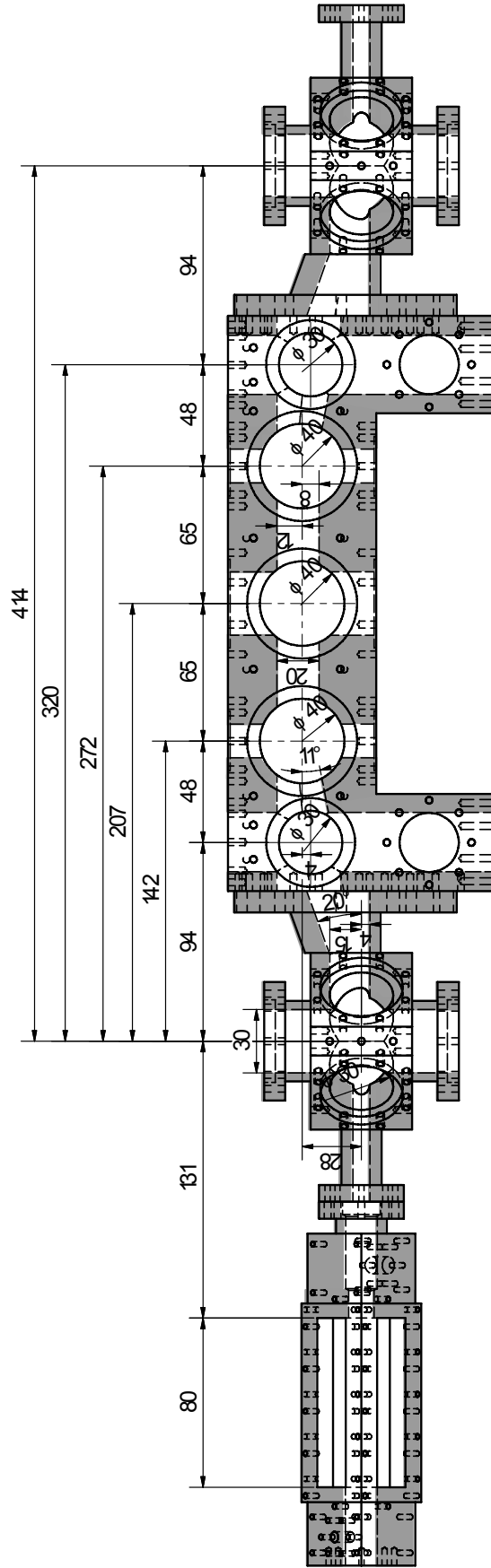


Figure C.1.: CAD drawing of the vacuum chamber with the exact positions of the windows and the walls. The position of the 3D MOT with respect to the main chamber is shown here for the configuration used, and can be changed by mounting it in another position. The gray coloring shows the cross section to help identify the space available for the atoms. The right 2D MOT and the differential pumping stages between 2D and 3D-MOT, are not shown.

## C.2. Bias coils

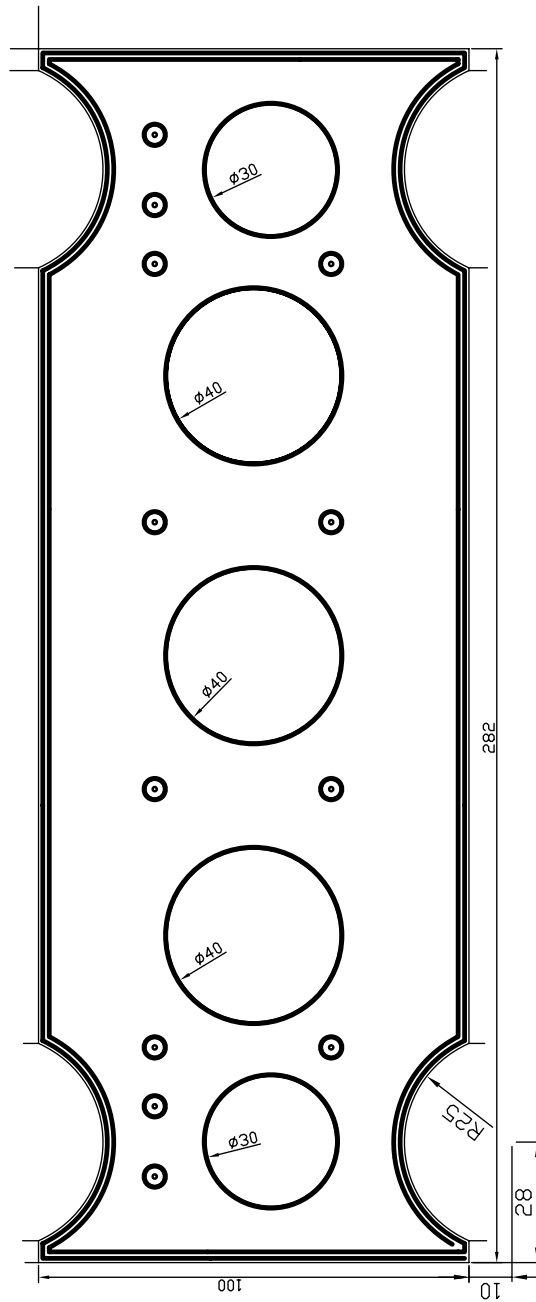


Figure C.2.: CAD drawing of the bias coils for the main chamber. These coils are implemented as two double sided printed circuit boards. There are two loops of one millimeter width on either side, an external wire connection in one of the corners connects the front and back side.





## D.2. AD9956

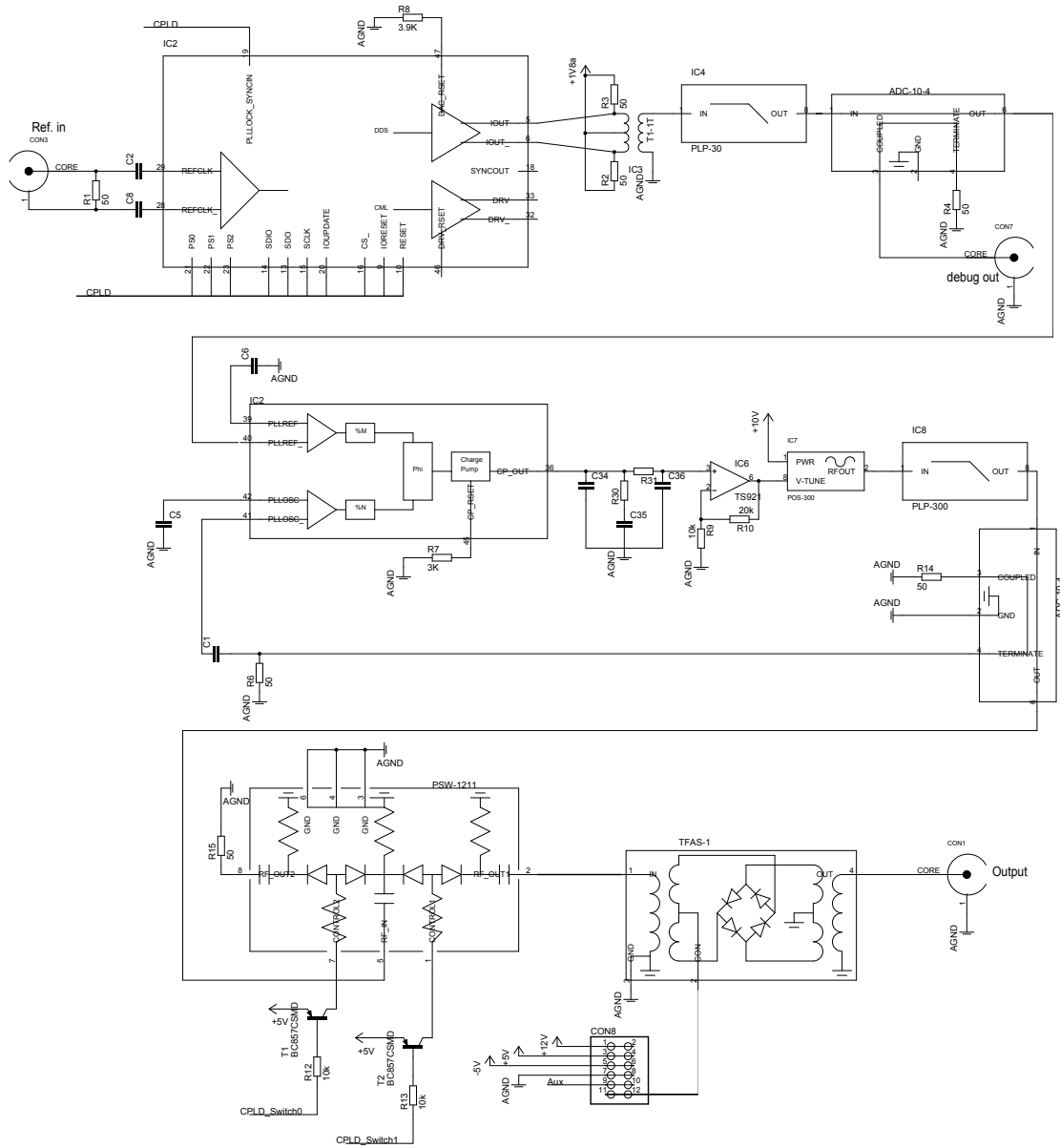


Figure D.2.: RF section of AD9956 ISA card. The analog signal to control the amplitude was originally intended to be supplied by a CPLD controlled DAC (figure D.3).

## D. Electronic circuits

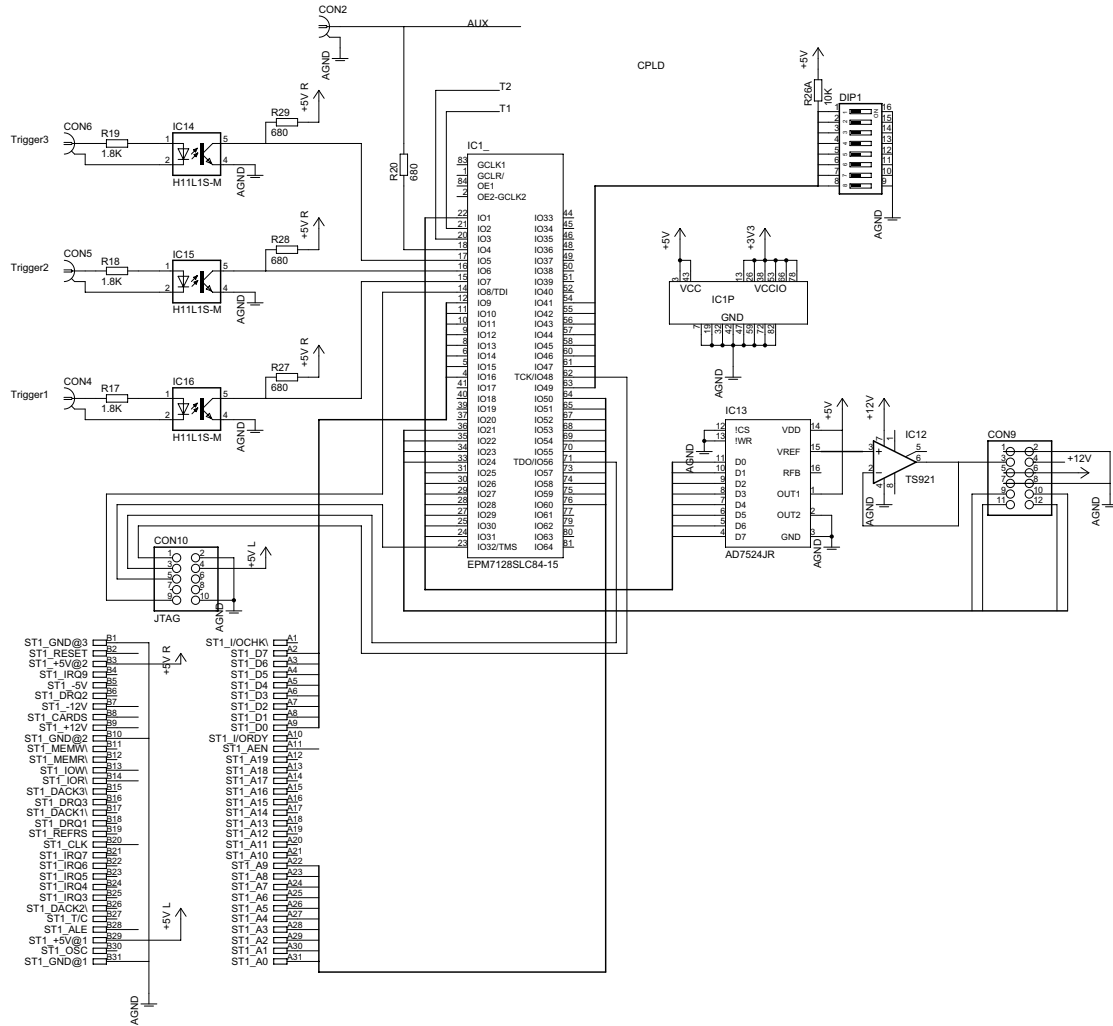


Figure D.3.: Digital section of the AD9956 ISA card. The central component is the CPLD (figure D.5 and following) which connects the DDS, the DAC, three optocoupled inputs and the ISA bus.

## D. Electronic circuits

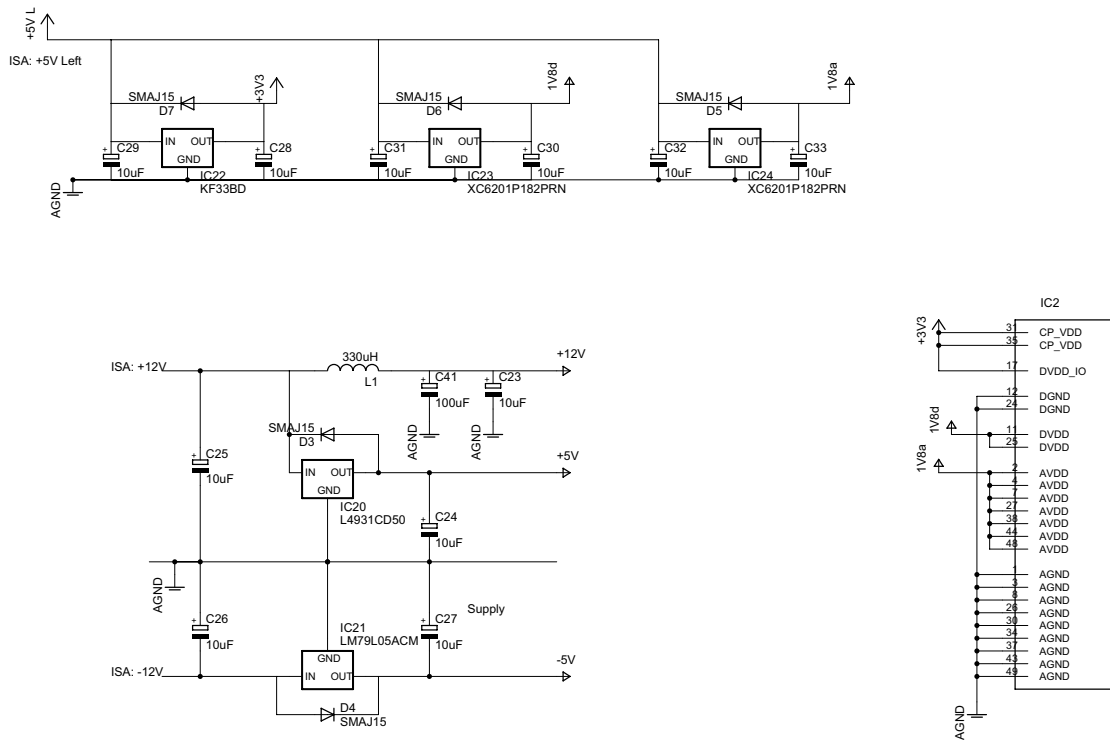


Figure D.4.: Power section of the AD9956 ISA card.

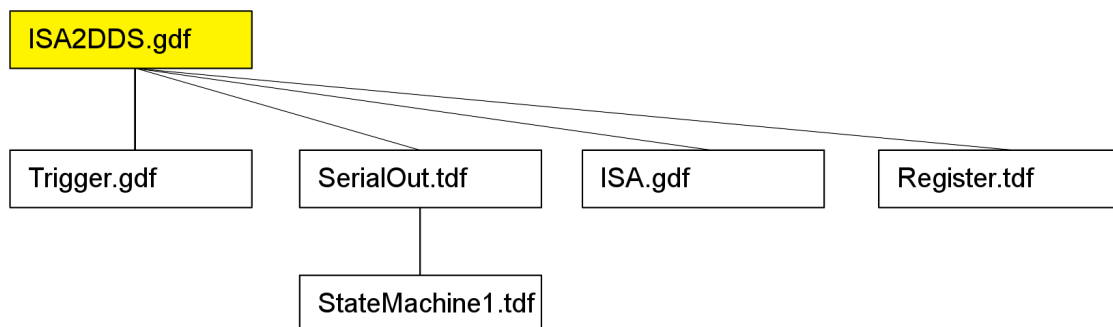


Figure D.5.: Overview of the design files of the CPLD.

## D. Electronic circuits

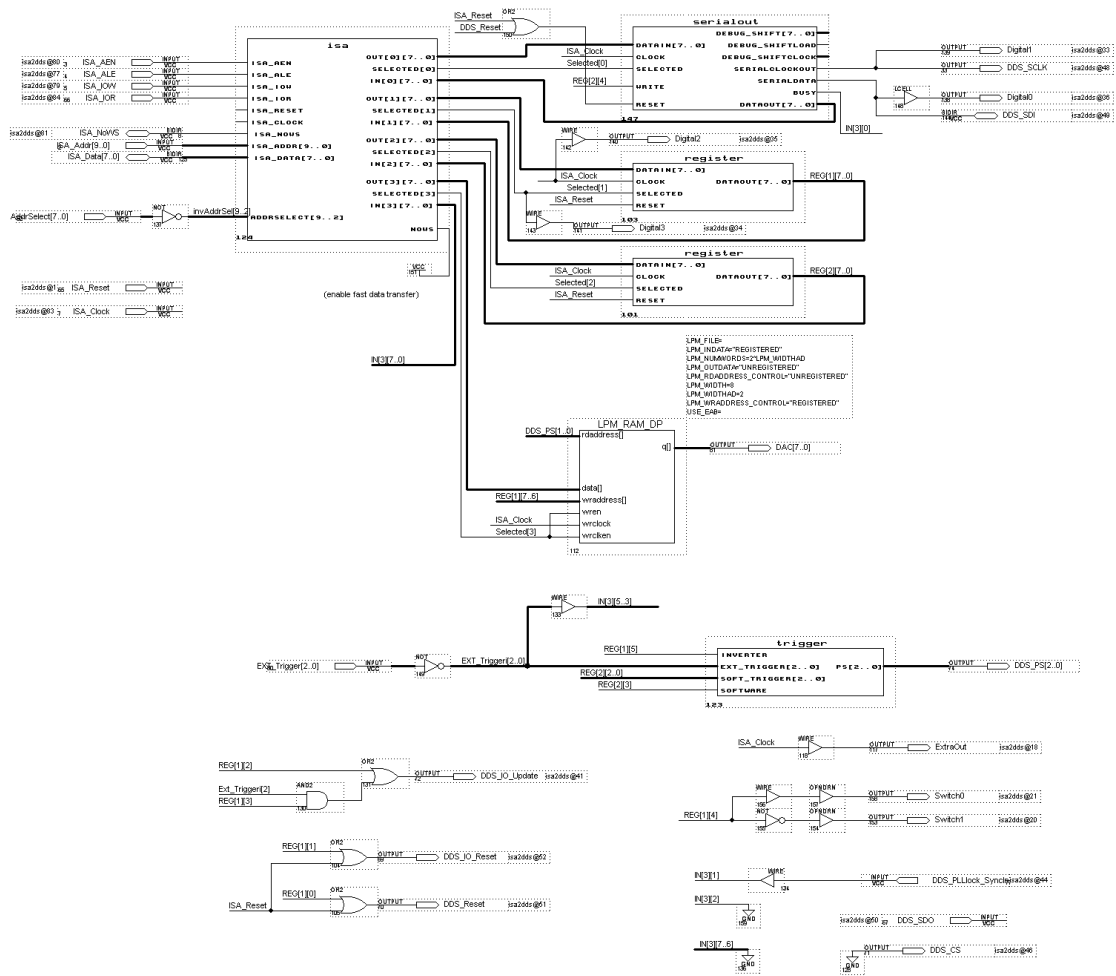


Figure D.6.: ISA2DDS.gdf, main file of the CPLD.

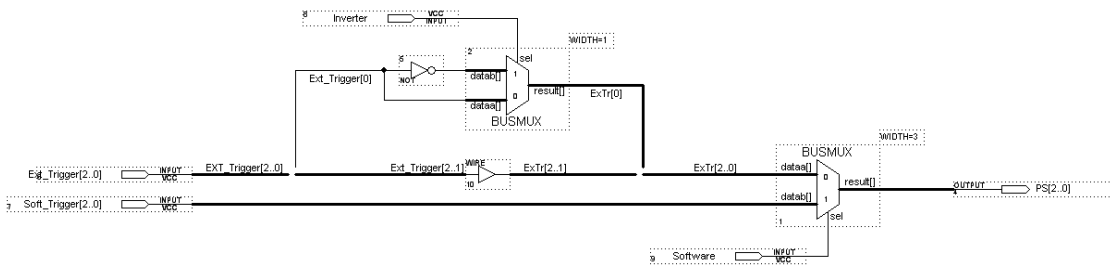


Figure D.7.: Trigger.gdf

## D. Electronic circuits

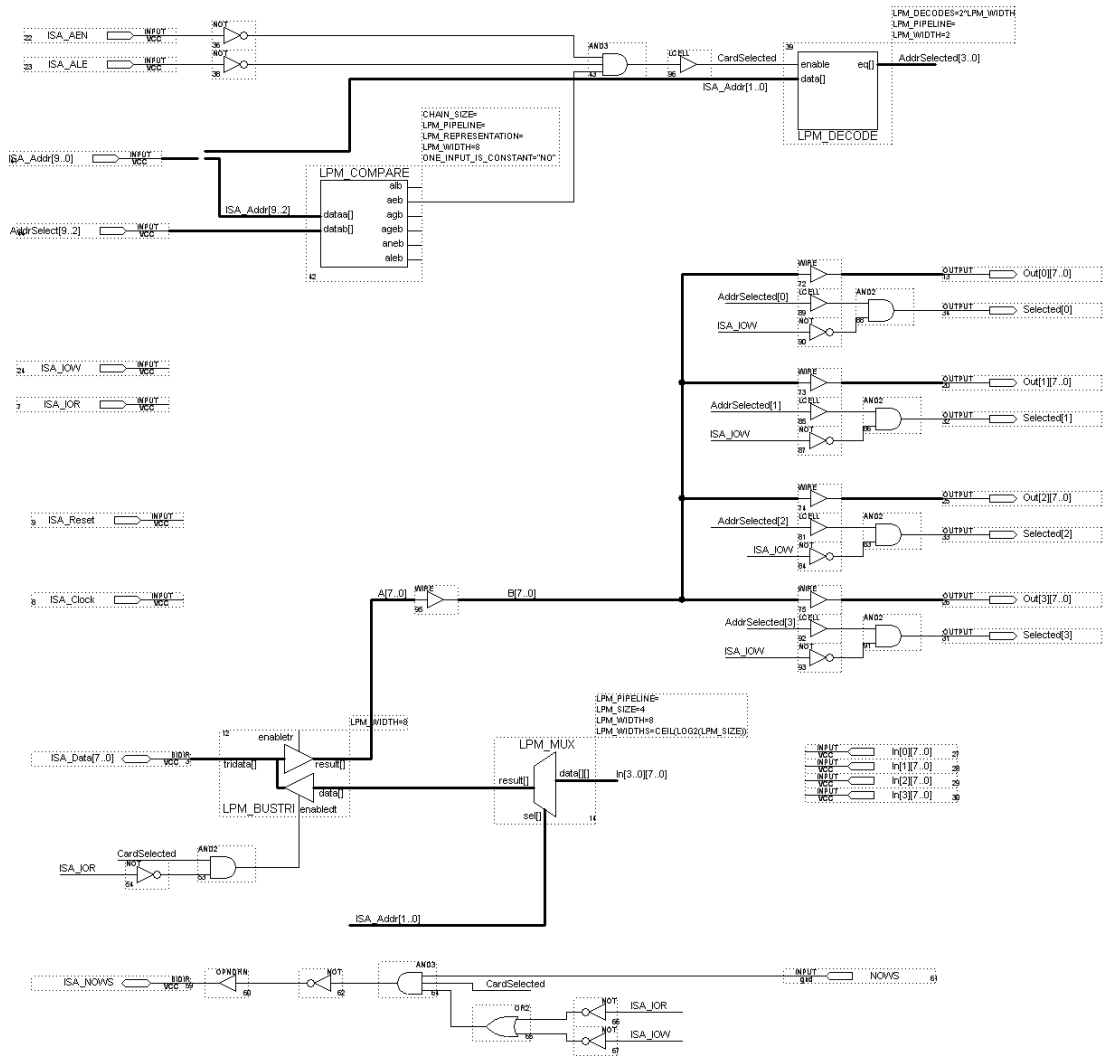


Figure D.8.: ISA.gdf

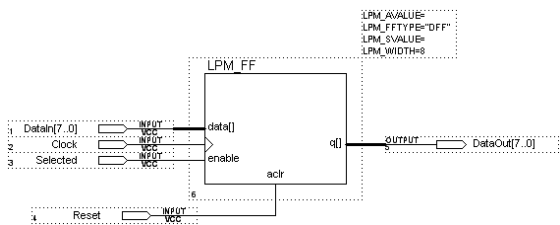


Figure D.9.: Register.gdf



Listing D.1: Statemachine1.tdf

```

1  SUBDESIGN statemachine1
3  (
    clk , reset   : INPUT;
5    load        : INPUT;
    write         : INPUT;
7    shiftLoad ,
    shiftClock ,
9    ddsClock ,
    outputEnable ,
11   busy        : OUTPUT;
    )
13 VARIABLE
    ss: MACHINE OF BITS (StateBits[5..0])
15     WITH STATES (sWait=B"010000",
        sW0 =B"000000", sW1 =B"000001", sW2 =B"000010", sW3 =B"000011",
17     sW4 =B"000100", sW5 =B"000101", sW6 =B"000110", sW7 =B"000111",
        sW8 =B"001000", sW9 =B"001001", sW10=B"001010", sW11=B"001011",
19     sW12=B"001100", sW13=B"001101", sW14=B"001110", sW15=B"001111",
        sR0 =B"100001", sR1 =B"100011", sR2 =B"100000", sR3 =B"100010",
21     sR4 =B"100101", sR5 =B"100111", sR6 =B"100100", sR7 =B"100110",
        sR8 =B"101001", sR9 =B"101011", sR10=B"101000", sR11=B"101010",
23     sR12=B"101101", sR13=B"101111", sR14=B"101100", sR15=B"101110",
        sR16=B"110001", sR17=B"110011", sR18=B"110000", sR19=B"110010",
25     sR20=B"110101", sR21=B"110111", sR22=B"110100", sR23=B"110110",
        sR24=B"111001", sR25=B"111011", sR26=B"111000", sR27=B"111010",
27     sR28=B"111101", sR29=B"111111", sR30=B"111100", sR31=B"111110" );
    BEGIN
29     ss.clk    = clk;
        ss.reset = reset;
31
    TABLE
33     % current  current  => next  next  %
        % state  input    => state  output %
35     ss , load , write => ss , shiftLoad , shiftClock , ddsClock , busy , outputEnable ;
        sWait , 0 , X => sWait , 1 , 0 , 0 , 0 , 0 ;
37     sWait , 1 , 0 => sR0 , 1 , 0 , 0 , 0 , 0 ;
        sWait , 1 , 1 => sW0 , 1 , 0 , 0 , 0 , 0 , 1 ;
39
        sW0 , X , X => sW1 , 1 , 1 , 0 , 1 , 1 ;
41     sW1 , X , X => sW2 , 0 , 0 , 1 , 1 , 1 ;
        sW2 , X , X => sW3 , 0 , 1 , 0 , 1 , 1 ;
43     sW3 , X , X => sW4 , 0 , 0 , 1 , 1 , 1 ;
        sW4 , X , X => sW5 , 0 , 1 , 0 , 1 , 1 ;
45     sW5 , X , X => sW6 , 0 , 0 , 1 , 1 , 1 ;
        sW6 , X , X => sW7 , 0 , 1 , 0 , 1 , 1 ;
47     sW7 , X , X => sW8 , 0 , 0 , 1 , 1 , 1 ;
        sW8 , X , X => sW9 , 0 , 1 , 0 , 1 , 1 ;
49     sW9 , X , X => sW10 , 0 , 0 , 1 , 1 , 1 ;
        sW10 , X , X => sW11 , 0 , 1 , 0 , 1 , 1 ;
51     sW11 , X , X => sW12 , 0 , 0 , 1 , 1 , 1 ;
        sW12 , X , X => sW13 , 0 , 1 , 0 , 1 , 1 ;
53     sW13 , X , X => sW14 , 0 , 0 , 1 , 1 , 1 ;

```

*D. Electronic circuits*

```

55   sW14, X, X => sW15, 0, 1, 0, 1, 1;
      sW15, X, X => sWait, 0, 0, 1, 1, 1;

57   sR0, X, X => sR1, 0, 0, 1, 1, 0;
      sR1, X, X => sR2, 0, 0, 1, 1, 0;
59   sR2, X, X => sR3, 0, 0, 0, 1, 0;
      sR3, X, X => sR4, 0, 0, 0, 1, 0;
61   sR4, X, X => sR5, 0, 0, 1, 1, 0;
      sR5, X, X => sR6, 0, 0, 1, 1, 0;
63   sR6, X, X => sR7, 0, 0, 0, 1, 0;
      sR7, X, X => sR8, 0, 0, 0, 1, 0;
65   sR8, X, X => sR9, 0, 0, 1, 1, 0;
      sR9, X, X => sR10, 0, 0, 1, 1, 0;
67   sR10, X, X => sR11, 0, 0, 0, 1, 0;
      sR11, X, X => sR12, 0, 0, 0, 1, 0;
69   sR12, X, X => sR13, 0, 0, 1, 1, 0;
      sR13, X, X => sR14, 0, 0, 1, 1, 0;
71   sR14, X, X => sR15, 0, 0, 0, 1, 0;
      sR15, X, X => sR16, 0, 0, 0, 1, 0;
73   sR16, X, X => sR17, 0, 0, 1, 1, 0;
      sR17, X, X => sR18, 0, 0, 1, 1, 0;
75   sR18, X, X => sR19, 0, 0, 0, 1, 0;
      sR19, X, X => sR20, 0, 0, 0, 1, 0;
77   sR20, X, X => sR21, 0, 0, 1, 1, 0;
      sR21, X, X => sR22, 0, 0, 1, 1, 0;
79   sR22, X, X => sR23, 0, 0, 0, 1, 0;
      sR23, X, X => sR24, 0, 0, 0, 1, 0;
81   sR24, X, X => sR25, 0, 0, 1, 1, 0;
      sR25, X, X => sR26, 0, 0, 1, 1, 0;
83   sR26, X, X => sR27, 0, 0, 0, 1, 0;
      sR27, X, X => sR28, 0, 0, 0, 1, 0;
85   sR28, X, X => sR29, 0, 0, 1, 1, 0;
      sR29, X, X => sR30, 0, 0, 1, 1, 0;
87   sR30, X, X => sR31, 0, 0, 0, 1, 0;
      sR31, X, X => sWait, 0, 0, 0, 1, 0;
89
END TABLE;
91 END;

```



## D. Electronic circuits

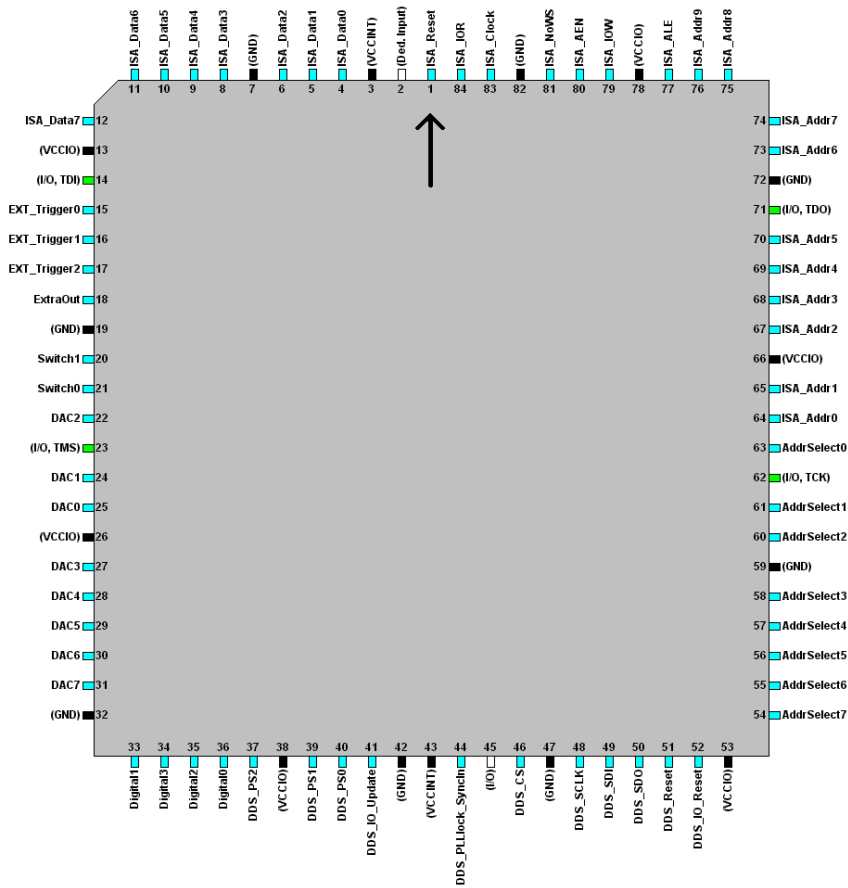


Figure D.11.: Pinout of the CPLD

### **D.3. PPG20**

This device is based on a PPG-20 (Digital Signal Technology) frequency generator that can generate up to 20 MHz and has two outputs with a controlled phase difference. One output is output directly, the other is used for the demodulation of the input signal in a mixer. The resulting error signal is low pass filtered with 2.5 MHz.

In order to program the PPG-20 a microcontroller (Motorolla MC68HC705J1A) with a LCD and some keys has been added. The assembler program allows modification of the frequency, the phase as well as the amplitude of each output.

### D. Electronic circuits

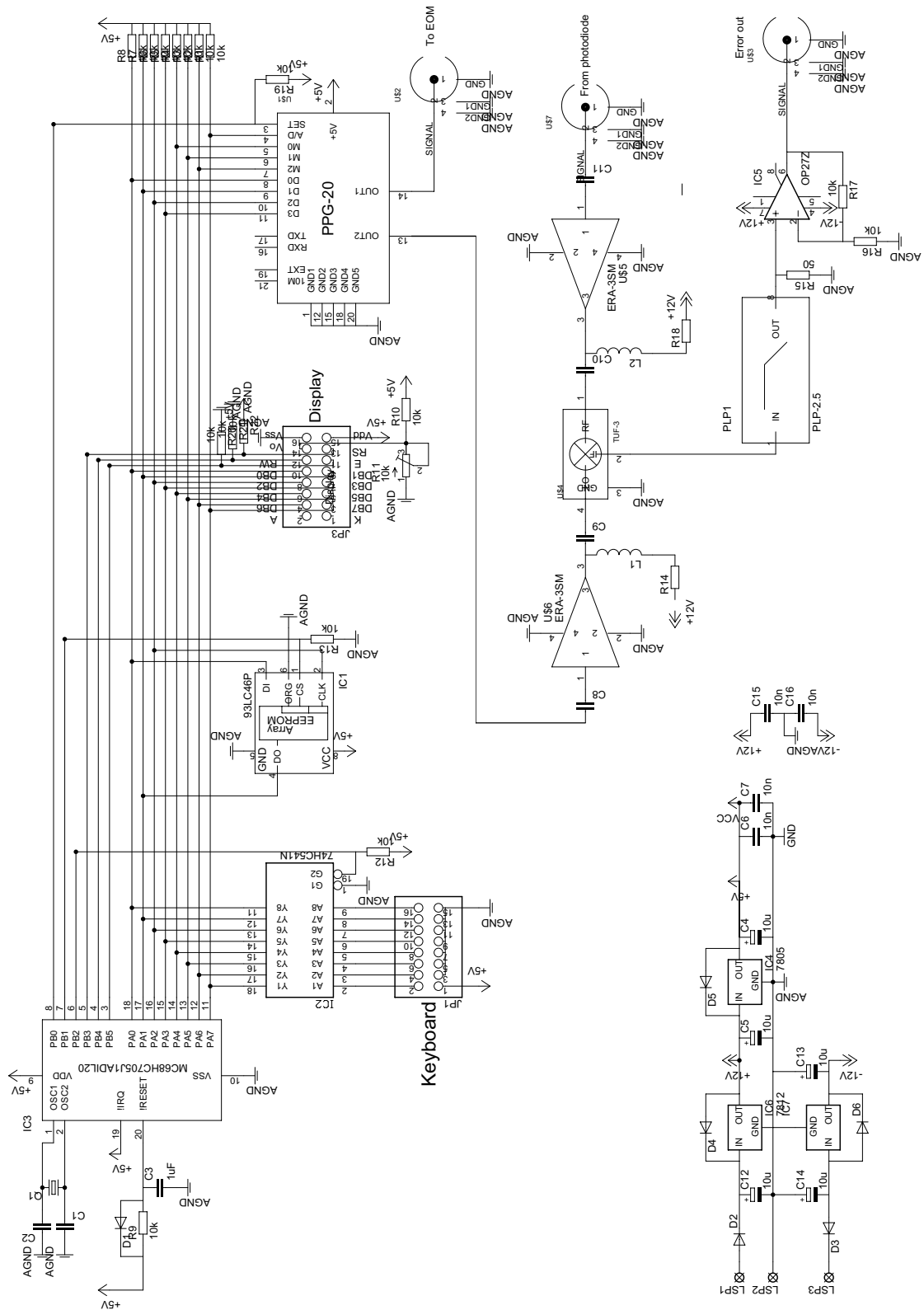


Figure D.12.: Schematic of the PPG-20 board.

## D.4. 100 to 10 MHz

Because the frequency reference of the Raman system is the best reference available in the experiment, it would be logical to use it as the reference for all devices. Unfortunately most commercial devices like synthesizers and spectrum analyzers can only make use of a 10 MHz reference signal, but not a 100 MHz signal. The reference on the other hand only outputs 100 MHz, the internal 10 MHz is not output.

To make a 10 MHz signal out of the 100 MHz a circuit has been designed that first converts the 100 MHz sine wave in TTL signal, which then feeds the CPLD (Altera EPM7032SLC-10) which has been programmed with a numeric controlled oscillator with a fixed frequency of 1/10th of the reference. Its output feeds a rudimentary DAC made of 4 resistors with the ratio 1:2:4:8 and some fast operational amplifiers as output buffer to create 4 sine wave outputs, as well as 2 TTL outputs at 10 MHz. The remaining space in the CPLD has been used to create a 24 stage ripple divider to get a 0.6 Hz signal for a LED to signal correct operation.

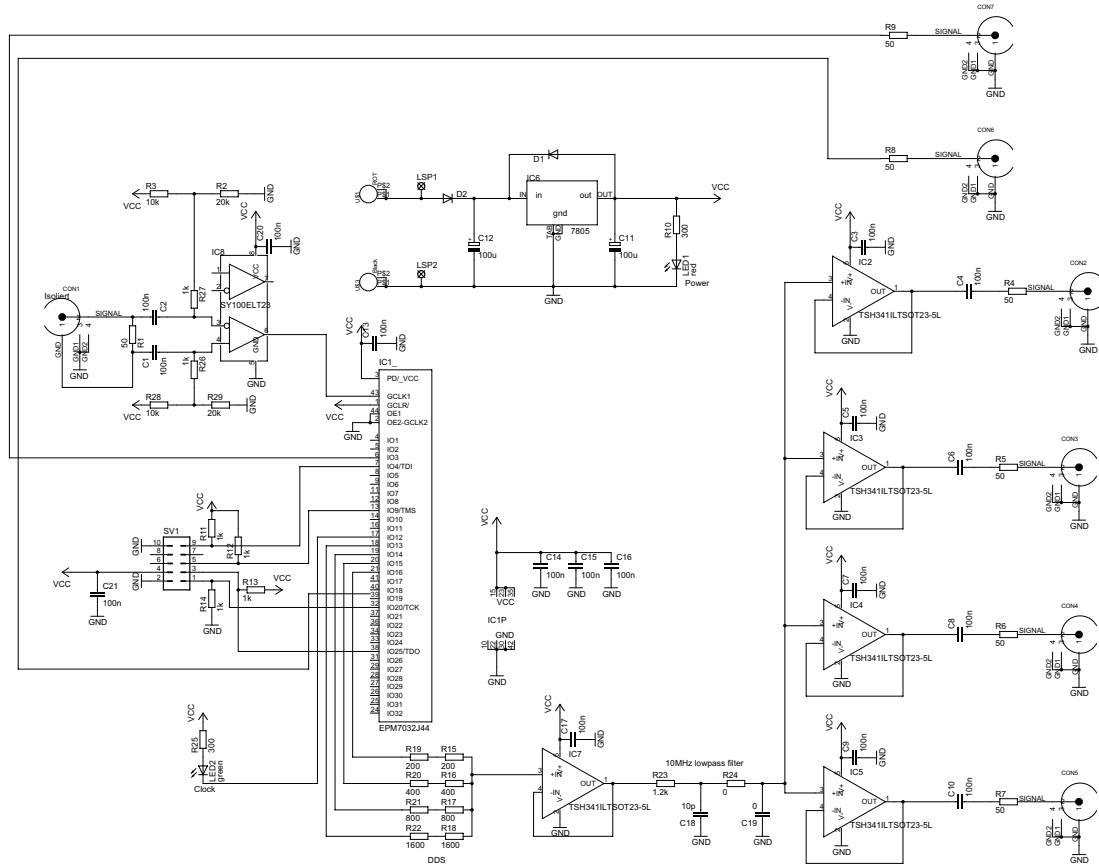


Figure D.13.: Schematic of the 100 to 10 MHz frequency divider.

Listing D.2: Source code of CPLD

———— *top level design* ————

#### D. Electronic circuits

```
2
— Input is 100 MHz
4 — output is (A,B,C,D) as 10 MHz sine wave
— and LED is  $10\text{MHz}/2^{24} = 0.596 \text{ Hz TTL}$ 
6
— Pins
8 — A,B,C,D are fast slewrate output
— LED is slow slewrate output
10 — Macrocells
— DDS10 are turbo speed
12 — MyFreqDiv are normal slow speed
— tco=10ns
14 — Clock=100MHz

16 — note: in simulation the clock must start with 10ns delay

18 function DDS10(clock) returns (A,B,C,D);
function MyFreqDiv(in) with (width) returns (out);
20
subdesign FreqDiv100To10
22 (
    clock : input;
24 A,B,C,D : output;
    led : output;
26 TTL1,TTL2 : output;
)
28 variable
    dds : DDS10;
30 FD : MyFreqDiv with (width=24);
begin
32 dds.clock=clock;
    A=dds.A;
34 B=dds.B;
    C=dds.C;
36 D=dds.D;
    fd.in=dds.A;
38 led=fd.out;
    TTL1=A;
40 TTL2=A;
end;

1 ————— subdesign —————

3 — simple frequency divider
—
```

## D. Electronic circuits

- 5 — *The timing analyzer does not like this ripple clock.*
- *It has a huge skew of almost 200ns when using 24 stages.*
- 7 — *(455ns for 24 stages without 'turbo bit')*
- *As it is only for a LED, ignore the analyzer.*
- 9 — *Do not use this design for any further signal processing.*

```
11 parameters
   (
13   width = 2
   );
15 subdesign MyFreqDiv
   (
17   in : input;
     out : output;
19 )
   variable
21   d[width-1..0] : dff;
   begin
23   d[].d=!d[].q;
     d[0].clk=in;
25   for i in 1 to width-1 generate
     d[i].clk=d[i-1].q;
27   end generate;
     out=d[width-1].q;
29 end;

1  ————— subdesign —————

3  — compile with
   — tco=10ns
5  — state machine encoding=user-encoded

7 subdesign DDS10
   (
9   clock : input;
     A,B,C,D : output;
11 )
   variable
13   ss : machine of bits (A,B,C,D,E) with states
     (s0=B"00000", — 0
15     s1=B"00010", — 1
     s2=B"01010", — 5
17     s3=B"10100", — 10
     s4=B"11100", — 14
19     s5=B"11111", — 15
```

*D. Electronic circuits*

```

21         s6=B"11101", — 14
           s7=B"10101", — 10
           s8=B"01011", — 5
23         s9=B"00011"); — 1
begin
25     ss.clk=clock;
table
27     ss => ss;
           s0 => s1;
29     s1 => s2;
           s2 => s3;
31     s3 => s4;
           s4 => s5;
33     s5 => s6;
           s6 => s7;
35     s7 => s8;
           s8 => s9;
37     s9 => s0;
end table;
39 end;
```

## D.5. 100 to 400 MHz

This circuit uses two frequency doublers to obtain the fourth harmonic of the input. Optionally it can also use an internal 100 MHz oscillator. Besides the 13 outputs at 400 MHz it also outputs the 100 MHz it uses as reference as well as the 200 MHz intermediate.

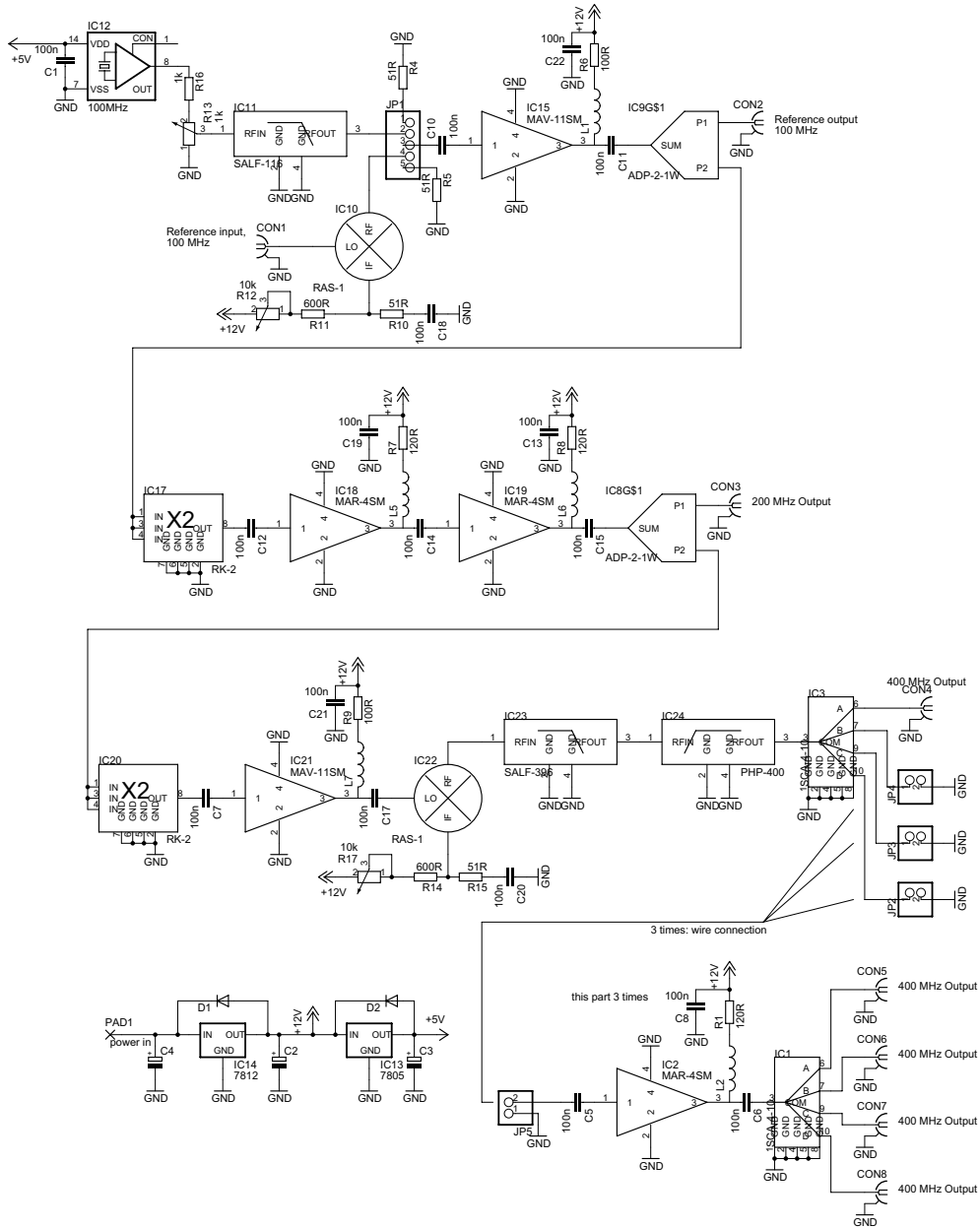


Figure D.14.: Schematic of the 100 to 400 MHz chain.



## D.6. FreqGenFix and FreqGenFix2

This circuit uses an ADF4002 (Analog Devices) to phase lock a VCO to an external reference frequency ( $F_{ref}$ ).

The VCO frequency  $F_{vco}$  is given by:

$$F_{vco} = F_{ref} \frac{p}{q} \quad (D.1)$$

where  $p$  is an integer between 1 and 8191 and  $q$  is between 1 and 16383. For a fixed frequency reference the  $q$  parameter is often set to make  $F_{ref}/q$  1 MHz which makes  $p$  the output frequency in MHz. The  $p$  and  $q$  values should be chosen small though, so that the phase comparator frequency remains high and does not limit the feedback bandwidth.

The single channel device also has the ability to change the output power via the front panel in 0.5 dB steps between 0 and -31.5 dBm. The dual channel device has one potentiometer for the power for each channel, and an additional board to switch between the two channels under external control.

For the operation of the ADF4002 it is necessary to use a small computer to supply it with about 100 bits of information it needs. This is solved by using a Conrad C-Control II microcontroller which is a system complete with display, keyboard, processor and an extension bus. The board with the ADF4002 and the VCO connect to this bus.

Of the two frequency generator boards of the dual channel device one is identical with the board of the single channel device, the other only differs in its connection to the microcontroller.

## D. Electronic circuits

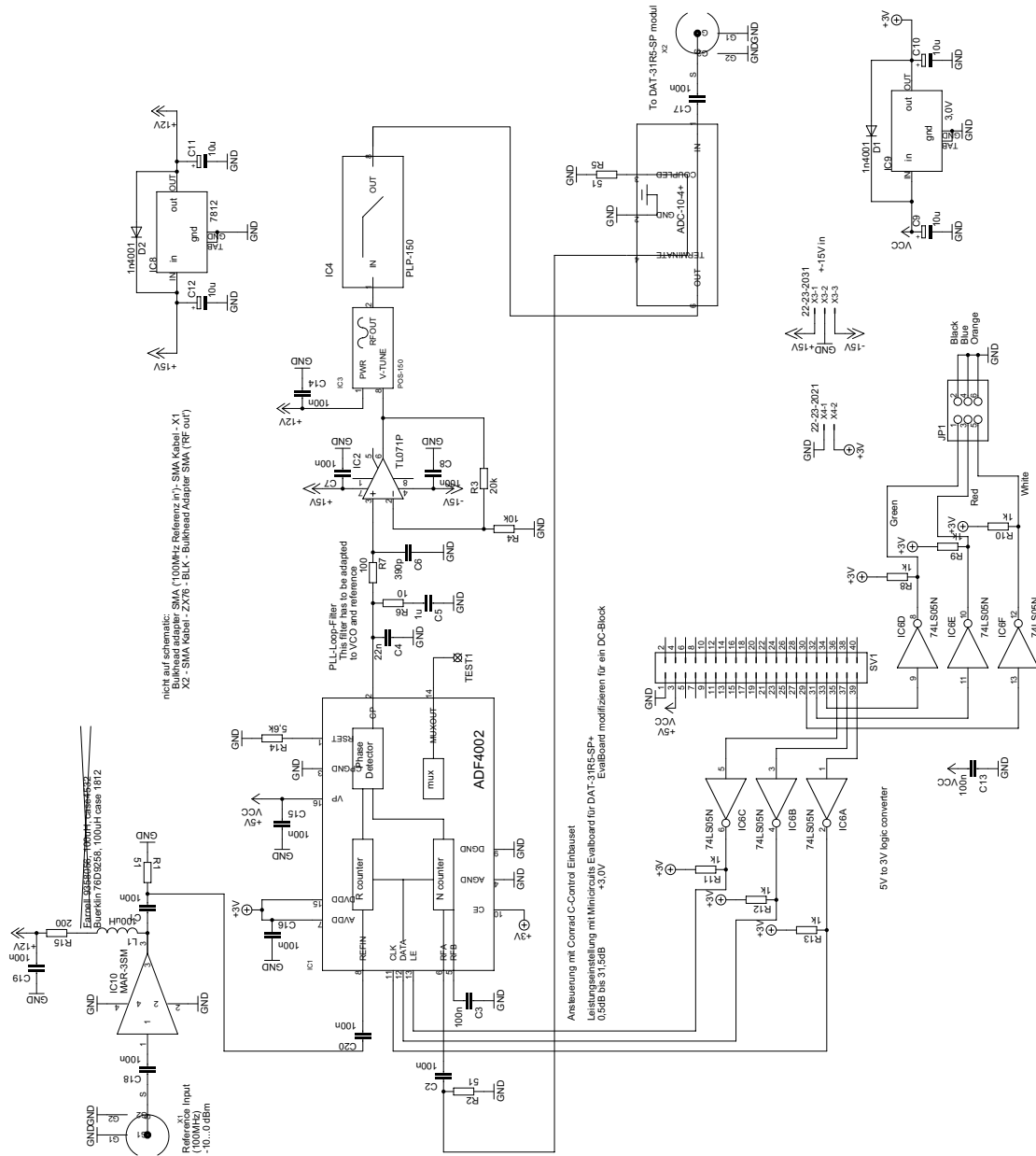


Figure D.15.: Schematic of the ADF4002 board to phase lock a VCO to an external reference.

### D. Electronic circuits

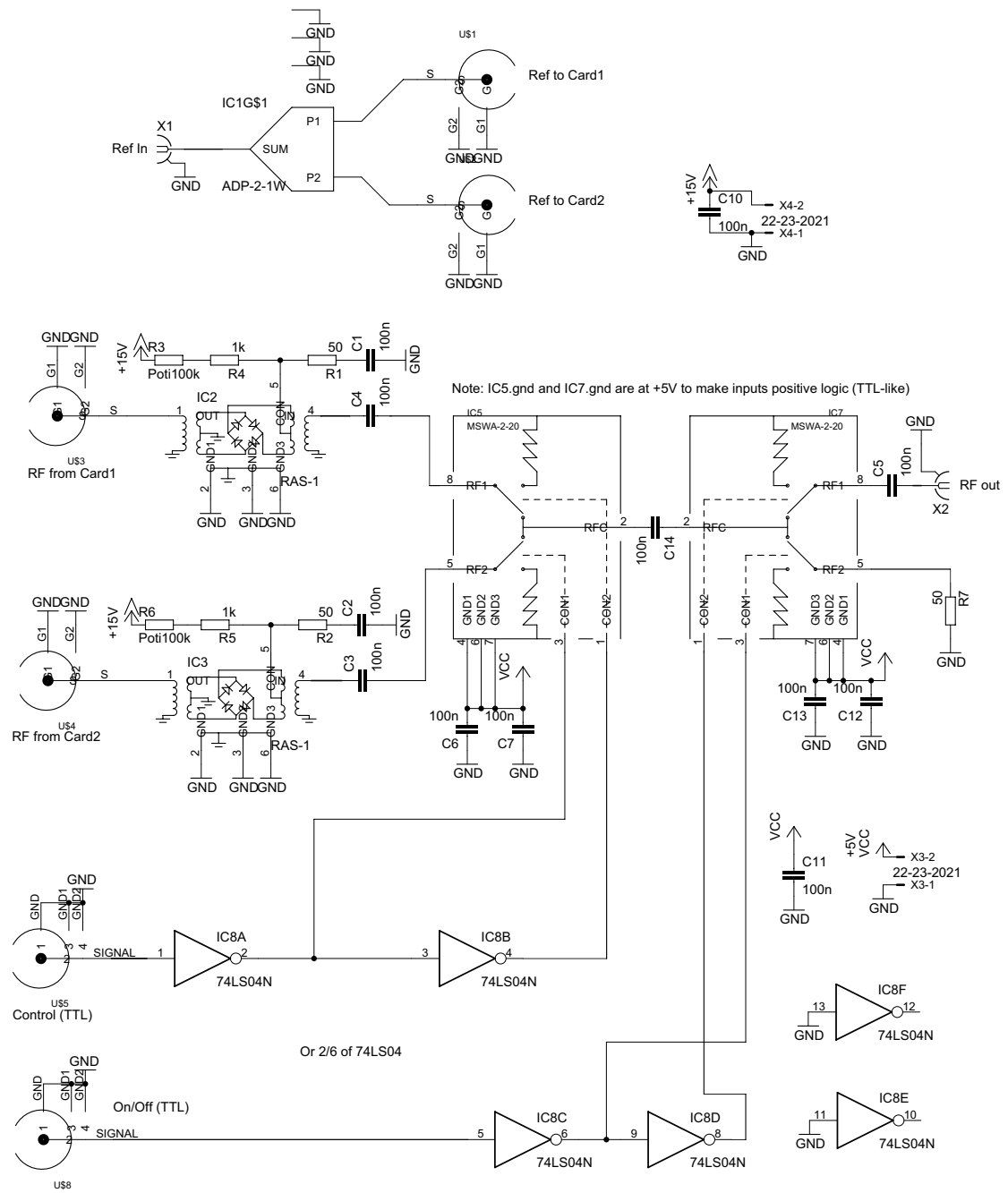


Figure D.16.: Schematic of the combiner board to switch between two ADF4002 signals.



## D.8. PLL\_Beat

The circuit is similar to the FreqGenFix (appendix D.6) with the difference that the VCO is an external beat between two lasers, and the circuit has an additional divider to extend the input range of the beat frequency to 800 MHz.

The software allows to change the parameters of the dividers ( $p=1\dots 8191$ ,  $q=1\dots 16383$ ), as well as the gain and the sign of the output . The beat frequency is given by:

$$F_{beat} = F_{ref} \frac{2p}{q} \quad (\text{D.2})$$

Table D.1.: Key parameters of the ADF4002 phase lock circuit.

Parameter	value	unit
Reference frequency	10...300	MHz
Reference power	-25...+5	dBm
Beat frequency	10...800	MHz
Beat power	-10...+5	dBm

## D. Electronic circuits

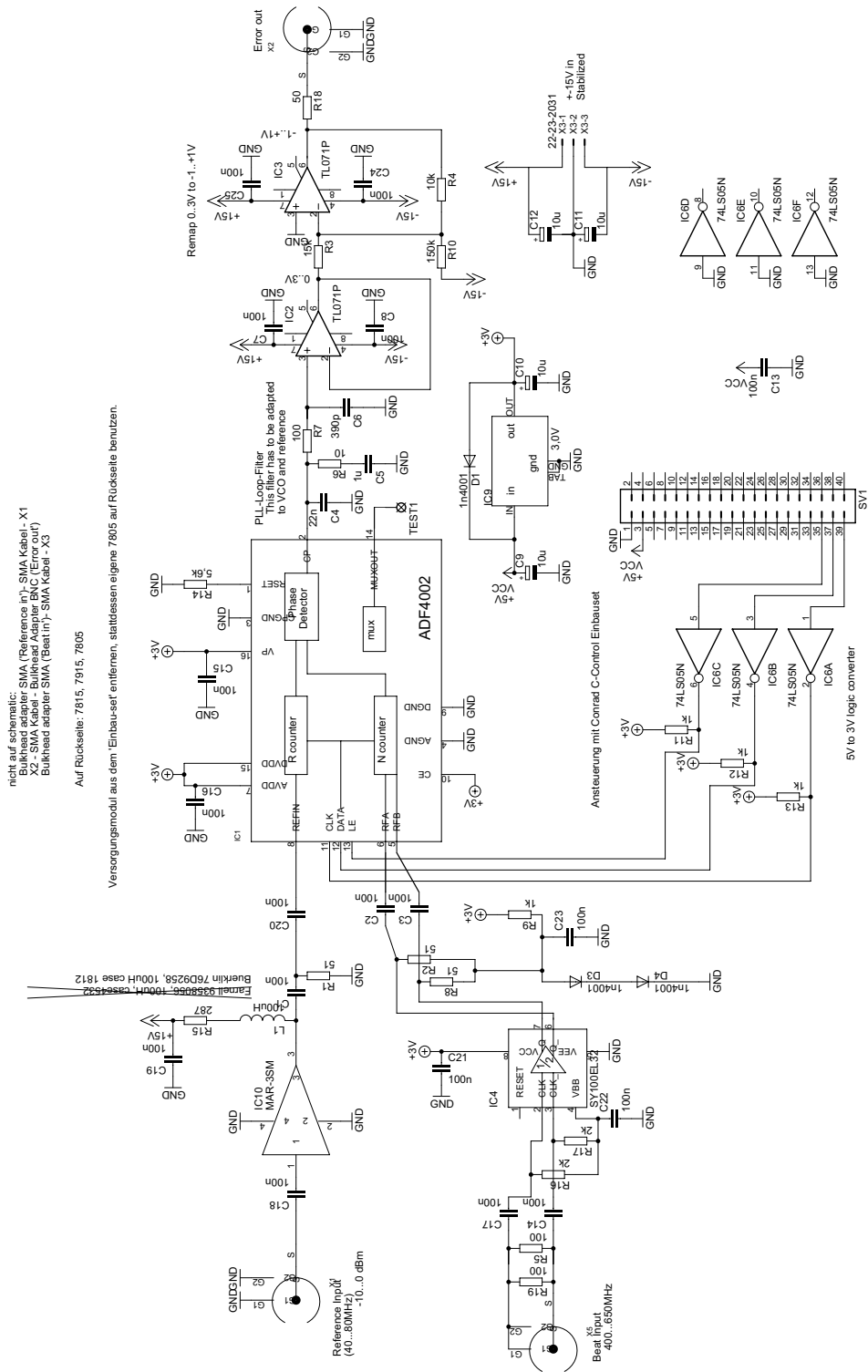


Figure D.18.: Schematic of the ADF4002 board for phase locking an external VCO or laser beat to an external reference frequency.

## D.9. Frequency to Voltage converter

The first part of this frequency to voltage converter has some amplifiers before a frequency divider (U891) with a factor 64, 128 or 256. Then comes the actual frequency to voltage converter that is build around the VFC110 which is limited to 4 MHz. This limits the input frequency to 250, 500, or 1000 MHz depending on the divider setting. The output of the VCF110 is low pass filtered by a UAF42 to about 200 kHz. The output amplifier scales the output to 10 V and adds an external control signal to produce an error signal that is zero at the desired input frequency. The other two op-amps at the output check if the output signal is small and light a LED in red or green, to signal that the system is in lock.

Table D.2.: Key parameters of the frequency to voltage circuit.

Parameter	value	unit
Input frequency (/64, /128, /256)	50...250, 100...500, 200...1000	MHz
Input power	-60...-30	dBm
Output ( $V_{control} = 0$ )	0...10	V

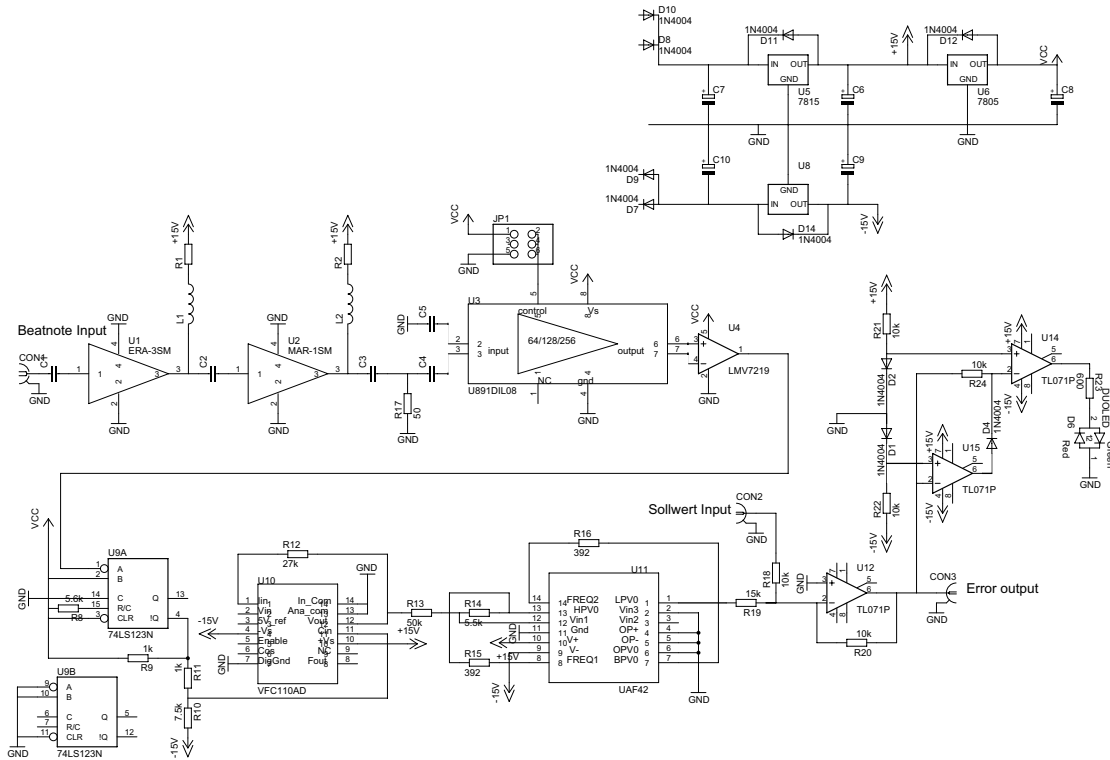


Figure D.19.: Schematic of the frequency to voltage circuit.

## D.10. PID

The proportional-integral-differential controller (PID) consists of 3 major components: an input stage and two generic PID circuits, one optimized for fast current signals and one optimized for slow piezo signals. The PCB with the input stage also contains a triangle oscillator to scan the piezo to find the desired rubidium transition of the laser. The boards are designed to be used in series: first input stage, then the fast PID and finally the slow PID. The fast PID steers the current while trying to keep the input signal small, the slow PID steers the piezo voltage in an attempt to keep the fast PID output small. In this way one has a small amplitude at high speeds, which keeps the noise down and protects the laser diode from any current spikes which could come from spikes in the error signal, and have a large amplitude at much lower speeds keeping the current away from saturation.

The input stage can remove large offsets. It also can change the frequency and amplitude of the scan oscillator. It also has a voltage reference for the generation of offset signals.

The PID module has optional an amplifier/attenuator and an optional inverter. The PID circuit itself is a textbook circuit, with a fixed gain proportional part, because most of the day to day tuning involves correcting the overall gain of the loop, not its frequency dependence. The following two op-amps are a low pass filter for the piezo, the current-PID skips these two.

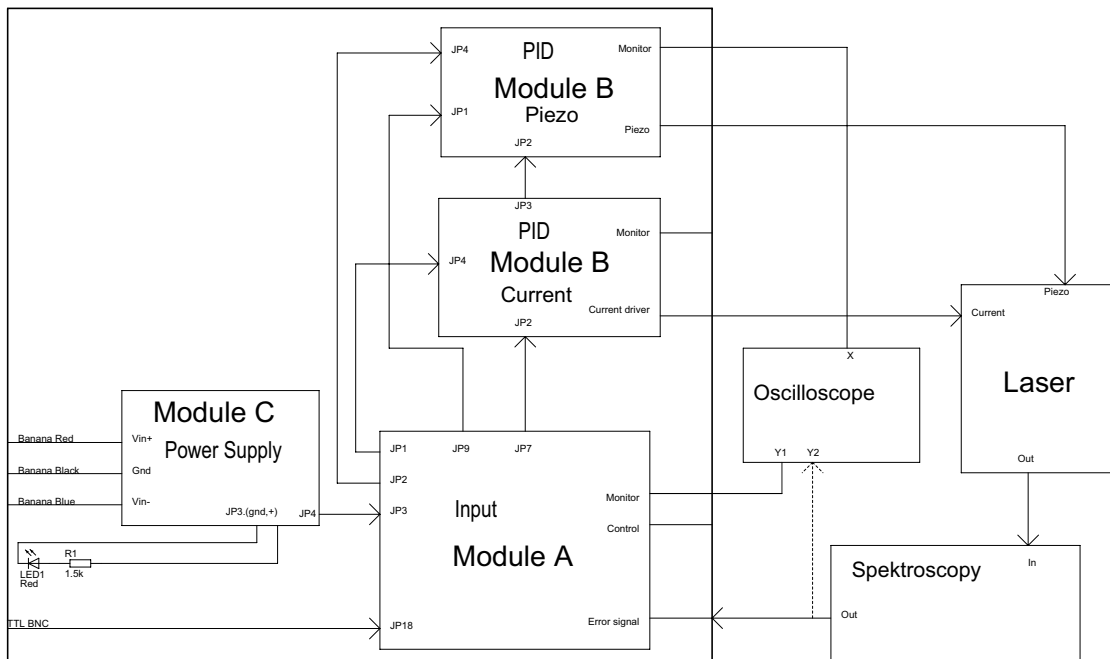


Figure D.20.: Overview of the connections between the various modules of the PID including the typical application in laser stabilization.



### D. Electronic circuits

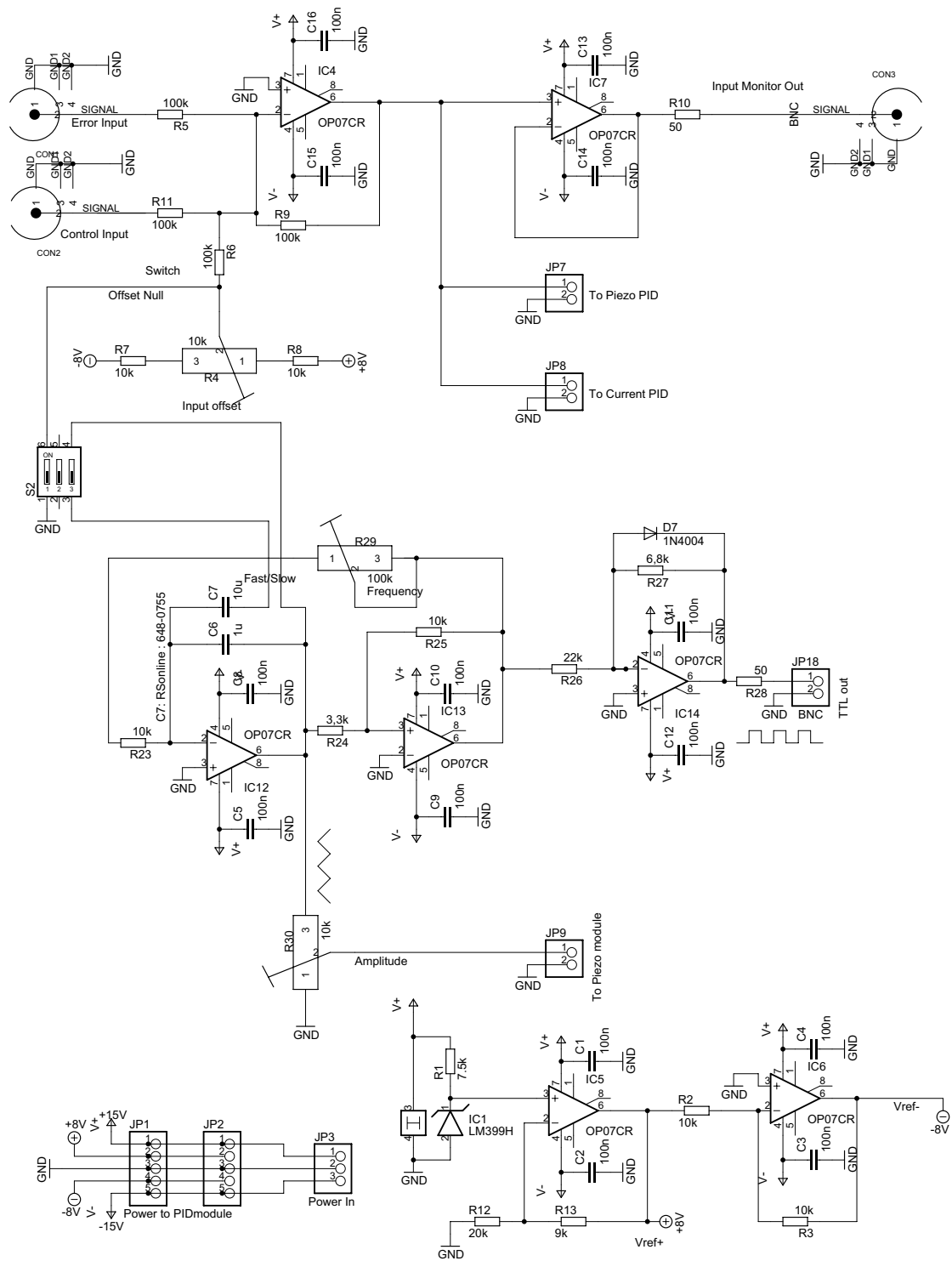


Figure D.21.: Schematic of the input module containing the input with offset correction, scan oscillator and reference voltage.



D. Electronic circuits

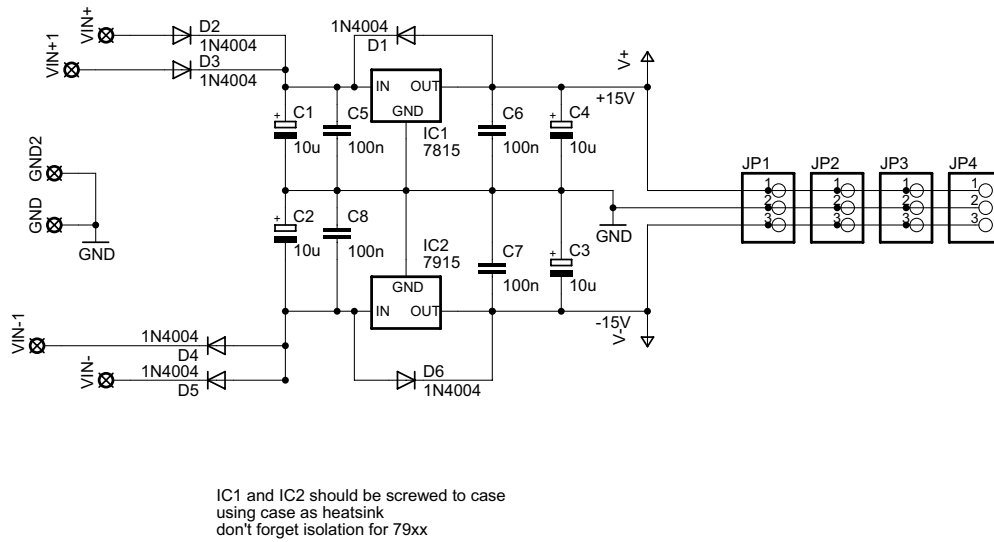


Figure D.23.: Schematic of the power supply section of the PID device.

## D.11. FPGA DAC

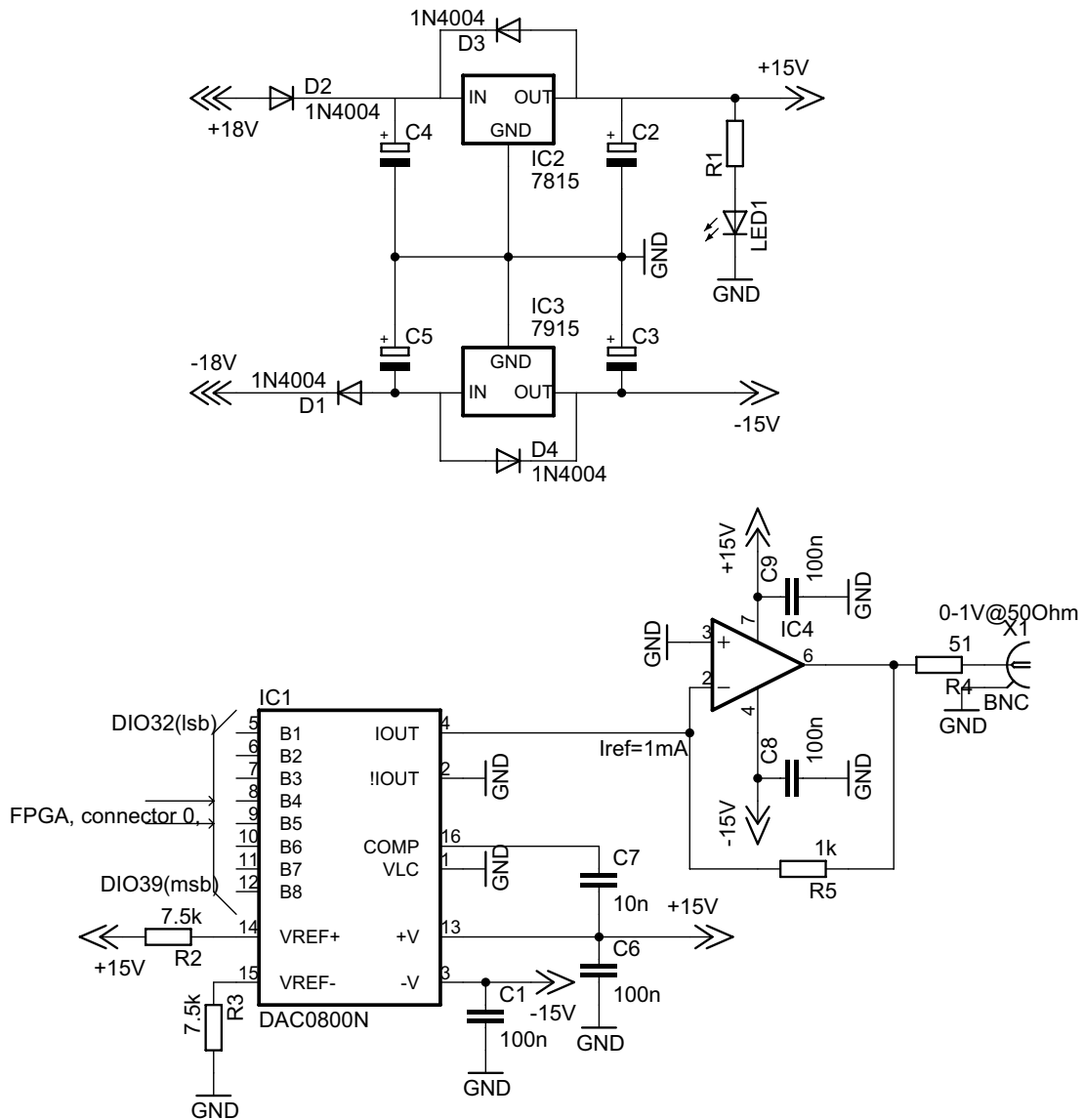


Figure D.24.: The 8 bit DAC of the FPGA. The DAC is much faster than needed, even video signals can be (and have been) generated with it, but it was the lowest cost solution.

# D.12. Laser Current Driver

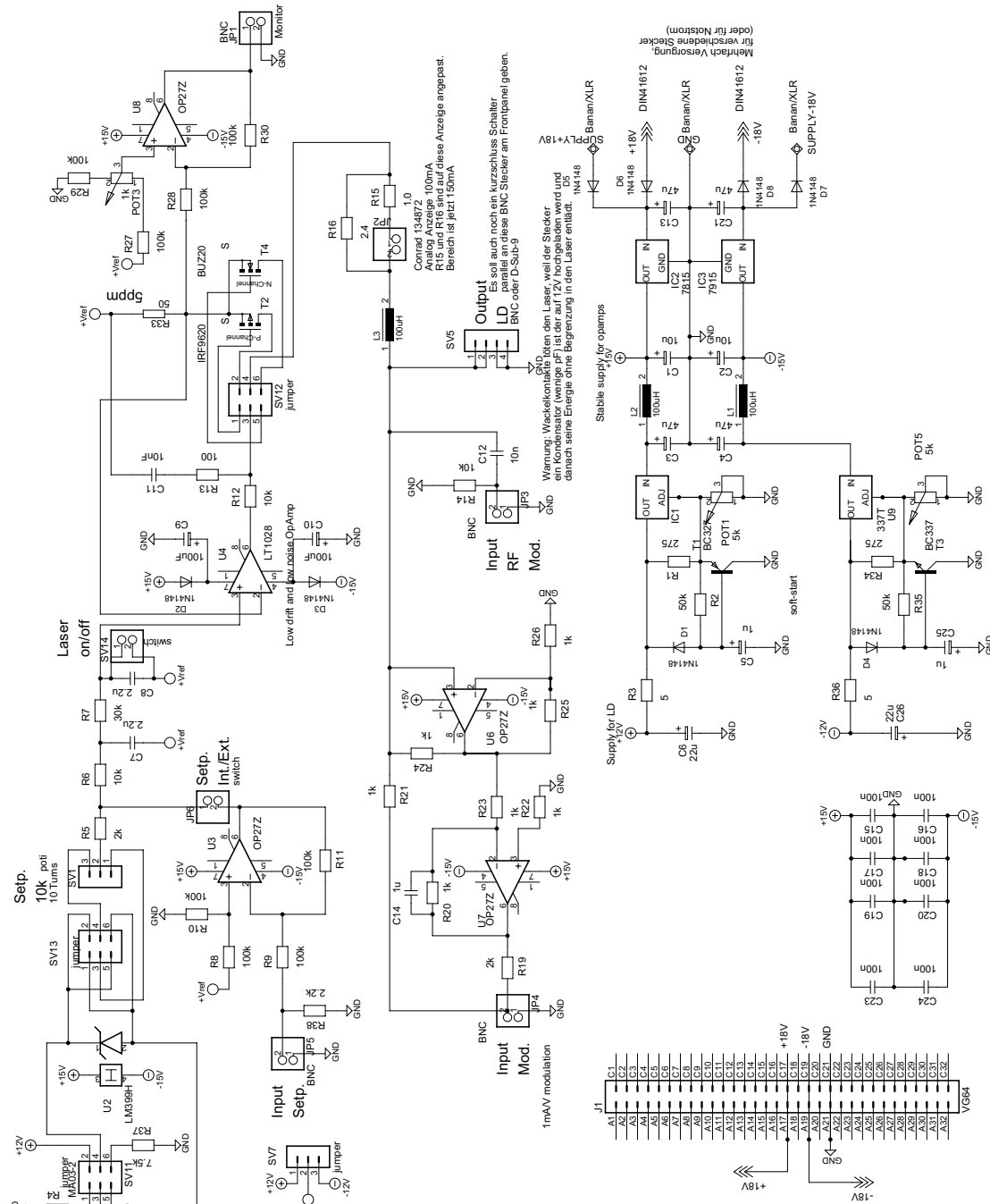


Figure D.25.: Schematic of the laser current driver. This current driver is closely related to [107].

## **D.13. Photodiodes**

There are several types of photodiodes in use, each optimized for its application:

- in the telescopes for optimizing the fiber input couplers,
- spectroscopy for determining the laser frequency
- to detect the atomic state,
- to measure the beat frequency of two lasers.

A summary of all photodiode circuits is given in table D.3.

The photodiodes in the fiber output assemblies for optimizing the fiber input coupler, are large area diodes. They are positioned near the edge of the beams to avoid obstructing the beam itself. The diodes are connected to a switchbox which collects all photodiode signals. From the switchbox the signals are sent to measurement devices, either a passive current measurement gauge with selectable shunt resistor or a transimpedance amplifier with selectable feedback resistor and a gauge (see figure D.26), [or simply a multimeter].

The photodiodes in the spectroscopy are based on large area photodiodes with a transimpedance amplifier with a 10 k $\Omega$  feedback resistor, designed in a compact case, see figure D.27. They are used in combination with a Rubidium vapor cell to manually tune the lasers roughly to the correct wavelength before the actual locking scheme can start.

The photodiode circuit for the MTS has two outputs: one AC coupled output for the modulation signal at 7 MHz, and one DC coupled output (without the modulation signal) for optimizing the optical alignment, see figure D.28.

The photodiodes in the state detection are based on very large area photodiodes with a fast transimpedance amplifier and a second signal amplifier, see figure D.29. Because the first amplifier has a large bias current, the final output has a 2 V offset.

The beat signals around 7 GHz are detected with Hamamatsu G4176-03 photodiodes. These photodiodes have SMA connectors and are biased to about 9 V to enhance the bandwidth.

D. Electronic circuits

Table D.3.: Parameters of photodiodes

Application	Figure	Photodiode	Sensitive area	Bandwidth	Sensitivity
Fiber	D.26	Silonex SLSD-71N2	$5.1 \times 5.1 \text{ mm}^2$	*1	*2
Spectroscopy	D.27	Hamamatsu S2386-44K	$3.6 \times 3.6 \text{ mm}^2$	50 kHz	5 V/mW
MTS	D.28	EG&G Opto- electronics FND-100Q	$\phi 2.5 \text{ mm}$	180 MHz	AC *3: 3.5 V/mW DC *3: 0.25-5.25 V/mW
State detection	D.29	Hamamatsu S5107	$10 \times 10 \text{ mm}^2$	65 kHz	0.085 V/ $\mu\text{W}$
RF, 7 GHz	D.30	Hamamatsu G4176-03	$0.2 \times 0.2 \text{ mm}^2$	11 GHz	$7.4 \frac{\text{mV}_{rf,50\Omega}}{\text{mW}_{Opt}}$
RF, 1 GHz	D.31	Hamamatsu S5973	$\phi 0.2 \text{ mm}$	1000 MHz	$11 \frac{\text{mV}_{rf,50\Omega}}{\text{mW}_{Opt}}$

\*1: Depends on measurement device, typically  $< 1 \text{ kHz}$ .

\*2: Depends on setting of measurement device. The diode itself has a sensitivity of  $0.5 \text{ A/W}$  which has to be multiplied with the feedback resistor of the “CasiMeterPlus”.

\*3: Calculated value.

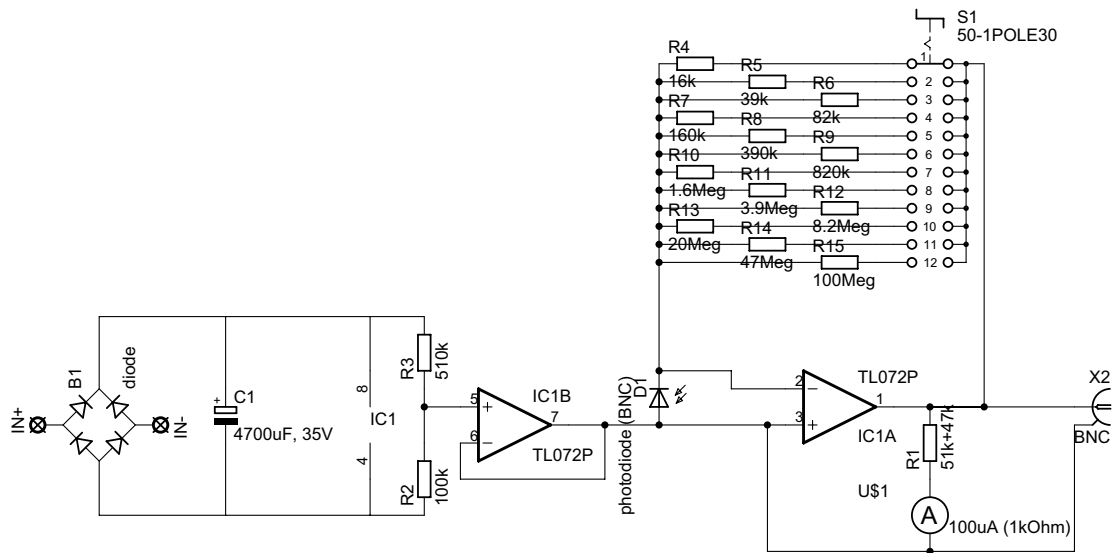


Figure D.26.: “CasiMeterPlus”

D. Electronic circuits

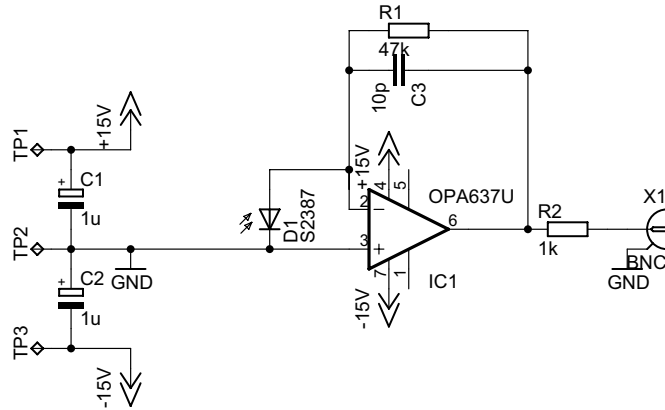


Figure D.27.: Schematic of the photodiode circuit for the spectroscopy with vapor cell.

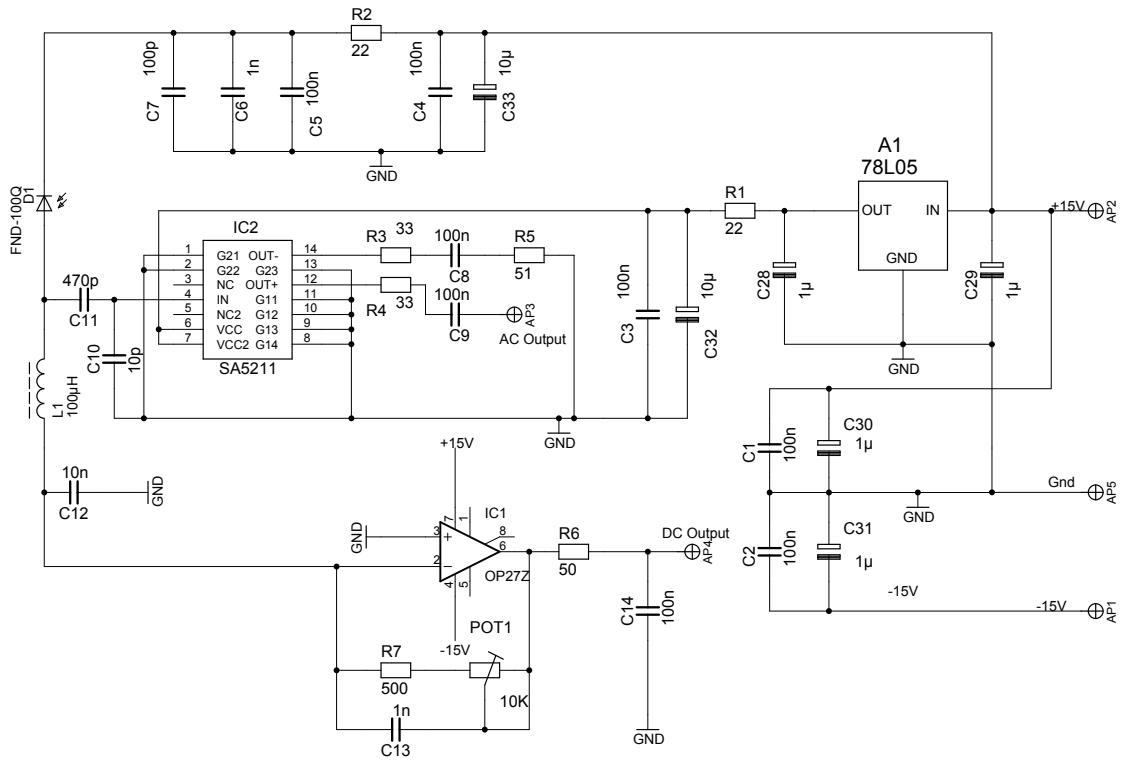


Figure D.28.: Schematic of the circuit for the photodiode of the MTS.



### D. Electronic circuits

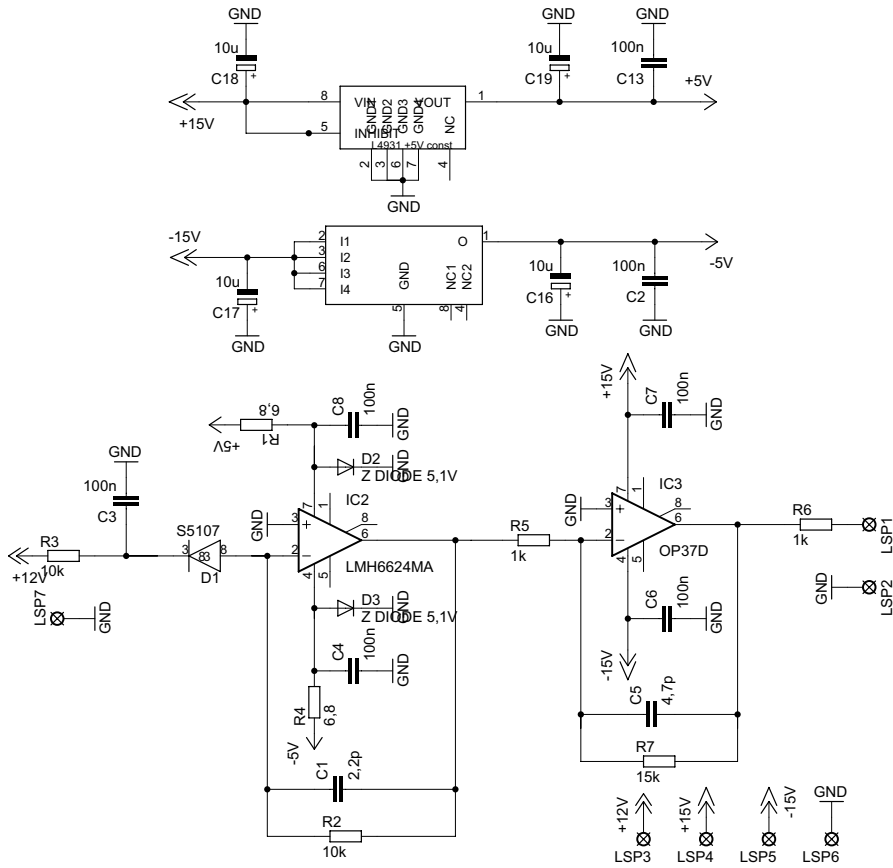


Figure D.29.: Schematic of the circuit for the state detection photodiode.

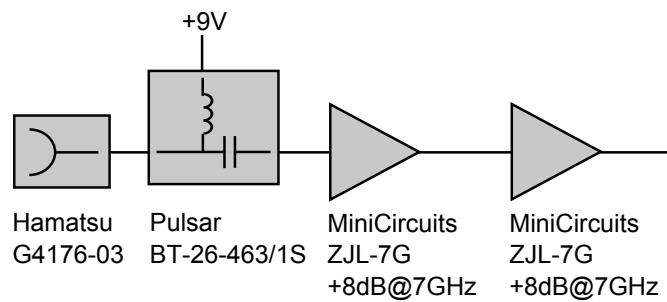


Figure D.30.: Schematic of the circuit for the detection of beat frequencies at about 7 GHz. The components are modules that connect directly with SMA connectors.

D. Electronic circuits

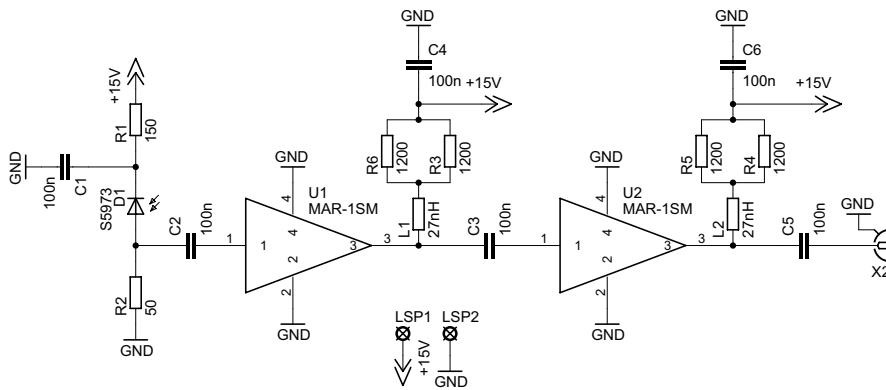


Figure D.31.: Schematic of the photodiode circuit for receiving beat frequencies up to 1 GHz.

# E. Source code

## E.1. Bias coil optimization

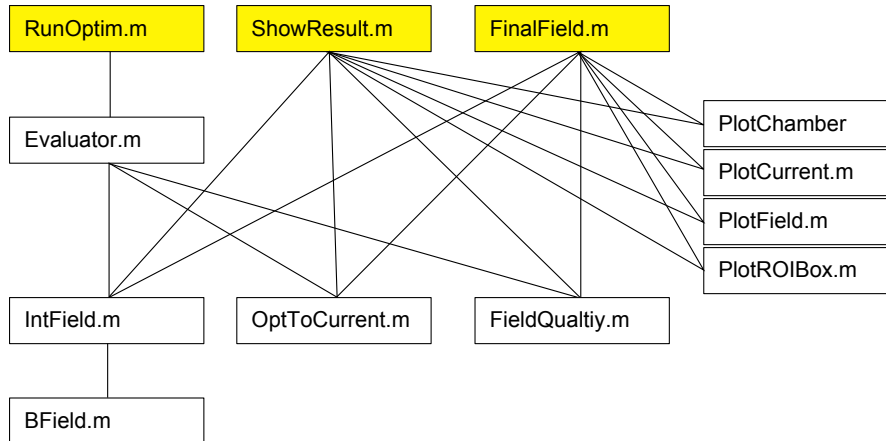


Figure E.1.: An overview of the various files for the bias coil optimization. The top line are the main files, the lower boxes are the subprograms and the lines between them indicate who calls which subprograms.

Listing E.1: FinalField.m: Simulation of the final choosen magnetic bias field.

```

1 % FinalField
2
3 % Directions:
4 % x : sideways, in the direction of the laser beams
5 % y : vertical, in the direction of gravity
6 % z : length wise, in the direction of the atoms
7
8 %----- init current -----
9 current=OptToCurrent( [ -0.005 -0.001 0 -0.006 -0.015 ...
10    -0.015 -0.015 -0.015 -0.015 -0.015 -0.0075 ]);
11
12 %----- init measurement positions -----
13 roiX=0.010;%region of interest, in mm
14 roiY=0.020;
15 roiZ=0.272-0.020;
16 [x,y,z]=meshgrid(-roiX/2:roiX/4:roiX/2, ...
17    -roiY/2:roiY/4:roiY/2, ...
18    -roiZ/2:roiZ/20:roiZ/2);

```

## E. Source code

```

p=[ reshape(x,prod(size(x)),1),...
20  reshape(y,prod(size(y)),1),...
  reshape(z,prod(size(z)),1)];
22
%----- calculate field -----
24 for i=1:size(p,1)
    f(i,:)=IntField(reshape(p(i,:),3,1),current)';
26 end

28 % deviation of field from mean, abs(B-Bmean)
  [quality,avg,dev]=FieldQuality(p,f);
30
%----- field in roi box -----
32 figure
  subplot(2,2,1);
34 dev=reshape(dev, size(z));
  slice(x,y,z,dev,[-roiX/2,roiX/2],[-roiY/2,roiY/2],[-roiZ/2,roiZ/2] );
36 h=findobj(gca,'FaceColor','flat');
  set(h,'FaceColor','interp');
38 axis equal
  view(26,58);
40 camup([0,1,0]);
  colorbar
42 colormap(mycolorbar)
  title 'Deviation'
44
  subplot(2,2,2);
46 v=reshape(f(:,1), size(z));
  slice(x,y,z,v,[-roiX/2,roiX/2],[-roiY/2,roiY/2],[-roiZ/2,roiZ/2] );
48 h=findobj(gca,'FaceColor','flat');
  set(h,'FaceColor','interp');
50 axis equal
  view(26,58);
52 camup([0,1,0]);
  colorbar
54 colormap jet
  title 'Xlaser'
56
  subplot(2,2,3);
58 v=reshape(f(:,2), size(z));
  slice(x,y,z,v,[-roiX/2,roiX/2],[-roiY/2,roiY/2],[-roiZ/2,roiZ/2] );
60 h=findobj(gca,'FaceColor','flat');
  set(h,'FaceColor','interp');
62 axis equal
  view(26,58);
64 camup([0,1,0]);
  colormap jet
66 colorbar

```

## E. Source code

```

title 'Y-(-gravity)'
68
subplot(2,2,4);
70 v=reshape(f(:,3) ,size(z));
   slice(x,y,z,v,[-roiX/2,roiX/2],[-roiY/2,roiY/2],[-roiZ/2,roiZ/2] );
72 h=findobj(gca, 'FaceColor', 'flat');
   set(h, 'FaceColor', 'interp');
74 axis equal
   view(26,58);
76 camup([0,1,0]);
   colormap jet
78 colorbar
   title 'Z-(atom)'

```

Listing E.2: OptToCurrent.m

```

1 function [ current ] = OptToCurrent( v )
   %OPTTOCURRENT Summary of this function goes here
3 % converts a set of 11 parameters in v to 2x60 elements in current

5 % Directions:
   % x : sideways, in the direction of the laser beams
7 % y : vertical, in the direction of gravity
   % z : length wise, in the direction of the atoms
9
   current=zeros(2,60,3);
11 xSize=0.065+0.010; %(size of interferometer chamber)
   ySize=0.070; %+0.030;
13 zSize=0.272;
   for i=0:19
15     current(1,0+i+1,:)= [+xSize/2,-ySize/2,-(zSize/2)+i*zSize/20];
   end
17 for i=0:9
     current(1,20+i+1,:)= [+xSize/2,-ySize/2+i*ySize/10,+(zSize/2)];
19 end
   for i=0:19
21     current(1,30+i+1,:)= [+xSize/2,+ySize/2,+(zSize/2)-i*zSize/20];
   end
23 for i=0:9
     current(1,50+i+1,:)= [+xSize/2,+ySize/2-i*ySize/10,-(zSize/2)];
25 end

27 for i=1:11 %11
     current(1,0+i,2)=current(1,0+i,2)+v(i);
29     current(1,22-i,2)=current(1,22-i,2)+v(i);
     current(1,30+i,2)=current(1,30+i,2)-v(i);
31     current(1,52-i,2)=current(1,52-i,2)-v(i);
   end
33

```

## E. Source code

```

current(1, :, 1) = current(1, :, 1); % +v(12);
35 current(2, :, :) = current(1, :, :);
current(2, :, 1) = -current(1, :, 1);

```

### Listing E.3: IntField.m

```

function [ field ] = IntField( position , list )
2 %function [ field ] = IntField( position , list )
  % position : position to be calculated
4 % list : array(1..number of wires, 1..number of wire points, x y z)

6 % vectorised for speed
  field = position * 0;
8 for i = 1 : size(list, 1)
    L1 = list(i, 1:end, 1:3);
10    L2 = [list(i, 2:end, 1:3) list(i, 1, 1:3)];
    L1 = reshape(L1, prod(size(L1))/3, 3);
12    L2 = reshape(L2, prod(size(L2))/3, 3);
    f = BField(position, L1, L2);
14    field = field + sum(f, 2);
end

```

### Listing E.4: BField.m

```

1 function [ field ] = BField( pos , cur1, cur2 )
  % function [ field ] = BField( pos , cur1, cur2 )
3 % pos : position to be calculated [i, xyz]
  % cur1, cur2 : current flowing from point cur1 to cur2 [i, xyz]
5 %
  % r = pos - cur1;
7 % dl = cur2 - cur1;
  % field = cross(dl, r) / (sum(r.*r)^1.5);
9 % (mu0*I/4Pi is set to 1;
  % true value is I*10^-7 [Tesla] or I*10^-3 [Gauss])
11 % (==> unit of outcome is 'mGauss per Ampere')

13 % (vectorised for speed)
  pos = pos * ones(1, prod(size(cur1))/3);
15 PC = cur1' - pos;
  CD = cur2' - cur1';
17 PD = cur2' - pos;
  cr = -cross(CD, PC);
19 field = ( (dot(PC, CD) ./ sqrt(dot(PC, PC))) - ...
            (dot(PD, CD) ./ sqrt(dot(PD, PD))) ) ./ (dot(cr, cr));
21 field = cr .* (ones(3, 1) * field);

```

### Listing E.5: FieldQuality.m

```

1 function [ quality , avg , dev ] = FieldQuality( position , field )
  %FIELDQUALITY evaluates the quality of the magnetic field

```

## E. Source code

```

3 %
  % position : list of x,y,z coordinates where field was evaluated [(:,3)]
5 % field : list of magnetic field vectors [(:,3)]
  % dev : length of (field - field_avgerage)
7 % quality : value indicating the quality of the field,
  %           (lower is better), typically: normalised mean of
9 %           absolute value of deviation from mean field

11 avg=mean(field);
  dev=zeros(size(field,1),1);
13 for i=1:size(field,1)
      dev(i)=sqrt( sum( (field(i,:) - avg).^2 ) );
15 end

17 q=[ max(dev)/sqrt(sum(avg.^2)), mean(dev)/sqrt(sum(avg.^2))];
  quality=q(2);

```

### Listing E.6: PlotCurrent.m

```

function [ ] = PlotCurrent( list )
2 %PLOTCURRENT Summary of this function goes here
  % Detailed explanation goes here
4 % list : array(1..number of wires,1..number of wire points, x y z)

6 hold on
  for i=1 : size(list,1)
8     plot3(list(i,:,1),list(i,:,2),list(i,:,3),'-xk','LineWidth',2);
      plot3([list(i,end,1),list(i,1,1)],...
10          [list(i,end,2),list(i,1,2)],...
            [list(i,end,3),list(i,1,3)],'-xk','LineWidth',2);
12 end

```

### Listing E.7: PlotField.m

```

function [ ] = PlotField( position, field )
2 %PLOTFIELD Summary of this function goes here
  % Detailed explanation goes here
4
  L=sum(field.^2,2);
6 field=0.3*field/sqrt(max(L));
  for i=1:size(position,1)
8     plot3(position(i,1),position(i,2),position(i,3),'.'');
      plot3([position(i,1),position(i,1)+field(i,1)*0.1],...
10          [position(i,2),position(i,2)+field(i,2)*0.1],...
            [position(i,3),position(i,3)+field(i,3)*0.1]);
12 end

```

### Listing E.8: PlotROIbox.m

```

function [ ] = PlotROIbox( )

```

## E. Source code

```

2 %PLOTROIBOX
   roiX=0.010;%region of interest
4  roiY=0.020;
   roiZ=0.252;
6  plot3([-roiX/2,+roiX/2,+roiX/2,-roiX/2,-roiX/2],...
        [-roiY/2,-roiY/2,+roiY/2,+roiY/2,-roiY/2],...
8        [-roiZ/2,-roiZ/2,-roiZ/2,-roiZ/2,-roiZ/2], 'g—');
   plot3([-roiX/2,+roiX/2,+roiX/2,-roiX/2,-roiX/2],...
10        [-roiY/2,-roiY/2,+roiY/2,+roiY/2,-roiY/2],...
        [+roiZ/2,+roiZ/2,+roiZ/2,+roiZ/2,+roiZ/2], 'g—');
12 plot3([-roiX/2,-roiX/2],[-roiY/2,-roiY/2],[-roiZ/2,+roiZ/2], 'g—');
   plot3([+roiX/2,+roiX/2],[-roiY/2,-roiY/2],[-roiZ/2,+roiZ/2], 'g—');
14 plot3([+roiX/2,+roiX/2],[+roiY/2,+roiY/2],[-roiZ/2,+roiZ/2], 'g—');
   plot3([-roiX/2,-roiX/2],[+roiY/2,+roiY/2],[-roiZ/2,+roiZ/2], 'g—');

```

Listing E.9: PlotChamber.m

```

1 function [ ] = PlotChamber( )
   %PLOTCHAMBER draws the central interferometer chamber
3
   % Directions:
5 % x : sideways, in the direction of the laser beams
   % y : vertical, in the direction of gravity
7 % z : length wise, in the direction of the atoms

9 z=[-136,-90,-90, 90, 90,136,136,-136]/1000;
   y=[ -91,-91,-35,-35,-91,-91, 35, 35]/1000;
11 for i=1:length(z)
       plot3([0.032,-0.032],[y(i),y(i)],[z(i),z(i)], 'm');
13 end
   y=[y,y(1)];
15 z=[z,z(1)];
       plot3(0.032*ones(1,length(z)),y,z, 'm');
17 plot3(-0.032*ones(1,length(z)),y,z, 'm');

19 Circle([ 0.032,0,0],0.040/2); % middle main window
   Circle([-0.032,0,0],0.040/2);

21 Circle([ 0.032,0,0.065],0.040/2);
23 Circle([-0.032,0,0.065],0.040/2);

25 Circle([ 0.032,0,-0.065],0.040/2);
   Circle([-0.032,0,-0.065],0.040/2);

27 Circle([ 0.032,-0.004, 0.1128],0.030/2); % preparation and
29 Circle([-0.032,-0.004, 0.1128],0.030/2); % detection window

31 Circle([ 0.032,-0.004,-0.1128],0.030/2);
   Circle([-0.032,-0.004,-0.1128],0.030/2);

```



## E. Source code

```

33 Circle ([ 0.032, -0.060, 0.113], 0.028/2); % pump hole
35 Circle ([ -0.032, -0.060, 0.113], 0.028/2);
   Circle ([ 0.032, -0.060, -0.113], 0.028/2);
37 Circle ([ -0.032, -0.060, -0.113], 0.028/2);
   Circle ([ 0.032, -0.060, 0.113], 0.050/2); % pump flange
39 Circle ([ -0.032, -0.060, 0.113], 0.050/2);
   Circle ([ 0.032, -0.060, -0.113], 0.050/2);
41 Circle ([ -0.032, -0.060, -0.113], 0.050/2);
   Circle ([ 0.032+0.013, -0.060, 0.113], 0.050/2);
43 Circle ([ 0.032+0.013, -0.060, -0.113], 0.050/2);

45 Circle ([ 0.032, +0.023, 0.031], 0.0015/2); % some screw holes
   Circle ([ -0.032, +0.023, 0.031], 0.0015/2);
47 Circle ([ 0.032, +0.023, -0.031], 0.0015/2);
   Circle ([ -0.032, +0.023, -0.031], 0.0015/2);
49 Circle ([ 0.032, +0.023, 0.091], 0.0015/2); % some screw holes
   Circle ([ -0.032, +0.023, 0.091], 0.0015/2);
51 Circle ([ 0.032, +0.023, -0.091], 0.0015/2);
   Circle ([ -0.032, +0.023, -0.091], 0.0015/2);
53 Circle ([ 0.032, +0.023, 0.1047], 0.0015/2); % some screw holes
   Circle ([ -0.032, +0.023, 0.1047], 0.0015/2);
55 Circle ([ 0.032, +0.023, -0.1047], 0.0015/2);
   Circle ([ -0.032, +0.023, -0.1047], 0.0015/2);
57 Circle ([ 0.032, +0.023, 0.121], 0.0015/2); % some screw holes
   Circle ([ -0.032, +0.023, 0.121], 0.0015/2);
59 Circle ([ 0.032, +0.023, -0.121], 0.0015/2);
   Circle ([ -0.032, +0.023, -0.121], 0.0015/2);
61 Circle ([ 0.032, -0.018, 0.031], 0.0015/2); % some screw holes
   Circle ([ -0.032, -0.018, 0.031], 0.0015/2);
63 Circle ([ 0.032, -0.018, -0.031], 0.0015/2);
   Circle ([ -0.032, -0.018, -0.031], 0.0015/2);
65 Circle ([ 0.032, -0.018, 0.091], 0.0015/2); % some screw holes
   Circle ([ -0.032, -0.018, 0.091], 0.0015/2);
67 Circle ([ 0.032, -0.018, -0.091], 0.0015/2);
   Circle ([ -0.032, -0.018, -0.091], 0.0015/2);

69 % dimensions of a 'Euro size PCB'
71 plot3 ([ 0.032, 0.032, 0.032, 0.032, 0.032], ...
         [ 0.050, 0.050, -0.050, -0.050, 0.050], ...
         [ 0.080, -0.080, -0.080, 0.080, 0.080], 'r');
   plot3 (-[ 0.032, 0.032, 0.032, 0.032, 0.032], ...
         [ 0.050, 0.050, -0.050, -0.050, 0.050], ...
         [ 0.080, -0.080, -0.080, 0.080, 0.080], 'r');

77 function [] = Circle (position, radius)
79 t = [0:0.025:1]*2*pi;
   plot3 (position(1)*ones(1, length(t)), ...

```

## E. Source code

```
81 position(2)+sin(t)*radius ,...
   position(3)+cos(t)*radius , 'm');
```

Listing E.10: RunOptim.m

```
%RUNOPTIM
2 x=zeros(1,11);
  optim=optimset('MaxIter', 1, 'MaxFunEval', 50 ,...
4   'Display', 'iter', 'LargeScale', 'off');
  i=0;
6 while true
    i=i+1
8   [x,v]=fminunc('Evaluator',x,optim);
    fid=fopen('test6.txt','at+');
10   fseek(fid,0,'eof');
    fprintf(fid,'%15.8g',x);
12   fprintf(fid,'\n');
    fclose(fid);
14 end
```

Listing E.11: Evaluator.m

```
function [ merit ] = Evaluator( v )
2 %evaluates the parameter vector v for optimization
  %
4 % use with matlab function 'fminsearch':
  % [x,v]=fminsearch('Evaluator',zeros(1,11),...
6 %       optimset('MaxIter',5,'MaxFunEval',20,'Display','iter'))
  % showresult(x)
8
  current=OptToCurrent(v);
10
  roiX=0.010;%region of interest
12 roiY=0.020;
  roiZ=0.272-0.020;
14 [x,y,z]=meshgrid(-roiX/2:roiX/4:roiX/2, ...
                   -roiY/2:roiY/4:roiY/2, ...
16                   -roiZ/2:roiZ/20:roiZ/2);
  p=[ reshape(x,prod(size(x)),1),...
18     reshape(y,prod(size(y)),1),...
     reshape(z,prod(size(z)),1)];
20
  for i=1:size(p,1)
22     f(i,:)=IntField(reshape(p(i,:),3,1),current)';
  end
24
  [quality ,avg ,dev]=FieldQuality(p,f);
26 merit=quality;
```

Listing E.12: ShowResult.m

```

function [    ] = ShowResult( v )
2
    current=OptToCurrent(v);
4 roiX=0.010;%region of interest
    roiY=0.020;
6 roiZ=0.272-0.020;
    [x,y,z]=meshgrid(-roiX/2:roiX/4:roiX/2, ...
8                    -roiY/2:roiY/4:roiY/2, ...
                    -roiZ/2:roiZ/20:roiZ/2);
10 p=[ reshape(x,prod(size(x)),1),...
        reshape(y,prod(size(y)),1),...
12      reshape(z,prod(size(z)),1)];
    for i=1:size(p,1)
14        f(i,:)=IntField(reshape(p(i,:),3,1),current)';
    end
16 [quality,avg,dev]=FieldQuality(p,f);
    quality
18 avg

20 figure; % 3D field arrows
    plotCurrent(current);
22 PlotField(p,f);
    PlotROIbox;
24 PlotChamber;
    axis equal
26 view(26,58);
    camup([0,1,0]);

28
    figure( % 3D color box)
30 dev=reshape(dev, size(z));
    slice(x,y,z,dev,...
32        [-roiX/2,roiX/2],[-roiY/2,roiY/2],[-roiZ/2,roiZ/2] );
    h=findobj(gca, 'FaceColor', 'flat');
34 set(h, 'FaceColor', 'interp');
    axis equal
36 view(26,58);
    camup([0,1,0]);
38 colormap(mycolorbar)
    % colormap jet
40 colorbar

```

## E.2. Instantaneous frequency analysis

Listing E.13: InstFreqAna.m

```

%% Settings
2 Samplerate=2.5E9; % 2.5 GS/s
% --> 1us=2500S
4 blocksize=2500;
%% Load and process data
6 data_f=[];
  data_a=[];
8 data_t=[];
  for FileNumber=0:14
10     start=length(data_t);
      for Channel=1:4
12         filename=['C' num2str(Channel, '%i') 'dds' ...
                    num2str(FileNumber, '%05i') '.dat'];
14         M=dlmread(filename, '\t');
           t=M(:,1);
16         y=M(:,2);
           for k=0:floor(length(y)/blocksize)-1
18             % take block of data
               block_t=t(k*blocksize+1:(k+1)*blocksize);
20             block_y=y(k*blocksize+1:(k+1)*blocksize);
               % use fft to estimate initial guess of frequency
22             [A,f,phi]=FitSin(block_y);
               data_f(start+k+1,Channel)=f*Samplerate/blocksize;
24             % instantaneous frequency in Hz
               data_a(start+k+1,Channel)=A;
26             % fourrier component scales like amplitude
               data_t(start+k+1)=mean(block_t);
28         end
      end
30 end
%% Show results
32 figure
  plot(data_t*1e3,data_f(:,[1,3,4])/1e6,'-');
34 % Channel 2 has a problem: no signal
  ylabel('Instantaneous_Frequency_(MHz)')
36 xlabel('Time_(ms)')
  xlim([-0.2,2.6])
38 set(gca,'xtick',[-0.2:0.2:2.6])
  ylim([190,225])
40 legend('7D_Front','8C_Top','6A_Bottom')
  title('Frequency')
42 grid on
  figure % detail of second frequency jump
44 plot(data_t*1e3,data_f(:,[1,3,4])/1e6,'-');

```

## E. Source code

```
ylabel('Instantaneous_Frequency_(MHz)')
46 xlabel('Time_(ms)')
    xlim([0.9,1.2])
48 set(gca,'xtick',[0.9:0.02:1.2])
    ylim([190,225])
50 legend('7D_Front','8C_Top','6A_Bottom')
    title('Frequency')
52 grid on
```

Listing E.14: FitSin.m

```
function [ A,f,phi ] = FitSin( y )
2 %FITSIN, fit a sin on data y

4 % use fft to estimate initial guess of frequency
  f=fft(y);
6 [a,1]=max(abs(f(1:floor(length(y)/2))));
    % only search in first half of fft
8 x=(0:length(y)-1)/length(y);
    % use sine fit for more accurate (instantaneous) frequency estimate
10 % because fft over 1us is limited to 1MHz resolution
    startParam=[2*abs(f(1))/length(y),1-1,angle(f(1))];
12 r=lsqcurvefit(@fitfunc,startParam,x,y);
    A=r(1);
14 f=r(2);
    phi=r(3);
16
function y=fitfunc(param,t)
18 y=param(1)*cos(2*pi*t*param(2)+param(3));
```

### E.3. Labview FPGA

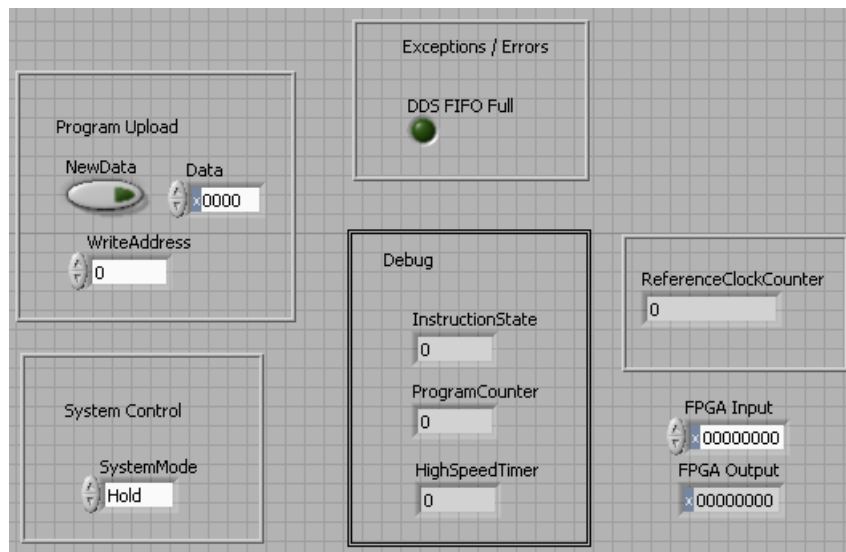


Figure E.2.: Front panel of the main FPGA vi. This is effectively the PCI interface.

## E. Source code

Table E.1.: Overview of the instructions. *s* is source register, *d* is destination register, *hhhhllll* is a 32 bit constant value, *x* is a don't care. Only the lower 3 bits of the second byte are used to determine the instruction, the upper 5 bits of that byte are ignored (reserved for future expansion).

Opcode	Machine Code (hex)	Description
NOP	xx00 xxxx xxxx	No Operation
SET	xd01 hhhh 1111	Set register <i>d</i> to value <i>hhhhllll</i>
JMP	sx02 dddd xxcc	Jump to address <i>dddd</i> if condition <i>cc</i> is met. cc: 0=always, 1=never, 2=equal, 3=not equal.
ADD	sd03 hhhh 1111	Add value <i>hhhhllll</i> to register <i>s</i> and store result in <i>d</i> .
WAIT	sx04 hhhh 1111	Wait until register <i>s</i> is equal to value <i>hhhhllll</i> , implies "SET Comp <i>hhhhllll</i> "
Invalid	sx05 hhhh 1111 : sx07 hhhh 1111	Crash, these instructions never end. A system reset is necessary. Reserved for future expansion.

Note: There is no need for a "move"-instruction as it can be realized with "ADD *s,d,+0*".

Table E.2.: Overview of the registers.

Reg. number	Name	Read / Write	Size (bit)	Description
0	DDS	R/W	32	
1	DIO	R/W	32	32 Digital output channels
2	High Speed Timer	R/W	32	100 MHz counter
3	Compare	R/W	32	
4	DAC	R/W	8	8 Bit analog output
5	DDS_Special	R/W	4	
6	FPGA_Input	R	32	Can be set through the PCI bus
7	FPGA_Output Memory1	R/W	32	Can be set by the FPGA program, can also be used as an additional counter
8..15	Invalid			Map to 0 (DDS)

## E. Source code

Listing E.15: Example of the program/experimental sequence that is executed by the FPGA.vi. The \$-sign indicates a hexadecimal number. The first number on a line is the memory address. There has been no assembler for this code implemented, only a disassembler.

```

$0000 : NOP
2 $0003 : SET HST $00000000           % clear timer
  $0006 : ADD DAC = DAC + $00000010   % increase DAC
4 $0009 : SET DDS $47444644           % initialize DDS
  $000C : SET DDS $6C459445           % frequency
6 $000F : SET DDS $8B464646
  $0012 : SET DDS $43477347
8 $0015 : SET DDS $95488148
  $0018 : SET DDS $8149D749
10 $001B : SET DDS $00400040           % phase
  $001E : SET DDS $00410041
12 $0021 : WAIT HST $00030D40         % wait 2 ms
  $0024 : NOP
14 $0027 : SET HST $00000000           % clear timer
  $002A : ADD DAC = DAC + $00000010   % increase DAC
16 $002D : SET DIO $01F40231           % new DIO state,
  $0030 : SET DIO $01F40230           % trigger analog out
18 $0033 : SET DDS_Special $00000001  % make DDS use new value
  $0036 : SET DDS_Special $00000000
20 $0039 : WAIT HST $05F5E100         % wait until next state
  $003C : NOP
22 $003F : SET DIO $F1F40201           % new DIO state
  $0042 : SET DIO $F1F40200           % trigger analog out
24 $0045 : WAIT HST $06115840         % wait until next state
  $0048 : NOP
26 $004B : SET DIO $F1F00201
  $004E : SET DIO $F1F00200
28 $0051 : WAIT HST $0623A7C0
  $0054 : NOP
30 % ...
  % (more repetitions of NOP/SET DIO/SET DIO/WAIT)
32 % ...
  $0117 : SET DIO $F0020001
34 $011A : SET DIO $F0020000
  $011D : WAIT HST $06E976D0
36 $0120 : NOP
  $0123 : SET DIO $000403D1
38 $0126 : SET DIO $000403D0
  $0129 : WAIT HST $06F29E90
40 $012C : NOP
  $012F : JMP ALWAYS $012C           % wait until eternity

```



E. Source code

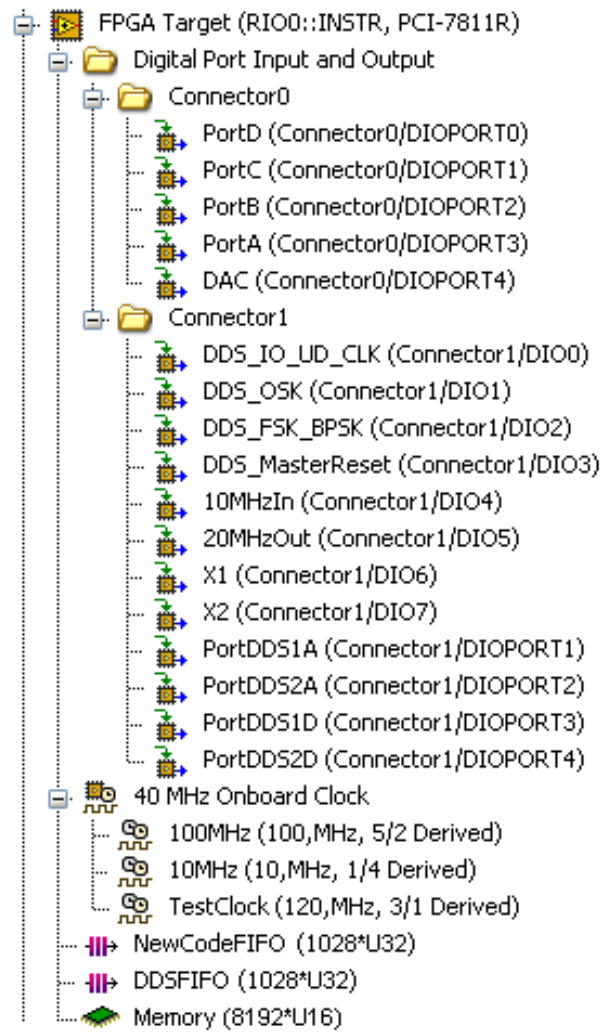


Figure E.3.: Settings of the main FPGA vi.

## E. Source code

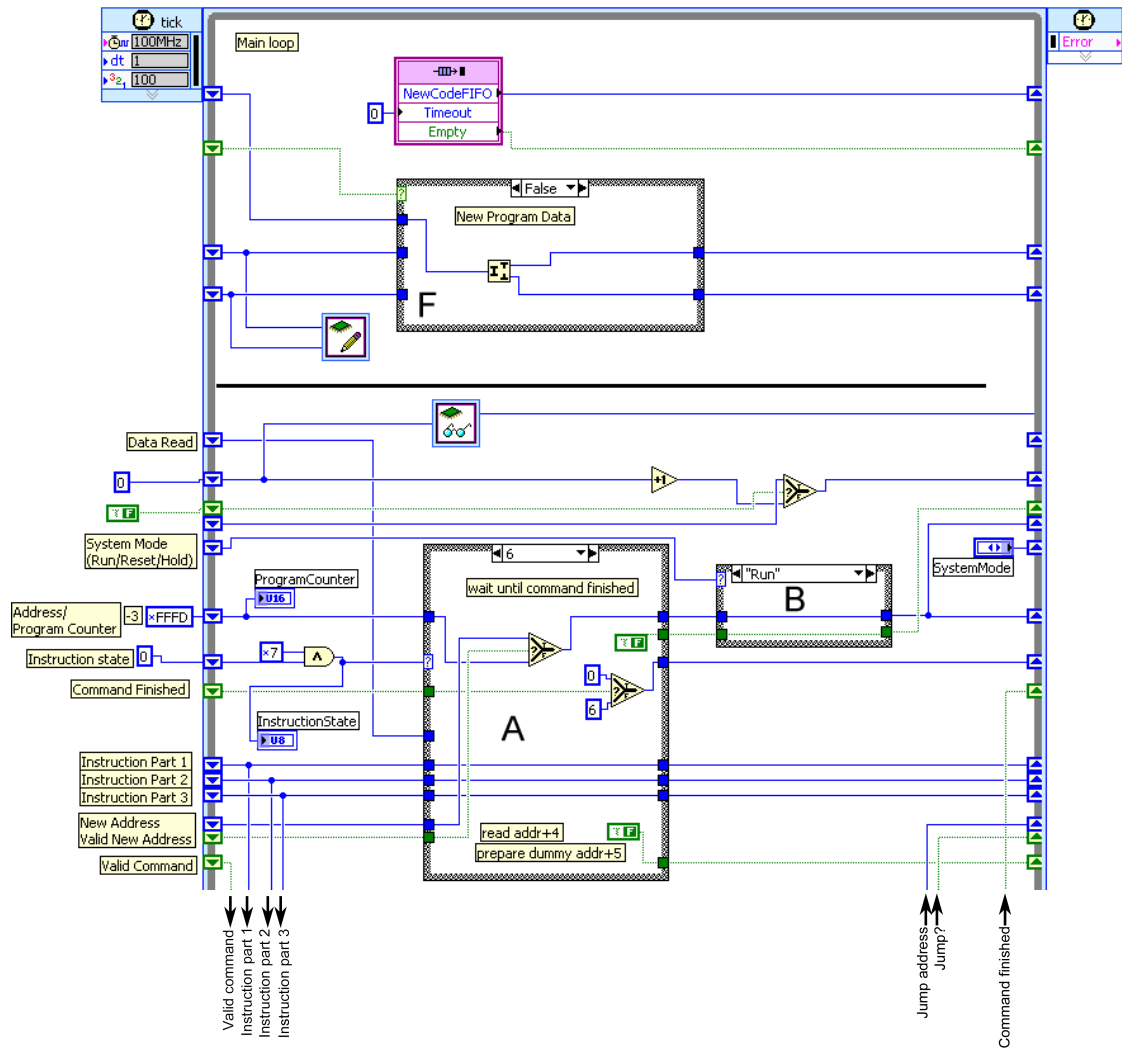


Figure E.4.: Upper half of the main loop of the main FPGA vi, see also figures E.5 and E.6. This part shows the reading of program data as well as the main state machine. The big characters refer to other code blocks shown in figure E.7 to E.13.

## E. Source code

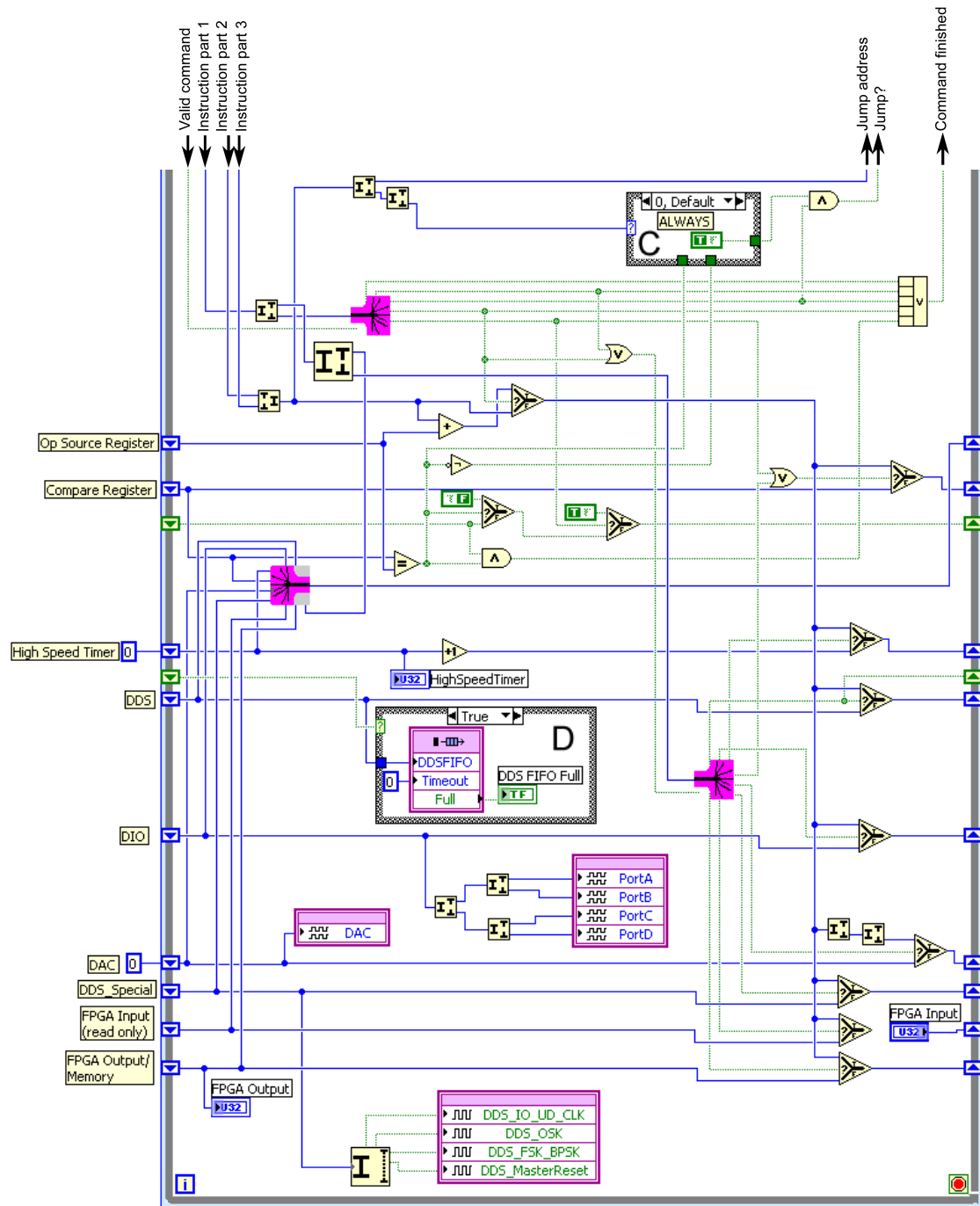


Figure E.5.: Lower half of the main loop of the main FPGA vi, see also figures E.4 and E.6. This part shows the registers and operations on them. The big characters refer to other code blocks shown in figure E.7 to E.13.

E. Source code

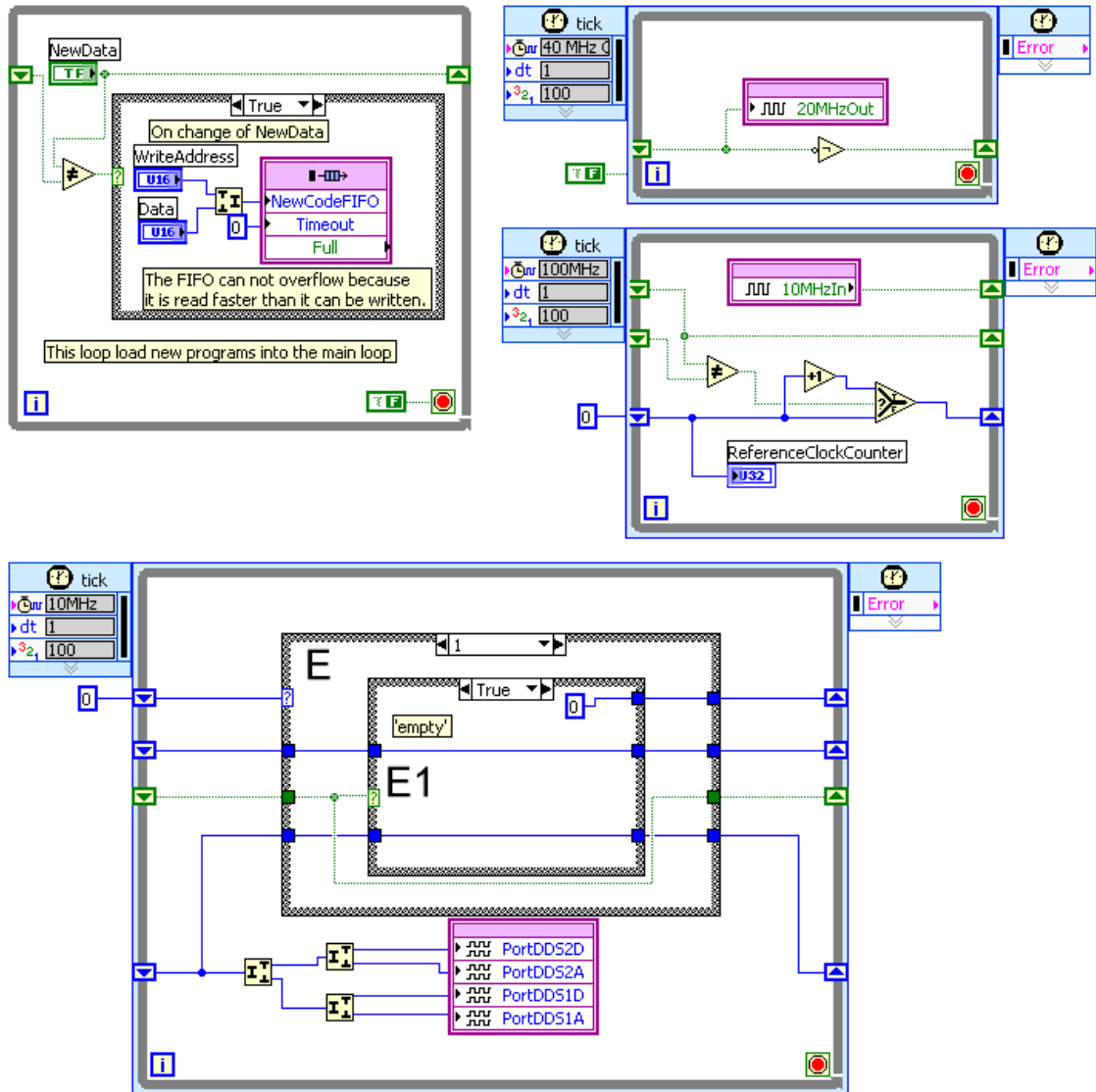


Figure E.6.: The auxiliary parts of the main FPGA vi, see also figures E.4 and E.5. These are loops for the DDS, loading the program, as well as a loop for generating a 20 MHz signal to synchronize external devices to the FPGA, and a counter to synchronize the computer (or the FPGA) with an external signal (with the aid of some more software). The big characters refer to other code blocks shown in figure E.7 to E.13.

E. Source code

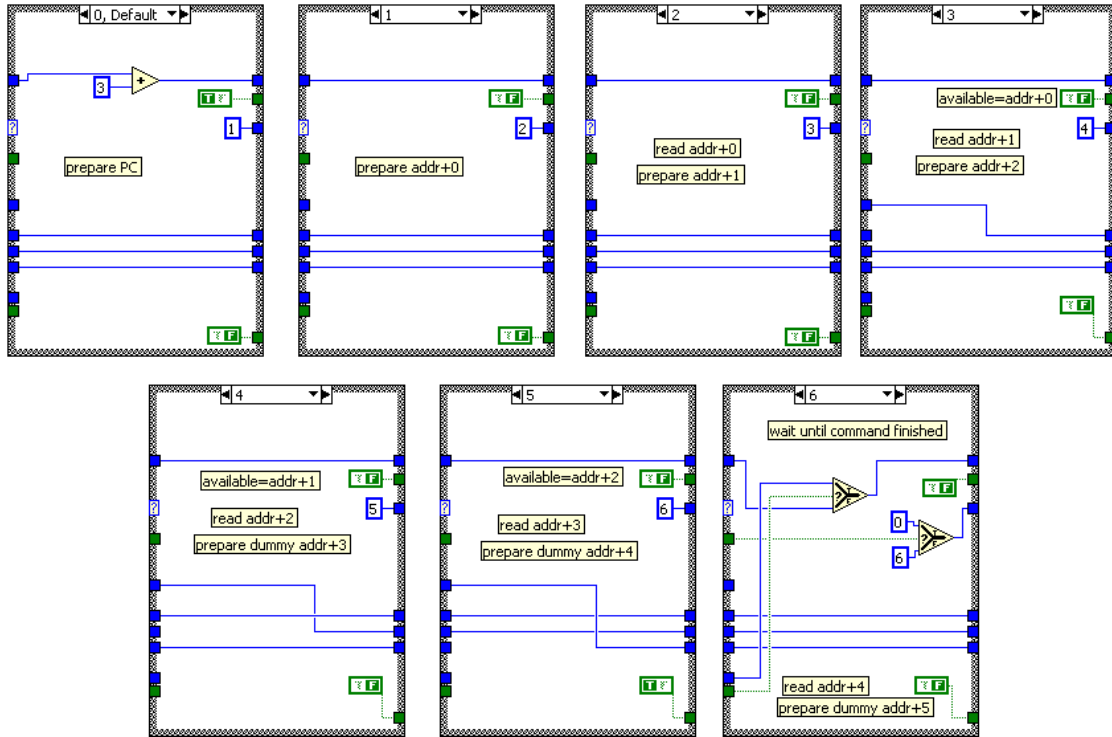


Figure E.7.: Switch case A: inner state machine of the processor.

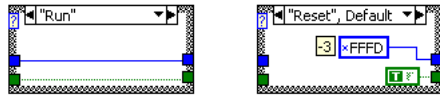


Figure E.8.: Switch case B: Global control of the program. Starting address is -3 because the first thing the CPU does is go to next instruction which increases the program counter.

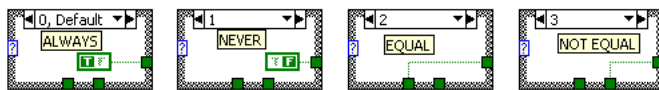


Figure E.9.: Switch case C:

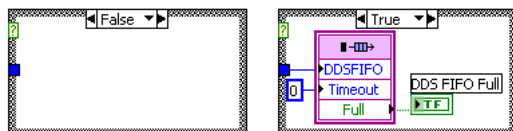


Figure E.10.: Switch case D: Loading data into the pipeline to the DDS.

E. Source code

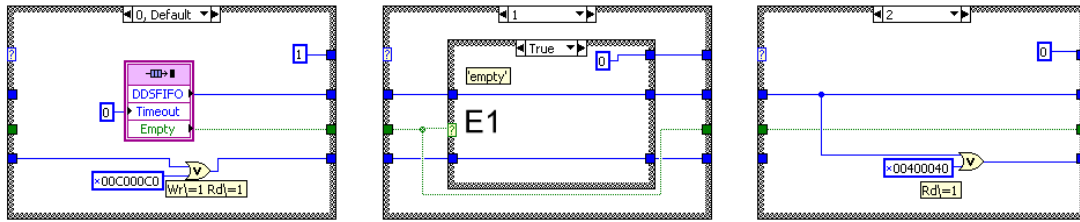


Figure E.11.: Switch case E: State machine for the DDS. Wait for data in pipeline, send new data to DDS.

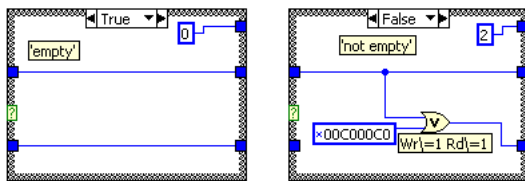


Figure E.12.: Switch case E1: Wait for data in pipeline to DDS.

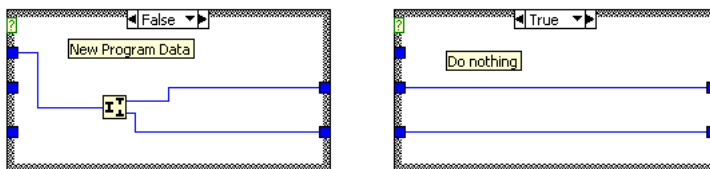


Figure E.13.: Switch case F: part of writing the data into the program memory.

# List of symbols and abbreviations

Symbol	Name	Unit	Reference
$\vec{A}$	Enclosed area of Sagnac and Mach-Zehnder interferometer	m <sup>2</sup>	ch. B
$\vec{a}$	Acceleration, $\in \mathbb{R}^3$	m/s <sup>2</sup>	eq. 2.35
$\mathcal{B}$	Start point of an interferometer path (splitter), $\in \mathbb{R}^3$	m	ch. B
$b$	Number of bits	-	ch. 4.3.4
$\vec{b}$	Coordinate on Bloch sphere, $\in \mathbb{R}^3$	-	ch. 2.1.4
$\vec{C}$	Quantum mechanical state vector, $\in \mathbb{C}^2$	-	ch. 2.1.3
$\mathcal{C}_{\mathfrak{N}}^{(M)}(\mathfrak{l})$	(Gauss-sum factorization) Factorization result, $ \mathcal{C}_{\mathfrak{N}}^{(M)}(\mathfrak{l})  = 1 \rightarrow$ factor, $ \mathcal{C}_{\mathfrak{N}}^{(M)}(\mathfrak{l})  = 0 \rightarrow$ non-factor, $\in \{-1..1\}$	-	eq. 5.10
$c$	Speed of light	m/s	tab. A.1
$c_g, c_e$	Component factors of wave function	-	ch. 2.1.3
$c_m(\mathfrak{l})$	(Gauss-sum factorization), component of $\mathcal{C}_{\mathfrak{N}}^{(M)}(\mathfrak{l}), \in \{-1..1\}$		eq. 5.9
$D$	Doppler shift rate, $D = 1/\lambda$	Hz/(m/s)	eq. 3.1
$\mathcal{D}$	End point of an interferometer path (recombiner), $\in \mathbb{R}^3$	m	ch. B
$E$	Energy	J	
$ e\rangle$	Excited state	-	eq. 2.1
$F$	Hyperfine quantum number	-	fig. A.1
$f$	Frequency	Hz	
$G$	Fourier transform of $g$		
$g$	Sensitivity function	-	
$\vec{g}$	Gravity	m/s <sup>2</sup>	ch. 2.5.3.5
$ g\rangle$	Ground state	-	eq. 2.1
$H$	Weighting function, $H = 2\pi fG$		
$h$	Planck's constant	Js	ch. 1.2
$h_m$	Wavefront error map of the $m$ th optical component	m	ch. 2.5.3.6
$\hbar$	Planck's constant divided by $2\pi$	Js	tab. A.1
$I$	Intensity	W/m <sup>2</sup>	
$i$	Imaginary unit ( $i = \sqrt{-1}$ )	-	
$ i\rangle$	Intermediate state	-	fig. 2.1

List of symbols and abbreviations

Symbol	Name	Unit	Reference
$\vec{k}$	Wave vector ( $2\pi/\lambda$ ), $\in \mathbb{R}^3$	rad/m	
$k_s, k_c$	Support variable for rotation matrix	-	eq. 2.25
$k_b$	Boltzmann's constant	J/K	tab. A.1
$L$	Length between successiv pulses of a matter wave interferometer	m	ch. 2.2
$l$	Length of perimeter of a ringlaser	m	eq. 1.2
$\iota$	(Gauss-sum factorization) test factor, $\in \mathbb{N}$	-	ch. 5.5
$\mathbf{M}$	Time evolution matrix, $\in \mathbb{R}^{3 \times 3}$	-	ch. 2.1.4
$M$	(Gauss-sum factorization), number of terms - 1, $\in \mathbb{N}$		eq. 5.10
$m$	Mass	kg	
$\mathbf{m}$	(Gauss-sum factorization), number of pulses - 1, $\in \mathbb{N}$		eq. 5.10
$\mathbf{m}$	Time evolution matrix, $\in \mathbb{C}^{2 \times 2}$	-	ch. 2.1.3
$m_f$	Zeeman quantum number	-	fig. A.1
$N$	Number of atoms	-	
$\mathfrak{N}$	(Gauss-sum factorization) number to be factorized, $\in \mathbb{N}$	-	ch. 5.5
$\tilde{N}$	Normalization factor	-	eq. 2.43
$n(\vec{r})$	Refractive index at position $\vec{r}$	-	eq. 2.66
$n_f, n_\phi$	Digital tuning word, $\in \mathbb{N}$	-	ch. 4.3.4
$\vec{n}$	Surface normal of mirror, $\in \mathbb{R}^3$	-	ch. 2.5.3.5
$P(\clubsuit)$	Probability of $\clubsuit$	-	
$P(\vec{r}, \vec{v}, t)$	Probability density of atomic cloud	$\frac{1}{\text{m}^3 \cdot (\frac{\text{m}}{\text{s}})^3}$	eq. 2.43
$P_j$	Path of interferometer arm $j$	-	ch. B
$p$	Impuls	Kg·m/s	
$\mathbf{p}$	Multiplier factor, $\in \mathbb{N}$	-	eq. 4.4
$\mathbf{q}$	Divider factor, $\in \mathbb{N}$	-	eq. 4.4
$R$	Scattering rate	1/s	ch. 2.5.4
$r$	Comb line number	-	eq. 4.6
$\vec{r}$	Position, $\in \mathbb{R}^3$	m	
$S(f)$	Noise power spectral density	W/Hz	
$S$	Interferometer signal ( $0 \rightarrow  g\rangle, 1 \rightarrow  e\rangle$ )	-	ch. 2.3
$T$	Time of free evolution	s	
$\bar{T}$	Temperature	K	ch. 2.4
$t$	Time coordinate	s	
$u(\spadesuit)$	Uncertainty of $\spadesuit$		
$u_x, u_y, u_z$	Components of rotation axis	-	eq. 2.25
$\vec{u}$	Rotation axis, $\vec{u} = (u_x, u_y, u_z) \in \mathbb{R}^3$	-	eq. 2.25
$v$	Velocity	m/s	



*List of symbols and abbreviations*

Symbol	Name	Unit	Reference
$\vec{v}$	Velocity, $\in \mathbb{R}^3$	m/s	
$x$	Space coordinate	m	ch. 2.5.3.6
$\vec{x}$	Space coordinate vector, $\vec{x} = (x, y) \in \mathbb{R}^2$	m	ch. 2.5.3.6
$y$	Space coordinate	m	ch. 2.5.3.6
$\alpha$	Angle between atomic velocity and mirror normal	rad	ch. 2.5.3.5
$\beta$	Angle between gravity and mirror normal	rad	ch. 2.5.3.5
$\Gamma$	Linewidth of the transition	rad/s	tab. A.2
$\Delta$	Detuning in the Raman process between the two laser fields and $ i\rangle$	rad/s	fig. 2.1
$\delta$	Detuning	rad/s	ch. 2.1.1
$\theta$	Interferometer signal offset	-	ch. 2.3
$\vec{\kappa}$	Spatial frequency, $\in \mathbb{R}^2$	1/m	ch. 2.5.3.6
$\lambda$	Wavelength	m	
$\xi$	Interferometer signal amplitude	-	ch. 2.3
$\sigma$	Width of a distribution		
$\tau$	Pulse length	s	
$\phi$	Phase	rad	
$\chi$	High frequency components of sensitivity function	-	eq. 2.54
$ \Psi\rangle$	Wave function	-	ch. 2.1.3
$\Omega$	Rabi frequency	rad/s	ch. 2.1.2
$\vec{\Omega}$	Rotation rate, $\in \mathbb{R}^3$	rad/s	
$\omega$	Laser frequency	rad/s	

*List of symbols and abbreviations*

Abreviation	Description	Reference
2D	2D MOT (in variable subscript)	
3D	3D MOT/molasses (in variable subscript)	
ADC	Analog to Digital Converter	
AOM	Acousto Optic Modulator	
BEC	Bose-Einstein Condensate	
CPLD	Complex Programmable Logic Device (similar to FPGA)	
DAC	Digital to Analog Converter	
DDS	Direct Digital Synthesizer	ch. 4.3.4
EOM	Electro Optic Modulator	ch. 4.2.1
FTW	Frequency Tuning Word	ch. 4.3.4
FIFO	First-in-first-out buffer	
FPGA	Field Programmable Gate Array	ch. 4.4.3
fv	Frequency to voltage converter (in variable subscript)	
GPS	Global Positioning System	fig. 4.7
HWP	Half Wave Plate	
IF	Intermediate Frequency (in a mixer)	
ISA	Industry Standart Architecture	ch. D.2, [81]
MOT	Magneto Optical Trap	[53]
OCXO	Ovenized Crystal Oscillator	fig. 4.7
OPLL	Optical Phase Locked Loop	
QWP	Quarter Wave Plate	
PCB	Printed Circuit Board	
PCI	Periferal Component Interface	
PID	Proportional-Integral-Differential controller	ch. D.10
PLL	Phase Locked Loop	
POW	Phase Offset Word	ch. 4.3.4
ppm	Part per million	
R1	Raman master laser (in variable subscript)	
R2	Raman slave laser (in variable subscript)	
rect	Rectangle function: 1 for $ t  < 1/2$ , 0 otherwise	
ref	Reference (in variable subscript)	
RF	Radio Frequency	
sinc	Sinc function: $\text{sinc}(x) = \frac{\sin(x)}{x}, 1$ when $x=0$	
SRD	Step Recovery Diode	
SSR	Solid State Relay	
TA	Tapered Amplifier	
UHV	Ultra High Vacuum	ch. 3.1
USB	Universal Serial Bus	
VCO	Voltage Controled Oscillator	

# Bibliography

- [1] CDDIS NASA, “VLBI - measuring our changing earth”, online, 2009, URL <http://lupus.gsfc.nasa.gov/brochure/bintro.html>.
- [2] IERS.org, “Very long baseline radio interferometry (VLBI)”, Online, 2001, [www.iers.org](http://www.iers.org) → science background → Earth rotation → UT1 → VLBI <http://www.iers.org/MainDisp.csl?pid=99-121>.
- [3] C. Ma, E. F. Arias, T. M. Eubanks, A. L. Fey, A.-M. Gontier, C. S. Jacobs, O. J. Sovers, B. A. Archinal and P. Charlot, “The international celestial reference frame as realized by very long baseline interferometry”, *The Astronomical Journal*, 1998, vol. 116, pp. 516–546, URL <http://www.iop.org/EJ/abstract/1538-3881/116/1/516/>.
- [4] M. L. Foucault, “Physical demonstration of the rotation of the earth by means of the pendulum”, *Journal of the Franklin Institute*, 1851, pp. 350–353, [http://www.fi.edu/time/journey/Pendulum/foucault\\_paper\\_page\\_one.html](http://www.fi.edu/time/journey/Pendulum/foucault_paper_page_one.html) This is a translation of the French original: M. L. Foucault, "Démonstration expérimentale du mouvement de rotation de la Terre", *Journal des Débats*, 31 March 1851.
- [5] J. Bohnenberger, “Beschreibung einer Maschine zur Erläuterung der Geseze der Umdrehung der Erde um ihre Axe, und der Veränderung der Lage der letzteren”, *Tübinger Blätter für Naturwissenschaften und Arzneikunde*, 1817, vol. 3, pp. 72–83, URL [http://www.ion.org/museum/files/File\\_1.pdf](http://www.ion.org/museum/files/File_1.pdf).
- [6] D. Bardas et al., “Hardware Development for Gravity Probe-B”, in “SPIE Proceedings - Cryogenic Optical Systems and Instruments II”, SPIE, 1986, vol. 619 of *Proceedings of SPIE* pp. 29–46, URL [http://einstein.stanford.edu/content/sci\\_papers/papers/BardasD\\_1986\\_06.pdf](http://einstein.stanford.edu/content/sci_papers/papers/BardasD_1986_06.pdf).
- [7] B. Muhlfelder, J. M. Lockhart and G. M. Gutt, “The Gravity Probe B gyroscope readout system”, in “2003 COSPAR Adv. Space Res.”, 2003, vol. 32 pp. 1397–1400.
- [8] R. Kahn, F. Everitt, B. Muhlfelder and T. Langenstein, “The Gravity Probe B Experiment - Science Results - NASA Final Report”, Tech. rep., Stanford University, 2008.
- [9] J. Lense and H. Thirring, “Über den Einfluss der Eigenrotation der Zentralkörper auf die Bewegung der Planeten und Monde nach der Einsteinschen Gravitationstheorie”, *Physikalische Zeitschrift*, 1918, vol. 19, pp. 156–163.

## Bibliography

- [10] M. G. Sagnac, “Sur la preuve de la réalité de l'éther lumineux par l'expérience de l'interféromètre tournant”, *Compt. Rend. des Sc. d. l'Acad. d. Sc.*, 1913, vol. 157, pp. 1410–1413.
- [11] M. G. Sagnac, “L'éther lumineux démontré par l'effet du vent relatif d'éther dans un interféromètre en rotation uniforme”, *Compt. Rend. des Sc. d. l'Acad. d. Sc.*, 1913, vol. 157, pp. 708–710.
- [12] A. A. Michelson, H. G. Gale and F. Pearson, “The effect of earth's rotation on the velocity of light”, *Astrophysical Journal*, 1925, vol. 61, pp. 140–145.
- [13] W. M. Macek and D. T. M. Davis, “Rotation rate sensing with traveling-wave ring lasers”, *Applied Physics Letters*, 1963, vol. 2, no. 3, pp. 67–68.
- [14] G. Stedman, R. Hurst and K. Schreiber, “On the potential of large ring lasers”, *Optics Communications*, 2007, vol. 279, no. 1, pp. 124–129.
- [15] T. Klügel, U. Schreiber, M. Schneider, S. Riepl, W. Schlüter, H. Weber and G. Stedman, “Realisierung des Großringlasers G auf der Fundamentalstation Wettzell, Begutachtung des FGS Forschungsprogramms 2001-2005”, Online, 2000, URL <http://www.fs.wettzell.de/publ/publ/wtz152.pdf>.
- [16] T. Hänsch and A. Schawlow, “Cooling of gases by laser radiation”, *Optics Communications*, 1975, vol. 13, no. 1, pp. 68–69.
- [17] S. Chu, L. Hollberg, J. E. Bjorkholm, A. Cable and A. Ashkin, “Three-dimensional viscous confinement and cooling of atoms by resonance radiation pressure”, *Phys. Rev. Lett.*, 1985, vol. 55, pp. 48–51, URL <http://link.aps.org/doi/10.1103/PhysRevLett.55.48>.
- [18] E. Raab, M. Prentiss, A. Cable, S. Chu and D. Pritchard, “Trapping of Neutral Sodium Atoms with Radiation Pressure”, *Physical Review Letters*, 1987, vol. 59, no. 23, pp. 2631–2634.
- [19] P. D. Lett, R. N. Watts, C. I. Westbrook, W. D. Phillips, P. L. Gould and H. J. Metcalf, “Observation of atoms laser cooled below the doppler limit”, *Phys. Rev. Lett.*, 1988, vol. 61, pp. 169–172.
- [20] J. Dalibard and C. Cohen-Tannoudji, “Laser cooling below the Doppler limit by polarization gradients: Simple theoretical models”, *J. Opt. Soc. Am. B*, 1989, vol. 6, pp. 2023–2045.
- [21] P. J. Ungar, D. S. Weiss, E. Riis and S. Chu, “Optical molasses and multilevel atoms: Theory”, *J. Opt. Soc. Am. B*, 1989, vol. 6, pp. 2058–2071, URL <http://www.opticsinfobase.org/abstract.cfm?URI=josab-6-11-2058>.
- [22] A. Aspect, E. Arimondo, R. Kaiser, N. Vansteenkiste and C. Cohen-Tannoudji, “Laser cooling below the one-photon recoil energy by velocity-selective coherent population trapping”, *Phys. Rev. Lett.*, 1988, vol. 61, no. 7,

## Bibliography

- pp. 826–829, URL <http://link.aps.org/doi/10.1103/PhysRevLett.61.826>.
- [23] M. H. Anderson, J. R. Ensher, M. R. Matthews, C. E. Wieman and E. A. Cornell, “Observation of Bose-Einstein condensation in a dilute atomic vapor”, *Science*, 1995, vol. 269, p. 198.
- [24] K. B. Davis, M.-O. Mewes, M. R. Andrews, N. J. van Druten, D. S. Durfee, D. M. Kurn and W. Ketterle, “Bose-Einstein condensation in a gas of sodium atoms”, *Phys. Rev. Lett.*, 1995, vol. 75, p. 3969.
- [25] K. Eckert, P. Hyllus, D. Bruß, U. Poulsen, M. Lewenstein, C. Jentsch, T. Müller, E. Rasel and W. Ertmer, “Differential atom interferometry beyond the standard quantum limit”, *Physical Review A*, 2006, vol. 73, no. 1, 013814, URL <http://link.aps.org/abstract/PRA/v73/e013814>.
- [26] A. Einstein, “Über einen die Erzeugung und Verwandlung des Lichtes betreffenden heuristischen Gesichtspunkt”, *Annalen der Physik*, 1905, vol. 322, no. 6, pp. 132–148, URL <http://einstein-annalen.mpiwg-berlin.mpg.de/annalen/alphabetical/HUN315QN>.
- [27] A. Einstein, “Ist die Trägheit eines Körpers von dessen Energieinhalt abhängig?”, *Annalen der Physik*, 1905, vol. 18, pp. 639–643.
- [28] L. de Broglie, “Recherches sur la théorie des quanta”, Ph.D. thesis, Paris, 1924, *Annales de Physique (10e série) III (1925) 22*. Reproduced in: L. de Broglie, *Recherches sur la théorie des quanta (Fondation Louis de Broglie, Paris, 1992)*.
- [29] N. Ramsey, “A Molecular Beam Resonance Method with Separated Oscillating Fields”, *Physical Review*, 1950, vol. 78, no. 6, pp. 695–699.
- [30] C. Bordé, “Atomic interferometry with internal state labelling”, *Phys. Lett. A*, 1989, vol. 140, no. 10, p. 126.
- [31] F. Riehle, T. Kisters, A. Witte, J. Helmcke and C. Bordé, “Optical ramsey spectroscopy in a rotating frame: Sagnac effect in a matter-wave interferometer”, *Phys. Rev. Lett.*, 1991, vol. 67, p. 177.
- [32] M. Kasevich and S. Chu, “Atomic interferometry using stimulated Raman transitions”, *Physical Review Letters*, 1991, vol. 67, no. 2, pp. 181–184.
- [33] J. Le Gouët, T. Mehlstaubler, J. Kim, S. Merlet, A. Clairon, A. Landragin and F. Dos Santos, “Limits to the sensitivity of a low noise compact atomic gravimeter”, *Appl. Phys. B*, 2008, vol. 92, pp. 133–144.
- [34] A. Peters, K. Chung and S. Chu, “High-precision gravity measurements using atom interferometry”, *Metrologia*, 2001, vol. 38, no. 1, pp. 25–61.

## Bibliography

- [35] G. Lamporesi, A. Bertoldi, L. Cacciapuoti, M. Prevedelli and G. Tino, “Determination of the Newtonian Gravitational Constant Using Atom Interferometry”, *Physical Review Letters*, 2008, vol. 100, no. 5, p. 50801.
- [36] J. Fixler, G. Foster, J. McGuirk and M. Kasevich, “Atom Interferometer Measurement of the Newtonian Constant of Gravity”, *Science*, 2007, vol. 315, no. 5808, p. 74.
- [37] H. Müller, S.-W. Chiow, Q. Long, C. Vo and S. Chu, “A new photon recoil experiment: towards a determination of the fine structure constant”, *Applied Physics B: Lasers and Optics*, 2006, vol. 84, pp. 633 – 642, URL <http://www.springerlink.com/content/6461n28205084866/?p=8e39923fe851409683b1327b15207102&pi=0>.
- [38] B. Canuel et al., “Six-axis inertial sensor using cold-atom interferometry”, *Phys. Rev. Lett.*, 2006, vol. 97, pp. 010402–1.
- [39] T. Gustavson, A. Landragin and M. Kasevich, “Rotation sensing with a dual atom-interferometer Sagnac gyroscope”, *Classical and Quantum Gravity*, 2000, vol. 17, no. 12, pp. 2385–2398.
- [40] IERS.org, “Excess of the duration of the day to 86400 s and angular velocity of the earth’s rotation, since 1623”, Online, 2001, [www.iers.org](http://www.iers.org) → science background → Earth rotation → UT1 → Yearly values (<http://www.iers.org/MainDisp.csl?pid=95-103>).
- [41] G. Stedman et al., “Ring-laser tests of fundamental physics and geophysics”, *Reports on Progress in Physics*, 1997, vol. 60, pp. 615–688.
- [42] H. Igel, U. Schreiber, A. Flaws, B. Schuberth, A. Velikoseltsev and A. Cochard, “Rotational motions induced by the M8.1 Tokachi-oki earthquake, september 25, 2003”, *Geophys. Res. Lett.*, 2005, vol. 32, p. L08309.
- [43] C. Jentsch, T. Müller, E. Rasel and W. Ertmer, “HYPER: A Satellite Mission in Fundamental Physics Based on High Precision Atom Interferometry”, *General Relativity and Gravitation*, 2004, vol. 36, no. 10, pp. 2197–2221.
- [44] L. Ju, D. G. Blair and C. Zhao, “Detection of gravitational waves”, *Rep. Prog. Phys.*, 2000, vol. 63, pp. 1317–1427, URL <http://www.gravity.uwa.edu.au/docs/review.pdf>.
- [45] J. Anandan and R. Chiao, “Gravitational radiation antennas using the sagnac effect”, *General Relativity and Gravitation*, 1982, vol. 14, no. 6, pp. 515–521.
- [46] F. Sorge, D. Bini and F. de Felice, “Gravitational waves, gyroscopes and frame dragging”, *Classical and Quantum Gravity*, 2001, vol. 18, no. 15, pp. 2945–2958.

## Bibliography

- [47] C. Jentsch, “Konzeption und Aufbau eines Experiments zur quantenlimitierten Inertialsensorik mit lasergekühlten Rubidiumatomen”, Ph.D. thesis, Institute of Quantum Optics, Leibniz University Hannover, 2004.
- [48] T. Müller, “Realisierung eines Atominterferometers zur hochauflösenden Inertialsensorik mit kalten Rubidiumatomen”, Ph.D. thesis, Institute of Quantum Optics, Leibniz University Hannover, 2007.
- [49] T. Gustavson, P. Bouyer and M. Kasevich, “Precision Rotation Measurements with an Atom Interferometer Gyroscope”, *Physical Review Letters*, 1997, vol. 78, no. 11, pp. 2046–2049.
- [50] F. Yver-Leduc, P. Cheinet, J. Fils, A. Clairon, N. Dimarcq, D. Holleville, P. Bouyer and A. Landragin, “Reaching the quantum noise limit in a high-sensitivity cold-atom inertial sensor”, *Journal of Optics B: Quantum and Semiclassical Optics*, 2003, vol. 5, no. 2, pp. 136–142.
- [51] W. Ertmer et al., “Matter wave explorer of gravity (MWXG)”, *Experimental Astronomy*, 2009, vol. 23, pp. 611–649.
- [52] C. Doppler, “Über das farbige Licht der Doppelsterne und einiger anderer Gestirne des Himmels”, *Abhandlungen der k. böhm. Gesellschaft der Wissenschaften*, 1842, vol. V. Folge, Bd. 2, pp. 465–482, URL [http://de.wikisource.org/wiki/%C3%9Cber\\_das\\_farbige\\_Licht\\_der\\_Doppelsterne\\_und\\_einiger\\_anderer\\_Gestirne\\_des\\_Himmels](http://de.wikisource.org/wiki/%C3%9Cber_das_farbige_Licht_der_Doppelsterne_und_einiger_anderer_Gestirne_des_Himmels).
- [53] H. J. Metcalf and P. van der Straten, *Laser Cooling and Trapping*, Springer, 1999.
- [54] D. A. Steck, “Rubidium 87 D line data, revision 2.1”, Online, 2008, URL <http://steck.us/alkalidata/rubidium87numbers.pdf>.
- [55] R. Feynman, F. Vernon Jr and R. Hellwarth, “Geometrical Representation of the Schrödinger Equation for Solving Maser Problems”, *Journal of Applied Physics*, 1957, vol. 28, no. 1, p. 49.
- [56] M. Kasevich and S. Chu, “Measurement of the gravitational acceleration of an atom with a light-pulse atom interferometer”, *Applied Physics B: Lasers and Optics*, 1992, vol. 54, no. 5, pp. 321–332.
- [57] B. Dubetsky and M. Kasevich, “Atom interferometer as a selective sensor of rotation or gravity”, *Physical Review A*, 2006, vol. 74, no. 2, p. 23615.
- [58] K. Bongs, R. Launay and M. Kasevich, “High-order inertial phase shifts for time-domain atom interferometers”, *Applied Physics B: Lasers and Optics*, 2006, vol. 84, no. 4, pp. 599–602.
- [59] C. Antoine and C. Bordé, “Exact phase shifts for atom interferometry”, Arxiv preprint physics/0210083, 2002.

## Bibliography

- [60] C. Antoine and C. J. Bordé, “Quantum theory of atomic clocks and gravito-inertial sensors: an update”, *J. Opt. B*, 2003, vol. 5, p. 199.
- [61] C. Antoine and C. J. Bordé, “Exact phase shifts for atom interferometry”, *Phys. Let. A*, 2003, vol. 306, p. 277.
- [62] C. Antoine and C. Bordé, “Quantum theory of atomic clocks and gravito-inertial sensors: an update”, *Journal of Optics B: Quantum and Semiclassical Optics*, 2003, vol. 5, no. 2, pp. 199–207.
- [63] C. Antoine, “Matter wave beam splitters in gravito-inertial and trapping potentials: generalized ttt scheme for atom interferometry”, *Applied Physics B: Lasers and Optics*, 2006, vol. 84, no. 4, pp. 585–597.
- [64] G. Foster, J. Fixler, J. McGuirk and M. Kasevich, “Method of phase extraction between coupled atom interferometers using ellipse-specific fitting”, *Optics Letters*, 2002, vol. 27, no. 11, pp. 951–953.
- [65] B. L. Swinkels, T. J. Wendrich, N. Bhattacharya, A. Wielders and J. J. M. Braat, “Absolute distance metrology for space interferometers”, in J. Antebi and D. Lemke (eds.), “Astronomical Structures and Mechanisms Technology”, SPIE, 2004, vol. 5495 of *Proceedings of SPIE* pp. 314–318, URL <http://www.optica.tnw.tudelft.nl/publications/docs/2004%20pdf%20files/2004.031.pdf>.
- [66] G. Tackmann, “Konzepte für die kohärente Manipulation von Materiewellen mit der Atom-Licht-Wechselwirkung für die Präzisionsatominterferometrie”, Master’s thesis, Institut für Qantenoptik, Universität Hannover, 2009.
- [67] J. Fils, F. Leduc, P. Bouyer, D. Holleville, N. Dimarcq, A. Clairon and A. Landragin, “Influence of optical aberrations in an atomic gyroscope”, *The European Physical Journal D-Atomic, Molecular and Optical Physics*, 2005, vol. 36, no. 3, pp. 257–260.
- [68] P. Cheinet, B. Canuel, F. P. D. Santos, A. Gauguet, F. Yver-Leduc and A. Landragin, “Measurement of the sensitivity function in a time-domain atomic interferometer”, *IEEE Transactions on Instrumentation and Measurement*, 2008, vol. 57, no. 6, pp. 1141–1148.
- [69] R. V. Shack and B. C. Platt, “Production and use of a lenticular Hartmann screen”, *J. Opt. Soc. Am.*, 1971, vol. 61, pp. 656–660.
- [70] C. L. G. Alzar, P. G. Petrov, D. Oblak, J. H. Müller and E. S. Polzik, “Compensation of eddy-current-induced magnetic field transients in a MOT”, arXiv:physics/0701251, 2007, URL <http://arxiv.org/abs/physics/0701251>.
- [71] T. L. Gustavson, “Precision rotation sensing using atom interferometry”, Ph.D. thesis, stanford university, 2000.



## Bibliography

- [72] M. Gilowski, C. Schubert, M. Zaiser, W. Herr, T. Wübbena, T. Wendrich, T. Müller, E. Rasel and W. Ertmer, “Narrow bandwidth interference filter-stabilized diode laser systems for the manipulation of neutral atoms”, *Optics Communications*, 2007, vol. 280, p. 443.
- [73] C. Schubert, “Realisierung eines schmalbandigen Diodenlasersystems hoher Ausgangsleistung für Präzisionsmessungen  $^{87}\text{Rb}$  Atomen”, Master’s thesis, Institut für Qantenoptik, Leibniz Universität Hannover, 2007.
- [74] X. Baillard, A. Gauguet, S. Bize, P. Lemonde, P. Laurent, A. Clairon and P. Rosenbusch, “Interference-filter-stabilized external-cavity diode lasers”, *Optics Communications*, 2006, vol. 266, no. 2, pp. 609–613.
- [75] J. Snyder, R. Raj, D. Bloch and M. Ducloy, “High-sensitivity nonlinear spectroscopy using a frequency-offset pump”, *Opt. Lett.*, 1980, vol. 5, no. 4, pp. 163–165.
- [76] M. Gilowski, “Aufbau und Charakterisierung eines Raman-Lasersystems zur Sagnac-Interferometrie mit kalten Atomen”, Diplomarbeit, Institut für Qantenoptik, Universität Hannover, 2005.
- [77] P. Berg, “Analyse und Unterdrückung von Phasenrauschen in der Atominterferometrie”, Master’s thesis, Institut für Qantenoptik, Universität Hannover, 2009, in preparation.
- [78] J. Le Gouët, J. Kim, C. Bourassin-Bouchet, M. Lours, A. Landragin and F. P. D. Santos, “Wide bandwidth phase-locked diode laser with an intracavity electro-optic modulator”, *Optics Communications*, 2009, vol. 282, pp. 977–980.
- [79] E. Murphy and C. Slattery, “All about direct digital synthesis”, *Analog Dialogue*, 2004, vol. 38-08, pp. 1–5, URL <http://www.analog.com/library/analogDialogue/archives/38-08/dds.pdf>.
- [80] H. Nyquist, “Certain Topics in Telegraph Transmission Theory”, in “Transactions of the A. I. E. E.”, American Telephone and Telegraph Co., New York, NY, 1928 pp. 617–644, URL <http://www.loe.ee.upatras.gr/Comes/Notes/Nyquist.pdf>.
- [81] E. Solari, *ISA and EISA Theory and Operation*, Annabooks/Rtc Books, 1992.
- [82] National Instruments, “FPGAs - under the hood”, Online, URL <http://zone.ni.com/devzone/cda/tut/p/id/6983>.
- [83] M. Gilowski, T. Wendrich, T. Müller, C. Jentsch, W. Ertmer, E. Rasel and W. Schleich, “Gauss Sum Factorization with Cold Atoms”, *Physical Review Letters*, 2008, vol. 100, no. 3, p. 30201.

## Bibliography

- [84] M. Mehring, K. Müller, I. Averbukh, W. Merkel and W. Schleich, “NMR Experiment Factors Numbers with Gauss Sums”, *Physical Review Letters*, 2007, vol. 98, no. 12, p. 120502.
- [85] M. Štefaňák, W. Merkel, W. P. Schleich, D. Haase and H. Maier, “Factorization with gauss sums: scaling properties of ghost factors”, *New Journal of Physics*, 2007, vol. 9, no. 10, p. 370, URL <http://stacks.iop.org/1367-2630/9/370>.
- [86] X. Peng and D. Suter, “NMR implementation of factoring large numbers with gauß sums: Suppression of ghost factors”, arXiv:0803.3396v1, 2008.
- [87] W. Merkel, I. S. Averbukh, B. Girard, G. G. Paulus and W. P. Schleich, “Factorization of numbers with physical systems”, *Fortschr. Phys.*, 2006, vol. 54, pp. 856–865.
- [88] W. Petrich, M. H. Anderson, J. R. Ensher and E. A. Cornell, “Behavior of atoms in a compressed magneto-optical trap”, *J. Opt. Soc. Am. B*, 1994, vol. 11, no. 8, pp. 1332–1335.
- [89] H. Müller, S. Chiow, Q. Long and S. Chu, “Phase-locked, low-noise, frequency agile titanium: sapphire lasers for simultaneous atom interferometers”, *Optics Letters*, 2006, vol. 31, no. 2, pp. 202–204.
- [90] A. Velikoseltsev, “The development of a sensor model for large ring lasers and their application in seismic studies”, Ph.D. thesis, Technischen Universität München, 2005.
- [91] H. Müller, S. Chiow, Q. Long, S. Herrmann and S. Chu, “Atom Interferometry with up to 24-Photon-Momentum-Transfer Beam Splitters”, *Physical Review Letters*, 2008, vol. 100, no. 18, p. 180405.
- [92] H. Müller, S. wey Chiow, S. Herrmann and S. Chu, “Atom interferometers with scalable enclosed area”, arXiv:0903.4192v1, 2009.
- [93] H. Müller, S. Chiow and S. Chu, “Atom-wave diffraction between the Raman-Nath and the Bragg regime: Effective Rabi frequency, losses, and phase shifts”, *Physical Review A*, 2008, vol. 77, no. 2, p. 23609.
- [94] J. McGuirk, M. Snadden and M. Kasevich, “Large Area Light-Pulse Atom Interferometry”, *Physical Review Letters*, 2000, vol. 85, no. 21, pp. 4498–4501.
- [95] T. Lévèque, A. Gauguet, F. Michaud, F. P. D. Santos and A. Landragin, “Enhancing an atom interferometer area using double-diffraction”, arXiv:0904.3266v1, 2009.

## Bibliography

- [96] M. Kasevich, “Various links to recent presentations of Kasevich”, Online, 2006-2008, [http://www.fi.infn.it/GGI-grav-space/EGS\\_w/pdf/kasevich.pdf](http://www.fi.infn.it/GGI-grav-space/EGS_w/pdf/kasevich.pdf) or <http://inpa.lbl.gov/blnv2/files/Friday/Session9/Kasevich.pdf> or [http://www.physics.ucla.edu/quantum\\_to\\_cosmos/q2c06/kasevich.ppt](http://www.physics.ucla.edu/quantum_to_cosmos/q2c06/kasevich.ppt) or <http://scpnt.stanford.edu/pnt/PNT08/Posters/SCPNT-EPposter2008.pdf>.
- [97] G. Stedman, K. Schreiber and H. Bilger, “On the detectability of the Lense-Thirring field from rotating laboratory masses using ring laser gyroscope interferometers”, *Classical and Quantum Gravity*, 2003, vol. 20, no. 13, pp. 2527–2540.
- [98] A. Vogel et al., “Bose-Einstein condensates in microgravity”, *Appl. Phys. B*, 2006, vol. 84, pp. 663–671.
- [99] T. van Zoest, “Realisierung erster quantenentarteter Gase unter Schwerelosigkeit”, Ph.D. thesis, Gottfried Wilhelm Leibniz Universität Hannover, 2008.
- [100] T. van Zoest, “Pilotproject "QUANTUS", QUANTensysteme Unter Schwerelosigkeit”, in “DPG Frühjahrstagung 2008”, Presentation, 2008 URL <http://www.iqo.uni-hannover.de/quantus/Quantus%20-%20Publications.html>, a corresponding article is in preparation (T. van Soest et al, "BEC in microgravity").
- [101] A. E. Leanhardt, T. A. Pasquini, M. Saba, A. Schirotzek, Y. Shin, D. Kielpinski, D. E. Pritchard and W. Ketterle, “Cooling Bose-Einstein condensates below 500 picokelvin”, *Science*, 2003, vol. 301, pp. 1513–1515.
- [102] E. Streed, A. Chikkatur, T. Gustavson, M. Boyd, Y. Torii, D. Schneble, G. Campbell, D. Pritchard and W. Ketterle, “Large atom number Bose-Einstein condensate machines”, *Review of Scientific Instruments*, 2006, vol. 77, p. 023106.
- [103] M. Horikoshi and K. Nakagawa, “Atom chip based fast production of Bose-Einstein condensate”, *Applied Physics B*, 2006, vol. 82, pp. 363–366.
- [104] Based the location of the lab on <http://maps.google.com>.
- [105] D. A. Steck, “Rubidium 85 D line data, revision 0.2”, Online, 2008, URL <http://steck.us/alkalidata/rubidium85numbers.pdf>.
- [106] F. Hasselbach and M. Nicklaus, “Sagnac experiment with electrons: Observation of the rotational phase shift of electron waves in vacuum”, *Physical Review A*, 1993, vol. 48, no. 1, pp. 143–151.
- [107] K. G. Libbrecht and J. L. Hall, “A low-noise high-speed diode laser current controller”, *Review of Scientific Instruments*, 1993, vol. 64, no. 8, pp. 2133–2135.

# Curriculum vitae

## Personal data:

Name: Thijs Jan Wendrich  
Born: Feb. 12. 1980 in Dordrecht, the Netherlands  
Nationality: Dutch

## Doctoral studies:

Since Mai 2004 PhD student at the Institute of Quantum Optics of the University of Hannover in the group of Prof. E.M. Rasel  
Title of the thesis: "High resolution rotation sensor based on cold atom interferometry"

## University education:

1998-2004 Study of "Technische Natuurkunde" (Applied Physics) at Delft University of Technology, Delft (the Netherlands)  
Jan. 2004 Diploma: Master of Science  
Title of the thesis: "Frequency locking a diode laser to a high finesse Fabry-Perot cavity"  
Sept.-Dec. 2002 Internship at Océ Technologies, Venlo (NL)  
Sept. 2001 Diploma: Bachelor of Science  
Sept. 1999 Diploma: Propedeuse, with honours

## Schooling:

-1998 VWO, Farel College, Ridderkerk (NL)

# List of publications

- T. Müller, M. Gilowski, M. Zaiser, T. Wendrich, W. Ertmer, E. M. Rasel, "A compact dual atom interferometer gyroscope based on laser-cooled rubidium", *Eur. Phys. J. D*, 53, 273-281 (2009).
- T. Wendrich, M. Gilowski, C. Schubert, E. M. Rasel, W. Ertmer, "High Resolution Cold Atom Rotation Sensor", *EFTF 2008*, (2008)
- M. Gilowski, T. Wendrich, T. Müller, Ch. Jentsch, W. Ertmer, E.M. Rasel, W.P. Schleich, "Gauss sum factorization with cold atoms", *Phys. Rev. Lett.* 100, 030201 (2008).
- T. Müller, T. Wendrich, M. Gilowski, C. Jentsch, E.M. Rasel, W. Ertmer, "Versatile compact atomic source for high resolution dual atom interferometry", *Phys. Rev. A* 76, 063611 (2007).
- M. Gilowski, Ch. Schubert, M. Zaiser, W. Herr, T. Wubbena, T. Wendrich, T. Müller, E. M. Rasel, W. Ertmer, "Narrow bandwidth interference filter-stabilized diode laser systems for the manipulation of neutral atoms", *Optics Communications* 280, 2, 443, (2007).
- T. van Zoest, T. Müller, T. Wendrich, M. Gilowski, E. M. Rasel, T. Köne-  
mann, C. Lammerzahl, H-J. Dittus, A. Vogel, K. Bongs, K. Sengstock, W.  
Lewoczko, A. Peters, T. Steinmetz, J. Reichel, G. Nandi, W. Schleich, R.  
Walser, W. Ertmer, "Developments toward atomic quantum sensors", *Proc.*  
*SPIE* 6483, 648306-1-7, (2007).
- M. Gilowski, T. Müller, T. Wendrich, C. Schubert, W. Herr, E. M. Rasel,  
W. Ertmer, "High-resolution Sagnac interferometry with cold atoms", *CLEO*  
*Europe / IQEC 2007*, 925, (2007).
- A. Giorgini, F. Sorrentino, M. de-Angelis, M. Prevedelli, M. Schmidt, A.  
Senger, E. Kovalchuk, V. Josse, R. Nyman, P. Lugan, J. P. Brantut, F.  
Impens, A. Gauguet, J. Le-Gouet, F. Pereira-Dos-Santos, T. Mehlstauble,  
M. Zaiser, T. Müller, T. Wendrich, P. Bouyer, A. Landragin, A. Peters, E.  
M. Rasel, W. Ertmer, G. M. Tino, "Future inertial atomic quantum sensors:  
state of art", *CLEO Europe 2007*, 934, (2007).
- T. Wendrich, M. Gilowski, T. Müller, W. Herr, C. Schubert, E. M. Rasel,  
W. Ertmer, "Cold atom Sagnac interferometer", *EFTF 2007*, 647, (2007).

## *Bibliography*

- T. Müller, T. Wendrich, M. Gilowski, C. Jentsch, E. M. Rasel, W. Ertmer, "Sagnac interferometry with cold atoms", EQEC 2005, 239, (2005).
- B. L. Swinkels, T. J. Wendrich, N. Bhattacharya, A. Wielders, and J. J. M. Braat, "Absolute distance metrology for space interferometers", Proc. SPIE 5495, 314-318 (2004).
- B. L. Swinkels, T. J. Wendrich, N. Bhattacharya, A. Wielders, and J. J. M. Braat, "Absolute distance metrology for space interferometers", ICSO 2004, 559-61, (2004).

# Acknowledgments

Writing a PhD-Thesis, and especially doing the research for it, is not something done by a single individual, even though it may look like that, there is a larger team behind it. Therefore I would like to thank a lot of people for making it possible.

First of all I should thank the professors Rasel and Ertmer for enabling me to study here and to provide the means of doing research without significant restrictions. Especially my direct supervisor Prof. Rasel should be thanked, for convincing me make my PhD here and for taking care of us when we had questions despite his interesting sense of time.

An experiment of this size can not be build nor maintained by one person alone; I must thank my colleges of the CASI experiment. It would not have been possible without them. They toke care of the optics when I was adding or repairing another piece of the electronics, or extending the software. The team has grown tremendously by now: four PhD students: Michael Gilowski, Christian Schubert, Gunnar Tackmann, Peter Berg, three diploma students Timmo Denker, Sven Abend, Manuel Popp and one exchange student John Debs (JD) from Australia. I also thank my predecessors Christian Jentsch and Tobias Müller for laying the foundations of the experiment.

More thanks go to my colleagues Michael Gilowski and Christian Schubert for reading the manuscript, and to Wouter van Drunen for his comments on the Dutch abstract.

For their support during the precision measurements of the frequencies of the lasers, I must thank the magnesium clock experiment.

The institute of quantum optics has provided a very encouraging environment to discuss many ideas with colleagues, to solve practical laboratory problems, as well as about more exotic and far future ideas. I therefore also thank the many colleagues of the other experiments of the institute that together have created this supportive environment.

I also wish to thank the mechanical workshop for their assistance in realizing the mechanical parts of the experiment, Kai-Martin Knaak for the lively discussions about electronics, and the secretaries for supporting us on the administrative side, and keeping order in our business.

Finally I want to thank my parents and my brother for supporting me.

